Compressive Failure Mechanics of Ice During Particle Embedment

By

Thomas Fitzpatrick

A thesis submitted to the

School of Graduate Studies

in partial fulfillment of the requirements for the degree of

Master of Engineering

Faculty of Engineering and Applied Science

Memorial University of Newfoundland

February 2024

St. John's Newfoundland

Abstract

In total, sixty-six (66) single particle tests were conducted with up to 10 repetitions per setpoint, and fifty-five (55) multi-particle tests were conducted including repetitions with twenty-five (25) being completed on pristine ice specimen. These small-scale ice-particle indentation tests have been completed in order to study the compressive failure of polycrystalline ice during rock indentation. These tests were conducted using a population of rock particles to explore the link between various parameters that influence the ice failure processes and the effect that the presence of these rocks may have on them. In this research program, parameters such as average rock diameter, temperature, indentation rate, indentation depth, and relative spacing of indentation zones from previously formed damage zones are considered as controlled variables.

For all experiments, rocks were taken from a population with diameters which were determined to be between 3/8" and 3/4", based on statistical analysis of the population. Three setpoint indentation rates were imposed, a slow rate of 0.01 mm/s, a moderate rate of 0.5 mm/s, and a fast rate of 10 mm/s. While for single particle indentation tests multiple rates were investigated, only a single representative rate of 0.5 mm/s was implemented for multi-particle tests. Tests were conducted at a nominal setpoint temperature between -10°C and -13°C. Single particle tests were completed at indentation positions 2D (26 mm). 5D (65 mm), and 7D (96 mm) away from previously formed damage zones, based on an average diameter D of 13mm. Two grain size ranges were considered for these tests. The total force and pressure were found to show dependencies on the indentation rate. Multi-particle tests were completed with constant weighed population of 170-grams of rocks taken from the same population of diameters between 3/8" and 3/4".

Analysis on all results obtained in the form of force trace data from the MTS, pressure data determined based on the forces observed, and analysis of images taken after indentation has been completed. Representative cases are outlined and described in this work for each combination of constants. Further analysis was completed on the outcomes of both multi-particle and single particle indentation tests, as well as comparisons between the two. Strong rate dependence was observed in the force and pressure data for single particle indentation tests, with observed forces and pressures trending upwards with increased rate until 0.5 mm/s and subsequently decreasing as rates approached 10 mm/s. These forces and associated trends from the MTS data were noted to be consistent with those observed during spherical steel indenter tests reported in the literature, and a comparison between the two is presented in this work. It was also determined that the effect of spacing from previously formed damage zones on single particle indentation was not significant; therefore, indentation events were assumed to be approximately independent. This was examined further based on a comparison with multi-particle indentation tests, since the trends observed in the data traces from these tests were consistent with those observed during single-particle testing. This led to the development of an empirical model which simulated multiparticle indentation based on an aggregation of previously completed single particle indentation tests. Using the assumption of independent indentation events, the simulated multi-particle events were compared with test data from laboratory experiments on multi-particle indentation. These comparisons yielded strong similarities between simulated and experimental results, further supporting the assumption of independence of indentation events for multi-particle indentation. The outcomes of this research will support a deeper understanding of the mechanics of a collision between offshore structure and ice feature with embedded rocks. Full details of these investigations are presented in this thesis.

Acknowledgements

I would first like to express my sincere gratitude to my supervisor Dr. Rocky Taylor for his continued and dedicated support, guidance, and instruction throughout the duration of my Master's program. I am truly grateful for the sharing of invaluable knowledge and advice in the areas of ice mechanics, compressive failure, experimentation, data analysis, and academic writing. I would like to show the deepest appreciation to Memorial University of Newfoundland for providing use of the cold room and associated facilities as well as an excellent place and environment to pursue my Master's degree. I would also like to thank C-CORE and Mr. Jan Thijssen of C-CORE for their continued guidance and support on this collaboration. Additionally, I would like to extend my gratitude to Mr. Craig Mitchell, and Mr. Matt Curtis of Memorial University of Newfoundland as well as Mr. Pritom Chakraborty for their guidance and assistance during laboratory testing at Memorial University. I would also like to thank past work term students Mr. Connor Kavanagh, Mr. Tyler Decker, Mr. Noah Marshall, and Mrs. Catherine Joseph for their assistance during experimental work. Similarly, I would like to thank everyone in the Ice Mechanics group for continued feedback and sharing of ideas. Funding for this work from Innovate NL, the Natural Sciences and Engineering Research Council (NSERC) of Canada, and Hibernia Management and Development Company Ltd. (HMDC) are gratefully acknowledged.

I would like to extend my sincere thanks and gratitude to my parents Janet and Mario Fitzpatrick for their unconditional support and encouragement through this thesis program and in everything I do. A special thanks as well to my entire family, to my dear friends, as well as my partner Kayla for their assistance, support, and inspiration through this all. None of this could have been possible without these people.

Table of Contents

List of Figures

List of Tables

List of Abbreviations and Symbols

E	Young's modulus
ν	Poisson's ratio
$\dot{\varepsilon}$	Strain rate
σ	Stress
P	Pressure
T_m	Melting temperature of ice in kelvin
p	Hydrostatic pressure
V_w	Specific volume of water
V_i	Specific volume of ice
S_i	Entropy of ice
S_w	Entropy of water
A	Constant representing change in Volume/Entropy term
hpz	High Pressure Zone
CHC	Canadian Hydraulic Center
NRC	National Research Council
D	Mean diameter of rock particles
D_N	Nominal diameter of rock particles
D_v	Vertical diameter of rock particles
D_H	Horizontal diameter of rock particles
r	Radius of rock particles
R	Effective radius of rock during indentation

A_N	Nominal surface area of rock
F	Load cell force
V_d	Vertical indentation depth
H_d	Horizontal distance
T	Hold time
S	Damage zone spacing distance
v	Indentation rate
n	User-prescribed number of rocks in a given simulation
D_i	Generated ‘n’ rock diameters in a given simulation
C_{gi}, I	Distance from upper ice specimen to each rock
G	Largest rock diameter in simulation population
d_{ind}	Indentation depth each rock indents into the ice specimen
NSERC	Natural Sciences and Engineering Research Council of Canada
HMDC	Hibernia Management and Development Company Ltd.
MTS	Materials Testing System
MUN	Memorial University of Newfoundland

1. Introduction

1.1 Overview

The aim of this research program is to understand local ice pressure created when soil (gravel) particles are compressed between two ice blocks. The purpose of these tests is to physically model ice-seabed interaction processes in a controlled environment. Experiments were conducted using a high-capacity MTS load frame in the cold room facility (walk-in refrigeration unit) located in Memorial University's thermodynamics laboratory. The MTS load frame facilitated the loading of ice blocks to simulate indentation forces caused by embedded soil particles. When embedded soil particles are compressed by an ice feature, local pressures occur at the ice-particle interfaces. These contact forces between the block and the soil will change based on how deep, how fast, and how long the embedment process is. This research explores how these local pressures affect the adherence of soil particles to ice features and their strength. The investigation of indentation of rock particles into ice is an important aspect of understanding subsea interactions involving ice features and gravelly soil. This thesis investigates the indentation of rock particles into an ice specimen, where observations are made to study the effect of changes in indentation rate and the relative spacing from previously formed damage zones on resulting force and pressure trends. Given that real ice-soil interactions will involve a multitude of individual ice-particle interactions, one of the primary aims of these tests is to assess the influence of distance between indentation sites to evaluate if multipoint ice-rock contacts may be modelled as the sum of independent, individual ice rock particle contacts. Single ice-particle indentation test results were initially considered separately and then compared with multi-contact ice-particle interactions. The research outlined in this thesis will inform future research on the nature of subsea interactions of icebergs with the ocean floor, and how this may affect potential risks related to subsea installations.

1.2 Background

When drifting ice features interact with the ocean floor, a phenomenon known as scouring occurs. This causes the soil on the ocean floor to form a furrow around the contact interface and leads to an accumulation of soil and gravel particles, which may embed themselves into the ice and potentially freeze into the feature. Should such ice surfaces subsequently come into contact with engineered structures, these embedded particles would be placed under pressure and could serve as “hard points” through which local pressures are transmitted. Such particles have the potential to result in the creation of an “armored” ice layer that could increase local pressures transmitted through the ice. At the same time, they may act as stress concentrators that weaken the ice and reduce peak local ice pressures. To better understand processes associated with such interactions, a series of experiments have been conducted to study the initial phase of ice particle embedment through compressive ice indentation tests on rock particles.

Ice behavior is strongly dependent on loading rates, and it is observed that the deformation of ice will be dominated by viscoelastic processes for low strain rates. Similarly, if strain rate is increased the effects of fracture, damage, and microstructural change become more prominent (Schulson & Duval, 2009). Ice failure and deformation processes during compressive ice loading are quite complex and during interactions with offshore structures produce intense local and global loads that often dominate design (ISO 19906, 2019). When ice fails compressively, small zones of high pressure are formed as a result of contact localization due to the creation of spalls and splits (Jordaan., 2001). These high-pressure zones (hpzs) are the features through which the majority of ice loads are transmitted. These hpzs have been observed to cover only 10% of the global interaction area (Taylor & Richard, 2014). Spalling or crushing are associated with various mechanisms such as microfracture, macrofracture dynamic recrystallization and localized pressure

melting, and significantly influence hpz formation and development (ISO 19906, 2019) (Jordaan., 2001) (Taylor & Richard, 2014).

1.3 Objectives

The focus of this research program is to increase the understanding of the compressive failure of ice in the presence of rock particles(s) by analyzing the local ice pressure created by soil (gravel) particle(s) when compressed between two ice blocks as an approximation for the mechanics which occur during scour. The primary aim of this research is to primarily explore how these local pressures affect the adherence of soil particles to ice features and the strength of these bonds. The overall objectives of this thesis are to:

- Examine the local pressure soil (gravel) particle(s) induce on the block samples.
- Examine the adherence strength of soil (gravel) particle(s) to the ice block samples.
- Analyze how the contact pressure imparted by soil particle(s) between two ice blocks evolve as the depth of embedment and pressure are increased.
- Examine the effects of soil particle types in terms of the size, shape, and dispersion.
- Assess the properties that affect the degree of embedment bonds and embedment depth.
- Investigate the interaction effects and local/global pressures of rocks in multiple particle embedment in an ice feature.
- Investigate effects embedment depth and rock pressures transmitted from ice features may have on a subsea pipeline or structure in the event of a collision.

1.4 Research Scope and Outline

The research presented in this thesis is focused on the investigation of the effects of rock particle indentation on ice samples, specifically concerning the crushing and fracture mechanics of the ice during compressive loading. A series of small-scale laboratory experiments were conducted in

which both single and multiple rock particle samples were compressed between two ice samples. The experiments were performed in the cold room facilities of Memorial University of Newfoundland using a Materials Testing System. This thesis aims to investigates the indentation of rock particles into an ice specimen, where observations are made to study the effect of changes in indentation rate and the relative spacing from previously formed damage zones on resulting force and pressure trends. These observations taken from single particles tests were subsequently compared to those observed in multiple particle tests. Based on the investigation of these tests, analyses of the local pressures and mechanics of indentation at the ice contact interface will be used to infer the potential mechanics of impact on a subsea structure or pipeline should an ice feature with embedded rocks come into contact.

This thesis has been categorized into six chapters. In Chapter 1, an introduction and outline of the research program has been provided. Chapter 2 consists of a review of relevant literature on ice mechanics, damage mechanics and fracture mechanics, including mechanical properties and behaviour of ice and compressive ice failure processes. Previous indentation test programs relative to the present program have also been reviewed. A detailed description of experimental methodology including the test set-up, procedures of ice preparation, testing and post-experimental works have been provided in Chapter 3. In Chapter 4, the test matrix for this research program and sample test results have been presented for both single and multiple particle tests. In Chapter 5, a detailed analysis of the results including observations of ice failure mechanisms and the effects of indentation rate, relative particle spacing from previously formed damage zones, single particle indentation and multiple particle indentation, and imposition of horizontal motion have been provided with comparison to the empirical model. A summary of the main findings and results have been discussed in Chapter 6 including conclusions and recommendations for future work.

2. Literature Review

This chapter serves to provide an accurate review of information that defines the background of contemporary research surrounding particle embedment and local ice pressure of armoured ice structures. This section also provides information related to this thesis research, and background experimentation done on topics related to the present work in order to expand the current understanding of the processes of particle embedment and local ice pressure of armoured ice structures.

Based on the review of selected sources and references, a review of knowledge gaps in these references was prepared to outline any missing information or details. By outlining experimental factors, variables, processes, and constraints in related research, any issues or limitations of these experiments were defined. Additionally, missing considerations in these previously identified processes that are important to particle embedment and local ice pressure of armoured ice structures have been outlined and defined. This help to identify specific research needed to develop a deeper knowledge base surrounding the relevant topics.

After all relevant information was reviewed, an overview of the up-to-date knowledge base surrounding the topic of particle embedment and local ice pressure of armoured ice structures was prepared. The review below summarizes new information for applications related to the study area and expands on how research should be focused moving forward to address any additional gaps.

2.1 Iceberg Subsea Interaction and Scour Mechanics

This section provides background information on details related to iceberg scour, primarily in the regions surrounding the Grand Banks and the Labrador Shelf. This section is not intended to be an exhaustive review of the subject matter but rather gives insight into the background and limiting

boundary conditions imposed by iceberg scour on soil particle embedment and related scour phenomena.

2.1.1 Background Information on Iceberg Scour

Icebergs form when masses of ice calve from glaciers, and the majority of icebergs in the North Atlantic originate from the west coast of Greenland, where iceberg production is concentrated in 21 glaciers (Murray, 1969). General estimates posit that it takes approximately three years for an iceberg to drift from its source glacier to the Grand Banks region (Kollmeyer, 1977). When these Icebergs begin drifting in oceanic and wind-driven currents, they have the potential to impinge upon the seafloor in water depths up to and occasionally exceeding 500 m (Woodworth-Lynas, 1992). Specifically, when an iceberg drifts into a water depth that is less than its draft, the keel can displace the sediment to form a scour or pit feature (King, 2002). This phenomenon, when occurring where seafloor sediments are unconsolidated, causes the ice keels to penetrate and plough forward creating curvilinear iceberg scour marks that are commonly tens of metres wide, 1-2 m deep and often several hundred meters (or even several kilometers) long (Woodworth-Lynas, 1992).

The scouring or pitting of icebergs causes the sediment and soil on the ocean floor to form piles and build up and eventually adhere into the ice feature; thus, forming an accumulation of soil particles which have imbedded themselves into the ice, and similarly freeze deeper into the feature. When these soil particles are placed under pressure (during the adhering process and after they have adhered) they create local pressures, which have the potential to result in the creation of an armoured ice structure or to act as weakening stress concentrations; Therefore, it is important to

understand the mechanics of iceberg scouring, a schematic of which can be seen below in Figure 1.

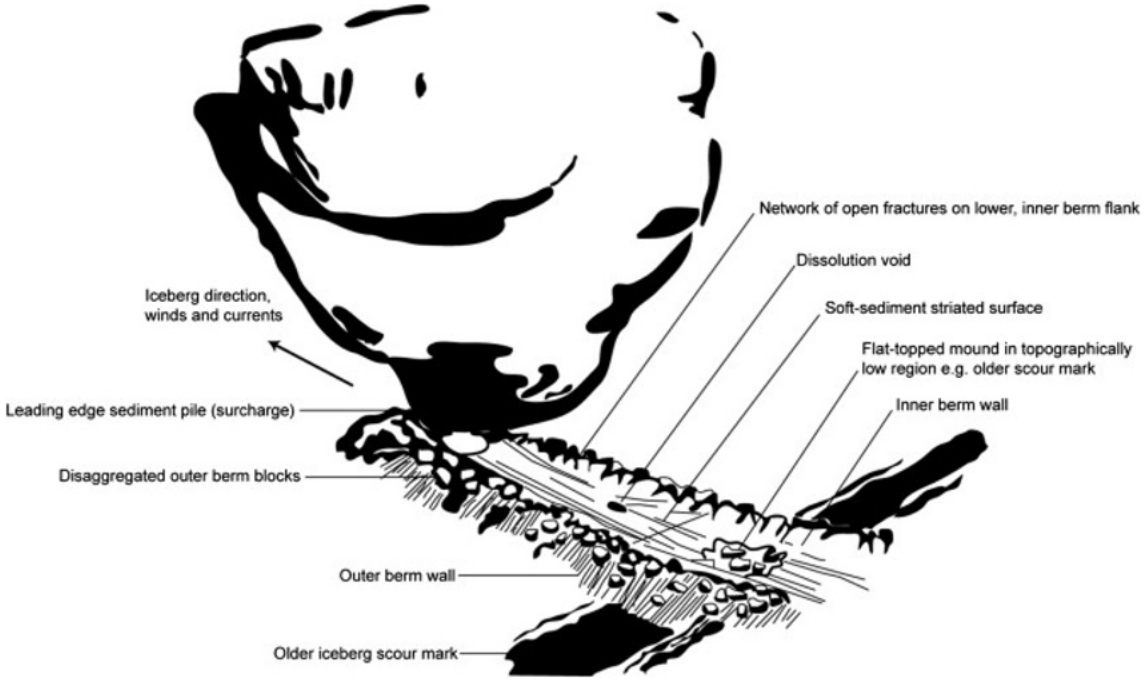

Figure 1- Iceberg scour through fine sediment (Woodworth-Lynas, 1992)

The iceberg conditions on the Labrador Shelf are much more severe than those on the Grand Banks, as Icebergs are more frequent than on the Grand Banks and the density of scours visible on the seabed is greater (King, 2002). Therefore, the focus of reported data on scour by King (2002), was centered on the Labrador Shelf, however information relevant to the Grand Banks will also be investigated. A number of specific aspects related to iceberg scour are of importance to understand the physical processes involved, and how they relate to soil embedment procedures and related embedment pressures. These include parameters such as how long, deep, wide, and frequent the iceberg scours are, as well as the drift speed at which the icebergs move.

2.1.2 Iceberg Scour Parameters and Topography

The typical scour topography seen in the areas surrounding the Grand Banks and Labrador Shelf regions are important to understand in order to apply these physical parameters to how the soil particles can potentially adhere to the iceberg itself. Figure 2 below gives a physical representation of a potential iceberg scour, and outlines how different scour profile shapes, lengths, widths, and depths can be obtained. Similarly, the shape of these profiles can be affected by the speed at which the iceberg drifts.

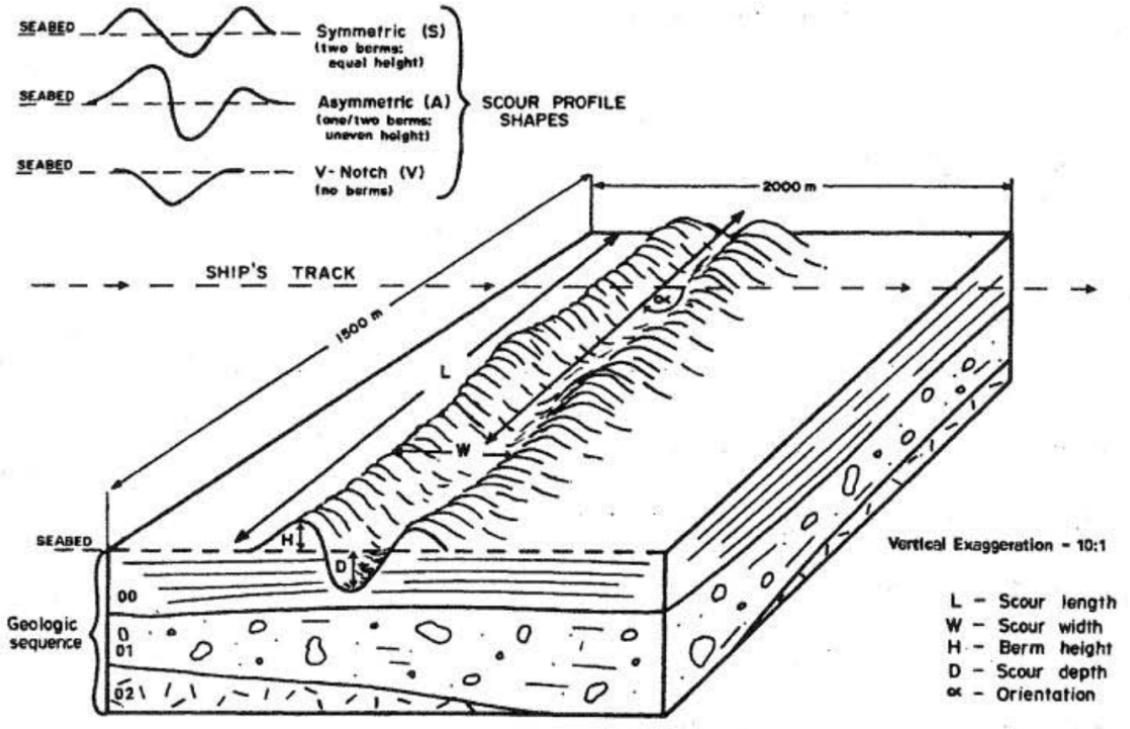

Figure 2 – Iceberg scour topography and dimensions (Geonautics, 1989)

King (2002) identified a number of studies which outlined scour parameters in pertinent study areas such as the Grand Banks and areas surrounding the Labrador Shelf. The main data sources and studies investigated by King (2002) included primarily the DIGS Mosaics, the Bjarni survey, the North Bjarni survey, the Grand Banks catalog, and regional ice scour database. This section

focuses on data for the Grand Banks region, with reference to the Bjarni regions as well. This information was implemented to develop a detailed risk assessment concerning the risk of impact of a scouring iceberg with a subsea pipeline, however, for the purposes of this thesis specific data which was aggregated for supporting this risk assessment proved more important to consider. One notable set of data concerning scour which was presented by King (2002) which was important for considerations surrounding armoured ice structure and iceberg-seabed interaction is mean scour lengths and iceberg drift speed for the Grand Banks regions, with considerations for the Makkovik bank as well.

King (2002) reported that, for the entire Grand Banks region, the mean scour length is 622 m, based on 2910 records. Additionally, it was noted that there was no significant observed relationship between scour length and water depth. The agreement between the Grand Banks means scours length and the mean scour length in the Bjami mosaic was considered, where it was observed that this relationship is reasonably good. Scour lengths were observed by King (2002) to be larger in the Grand Bank than on the Makkovik Bank which was said to be due to observed iceberg drift speeds on the Grand Banks which were roughly 0.34 m/s on average, which are higher than those on the Makkovik Bank, roughly 0.24 m/s; therefore, these would be expected to produce longer scour lengths, outlining an important relationship between scour length and iceberg drift speed which can extend to the expected forces which would be seen.

Overall, there has been much investigation into the details of iceberg scour and their mechanics; subsequently these details served as a beneficial starting point for considering the limiting boundary conditions on which particle adhesion is facilitated. With these boundary conditions

understood, considerations for previously completed studies of normal ice loading and crushing, as well as shear-frictional interaction of ice, provided a deeper understanding of the forces and trends involved in these types of interactions.

2.1.3 Local and Gload Pressure Effects for Ice-Structure Interaction Models

When considering crushing failure of ice against a structure or otherwise, for the global interaction area and local design, as described by Jordaan et al. (2005), area must be precisely defined in order to correctly determine related failure pressures and forces. These concepts discussed by Jordaan et al. (2005) and Murray (1969) relate directly to two types of loads, global loads, representing the maximum total force applied to the structure; local loads, representing the maximum force (or pressure) on particular areas of structural importance such as the plate between frames or other assemblies of structural elements considered important in design.

The global interaction area, described by Jordaan et al. (2005) as the nominal interaction area, is the area determined by the projection of the structure onto the original shape of the ice feature, without any reduction of the area for spalls and fractures that take place during the interaction. This can be seen in the schematic shown in Figure 3 below where the plane of interaction between an iceberg and a structure is defined.

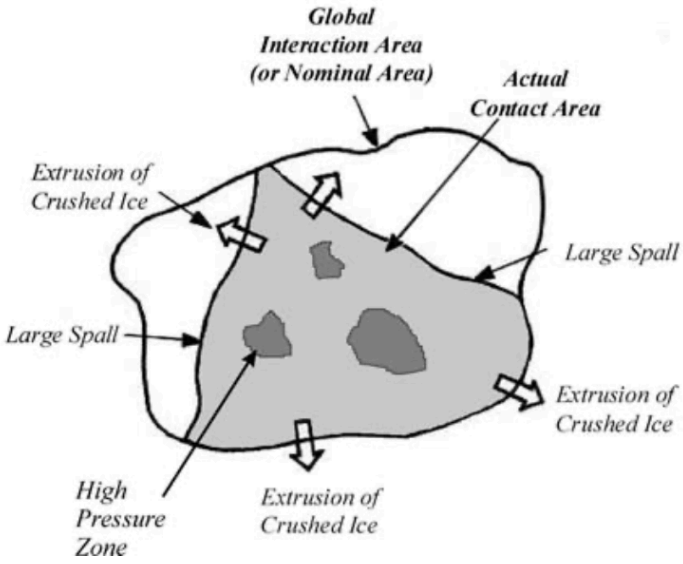

Figure 3 – Interaction plane between an iceberg and structure, Jordaan et al. (2005).

Within this global interaction area, there are smaller areas that are subjected to high local pressures which are considerably higher than the global average pressure. When designing, the local design area is important to consider as it acts as an expression for an area of a panel or the plating between frames on the structure to be designed, Jordaan et al. (2005). Estimated pressures on a local design area are expressed through this model for local design areas which can be seen in Figure 4 below, where the local area of high pressure which will be investigated for this model is isolated in the fixed structure.

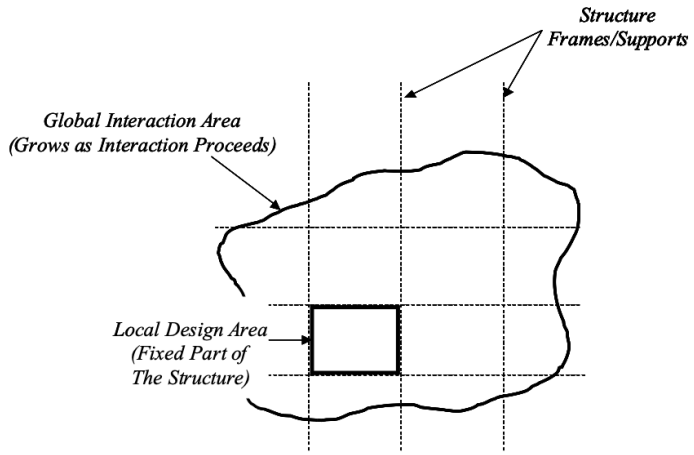

Figure 4 – Local pressure area design model, Jordaan et al. (2005).

These global pressures described by Jordaan et al. (2005) are typically represented for areas from ten square meters to hundreds of square meters, whereas the local pressures are associated with areas from 0.6 m^2 to 10 m^2. Designing for local pressure is an important factor in ice mechanics because the global loads are the sum of local loads.

2.2 Ice Mechanics

The unique mechanical properties of ice are important to understand when designing for the offshore environment as the potential for damage due to ice features in northern environments proposes a significant challenge to operations in these regions. An understanding of the details of ice mechanics and failure modes such as compressive and shear-friction failure of ice are integral for being able to predict and design for ice loads and interactions with offshore infrastructure. To outline these important details, a background review of relevant details of ice mechanics have been summarized in this chapter. Specifically, the mechanical behaviour and properties of ice are discussed, including the elastic and viscoelastic nature of ice as well as of the damage mechanics of ice with a focus on compressive failure. Background of these failure modes including related high-pressure zone, recrystallization, and pressure melting phenomena is included. Details of pressure-area models and ice strain-rate behaviour are outlined in order to highlight the relations between the ice failure modes and behaviour of ice interactions.

2.2.1 Mechanical Behaviour and Properties of Ice

Ice is an incredibly complex material, which behaves differently based on changes in material conditions such as temperature, loading rate, microstructure, and geometry. Ice under specific conditions may exhibit a variety of mechanical properties, including elasticity, viscoelasticity,

creep rupture and brittle failure (Schulson & Duval, 2009). Models of elasticity, viscoelasticity, and damage mechanics have been implemented in combination or individually in order to describe the complex behaviours of ice. These behaviours can be seen to be dependent on a number of factors including the relative stresses and loading rates of the ice. For low stress and slow loading rates, ice is seen to be a creeping, ductile material. For high stress, and fast loading rates it is typically characterized as an extremely brittle material with its general behaviour being dependent on the rate of deformation as well as the deformation history (Sanderson, 1988). Specifically, at a low loading rate, viscoelastic theory can be implemented in order to model the deformation of ice under stress, where the irreversible flow term is highly non-linear and time-dependent (Jordaan., 2001).

In addition to the effects on the behaviour of ice due to different modes of deformation, these behaviours are also governed by the type of ice which is being studied. There are largely considered to be two forms of ice which are present in the ocean, namely glacial ice, and sea ice. Glacial ice features, such as icebergs or ice islands which are formed due to perennial snow accumulation that morphs into a statistically isotropic granular ice microstructure similar to polycrystalline freshwater ice and typically has a modulus of elasticity which ranges from 9.0 GPa to 9.5 GPa (Cammaert & Muggeridge, 1988). Sea ice is seen to form based on the seasonal cooling and freezing of sea water and possesses a modulus of elasticity in a much wider range from 0.3 GPa to 10 GPa (Cammaert & Muggeridge, 1988). The two primary types of fully formed sea ice are typically divided into first-year sea ice and multi-year sea ice. First-year sea ice is defined as sea ice which has grown for no more than one winter and is thicker than 30 cm. Multi-year ice is defined as sea ice which has grown for more than at least one winter, through a melt cycle, and

into another re-freeze. For the present work, ice bergs (glacial ice) are the main type of ice of interest.

2.2.1.1 Elasticity

The behaviour of ice is heavily dependent on the form of loading that is observed. Specifically, for fast loading cases, freshwater granular ice is normally treated as an isotropic elastic material (Schapery, 1997) in which this property of the elasticity of the ice is characterized by two constants defined as the Young's modulus E, and Poisson's ratio, v. This characterization of the elastic modulus of ice can be determined by two primary methods, which include materials testing in both static and dynamic modes. Based on these forms of experiments, investigations by Mellor (1983) into the Young's modulus of sea ice revealed through the use of high frequency dynamic measurements that for a temperature range of -5° to -10°C a Young's modulus was measured to be between 9 to 9.5 MPa and similarly that Poisson's ratio varies from 0.3 to 0.33 for low porosity polycrystalline ice. Similar experiments were also completed by Sinha (1989) who investigated the Young's Modulus and Poisson's ratio of ice for a temperature range of -50° to 0°C. These experiments revealed that the effect of temperature was not particularly significant on the property of the elasticity of the ice as the Young's modulus was seen to again vary from 9 GPa to 10.16 GPa and the Poisson's ratio was observed to vary similarly from 0.308 to 0.365.

2.2.1.2 Viscoelasticity and Creep Behaviour of Ice

Viscoelasticity and the creep behaviour of ice are two other important properties of ice which drastically effect its behaviour under loading. Specifically, viscoelasticity is typically described as the property of a material that shows both elastic and viscous characteristics while undergoing

deformation. Materials which possess viscoelastic properties exhibit a relationship between stress and strain which is dependent primarily on the time and frequency of applied loading; therefore, this results in these materials displaying a time-dependent material response, where the response of stress depends directly on the nature of the applied strain and the strain rate. Lockett (1972) presents details of viscoelastic materials and explains that for these types of materials: Strain increases with time when the stress is constant, known as creep; stress decreases with time when the strain is constant, known as relaxation; the effective stiffness has dependency on the rate of applied load; hysteresis occurs when cyclic loading is applied, and the area in the hysteresis loop is a function of the loading rate; and that after an impact, the rebound of an object is less than 100%. Such behaviours are common in materials such as ice that are at high homologous temperatures (ice is typically at between 95-98% of its melting temperature).

Ice, being a viscoelastic material, will exhibit these behaviours, including the time-dependent stress-strain behaviour. More specifically, if a fixed strain is applied, the ice will exhibit a time-dependent stress relaxation. The time dependant nature of the stress and strain relationship of ice can be seen in Figure 5 and Figure 6 below, where the different phases of creep and recrystallization of ice during deformation are outlined based on different ratios of stress and strain.

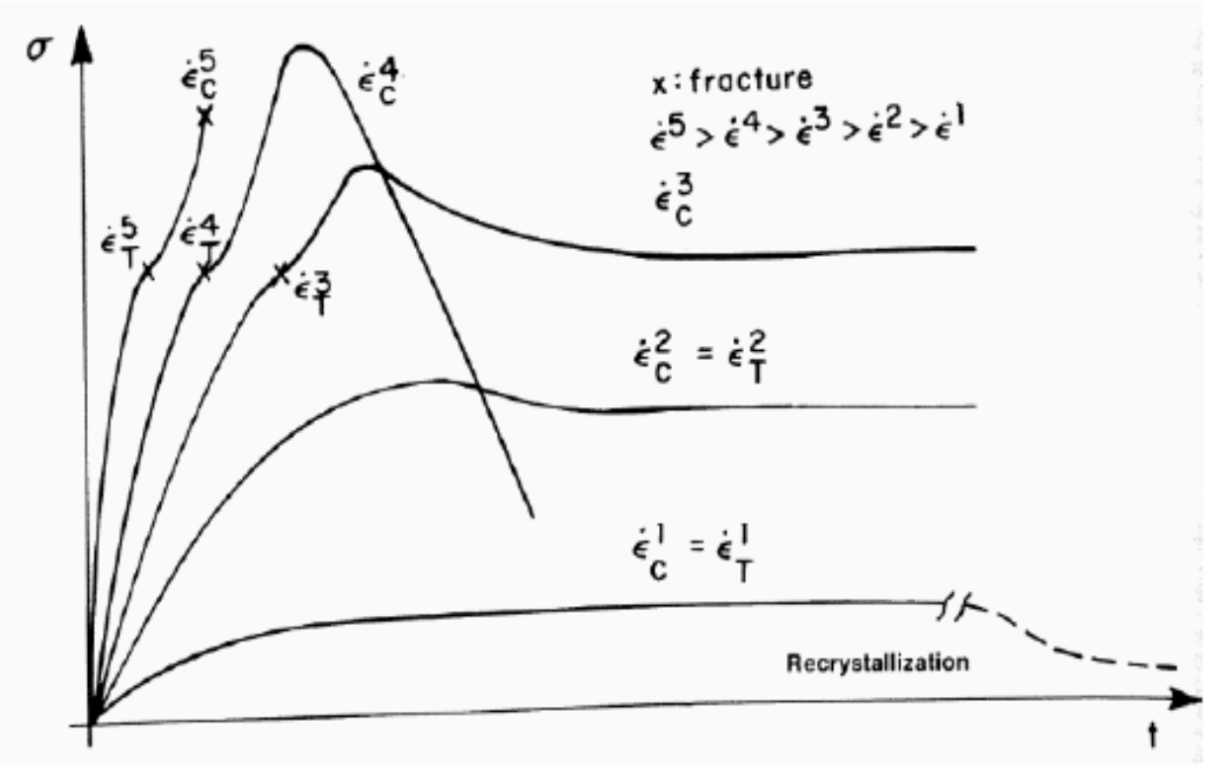

Figure 5 – Constant strain rate creep curve for ice (Nadreau & Michel, 1984)

As can be seen in Figure 5 above, for ice deformation under a constant strain rate, high strain rates will lead to a subsequent increase in the peak stresses which ultimately causes a transition to a brittle failure mode. Conversely, for low strain rates, the behaviour is observed to be purely creep, where the ice behaves similarly under tensile and compressive loadings. Finally, for intermediate strain rates, pressure softening is primarily observed and the response during compressive failure transitions to behaviour typically observed in the tensile mode.

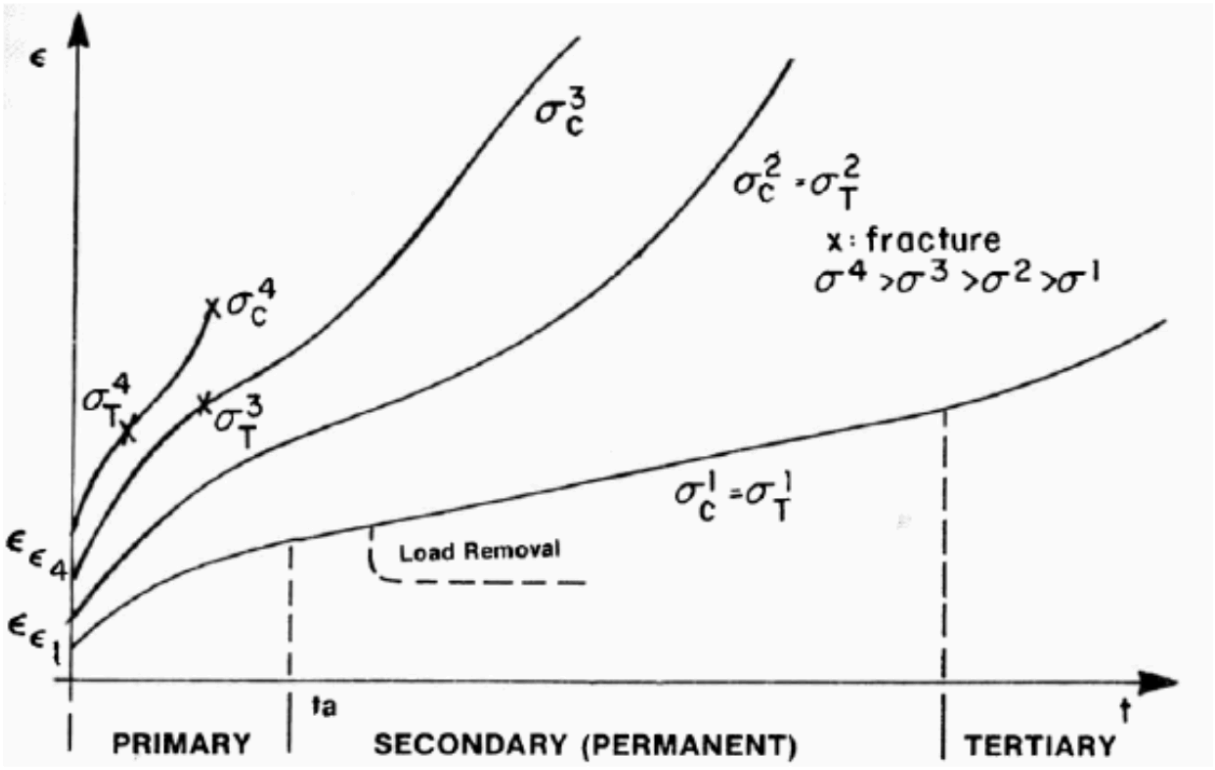

Figure 6 – Constant stress creep curve for ice (Nadreau & Michel, 1984)

Figure 6 above presents the different behaviour of ice under conditions of constant stress. In this plot, creep behaviour is divided into three specific components which consist of primary creep, secondary creep, and tertiary creep. Primary creep is associated with reversible grain boundary sliding that occurs when shear stresses act at grain boundaries, which result in time-dependent delayed elastic strain. This creep component occurs at the same time as elastic deformation of the grain, and in the case that compressive stresses are removed the grain will begin to attempt to recover its original shape (Sanderson, 1988). Secondary creep is described as the irrecoverable component of creep behaviour, and as the ice creeps at all stresses and shows no yield point it is highly nonlinear and time-dependent in this phase. Secondary creep is also known as steady-state creep, as it results in permanent deformation processes within the ice which subsequently give way

to irreversible rearrangements of the material (Nadreau & Michel, 1984). Finally, tertiary creep results from damage processes such as microcracking and dynamic recrystallization which effectively soften the ice and accelerate the associated strain-rates. While under conditions of constant stress, it can be seen above in Figure 6 that the ice begins to deform instantly due to a phenomenon of instantaneous elastic strain, which is then followed by time-dependent creep behaviour until the end of deformation (Nadreau & Michel, 1984).

2.2.1.3 Strain-Rate Behavior

During the indentation of ice, the indentation pressure, failure stress, and overall mechanisms of the ice are governed primarily by the indenter size, and the indentation rate. The effects of changes in indentation rate are shown in the Figure 7 below.

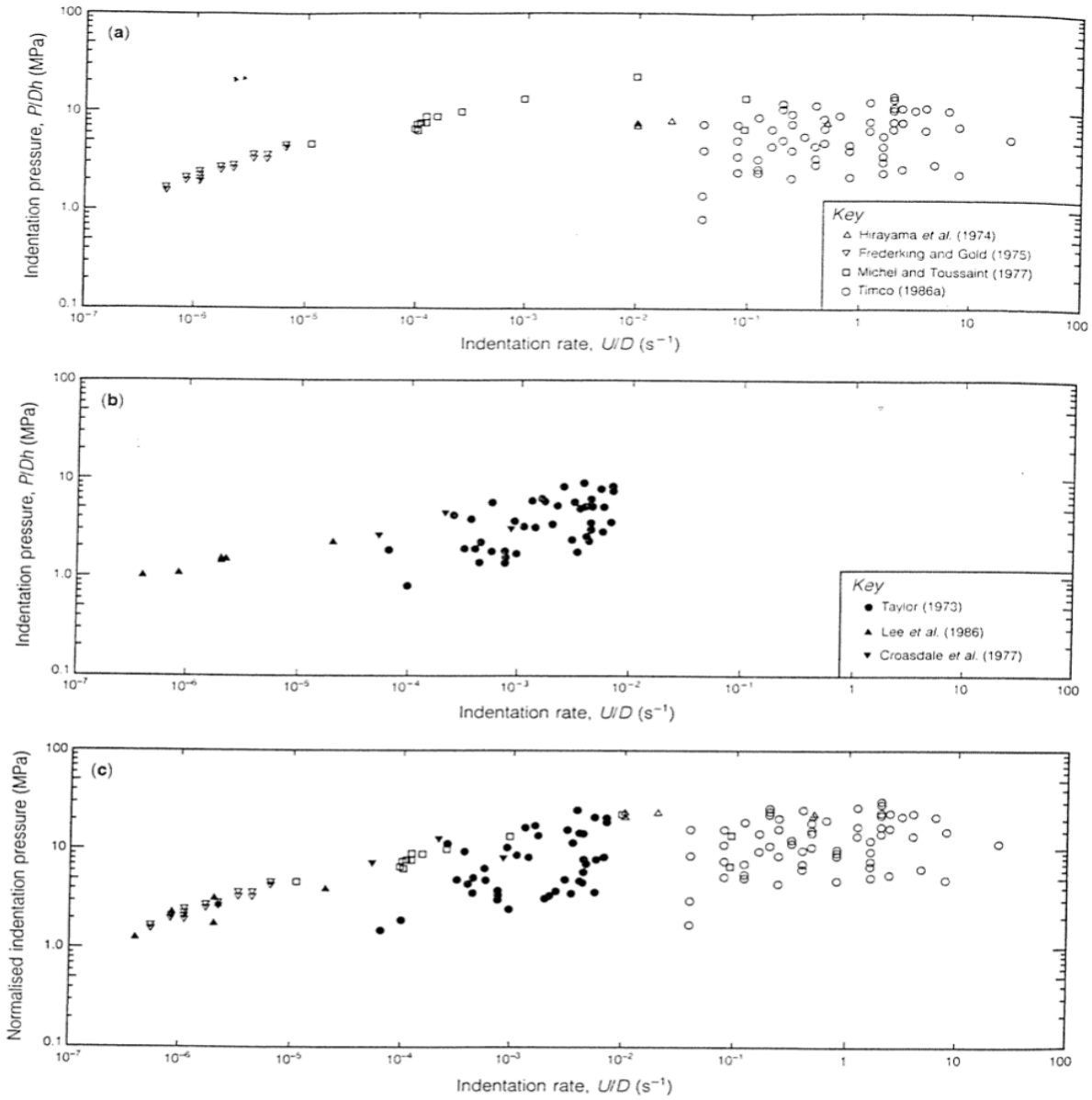

Figure 7 – Indentation data of indentation pressure (P/Dh) versus indentation rate (U/D) for (a) small-scale data measured in the laboratory for a number of experiments, (b) medium scale ice tests, and (c) combined small-scale and medium scale tests from (a) and (b) normalized to zero salinity and temperature of -10℃ (Sanderson, 1988)

The graph presented by Sanderson (1988) in Figure 7 above depicts indentation pressure plotted as a function of indentation rate; this plot outlines the relationship between the indentation rate and the indentation pressure observed in the interaction area. It can be seen that the pressures are relatively low overall at slow indentation rates, higher overall for moderate rates, and can be seen to be larger overall again but beginning to trend downwards at high rates.

These effects of indentation rate on the indentation pressures are related to similar phenomenon which are observed in the strain rate behavior of ice. As discussed previously, ice exhibits primarily ductile behaviour at lower rates of deformation and exhibits brittle behavior at higher rates of deformation. The plot presented by Schulson (2001) shown in Figure 8 below represents this phenomenon and relates this behavior to the ductile to brittle transition zones in the compressive failure of ice.

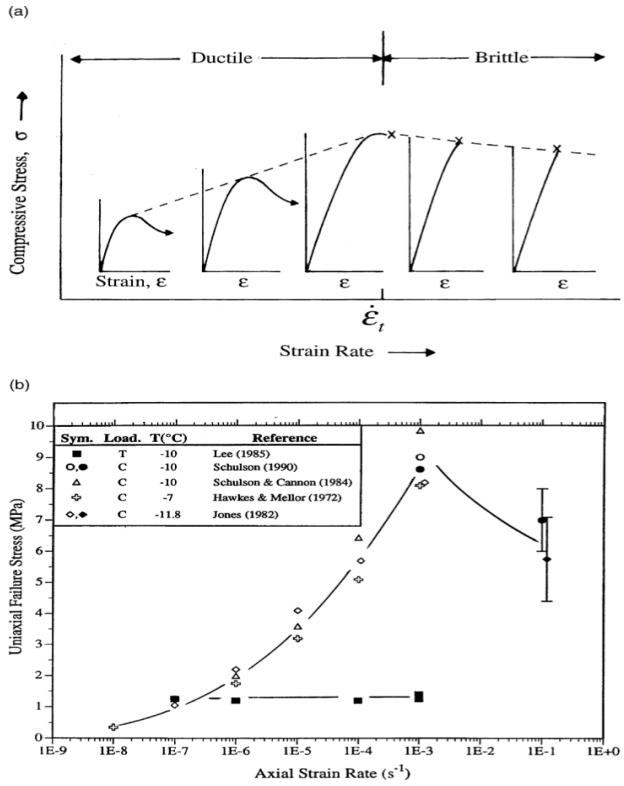

Figure 8 – (a) Plot representing the ductile to brittle transition of ice due to the effect of strain rate on the compressive stress-strain behavior of ice. (b) Graph illustrating the effect of uniaxial compressive strength of equiaxed and randomly oriented polycrystals of ice, with the peak representing the transition point in the ductile to brittle behavior (Schulson, 2001)

It can be seen from Figure 8a, at the lower rates the ice exhibits strain hardening initially, which is then followed by strain softening, strain-rate hardening and macroscopically ductile behavior. Conversely, at higher rates the ice exhibits primarily strain-rate softening and macroscopically brittle behavior. As it can be seen from Figure 8b, the failure stress will increase as the strain rate increases until a peak point which marks the brittle to ductile transition, after this point the failure stress is seen to begin to trend downwards from this peak value. This data trend presented in Figure 8 supports those observed in the pressure-rate graphs shown in Figure 7 above. Based on this information it can be seen that as the rate increases, so will failure pressure and stress, but only until a point, at which this relationship breaks down and the failure pressures and stresses will begin to trend downwards.

2.2.1.4 Dynamic Recrystallization

Dynamic recrystallization is given two general classifications of "rotation" and "migration" recrystallization regimes of Poirier and Guillopé (1979) where these phenomena are described widely as being the change of the grain size, shape, and orientation with little or no chemical change, due to deformation-induced reworking. More specifically, as presented by Urai et al. (1986), the term dynamic recrystallization can be best described as requiring the establishment of an array of grain boundaries in new material positions (Means, 1983); in other words, it is the formation and/or migration of grain boundaries (Vernon, 1981). Based on these definitions it is outlined by Urai et al. (1986) that when recrystallization is synchronous with deformation, it is called dynamic; conversely, in the absence of concurrent deformation, it is referred to as static recrystallization.

These processes of dynamic recrystallization result most interestingly in the observed increased softening of the material and resulting enhance creep behaviour, which give way due to increase or decrease in the grain boundary and overall grain size. However, it is important to note that, as stated by Duval et al. (1983), dynamic recrystallization does not initiate under low stresses and is periodic under intermediate stresses; similarly, that with increasing strain rate a continuous dynamic recrystallization process is observed and results in more distinct softening of ice. To further outline this, an expression proposed by Poirier (1985) is considered, which defines a new generated grain size as a result of recrystallization that depends only on the relative applied stress.

$$\frac{D}{b} = K\left(\frac{\sigma}{\mu}\right)^{-r} \qquad \textit{Equation 1}$$

Where, b, K, and μ are constants.

Expanding on this further, Urai et al. (1986) found that grain boundary energy is primarily a surface energy and that dynamic recrystallization of polycrystalline material under a triaxial load depends on hydrostatic pressure. Similarly, as described by Urai et al. (1986), defining that a decrease in four distinct types of energy is available as a driving force for dynamic recrystallization processes: intragranular lattice defect energy, grain boundary energy, chemical free energy, and external load-supporting elastic strain energy.

2.2.1.5 Localized Pressure Melting

Another important quality of ice behaviour is that of pressure melting, which is primarily a function of high pressure and can be likened to the processes of dynamic recrystallization. As described by experiments completed by Tammann (1903) and Bridgman (1912), the process of pressure melting results primarily based on pressure being increased gradually, and when the volume of the ice suddenly decreases the pressure-melting point is said to be reached (Nordell, 1990). Based on this explanation of the processes of pressure meting it can be described in other word that pressure melting is the decreasing in the melting point of ice due to an increased pressure (Nordell, 1990). This concept of pressure melting is expanded on and defined through the use of thermodynamics, which is shown in the expression below developed by Hobbs (1974).

$$\frac{dT_m}{dp} = \frac{(V_w - V_i)}{(S_w - S_i)} \qquad \textit{Equation 2}$$

In this equation T_m is the melting temperature of ice in Kelvin, p is hydrostatic pressure, V_w and V_i are the specific volumes of water and ice respectively, as well as S_w and S_i which are the entropy of water and ice respectively. This is known as the Clausius-Clapeyron's equation, which can be

rearranged using basic laws of thermodynamics to describe this pressure melting behaviour of an inverse relation between melting temperature and pressure.

When pressure melting occurs, the volume of ice will remain higher than that of the water produced through the meting process, so the numerator in the right-hand term must be negative. Through the laws of thermodynamics, we know that the change in volume entropy must remain positive due to the density of ice being higher than that of water, therefore the denominator in the right-hand term must remain positive. Based on this, the Clausius-Clapeyron's equation can be rearranged as such to show the inverse proportionality between melting temperature and pressure.

$$dT_m = -Adp \qquad \textit{Equation 3}$$

In this rearranged equation, A, is a constant comprised of the $\frac{\Delta V}{\Delta S}$ term, which depends on temperature. For ice at 0°C, A = 0.0742°C/MPa and at -10°C, A = 0.0833°C/MPa.

As previously described, experiments have been completed historically by various researchers including Tammann (1903), Tammann (1910), Bridgman (1912), and Nordell (1990). As such, the results from these experiments are important to compare and examine in order to develop a better understanding of this relationship between temperature and melting pressure. The plot shown below in Figure 9, represents and aggregate of the results obtained from these previously completed experiments.

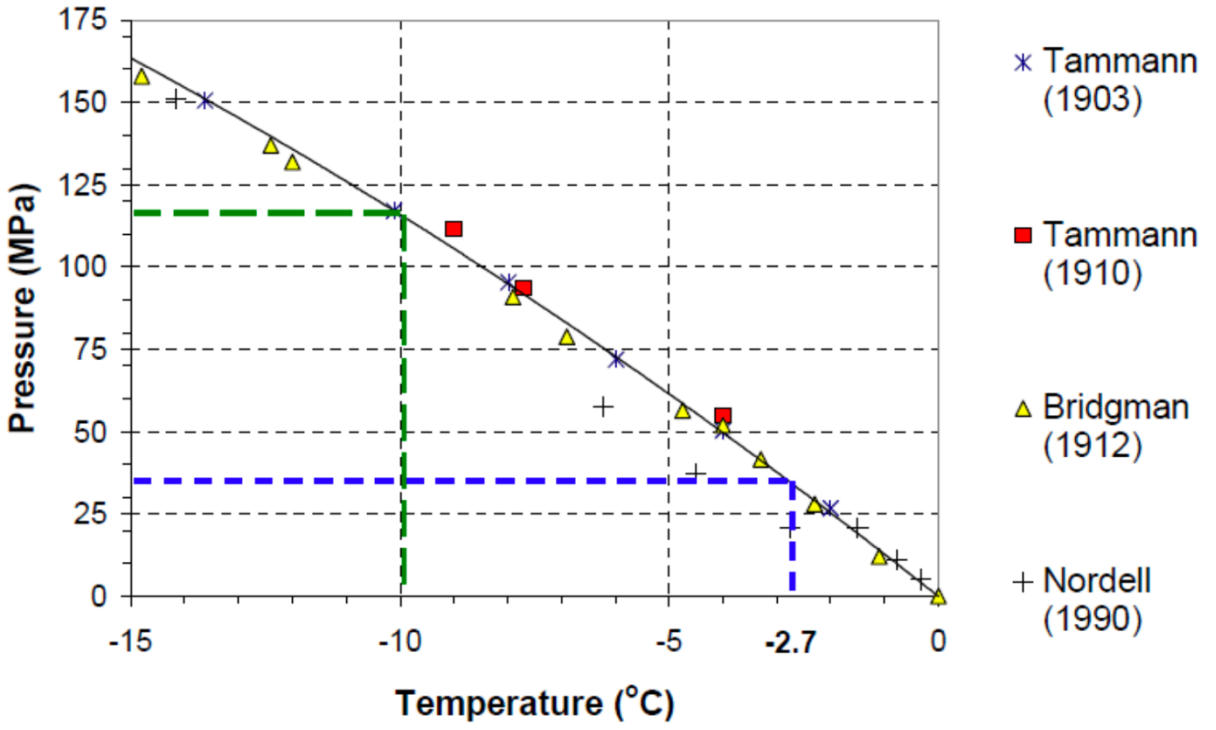

Figure 9 – Plot representing the pressure melting behavior of ice based on various experiments (Taylor., 2010)

As can be seen from Figure 9 above, at a temperature of -2.7°C the required pressure for melting to occur is 35 MPa; Similarly, it can be seen that when the temperature is as low as -10°C, the pressure required for melting will increase to 120 MPa.

2.2.2 Ice Fracture Mechanics and Failure Modes

During the loading process of ice, sudden or gradual changes in the deformation mechanisms occur as the ice begins to exhibit brittle behaviour and crack formation instead of the pure continuum creep and elasticity behaviour which has been previously discussed. The formation of cracks during this brittle failure behaviour occurs with two distinct control mechanisms: first nucleation (first appearance), and subsequent propagation of a crack (Sanderson, 1988). These mechanisms are dependent on the size of the cracks when they nucleate, as well as, in turn, the grain size of the

ice. The mechanisms involved with brittle failure and the formation of cracks varies based on the types of fracture which the ice is subject to, the primary forms of fracture are tensile fracture, and compressive fracture.

As discussed by Schulson et al. (1984), the physical process of crack nucleation will occur in order to relieve stress concentrations which develop at grain boundaries during the beginning of deformation; this is supported by Sanderson (1988) where these dislocations are described to tend to glide within grains and being to concentrate at grain boundaries until the stress concentrations are sufficient enough to nucleate cracks. Sanderson (1988) goes on to describe how during tensile fracture nucleation of cracks which are the size of the same order as the grain diameter, the largest of these cracks will generally lead to propagation and failure. However, it is important to note that the propagation of these nucleated or pre-existing cracks is dependent on the conditions present. For the case of tensile stress, criterion which have previously been developed for linear elastic fracture mechanics is based upon more conventional engineering materials such as steel; however, ice is generally much more complicated than steels due to its creep behaviour. Under rapid loading conditions, ice behaviour is considered to be approximately elastic allowing use of simple linear elastic fracture mechanics; however, when subjected to slower loading conditions where the ice specimen is much more prone to creep behaviour, which considers more complicated ductile behaviour at the advancing crack tips (Sanderson, 1988). A schematic depicting crack nucleation of ice under tension can be seen in Figure 10 below.

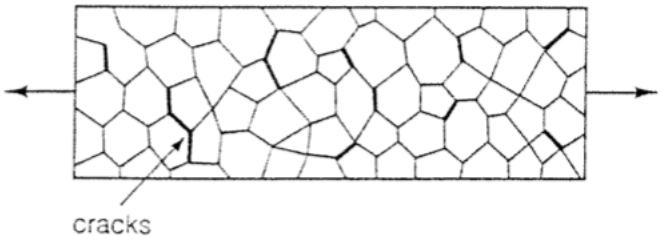

Figure 10 – Schematic diagram of ice under tension. Bold lines represent where cracks nucleate and may coalesce (Sanderson, 1988)

Under compressive stress, cracks will form under the same processes as those seen for tensile stresses, however, under compression cracks may also form across grains. Hallam (1986) describes that up to 50% of nucleated cracks formed under compression are trans granular in character. A criterion for defining the nucleation of cracks under compression presented by Hallam (1986), which suggests that a similar criterion to that which has already been developed for tensile loading should be implemented. This model assumes that crack nucleation under compressive stress occurs when the lateral tensile strain induced by Poisson expansion reaches the level already defined as critical for tensile crack nucleation. Based on this model, the stress required to nucleate a crack under compression would then be about three times that which is required in tension.

During indentation of ice, a feature may undergo a number of different unique primary failure modes. These failure modes which are experienced during the indentation process are governed by two primary factors: the indentation rate, and the aspect ratio (Sanderson, 1988). The principal failure modes which result from indentation are known as global failure modes, there are generally considered to be four primary types. Crack nucleation is somewhat similar both under tension and compression, however, the process of crack propagation under compressive stress is much less simple as under tension. This difference is primarily due to the fact that under compression the propagation of cracks is in general a stable process, while it is generally unstable during tension; similarly, that under compression the final failure generally occurs by the linkage of a large number

of cracks, not simply the catastrophic propagation of a single crack (Sanderson, 1988). The different principal mechanisms of ice failure due to compressive ice failure during indentation can be seen in Figure 11 below.

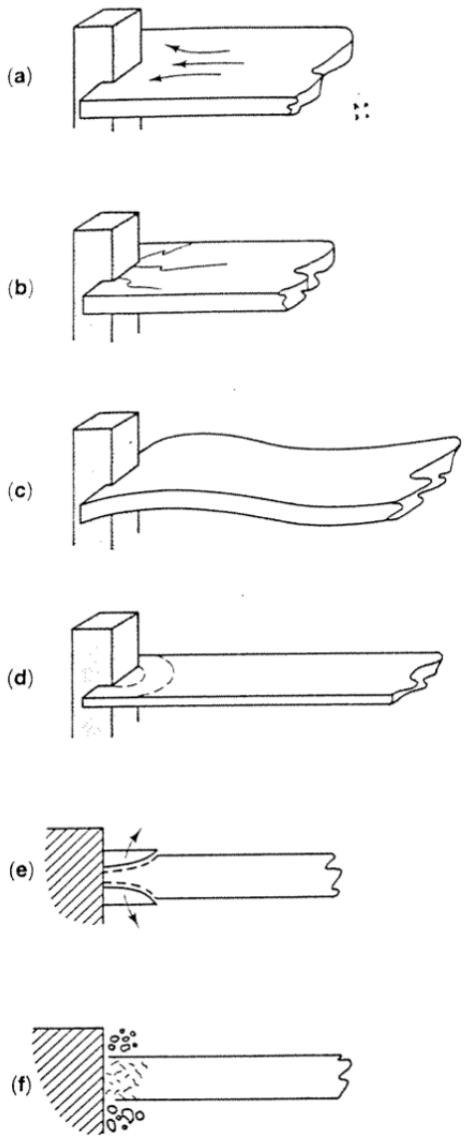

Figure 11 – Principal compressive failure mechanisms observed during laboratory indentation experiments. (a-f) creep, radial cracking, buckling, circumferential cracking, spalling, and crushing (Sanderson, 1988)

As outlined in by Sanderson (1988) and as is shown in Figure 11 above, The first of the global primary failure modes is creep, which has been discussed previously, and is the deformation of ice

without the formation of cracks as creep failure acts entirely in the continuum domain. The second primary global failure mode is that of radial cracking, where, above a certain level of stress, radial cracks will begin to form at the corners of the indentation zone as well as along the approximate line of indentation. Buckling is considered the third mode of primary global failure during indentation and elastic buckle formation is prone to occurring on thin ice, which leads to the unstable and rapid formation of circumferential cracks. The fourth primary global failure mode is considered to be circumferential cracks, which form as a result of elastic buckling or due to an overall applied out-of-plane bending moment which occurred due to an eccentric loading condition. These outlined failure modes are seen in the global failure regime, however Sanderson (1988) highlights two more primary failure modes which occur within the local failure regime which are considered to be spalling and crushing. Local spalling failure typically occurs during indentations at high indentation rates as well as low aspect ratios, where in-plane horizontal cracks will begin to propagate away from the contact zone as fragments of the ice begin to break away from ice specimen. Cataclastic crushing is seen to occur at higher rates of indentation, where the ice is pulverised into a powder and subsequently extruded upwards and downward at contact zone (Sanderson, 1988).

2.2.2.1 Pure Ice Crushing and Failure Under Normal Loading

Compressive ice failure and crushing are important failure mechanisms to consider, especially in offshore environments. Ice behaviour is heavily dependent on loading rates, and it is observed that the deformation of ice is more likely to be viscoelastic with lower loading rates; similarly, if loading rate is increased the effects of fracture, damage and microstructural change are observed to become more prominent. Ice failure and deformation are detailed processes with many different

considerations within the field of ice mechanics, with compressive ice failure being similarly complex. Compressive ice interactions on offshore structures, as described by Jordaan et al. (2008) have the potential to cause induced vibrations within the structures due to the cyclic nature of these processes. Specifically, when ice fails compressively, small zones of high pressure are formed by the creations of spalls and splits, these high-pressure zones (hpzs) are the avenue through which the majority of ice loads are transmitted. These high-pressure zones (hpzs), as discussed by Taylor et al. (2008) have been observed to cover roughly only 10% of the global interaction area; however, processes such as spalling or crushing, as described by Jordaan (2001) and Jordaan et al. (2008), are associated with various mechanisms such as macrofracture, microfracture, recrystallization and pressure melting, which influence the formation and development of these hpzs. Crushing has been observed by Taylor (2008) to be associated with damage processes occurring within hpzs while spalling fracture has been observed to be associated with stress, geometry, and internal flaws. Many internal flaws exist within ice naturally and become a very important considerations when making ice for use in experimental work. It has been observed that larger ice specimens have a higher probability of containing critical flaws, which result in a higher probability of the specimen fracturing at lower stress levels (Taylor., 2010).

As ice is a viscoelastic material and possesses a significant time dependence of stress-strain behaviour, variation in pressure can be observed in zones of high pressure within ice even when only low loading rates are applied (Sinha, 1979) (Jordaan., 2001). The ice then undergoes microstructural change under compressive states and becomes prone to fracture. Failure initiates in localized areas where the contact is made. The global interaction area, defined as the projection

of the structure onto the shape of the ice features, increases as the interaction continues. Jordaan et al. (2008) described this area to include the spall area or high- and low-pressure zones.

These processes detailed above which surround normal loading and crushing of ice are very complex, and as such there is a need to better understand them. Due to this, many experimental programs have been carried out both in the field and in laboratories to investigate these phenomena through indentation and crushing tests. These tests seek primarily to recreate the development of high-pressure zones within ice samples, a subsequently investigate the effects these have on the ice response based on a number of different parameters such as indenter size, indentation rate, temperature, and others. In addition to investigations of high-pressure zones, spalling and crushing of ice specimens are important areas of study. Details of these tests including experimental setup, ice sample production, testing parameters, and results obtained from past studies are summarized below.

2.3 Review of Past Indentation Experiments

2.3.1 Normal-Load Indentation Tests

Different indentation tests have been historically conducted in the past at full, medium, and small-scale in order to effectively investigate different phenomena or parameters such as material properties, pressure distributions, crushing behaviour, and the mechanisms of failure of ice in normal loading under an indenter. As a single particle indenting into an ice surface can be analogous to an indenter in normal loading, this section reviews specifically relevant small-scale indentation tests that have been conducted. These tests primarily focus on investigating failure processes, behaviour of high-pressure zones and microstructural modifications at various

indentation rates, temperatures, and ice specimen structures in order to understand better the results of pure local normal indentation of a rock particle into an ice feature.

One relevant small-scale indentation test which was centered around interactions between a small spherical indenter and polycrystalline ice which had a grain size between 3.35 and 4.75 mm. These tests were completed by Barrette et al. (2002) through the implementation of a Materials Testing System (MTS) test frame inside of a cold room facility, where the effect of temperature and displacement rate was investigated on the response of a singular high-pressure zone. The altered morphology of ice near and around the ice-indenter interface was also investigated through the physical characteristics of ice damage and layer formation in this region. A cylindrical steel mould with an internal diameter of 150 mm and a height of 60-130 mm was utilised for the ice samples used in the experiments. The indenter implemented in this experiment was a spherical steel indenter which had a diameter of 20 mm and possessed a radius of curvature of 25.6 mm. Additionally, this indenter was scaled down from the spherical indenter implemented in testing during the Hobson's Choice Ice Island medium-scale tests completed by Frederking et al. (1990). For experimental test runs a set indentation depth of 2.6 mm was used for all tests with varying indentation rates which ranged from 0.1 to 10 mm/s, as well as varying temperatures of -2℃, -10℃, and -20℃ which were utilised as temperature set points. The tests that were considered as the focus for data presentation in this report were at an indentation of 4 mm/s, data obtained from one of these tests which was performed at -10℃ can be seen below in Figure 12.

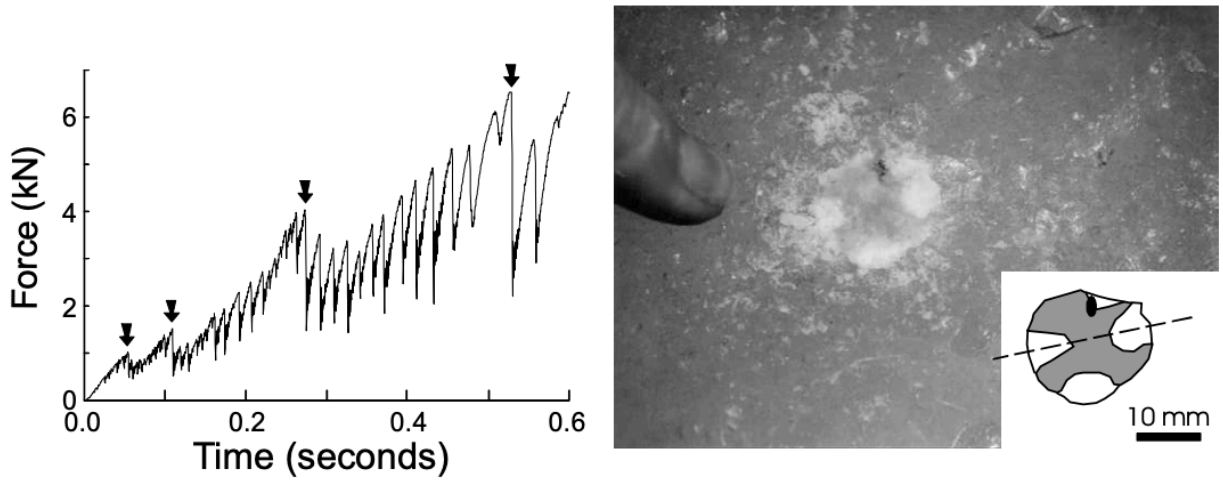

Figure 12 – Load data (left) with significant drops noted by arrows, and post-test ice surface (right) showing grey spots and crushed surface Barrette et al. (2002).

All tests were observed to have load cycling, with peak frequencies in the order of 50–100 Hz, as can be seen in Figure 12 (left) above which resulted in fine-grained, pulverized ice being produced as a result of the interaction for all cases; similarly, the size of the particles which were observed to result from tests ranged from a sub-mm, powder-like material to fragments up to 4 mm in maximum dimension. As can be seen in Figure 12 (right), this indented ice surface was characterized by a dark zone varying in shape and surface area, surrounded by lighter areas defined by crushed ice which represents a central recrystallized zone, with minor cracking, and microcracking on either side. For other tests it was determined that at the highest temperature test (–2 °C) mostly fine-grained ice with little evidence of microcracking was observed; conversely, the –20 °C test led predominantly to microcracking. Additionally, for all tests the damage zone was seen to extended up to a maximum depth of 4–5 mm.

Another notable small scale ice indenting experiment was conducted by Wells (2011), which was similar to the tests conducted by Barrette (2002) as detailed above as the indenter implemented in this experiment was a similar spherical steel indenter which had the same diameter of 20 mm and

possessed the same radius of curvature of 25.6 mm. This indenter was used to create a single high-pressure zone of ice-structure interaction, as was seen in the experiment conducted by Barrette (2002)

The general test setup for the two experiments were similar, however, Wells et al. (2011), implemented different experimental procedures and parameters particularly related to the ice specimen. The ice specimen had dimension of 20 x 20 x 10 cm, was constructed of freshwater ice that was polycrystalline with a grain size of roughly 4 mm and was unconfined in the test setup with any bubbles present within the ice being removed with a vacuum mould. For experimental testing runs, the temperature was held constant at -10℃ with indentation rates ranging from 0.2 to 10 mm/s and indentation depths ranging from 3 to 20 mm being implemented. To improve the analysis of physical processes of ice failure, local pressure distributions, and the dynamic activity of the high-pressure zone located at the ice-structure interface, high-speed video recording devices and tactile pressure sensors were implemented. Through conducting 26 experimental test runs, it was determined that the failure processes observed on the indentation of the test specimen were highly dependent on the rate of indentation. Based on the reported results this dependence of failure processes on indentation rates can be seen, as it was reported that the observed failure was primarily ductile and did not show evidence of spalling, crushing, or cyclic loading for tests with slow indentation speeds (0.2 m/s). Similarly, it was observed that the behaviour of ice failure exhibited a mixture of crushing and ductile failure but was overall generally unpredictable for indentation rates in the range of 2 to 5 mm/s; additionally, isolated crushing, localized spalling, and cyclic loading events were seen within this range. Finally, spalling within the failure processes was seen to become more dominate within tests with faster indentation (8-10 mm/s) as the results

exhibited brittle failure combined with mixed mode failure more frequently. Based on these observations, the different modes of ice failures observed during the various tests were organized into five distinct categories and can be seen represented in Figure 13 below.

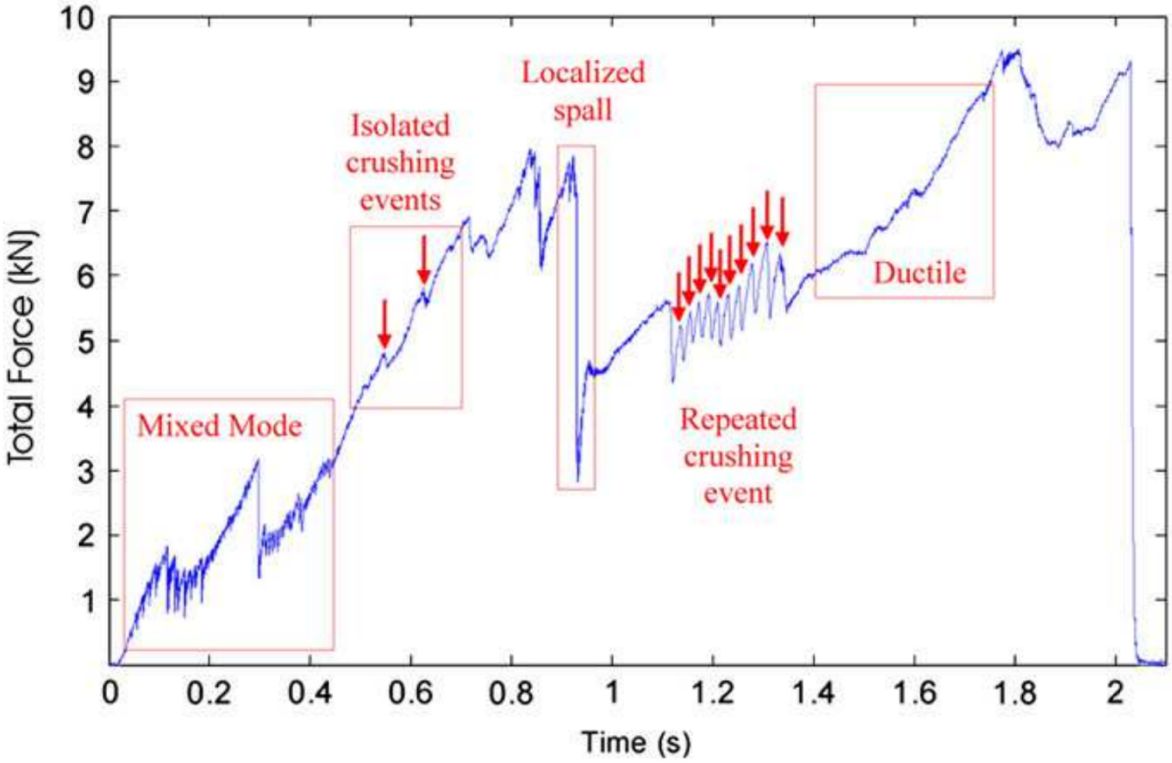

Figure 13 – *Graph of total force output from MTS, with failure modes identified* Wells et al. (2011).

Each failure mode was classified based on the observed physical response combined with the graphical representation shown in Figure 13 above. Ductile failure is described as a steady rise in the total force and contact area with time, which was attributed to the spherical shape of the indenter. This type of behaviour was most obvious at low indentation rates (0.2 mm/s) where very little localized spalling or crushing was seen to occur, however occasional isolated crushing events were observed in some cases. Faster indentation rates resulted in the observation of the ductile failure becoming more frequently disrupted by other failure processes such as isolated crushing events, localized spalls, and mixed mode. A localized spall is described as occurring when a single

flake of ice breaks away from the periphery of the damaged layer, which leads to a sharp drop in load where the pressure distribution indicates that just before the spall is released, there will be a localized increase in pressure signifying the creation of a high-pressure zone. Finally, when the spall is released a decrease in contact area and a relative reduction is pressure is observed. Isolated crushing events are designated based on a drop in total force combined with the reduction of pressure from the center of a formed high-pressure zone, with little change in contact area. The sudden failure of the damaged layer seen in this failure type causes a drop in pressure, which results in the extrusion of crushed ice particles from the periphery of the high-pressure zone. This type of isolated crushing behaviour was observed primarily at indentation rates ranging from 2 to 5 mm/s. Cyclic-load crushing events were much rarer and were classified based on increasing trend of total force during the failure events where the load cycling is not interrupted by any other failure behavior. Isolated and distinct regions of crushing were observed prominently in tests performed at rates from 2 to 5 mm/s, where this type of failure was seen most frequently and clearly. Finally, mixed mode failure was characterized and described as a combination of crushing and small localized spalling which had irregular force and pressure distributions along with multiple load drops. This type of failure behaviour was observed in tests where indentation rates were above 2 mm/s and additionally the failure for mixed mode behaviour possesses an increasing trend as the indentation rate is increased.

Another notable experiment which builds on the experiments completed by Barrette (2002) and Wells et al. (2011) were the experiments completed by Browne (2012) These experiments use a spherical steel indenters with diameters of 20 mm and 40 mm, as well as a radius of curvature of 25.6 mm and 51.2 mm, respectively. These indenters were used to produce and model a single

high-pressure zone on polycrystalline freshwater ice samples confined in steel moulds. The ice samples had dimensions of 150 mm and 300 mm in diameter and were fabricated through the implementation of 2.00-3.35 mm and 3.35-4.75 mm seeds. The tests were divided into two sets, test 1A and test 1B, where the ice was indented 2.5 mm with indentation rates tests from 2 mm to 10 mm at temperatures ranging from -5℃ and -15℃. The main difference between the tests was that test 1B uses the larger 40 mm indenter at a constant temperature of -10℃, while test 1A was more of a scoping study that considered different parameters throughout the experimental runs. Additionally, a number of different indentation systems were implemented during the Test 1A series. In total, six indentation systems were used, where two of these systems were rigid, which were roughly as stiff as the MTS used for the experiment; and four were compliant systems, which consisted of simply supported beams of specified levels of compliance.

Through the implementation of the above parameters, Browne (2012) investigated the effect of temperature, stiffness, and indentation rate using high-speed video, load data, displacement data, tactile pressure sensors, and thin section analysis of the specimen after completed tests. Based on the analysis of the results, it was observed that differences in temperature had an effect on the outcome of failure. Tests completed in warmer temperatures, around -5℃, resulted in more ductile failures which lead to a consistent increase in observed load with no evidence of a cyclic pattern. Conversely, tests completed under colder conditions, around -15℃, resulted in primarily crushing and spalling failure with a typical cyclic loading pattern being evident. Results also varied based on the type of indentation system which were implemented, where the relative structural feedback from each of the six indentation systems was seen to have significant effects on the amplitude as well as frequency of observed cyclic loading patterns. Specifically, tests observed with rigid

structures resulted in smaller drops in load than were observed with compliant structures, as the deflection under loading which was seen in the compliant structures resulted in the relative loading rate decreasing as the structure continued to deflect under the load until the strength of the ice was exceeded. Additionally, the cyclic loading was observed to have a linear relationship which followed a positive trend relative to both the stiffness of the implemented structure and the indentation rate.

Indentation tests with the implementation of conical shaped ice specimens were also completed for small scale experiments by Dillenburg (2012). These conical shaped ice specimens were constructed with 4-10 mm ice seeds and distilled, de-ionized, and deaerated water which was cooled to 0℃. This prepared water was then used to fill conical ice moulds, where the ice sample was then shaped with an ice shaping apparatus to produce a specimen with the desired cone angle of 30°. These samples were implemented primarily in a sample holder for numerous tests where crushing rates were varied between the range of 0.01 mm/s to 100 mm/s at temperatures of -5℃ and -10℃. In order to complete these experimental procedures, tests were run in a cold room with the use of a MTS load frame, which also recorded important data such as force and displacement. There was some variance in the test specimen implemented for the test procedure, as a cylindrical ice specimen was implemented as a comparison case for some test runs, as well as two experimental test which were completed with unshaped ice samples (i.e. did not meet the exact desired cone angle of 30° implemented for other tests) and four tests which were completed without the assistance of ice holder constraint. Additionally, a crushing plate and backing plate were implemented as a modification to the indentation system to facilitate these experiments. The crushing plate was constructed out of 19.05 mm thick stainless steel and the backing plate was

constructed out of 31.75 mm thick structural steel; both the crushing plate and backing plate had a diameter of 254 mm. The crushing plate was also sanded such that the contact surface possessed a coarse roughness in the range of 6.3-12.5 μm.

Each experimental test run was analyzed by Dillenburg (2012) in a number of different ways which included the use of high-speed video recordings for high-speed tests and typical digital camera images for slower tests. Additionally, each unique ice sample was weighed before and after each experiment along with the spalls which were produced on to the ice samples after crushing. Thin sections were also produced for both horizontal and vertical sections of the ice samples. Through the implementation of the above listed methods, the experimental data was processed with the assistance of Python software in order to calculate the nominal ice crushing pressure, energy, strength of ice, maximum crushing force, nominal pressure at the peak force, and the true crushing velocity. Analysis of this data showed ice deformation behaviour which was defined by three different ranges of deformation. The ductile range was defined as existing primarily in tests with crushing rates from 0.01 to 0.1 mm/s, where the spalls which resulted from these tests had weights ranging from 13 to 16 grams at both -5℃ and -10℃; Additionally, at crushing rates of 0.1 mm/s the spalls were found to weigh around 30 grams for tests performed at -5℃ and closer to 85 grams for tests performed at -10℃. The ductile to brittle range was defined as existing primarily in tests with crushing rates ranging from 0.3 to 3 mm/s, where tests completed at crushing rates above 3 mm/s saw a more significant tendency to spall along with an increase in ice mass of 15-60 grams being observed in tests done at -5℃ compared to -10℃. Finally, the brittle range was defined to exist primarily in tests with crushing rates from 10 to 100 mm/s. It was also found that, after analyzing the results of peak force, nominal pressure, and crushing strength, ice failure observed

during the transition from ductile to brittle behaviour during tests at -5℃ resulted in higher crushing rates when compared to tests completed at -10℃. Based on this analysis, it was also determined that ductile ice deformation is more temperature dependant than ductile to brittle or brittle ice deformation.

The effect of the ice specimen holder was observed by Dillenburg (2012) to have little effect on the results and the inclusion of a constraint was seen to reduce the nominal pressure variation in low crushing rate tests; ultimately leveling out the pressure to a constant level. However, in the case of higher crushing rates, different behaviour was observed, where increases in load were interrupted by recurring load drops. Finally, it was observed through a comparison of the conical shaped ice samples with the cylindrical sample, that a more controlled increase in load was present in the tests with the conical sample due to its shape.

The concepts investigated by Dillenburg (2012) concerning crushing interaction of conical ice specimen were expanded by Habib (2014). In the studies conducted by Habib (2014), the experiments were designed to improve the understanding of crushing and failure of ice under compressive loading. In all the tests the ice samples were made of polycrystalline freshwater ice and had an average diameter of 268.8 mm at the bottom and 25.4 mm at the top. Ice specimens having three different taper angles ranging from 13° to 30° and were prepared with ice seeds ranging from 0-4 mm and 4-10 mm based on several processes including water distillation, water deionization and water deaeration were utilized. After the ice specimen were completely frozen, they were then shaped into the appropriate taper angle with a shaping apparatus. These varied ice specimens were implemented to accurately study the variation of maximum force, pressure,

loading pattern and associated failure processes with the change of the taper angle. A Materials Testing System (MTS) load frame was used to conduct the experiments and collect the force data against time and indentation depth. To study the pressure variations within the contact area, tactile pressure-sensor technology was used in selected tests, while the failure behaviour of ice samples is observed from the recorded videos. In each test the parameters studied were ice specimen strength, maximum force from the data collected from the MTS data acquisition system, pressure distribution, the nature of loading, spall distributions and thin section picture analysis. The indentation for each test was done from the top surface of the ice sample to the depth of 70 mm, and indentation speeds from 0.1 mm/s to 10 mm/s were utilized in the experiments at temperatures of -10℃ and -5℃. Once tests were completed, the spalls produced were also collected and weighed for analysis. Thin sectioning was also completed on samples to facilitate further analysis of the outcomes from each test.

Slow speed tests (0.1 mm/s) were observed to mainly show ductile failure throughout the experiment where the maximum force for this ice sample was recorded as 355 kN and maximum pressure was 32.88 MPa up to the indentation depth of 6 mm. The spall mass distribution showed that there was small amount of spalling, dominated by a few large spalls. More dynamic failure was observed for medium speed tests (1 mm/s) where large load fluctuations, drops in loads, and some spalling events are observed which represented a combination of ductile and brittle failure. Analysis of spall distribution showed that tests at medium rates resulted in more large sized spalls compared to amount medium and small sized spalls. For faster speed tests (10 mm/s) more dynamic failure was again observed with similar load fluctuations, drops in loads, and spalling. From analysing images taken after tests it was observed that the failure was brittle in nature and

extensive random spalling were present. Temperature considerations were then investigated where tests completed at $-5℃$ were observed to result in failure process that show an inclination towards ductile failure, even at fast speed tests. An analysis of images taken after the completion of the test indicated that more spalling happened at the edges and the indentation zone was found to have smooth slippery finish at the center of the sample indicating the test was done at a warmer temperature. Overall, it was observed that the warmer test exhibits more ductile failure, dominated by damage, while the cold test experiences more brittle failure.

2.3.2 Shear-Load Friction Tests

An experimental set-up was constructed by Barrette (2008) to study the friction behaviour of level ice and ice rubble on different seabeds at large scale and realistic stress levels. Testing was conducted in the ice tank of the Canadian Hydraulic Centre (CHC) at the National Research Council (NRC) in Ottawa, Ontario inside a specially built concrete flume. The flume had dimensions of 6 m in length and 2.6 m in width, along with a height of 1.2 m. Frame motion for tests was facilitated by guide rails which were mounted onto the top of the flume's longitudinal walls; allowing for translational motion of the frame assembly along the sand surface, this was referred to as the wagon. The tests were performed with a 4 m^2 footprint with vertical stress levels up to 17 kPa. The sand implemented for these tests was determined to have diameters ranging between 0.16, 0.30 and 0.61 mm, and the angle of repose for the sample was 33°. The level ice samples were constructed with a saline solution (20–25%) and were prepared in a large pit inside the NRC-CHC ice tank by diluting sodium chloride into tap water. This water was then transferred into the flume until it reached the wagon's top rim, and the entire water surface outside the wagon was then covered with insulation and the cold room temperature was brought down to −15 °C to

allow for the sample to freeze. Ice rubble samples were constructed with a 6% saline solution, which was pumped out of the pit into 15 containers 2.4 m long, 0.4 m wide and 0.3 m deep. The water was added in increments of 20–30 mm and was allowed to freeze at an air temperature of−15 °C; and once frozen the ice was broken into rubble pieces of random size with a prybar.

During the testing procedure, the ice was moved horizontally a distance of about 120 mm across the sand surface with displacement rates ranging from 0.003 to 0.342 mm/s. Four position transducers measured vertical displacements for a total of 47 tests which were conducted with level ice and another 24 which were conducted with ice rubble. Based on level ice tests, a friction coefficient of 0.47 was observed for peak shear stress and 0.39 was observed for steady shear stress. Tests completed with ice rubble resulted in observed friction coefficient of 0.65 for the peak shear resistance and 0.62 for steady shear resistance; thus, outlining an increase of about 50% in shear resistance compared with level ice. This can be seen in Figure 14 below.

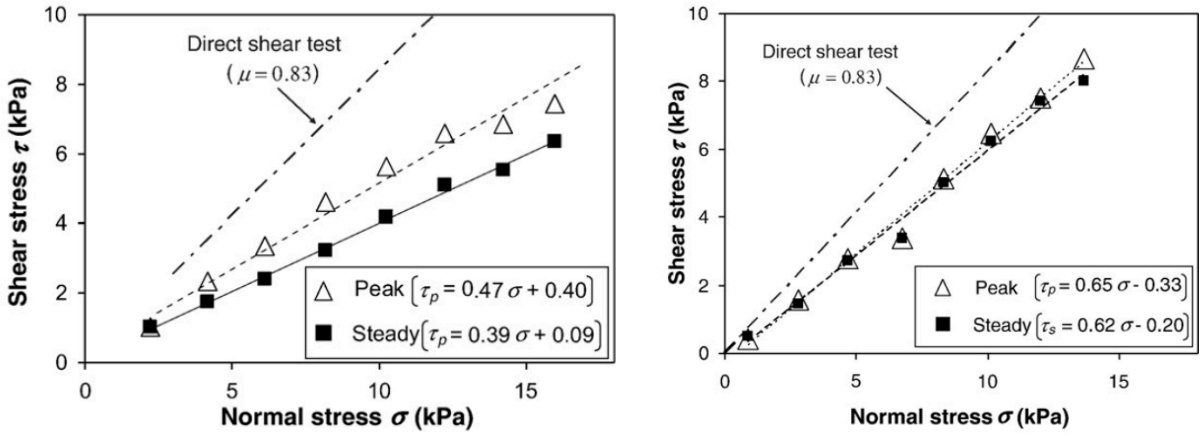

Figure 14 – *Columb relationship of shear and normal stress for level ice (left), and for ice rubble (right)* Barrette et al. (2008).

Based on observation of these results, as can be seen in Figure 14 above, a linear relationship was observed between the shear stress and normal stress for both tests. It was believed that shear failure had occurred at the ice–sediment interface and impacted the results for level ice; however, in the case of ice rubble the sand's internal friction was considered to have been fully mobilized which resulted in a skirting action of the ice, subsequently influencing the results for these tests. Additionally, observed sediment freeze-up was considered to have caused a substantial increase in sliding resistance, where the failure plane was believed to have migrated downward and laterally along the freezing front into the sand bed; thus, resulting in a concurrent increase in shear resistance up to levels comparable to the sand's internal friction. Similarly, sand compaction was determined to have potentially contributed also to this increase in sliding resistance.

The experiments detailed above in Barrette (2008) are expanded upon in a second study completed by Barrette (2009), where an experimental set-up was assembled in order to investigate outstanding issues regarding the sliding resistance of grounded ice pads built from artificially thickened ice cover with either level ice or ice rubble. The main difference in the simulations completed for the experimental test completed by Barrette (2009) was that experiments were completed on a clay seabed. The tests were completed inside the same specially built concrete flume as in Barrette (2008). The flume had unmodified dimensions of 6 m in length and 2.6 m in width, along with a height of 1.2 m. Frame motion for tests was facilitated by guide rails which were mounted onto the top of the flume's longitudinal walls allowing for translational motion of the frame assembly along the sand surface; this was referred to as the wagon. The ice was contained in a bottomless rectangular wagon such that the bottom of the ice was in contact with the clay, with a 4 m^2 footprint, and normal stress levels up to 23 kPa. Similar ice specimen construction was completed with the level ice samples being constructed with a saline solution (20–25%), while

being prepared in a large pit inside the NRC-CHC ice tank by diluting sodium chloride into tap water. This water was then transferred into the flume until it reached the wagon's top rim, and the entire water surface outside the wagon was then covered with insulation and the cold room temperature was brought down to −15 °C to allow for the sample to freeze. Ice rubble samples were constructed with a 6% saline solution, which was pumped out of the pit into 15 containers 2.4 m long, 0.4 m wide and 0.3 m deep. The water was added in increments of 20–30 mm and was allowed to freeze at an air temperature of −15 °C; and once frozen the ice was broken into rubble pieces of random size with a prybar. The clay was treated by a rototiller to ensure the mixture was homogeneous and was added to the flume in a slow process which consisted of three stages, after each of which 27 ppt saline solution was added to the clay. The clay was 350 mm thick, but 50 mm was removed just before testing began. The clay was categorized by moisture content, unit weight, specific gravity as well as shear strength of the clay, which were all obtained prior to initiating the test program.

Tests were completed by pulling the wagon with the ice sample affixed by way of an actuator over distances ranging from 40 to 100 mm per test while monitoring the horizontal forces required to do so. A total of 29 successful tests were conducted with level ice and another 32 with ice rubble. Tests completed with level ice specimen were observed to have only a small increase in shear resistance with an increase in normal stress, when enough time was allowed for the clay to consolidate. Conversely, for tests with ice rubble it was observed that an increase in normal stress systematically led to a significant increase in shear resistance. This was presumed to be due to shorter drainage paths for pore water evacuation within the ice, which suggested that ice rubble

material should be more suitable than level ice. The normal stress versus shear resistance plots for both level ice and ice rubble can be seen below, which was used for analysis of the results.

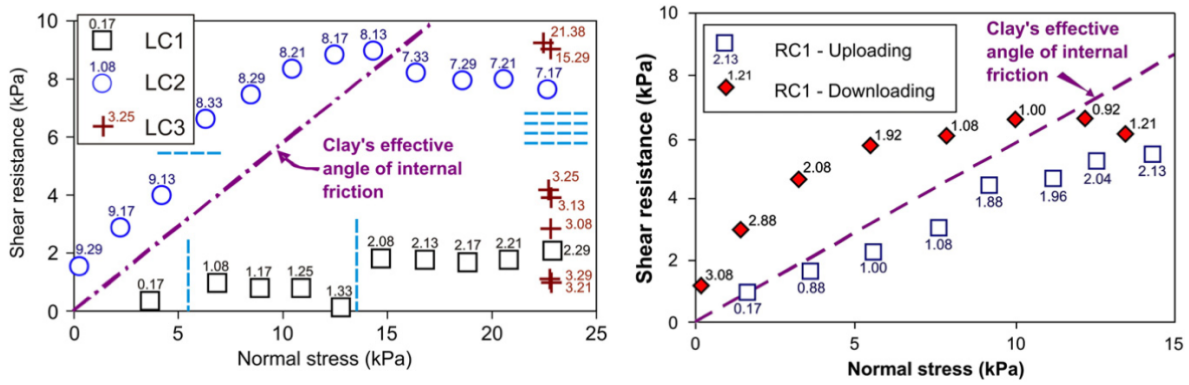

Figure 15 – Mohr-Columb relationship of shear resistance and normal stress for Level ice (left), and ice rubble (right) as presented by Barrette et al. (2008).

After completing testing and analysing the results, it was observed that the undrained shear strength of the scoured clay at the onset of testing was 16 and 17 kPa for level ice and rubble, respectively, which was considered to be relatively weak. Subsequently, it was observed that in future test the strength increased up to 42 kPa, which was primarily attributed to consolidation which took place over the course of the test program. A slight increase in undrained shear strength outside the scoured zone was also observed and was believed to be attributed to being a result of the sideward stresses exerted by the clay during vertical loading; however, it was noted that at no time in the course of the test program did the clay see normal stresses exceeding 23 kPa. Upon increasing and decreasing these normal stresses, it was observed that there was potential evidence for clay consolidation, when increasing the normal stress, and swelling, when decreasing the normal stress; additionally, it was determined that a peak response in the shear resistance could be attributed to dilatation. One inconsistency which was observed when investigating the above stress and shear results of the test was that the clay's undrained shear strength, as measured with a vane, was consistently higher than the sliding resistance of the ice in all tests. This parameter

progressively increased to levels well exceeding the maximum normal stress applied to the clay. As a consequence, it was determined based on these results that the vane data could not be relied upon to provide an accurate measure of sliding resistance.

Based on the completed literature review and analysis of previously completed experimental programs, certain research gaps have been identified in order to outline the relative need for the research presented in this thesis. Significant research has been completed concerning the compressive failure of ice due to indentation of a spherical steel indenter, however work has not been conducted to investigate how these failure mechanisms may change with indentation of unconstrained indenters. This research gap is further extrapolated to identify the lack of research using actual rock particles as would approximately be seen on a seabed. Finally, it is noted that the previously completed research identified above uses only a single point of indentation, instead of multiple indentation points occurring concurrently. Based on these gaps in the presented literature, a need for the research presented in this thesis was determined in order to investigate the nature of compressive ice failure due to indentation by single and multiple rock particles.

3. Experimental Methodology

3.1 Overview

In the present study, methods similar to those implemented for single steel indenter tests discussed above were utilized to investigate the indentation of rock particles into a confined ice specimen. In all tests relevant to these experiments, rock particles are compressed between two confined ice specimens mounted to the top and bottom platens of a materials testing (MTS) load frame to ensure only ice and rock came into contact during these experiments. The primary objective of these tests was to investigate the effects of changes in indentation rate and the relative spacing from previously formed damage zones on resulting force and pressure trends. Given that real ice-soil interactions will involve a multitude of individual ice-particle interactions, one of the primary aims of these tests is to assess the influence of distance between indentation sites to evaluate if multipoint ice-rock contacts may be modelled as the sum of independent, individual ice rock contacts. In each test, the parameters studied included the ice specimen strength, maximum force from the data collected from the MTS data acquisition system, pressure distribution, the nature of loading, and ice damage zones. Single ice-particle indentation test results and multi-contact ice-particle interactions will be considered individually and subsequently be compared.

All the tests, experiment preparation, sample preparation, and post experimental works were conducted in the cold room of the Thermal Lab at Memorial University of Newfoundland.

3.2 Design of Experiment

When Icebergs naturally drift, if the area of ocean is sufficiently shallow, they will drag along the ocean floor which is a phenomenon known as iceberg scour. When this occurs, rock and soil

particles have the potential to indent into the ice feature, embedding the rock particles within the ice. In the present study, a flat, rectangular ice specimen is mounted to the top plate and a similar, smaller ice specimen on the bottom soil-box plate which was designed to house loose soil but was instead frozen into an ice specimen in the same manner as the primary ice specimen. The MTS frame is implemented in order to effectively simulate the compression of rock particles between two ice surfaces. The load frame that was used to conduct the experiments is the MTS-SLA load frame, located at the cold room of MUN, which was implemented to facilitate the loading of ice blocks to simulate local compression and embedment of rock particles into the ice. Specifications of the machine are given below in Table 1. This model is specially designed for axial compression and horizontal friction testing, having a very high frame stiffness with a resistance to deformation of 1 x 10^6 kN/m. The MTS load frame can be seen in Figure 16 below.

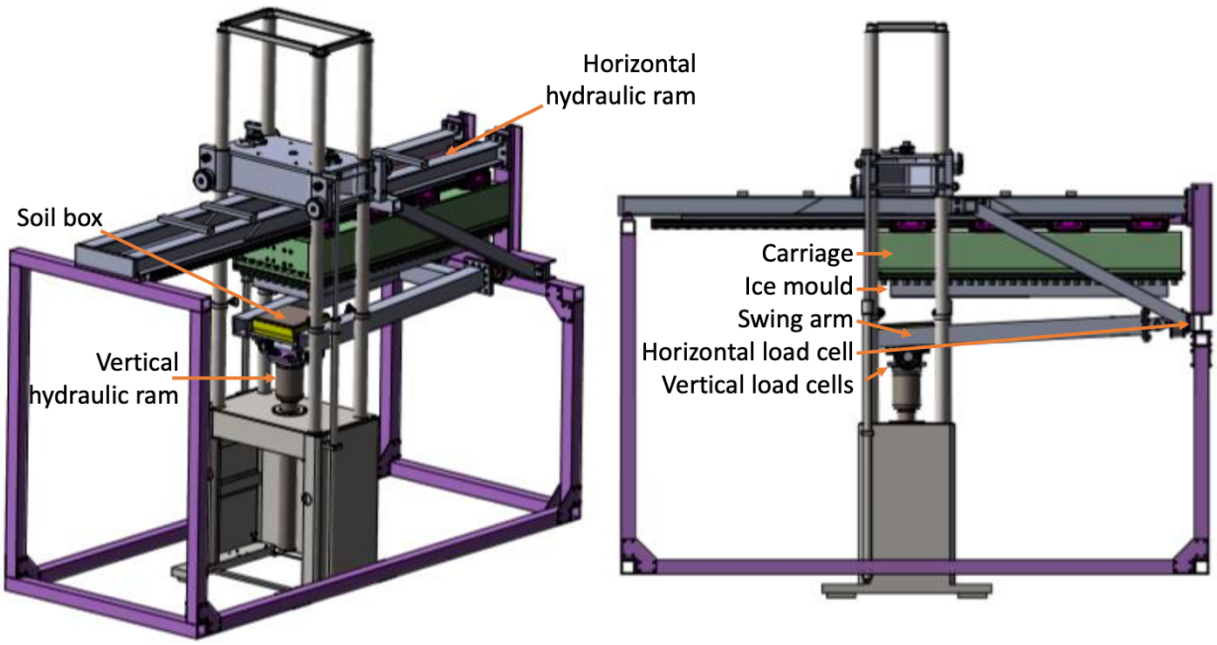

Figure 16 – Labelled image of MTS Load frame with ice mold and soil box, isometric view (left) and side view (right).

3.2.1 Experimental Setup Specifications

To study the ice-particle interaction processes two flat ice specimen, affixed to the top and bottom of the MTS, were used. The specifications of the top and bottom ice specimen moulds plates are given in Table 1.

Table 1 – Ice Mold and Soil Box Specifications

Item	LxWxH
Ice Mold	11x8x2
Soil Box	11x11

Ice specimen of dimensions 11”x8”x2” were used for all tests throughout this experimental program. Both the upper and lower ice specimen can be seen below in Figure 17, and the mould implemented for the upper ice specimen can be seen Figure 18 below.

Figure 17 – Lower ice specimen with rocks placed on top before testing (right), and with ice freshly frozen in soil box, and attached to vertical hydraulic ram (right).

Figure 18 – Upper ice specimen, frozen in ice mold before being affixed to horizontal carriage

.

3.2.2 Test Plan

When designing small-scale experiments, a number of factors presented a challenge when compared to the real scenario. Environmental parameters such as ice velocity, ice temperature, possible indentation depth of rock particles into the ice feature, and the contact time between the ice structures and the ocean floor are all examples of important parameters which were considered in the planning phase of the relevant experiments evaluated within this research program.

In design of experiments, certain factors were controlled during experiments, while other parameters were held constant throughout testing. The input-controlled parameters considered in the current research are discussed below.

Ice Indentation Rate: Ice-soil interaction can occur over a wide range of speeds depending on the drift speed and size of the ice. To cover a range of practical situations, indentation speeds of 0.01 mm/s, 0.5 mm/s, and 10 mm/s were utilized in the experiments. These setpoints provide a representative spectrum of rates ranging from slow speed (0.01 mm/s), moderate speed (0.5 mm/s), and fast speed (10 mm/s) tests.

Rock Indentation Depth: Ice-soil interaction can similarly occur over a wide range of depths into the feature depending on the drift speed of the ice and size of the ice and rock particles. To ensure the ice particle indentation was simulated properly as complete compression within an ice feature, two ice specimen were used to compress the rock on top and bottom surfaces to ensure complete compression of the particles between ice. Due to the size of the rock particles and limitations of the MTS load frame vertical clearance between top and bottom surfaces, indentation depths of 5 mm and 7 mm were implemented in experiments.

Horizontal Displacement: Ice-soil interaction similarly occur as ice is dragged over a wide range of distances horizontally across the ocean floor depending again on the drift speed of the ice and size of the ice and rock particles. To ensure the ice particle friction was simulated properly as shear applied after complete compression within an ice feature, two ice specimen were used to compress the rock on top and bottom surfaces to ensure complete compression of the particles between ice, after which the horizontal displacement would be imposed. Due to the size of the rock particles and limitations of the MTS load frame vertical clearance between top and bottom surfaces, horizontal displacements of 5 mm and 7 mm were implemented in experiments.

Relative Rock Particle Spacing: When Ice-soil interaction occurs, many individual rock and soil particles are pushed into the ice together. This leads to a potential for interaction between particles

in proximity to each other as well as between the particles and other previously formed damage zones. To effectively simulate this, a mean diameter value D was used to define the relative spacing for rock placement away from the damage zones at the indentation sites from prior tests. The distances were taken to be 7D, 5D, and 2D which represented spacings of 96 mm, 65 mm, or 26 mm respectively based on a D value of 13 mm.

In addition to the above parameters, there were few factors which have the potential to effect experimental results but could not be completely eliminated due to the restrictions of the laboratory and limitations of time. One factor was the size, shape, and orientation of each individual rock specimen which varied significantly between each unique specimen. This was taken into consideration during testing as a random variable in terms of orientation and shape, while the dimensions were measured and taken as a nominal area for each. Another factor is that the ice holders and ice moulds were limited in numbers. As well, there may be some dissimilarities of the ice specimen geometry due to variation during shaping of the sample. Another potential source of variability is the presence of air bubbles in the ice specimens. To minimize entrapped air, careful attention was paid to pour the chilled water very slowly into the ice moulds and efforts were made to be consistent to ensure the same quality of ice was achieved for all specimens.

3.4 Ice Sample Preparation

The ice specimens were fabricated to simulate iceberg ice by crushing freshwater, polycrystalline ice, frozen from filtered laboratory tap water, into ice seeds using an industrial ice crushing machine. To fabricate the ice specimen, the ice seed were placed into the metal mold and the void space was filled by flooding the mold with filtered tap water that was allowed to cool to near freezing in the cold room. To ensure the sample would freeze evenly, the ice seed was tamped

down with a flat piece of wood as the water was poured to ensure there were no air bubbles or uneven areas within the specimen. Additionally, this process was repeated up to three times for a single specimen in order to allow the ice to freeze in layers, where one layer was poured, flattened, and allowed to freeze in the cold room freezer at -10℃. This process would take up to 90 minutes for a single layer, at which point the ice seed and cooled water would again be filled over the frozen layer, flattened, and allowed to freeze. Layers would be frozen until the entire sample mold was filled, at which point the sample was allowed to finish freezing completely for anywhere from 12-24 hours. Freezing was additionally conducted with a pane of insulating foam placed over the exposed top layer of the ice specimen to ensure directional freezing. This same process of crushing seed ice, flooding and freezing the ice was implemented for a single large layer to produce the bottom ice specimen. The lower ice specimen, affixed to the vertical hydraulic ram, can be seen in Figure 17, as well as the upper ice specimen which can be seen in Figure 18. The ice crusher used to create ice seed which was used to fabricate the ice specimen can be seen in Figure 19 below.

Figure 19 – Ice crusher used to create ice seed.

3.5 Rock Sample Preparation

For the purposes of the experiments outlined in this work, the sample of rock particles were collected from a population of particles taken from the Memorial University concrete laboratory. The entire rock population was sieved into three separate population sizes, which were defined as Small (Less than 3/8”), Medium (between 3/8”–3/4”), and Large (Greater than 3/4”), rock particles. These populations were separated out and prepared for implementation in experimental programs. For all testing the Medium (between 3/8”–3/4”) population were implemented for use. Rocks were kept in the cold room cooler between uses in order to keep the temperature setpoint of the rocks consistent with the ambient temperature of the testing environment and ice conditions.

3.6 Testing Procedure

All compressive tests were completed in the cold room in the thermo-fluids lab located at Memorial University. All tests were completed with the same MTS load frame, water, ice, sample moulds, and rock populations.

3.6.1 Single-Particle Indentation Tests

For a given experiment, the top ice specimen was mounted to the upper mounting plate, which was fixed to the MTS crosshead. The bottom-mounted ice specimen was fixed to the modified soil box attachment, which was affixed to the MTS base plate attached to the vertical hydraulic ram. The hydraulic ram was used to control vertical displacement and the indentation rate of the lower ice specimen, while the upper ice specimen and MTS crosshead remained fixed in place during the test. Before each test, a rock particle of known dimensions was placed at a specific location at a defined distance away from a previous damage zone on the bottom ice specimen. For the final step before running the test program, procedure varied based on the test being completed. For single ice-particle indentation tests, the rock particle was brought up to position such that the rock sample

was in contact as close as possible with the ice specimen above. The top ice specimen position was adjusted such that indentation was conducted on pristine ice areas within the required set distance from the previous indentation zone. Once the ice specimens no longer had suitable areas of pristine ice to conduct the indentation tests, new ice specimens were prepared.

3.6.2 Multi-Particle Indentation Tests

For tests evaluating multi-contact ice-particle interactions, the same procedure was implemented, without considerations for relative spacing. Before each test, a random group of rocks were scooped from a bucket containing the total population of rocks used for testing. These samples were then weighed such that there was a consistent weight of 170 grams worth of rock particles for each test. Once the rocks were collected, they were spread evenly across the bottom ice specimen and the rock particles were brought up to position such that the rock samples were in contact as close as possible with the ice specimen above. After each test, the ice specimens no longer had suitable areas of pristine ice to conduct the indentation tests, and new ice specimens were prepared.

3.7 Statistical Analysis of Rock Samples

Statistical analysis of a sample of rock particles collected from a sieved population size between 3/8”–3/4” was completed to determine the mean rock particle diameter, which was determined to be 13 mm. Determining the particle size distribution of gravel rocks to verify soil sieving was achieved by converting the original image into binary form and applying object detection of blob analysis. Different segmentation techniques as well as photo editing were used to prevent appearance of white flecks, disappearance of rocks blending in with the background, and

separation of overlapping rocks in order to obtain accurate data related to the rock population. The gravel code output of medium, small, and large rocks was analyzed. Information about the rock particle size distribution was used in related analysis for multi-point contact modelling. The process of using the MATLAB image processing algorithm to gradually improve the gravel rock visibility can be seen below in Figure 20, and was achieved through the implementation of techniques including thresholding and various morphological functions used in combination with the watershed technique which involved the manipulation of the contrast and area function, as well as applying the aforementioned morphological functions.

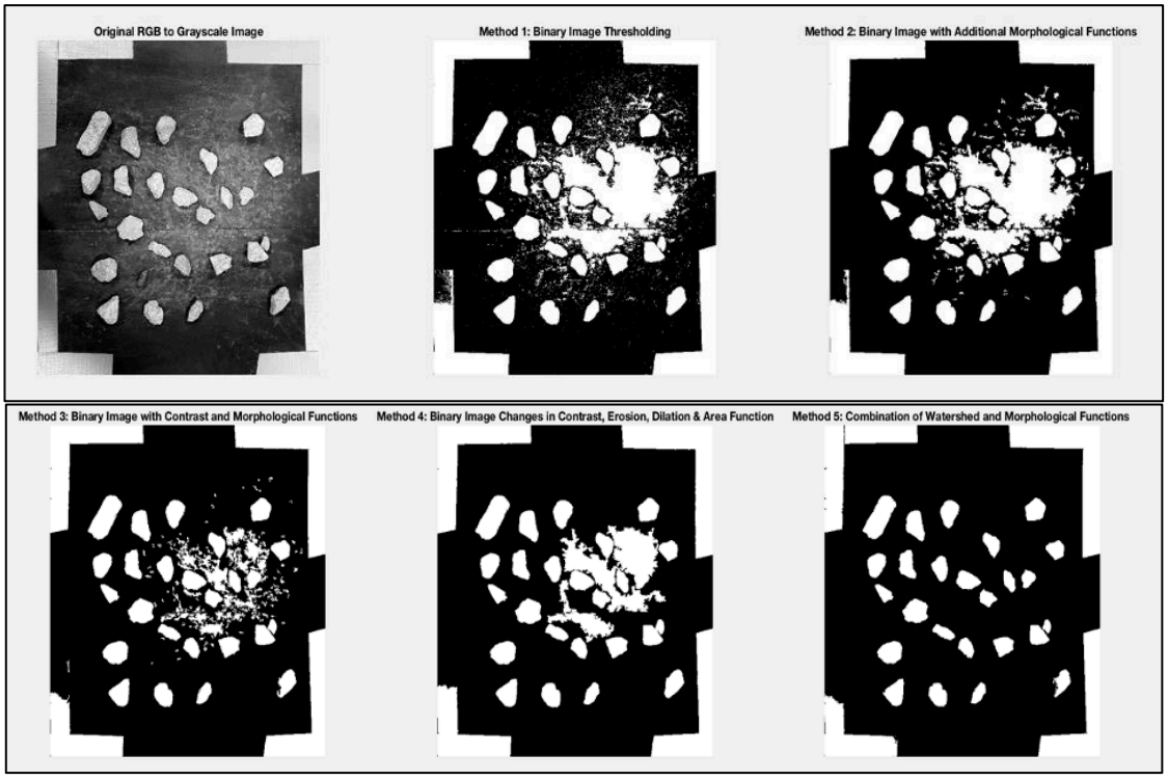

Figure 20 - Improvement of the MATLAB algorithm to remove any unwanted (non-rock) white blobs.

As can be seen below in Figure 21, the images were then numbered with the developed MATLAB algorithm and measured based on an analysis of pixil length which was then converted to millimetres based on a bounding region shape.

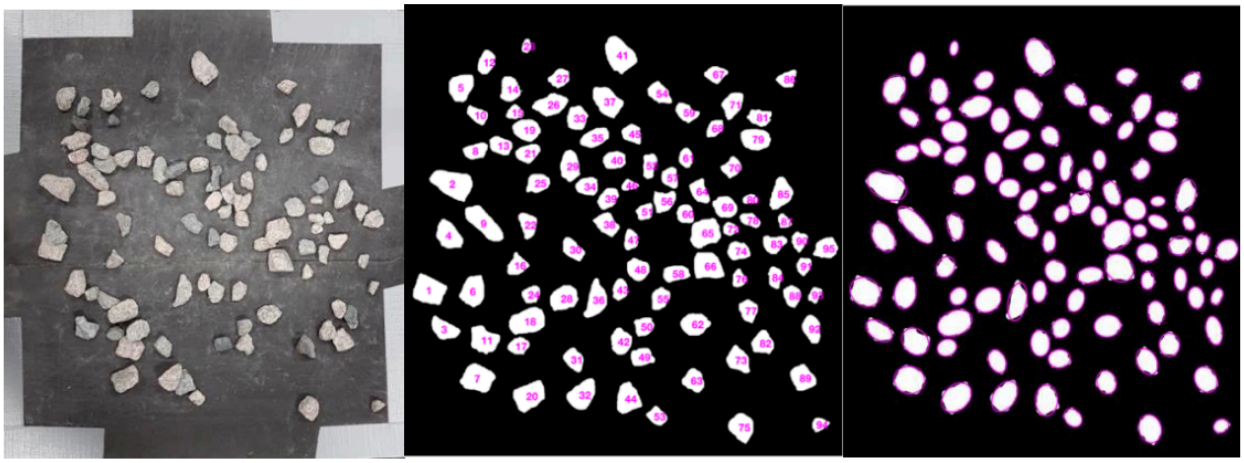

Figure 21 - Medium sample set with rocks labelled based on their true blob area and centroid, and a bounding region shape is applied.

For the purpose of the work presented related to single-particle indentation testing, the mean diameter value D was used to define the relative spacing for rock placement away from the damage zones at the indentation sites from prior tests. The distances were taken to be 7D, 5D, and 2D which represented spacings of 96 mm, 65 mm, or 26 mm respectively based on a D value of 13 mm. Additional analysis was completed on images of the photographed damage zones left behind after indentation and compared to pristine ice sections before testing was completed.

4.0 Experimental Results

4.1 Overview

This research program consisted of two independent experimental series, one set which examined the interaction of multi-particle indentation between ice specimens, and a second set which examined the interaction of single-particle indentation between ice specimens. For the purposes of this analysis the area and pressure are calculated based off measured vertical and horizontal diameters, relative to the plane of the MTS, of the individual rocks implemented for use during each experimental run, as can be seen in Figure 22 below.

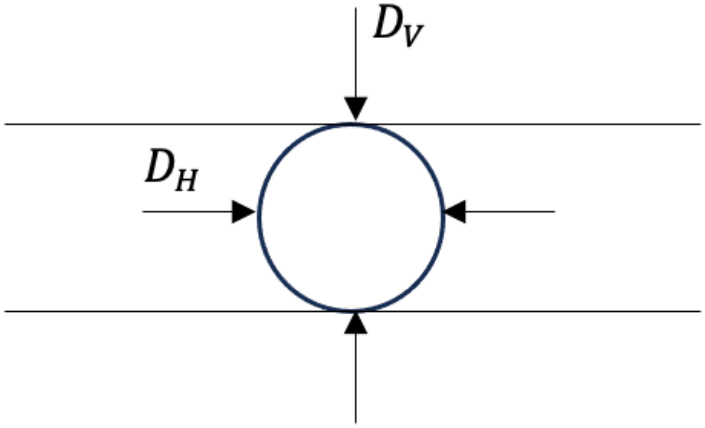

Figure 22 - Schematic showing the measuring convention for the horizontal and vertical diameters of a given rock, as measured relative to the plane of placement on the MTS.

The calculations for these values are implemented from the relationship of indentation depth assuming maximum indentation and measurements of nominal rock diameters as given below.

$$D_N = \frac{D_V + D_H}{2}$$ *Equation 4*

$$r = \frac{D_N}{2}$$ *Equation 5*

$$R = r^2 - (r - x)^2$$ *Equation 6*

$$A_N = 4 * \pi * (R)^2$$ *Equation 7*

$$P = \frac{F}{A_N}$$ *Equation 8*

Where, D_N is the nominal diameter of a rock particle for a given test; D_v is the vertical diameter for any given rock particle; D_H is the horizontal diameter for any given rock particle; r is the nominal radius of the rock particle; x is the relative indentation depth at a given point in time; R is the effective radius of the rock particle during indentation; A_N is the nominal surface area of a given rock particle; P is the pressure; and F is Force obtained from the load cell.

During the series of multi-particle indentation experiments, fifty-five (55) successful tests were completed, including repetitions on non-pristine ice. Of these tests, twenty-five (25) were completed on pristine ice samples. Tests were completed on a group of rock particles which were weighed out to a consistent weight of 170 grams, independent of the number of particles present in the samples to account for variability within the population. Initially, only vertical indentation was imposed on the rock samples, with horizontal motion being introduced later in tandem to an

initial vertical indentation phase. Parameters varied included indentation depth and horizontal motion displacement. Of these 25 tests completed on pristine ice, three test were completed with a 1-minute hold time up to a 5 mm vertical indentation with no horizontal motion, four tests were completed with a 1-minute hold time to a 7 mm vertical indentation with no horizontal motion. Two tests were completed with a 30-minute hold time up to a 7 mm vertical indentation with no horizontal motion. Additionally, four tests were completed with a 1-minute hold time up to a 5 mm vertical indentation and 5 mm of horizontal motion, four were completed with a 1-minute hold times up to a 5 mm vertical indentation with 7 mm of horizontal motion. Finally, four tests were completed with a 1-minute hold time up to a 7 mm vertical indentation with 5 mm of horizontal motion, and four tests were completed with a 1-minute hold time up to a 7 mm vertical indentation with 7 mm of horizontal motion. All tests were completed with medium sized rocks ~ 3/4 - 3/8-inch samples, at setpoint temperatures of -10°C.

The naming convention for each consecutive test has been prepared in a way such that the testing parameters for each test can be easily identified. An example of the test naming convention is given below.

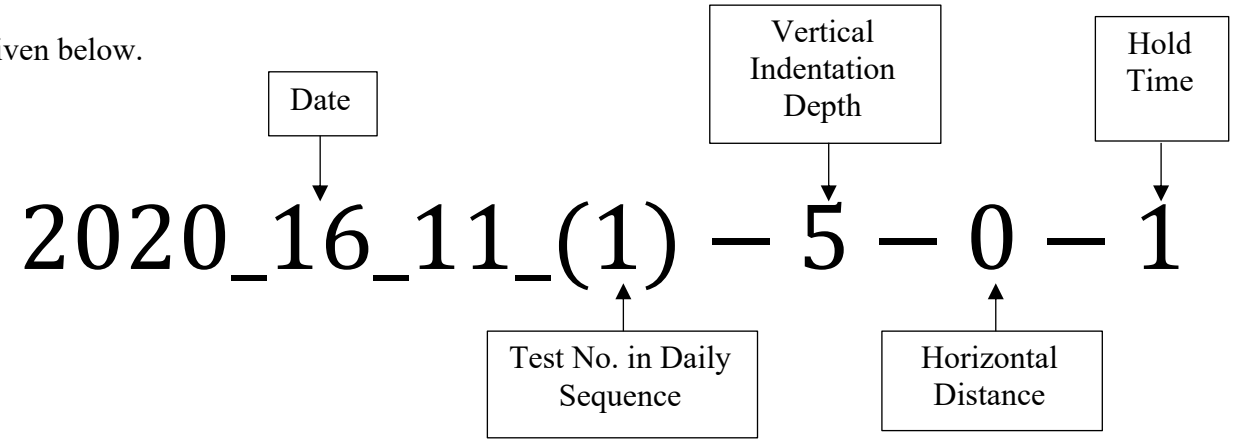

The test matrix for initial test cases without repetitions for the experimental program can be seen below in Table 2.

Table 2 – Test matrix for single-particle indentation tests

Test No.	**Test ID**	***Vd*** (mm)	***Hd*** (mm)	***T*** *(min)*
1	2020_16_11_(1)-5-0-1	5	0	1
2	2020_16_11_(4)-5-0-30	5	0	30
3	2021_18_11_(1)-7-0-1	7	0	1
4	2021_18_11_(4)-7-0-30	7	0	30
5	2021_19_11_(1)-7-0-1	7	0	1
6	2021_19_11_(4)-7-0-1	7	0	1
7	2021_20_11_(1)-7-0-30	7	0	30
8	2021_23_11_(1)-7-0-1	7	0	1

During the series of single-particle indentation experiments, sixty-six (66) tests in total were completed, with repetitions of up to 10 tests per setpoint. These tests consisted of only vertical indentation on single particles (no horizontal motion was imposed). Parameters varied included indentation rate and indentation site spacing. Of these 66 total tests, 30 tests were completed with an indentation rate of 0.5 mm/s, which consisted of three groups of ten tests completed at spacing S of 7D (96mm), 5D (65 mm), and 2D (26 mm) respectively. An additional 30 tests were completed at an indentation rate of 10 mm/s, which consisted of three groups of ten tests completed at spacings S equal to 7D (96 mm), 5D (65 mm), and 2D (26 mm) respectively. Finally, six tests were completed at an indentation rate of 0.01 mm/s, which consisted of three groups of two tests completed at the same spacing distances. The naming convention for each consecutive test has been prepared in a way such that the testing parameters for each test can be easily identified. An example of the test naming convention is given below.

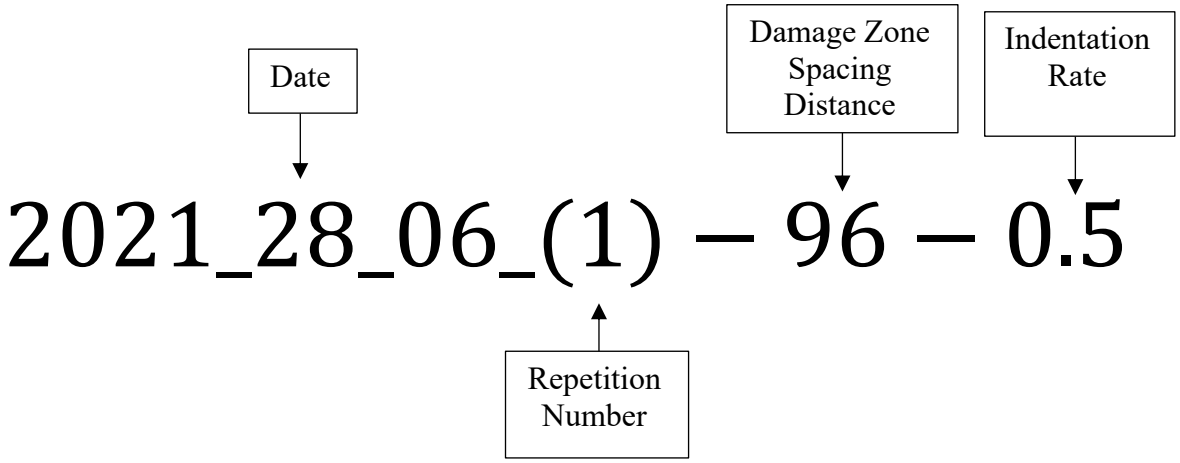

The test matrix for initial test cases without repetitions for the experimental program can be seen below in Table 3.

Table 3 – Test matrix for multi-particle indentation tests

Test No.	**Test ID**	***S*** (mm)	***v*** (mm/s)
1-10	2021_28_06_(1)-96-0.5	96	0.5
11-20	2021_28_06_(11)-65-0.5	65	0.5
21-30	2021_29_06_(1)-26-0.5	26	0.5
31-40	2021_06_07_(1)-96-10	96	10
41-50	2021_07_07_(1)-65-10	65	10
51-60	2021_08_07_(1)-26-10	26	10
61	2021_13_07_(1)-96-0.01	96	0.01
62	2021_13_07_(2)-65-0.01	65	0.01
63	2021_13_07_(3)-26-0.01	26	0.01

4.2 Results for Single Particle Embedment

Sixty-six (66) tests in total were completed for experiments investigating single-particle embedment. Of these 66 total tests, 30 tests were completed with an indentation rate of 0.5 mm/s, which consisted of three groups of ten tests completed at spacing S of 7D (96mm), 5D (65 mm), and 2D (26 mm) respectively. An additional 30 tests were completed at an indentation rate of 10 mm/s, which consisted of three groups of ten tests completed at spacings S equal to 7D (96 mm), 5D (65 mm), and 2D (26 mm) respectively. Finally, six tests were completed at an indentation rate of 0.01 mm/s, which consisted of three groups of two tests completed at the same spacing distances. All tests were completed with medium sized rock, to a depth of 7 mm with a nominal set point temperature of -10°C. In this section, three test are discussed which were completed at three different indentation speeds: 0.1 mm/s, 1 mm/s and 10 mm/s. Additionally, test results for spacings of 7D (96 mm), 5D (65 mm), and 2D (26 mm) are also presented and discussed.

4.2.1 Slow Rate Tests (0.01 mm/s)

Results obtained from slow speed tests primarily presented a combination of ductile and brittle failure modes throughout the indentation period. Despite a 60 second hold time being imposed throughout experimental runs; the initial indentation period was analyzed primarily for these tests in order to more accurately study the behaviour of compressive ice failure. Force-depth data collected from the MTS load cell and pressure-depth data calculated from Equation 4 through Equation 8 above are presented in Figure 23 and Figure 24. The maximum force for this ice sample was recorded as 2973 N and maximum pressure at full indentation was 3.42 MPa up to the indentation depth of 7 mm. The test referenced for the results in this section is denoted as 2021_13_07_(2)-65-0.01.

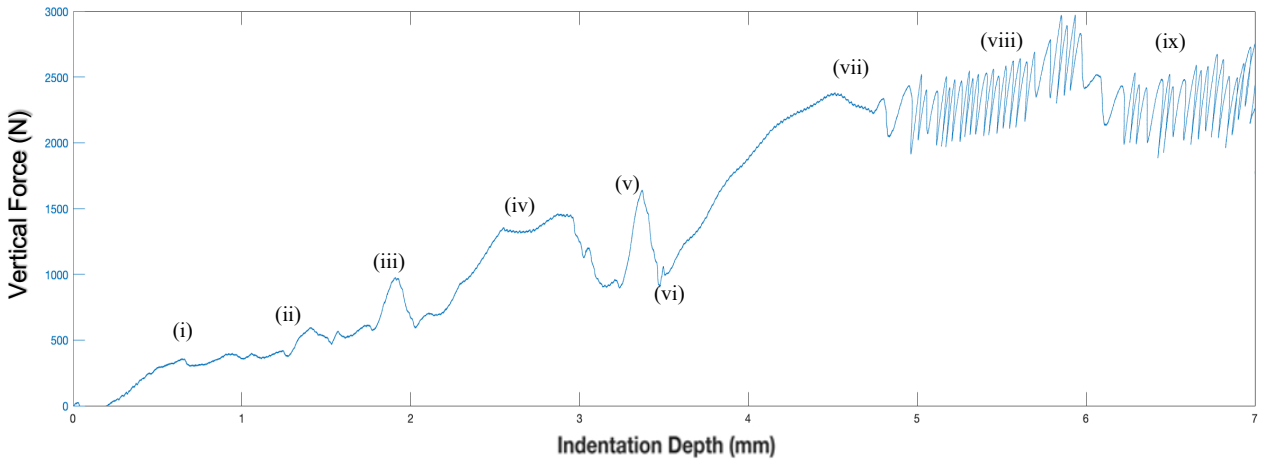

Figure 23 - Single particle force-indentation MTS load data completed at a rate of 0.01 mm//s to a depth of 7 mm.

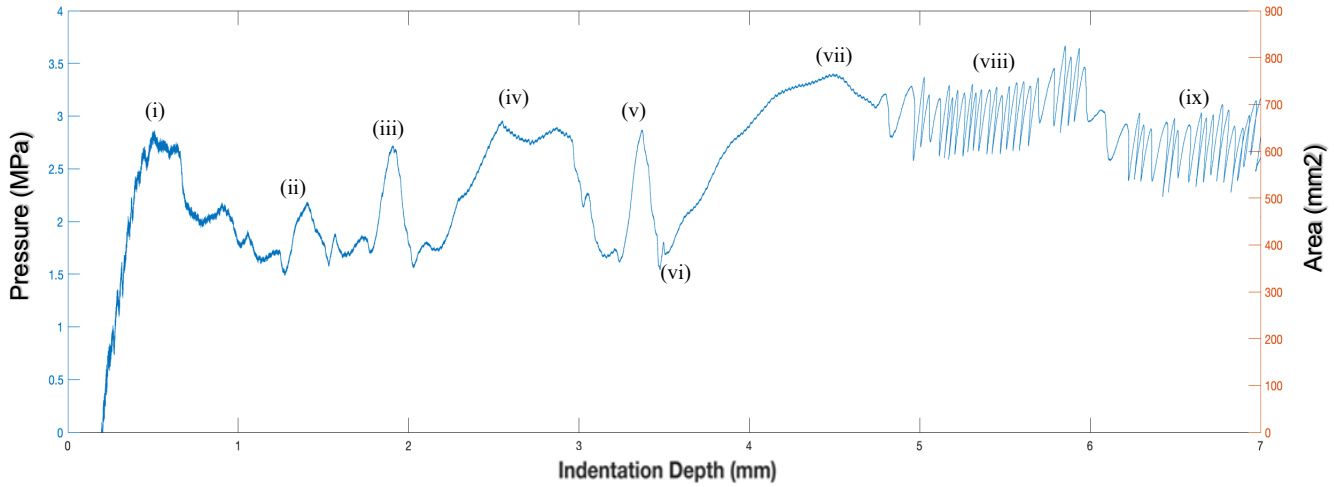

Figure 24- Single particle pressure-indentation data completed at a rate of 0.01 mm//s to a depth of 7 mm.

For this spacing at an indentation rate of 0.01 mm/s the curve can be seen to exhibit evidence of combined ductile and brittle failure, which gives way to two repeated crushing events as the indentation depth increased. Irregularities in the ice-particle contact geometry arising from asperities on the natural rock particles is a likely contributor which triggers localized spalling under conditions where more creep-dominated behaviour would typically be expected from smooth indenter tests. Specifically, as can be seen in Figure 23 and Figure 24, the behaviour noted in events (i) and (ii) show an increasing trend of both load and pressure as indentation depth and effective area increase. As the indentation progresses, it is noted in event (iii) that damage enhanced creep and slow crushing failure is beginning to occur as can be seen in the force-depth plot while one of the peak pressure points can be observed on the pressure-depth plots. Larger load drops and decreases of high-pressure zones can be observed at events (iv), (v), (vi), and another sharp load drop is observed at event (vii) which is followed by two repeated crushing events denoted by (viii) and (ix) which can be seen in the force-indentation plot. The data observed in the pressure-depth plot corresponds to these observations from the force-indentation plots for the same denoted events. The load cell data and calculated pressure-depth data were in generally good

agreement and compared well with the images taken after the tests were completed, as can be seen in Figure 25 below. Throughout the process of indentation of the rock at the slow rate, the rock particle indented fully and uniformly, with evidence of damaged enhanced creep and some spalling as well as repeated crushing events thought to be due to irregularities in the ice-particle contact geometry. As discussed previously, the images taken after indentation, shown in Figure 25, supports that combined ductile and brittle failure was observed with some spalling and crushing events occurring as well, with the overall failure of the ice being ductile in nature.

Figure 25 – Images taken after indentation of upper ice specimen (a)(b) and lower ice specimen (c).

Photographs of the primary upper and lower ice specimens and rock particles can be seen above in Figure 25, depicting the crushed ice and indented rock particles immediately after the test was completed for experimental test runs completed at an indentation rate of 0.01 mm/s at different spacing distances. These images taken after indentation in the case of the slow speed test show primarily crushing in the lower ice specimen, with mild crushing and a small, confined indent on the upper primary ice specimen. There is also evidence of small cracks propagating away from the primary indentation area on the upper indentation surface. One additional point of particular interest is the rock which had embedded itself into the ice and stuck in place, which suggests localized pressure melting and refreezing during the indentation and holding process.

4.2.2 Medium Rate Tests (0.5 mm/s)

Similarly, results obtained from medium speed tests primarily presented ductile failure modes throughout the indentation period. Despite a 60 second hold time being imposed throughout experimental runs; the initial indentation period was analyzed primarily for these tests in order to more accurately study the behaviour of compressive ice failure. Force-depth data collected from the MTS load cell and pressure-depth data are presented in Figure 26 and Figure 27. The maximum force for this ice sample was recorded as 4271 N and maximum pressure at full indentation was 5.48 MPa up to the indentation depth of 7 mm. The test referenced for the results in this section is denoted as Test 2021_28_06_(16)-65-0.5.

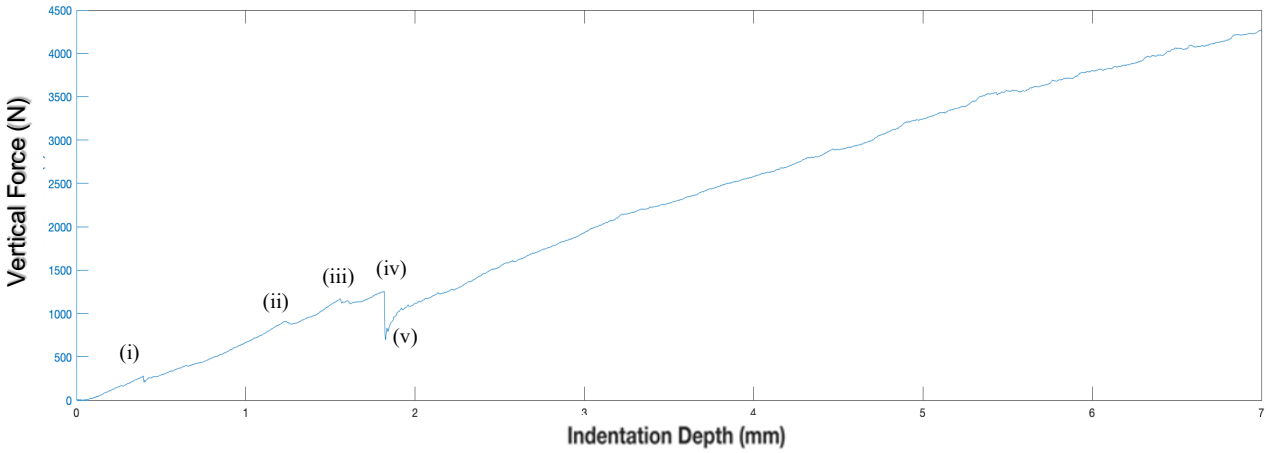

Figure 26 - Single particle force-indentation MTS load data completed at a rate of 0.5 mm//s to a depth of 7 mm.

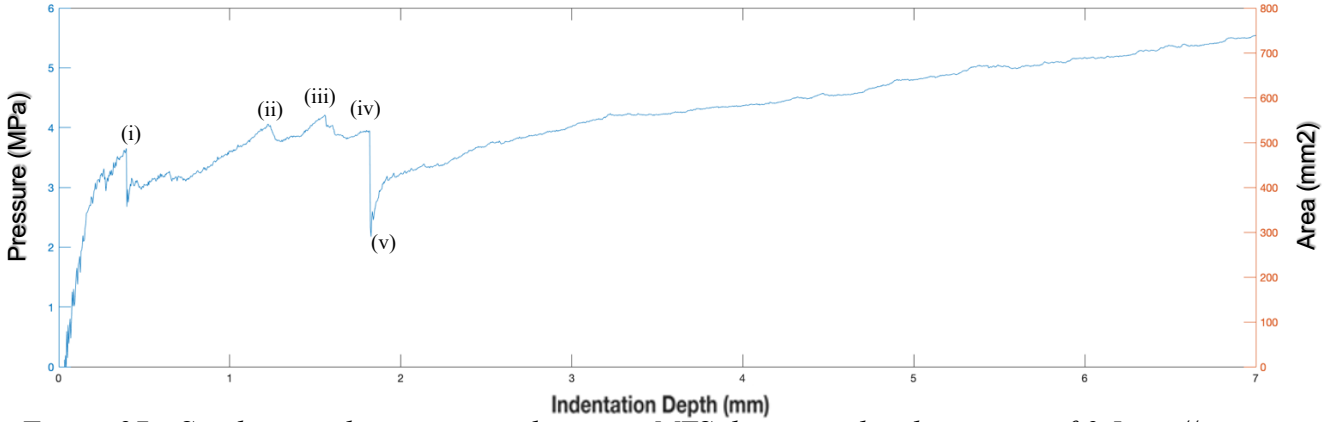

Figure 27 - Single particle pressure-indentation MTS data completed at a rate of 0.5 mm//s to a depth of 7 mm.

For the moderate rate of 0.5 mm/s it can be observed that the load continuously increases, with one localized spall near the beginning of indentation as the sample experiences slow crushing failure; this is representative of a failure mode which is typically referred to as a 'ductile' failure, and corresponds to a slow, continuous flow of crushed ice beneath the contact zone. Specifically, as can be seen in Figure 26 and Figure 27, the behavior noted event (i) shows an increasing trend of both load and pressure as indentation depth and effective area increase. As the indentation progresses, it is noted in event (ii) damage enhanced creep and slow crushing failure is beginning to occur with a small spalling event occurring as can be seen in the force-depth plot while one of the peak pressure points can be observed on the pressure-depth plots. Larger load drops and decreases of high-pressure zones can be observed at events (iii), (iv), and another sharp load drop is observed at event (v) which is additionally followed by a larger spalling event which can be seen in the force-indentation plot. The data observed in the pressure-depth plot additionally corresponds to these observations from the force-indentation plots for the same denoted events. Finally, the load begins to increase again consistently until the end of indentation. The load cell data and calculated pressure-depth data were in generally good agreement and compared well with the images taken after the tests were completed, as can be seen in Figure 28 below. Throughout the process of indentation of the rock at the moderate rate, the rock particle indented fully and uniformly, with evidence of a slow, continuous flow of crushed ice beneath the contact zone, with some spalling and crushing events. As discussed previously, the images taken after indentation, shown in Figure 28, supports that primarily ductile failure was observed with some spalling and crushing events occurring as well, with the overall failure being ductile in nature.

Figure 28 – Images taken after indentation of upper ice specimen (a) and lower ice specimen (b).

Photographs of the primary upper and lower ice specimens and rock particles can be seen above in Figure 28, depicting the crushed ice and indented rock particles immediately after the test was completed for experimental test runs completed at an indentation rate of 0.5 mm/s and different spacing distances. These images taken after indentation in the case of the moderate speed test show primarily crushing in the lower ice specimen, with mild crushing and a small, confined indent on the upper primary ice specimen. There is also evidence of small cracks propagating away from the primary indentation area on the upper indentation surface.

4.2.3 Fast Rate Tests (10 mm/s)

Results obtained from fast speed tests primarily presented brittle failure modes throughout the indentation period. Despite a 60 second hold time being imposed throughout experimental runs; the initial indentation period was analyzed primarily for these tests in order to more accurately study the behaviour of compressive ice failure. Force-depth data collected from the MTS load cell and pressure-depth data are presented in Figure 29 and Figure 30. The maximum force for this ice sample was recorded as 2707 N and maximum pressure at full indentation was 3.39 MPa up to the indentation depth of 7 mm. The test referenced for the results in this section is denoted as Test 2021_06_07_(10)-96-10.

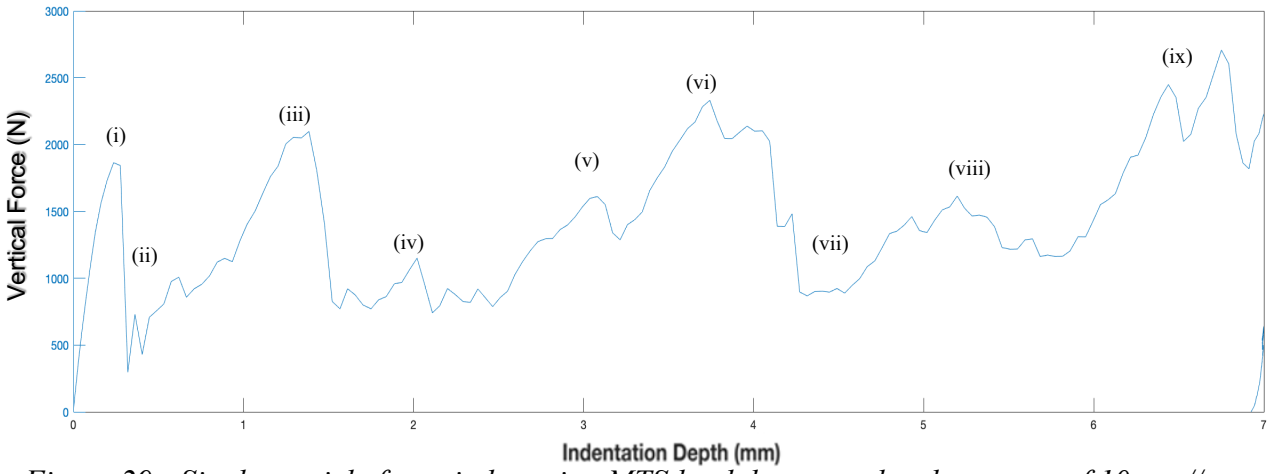

Figure 29 - Single particle force-indentation MTS load data completed at a rate of 10 mm//s to a depth of 7 mm.

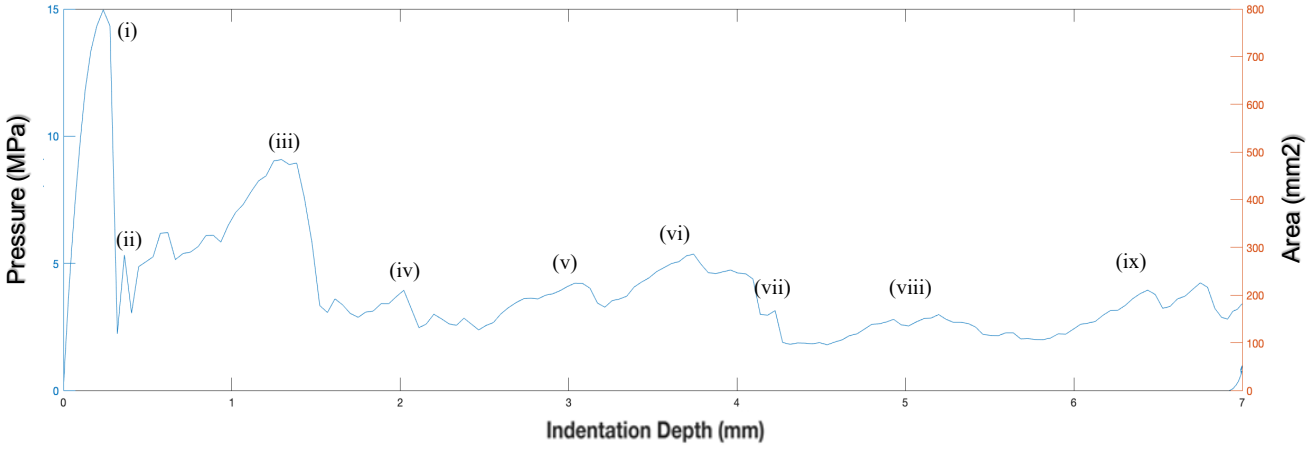

Figure 30 - Single particle pressure-indentation MTS data completed at a rate of 10 mm//s to a depth of 7 mm.

For the 10 mm/s test, the load builds steadily and undergoes typical phases of dynamic loading, with large spalls and associated load drops being observed throughout the duration of indentation. Specifically, as can be seen in Figure 29 and Figure 30, the behaviour noted in event (i) shows a rapid increasing trend of both load and pressure as indentation depth and effective area increase. As the indentation progresses, it is noted in event (ii) the first large spalling event takes place as can be seen in the force-depth plot while one of the peak pressure points can be observed on the pressure-depth plots. The load continues to build with small spalling events occurring until another larger load drop and decrease of high-pressure zones is observed at event (iii). Multiple small spalls occur again as well as another larger spall at event (iv) which gives way to continued load building Another load drop is observed at event (v), while the load continues to build steadily following this event. Additionally, the load reaches another maximum and a larger spalling event which can be seen in the force-indentation plot at event (vi). The load again begins to build while undergoing smaller spalling events as can be seen in (vii) and (viii). Finally, the load reaches a maximum at (ix) and undergoes multiple spalling events. The data observed in the pressure-depth plot additionally corresponds to these observations from the force-indentation plots for the same

denoted events; however, a larger spike in pressure is observed during the very beginning phases of indentation due to the large initial force reading at (i) combined with a very small effective area of particle contact. The larger initial pressure (i)(ii)(iii) and eventual lower taper of pressures near the middle (v)(vi) and end of indentation (viii)(ix) is to be expected due to the nature of progression of the contact area as indentation proceeds. The load cell data and calculated pressure-depth data were in generally good agreement and compared well with the images taken after the tests were completed, as can be seen in Figure 31 below. Throughout the process of indentation of the rock at the moderate rate, the rock particle indented fully and uniformly, with evidence of a slow, continuous flow of crushed ice beneath the contact zone, with some spalling and crushing events. As discussed previously, the images taken after indentation, shown in Figure 31, outlines that primarily ductile failure was observed with some spalling and crushing events occurring as well, with the overall failure being ductile in nature.

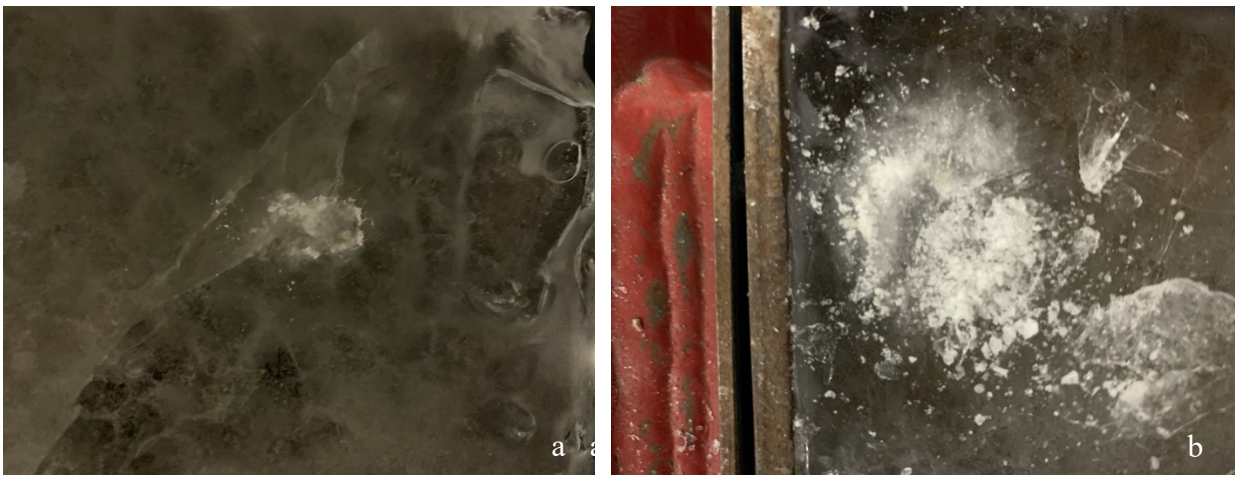

Figure 31 - Images taken after indentation of upper ice specimen (a) and lower ice specimen (b)

Photographs of the primary upper and lower ice specimens and rock particles can be seen above in Figure 31, depicting the crushed ice and indented damage areas immediately after the test was completed for experimental test runs completed at an indentation rate of 10.0 mm/s at different

spacing distances. These images show evidence of crushing with extensive spalling, which is characteristic of brittle failure. Such failures exhibited small zones of localized damage with much of the local material removed by fractures resulting from cracks propagating from beneath the ice-particle interface.

4.2.4 7D Spacing Case (96 mm)

Results obtained from tests completed at a 7D (96 mm) spacing distance primarily presented behaviour which was consistent with typical tests completed for the given conditions at the representative indentation rate of 0.5 mm/s, where ductile failure was observed throughout the indentation period. Despite a 60 second hold time being imposed throughout experimental runs; the initial indentation period was analyzed primarily for these tests in order to more accurately study the behaviour of compressive ice failure. Force-depth data collected from the MTS load cell and pressure-depth data are presented in Figure 32 and Figure 33 The maximum force for this ice sample was recorded as 5096 N and maximum pressure at full indentation was 4.07 MPa up to the indentation depth of 7 mm. The test referenced for the results in this section is denoted as Test 2021_28_06_(4)-96-0.5.

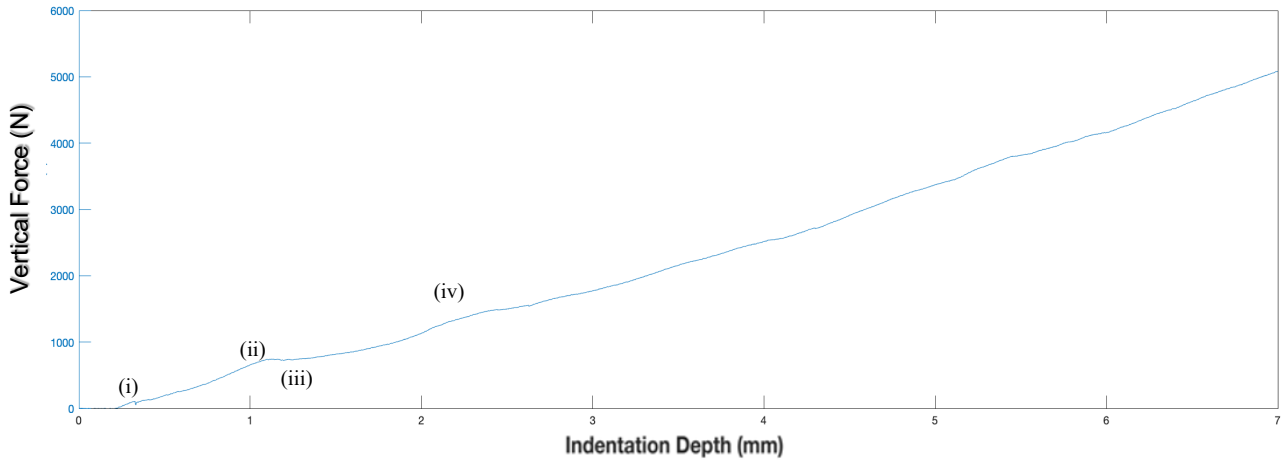

Figure 32 - Single particle force-indentation MTS load data completed at a rate of 0.5 mm/s to a depth of 7 mm for a 7D spacing case.

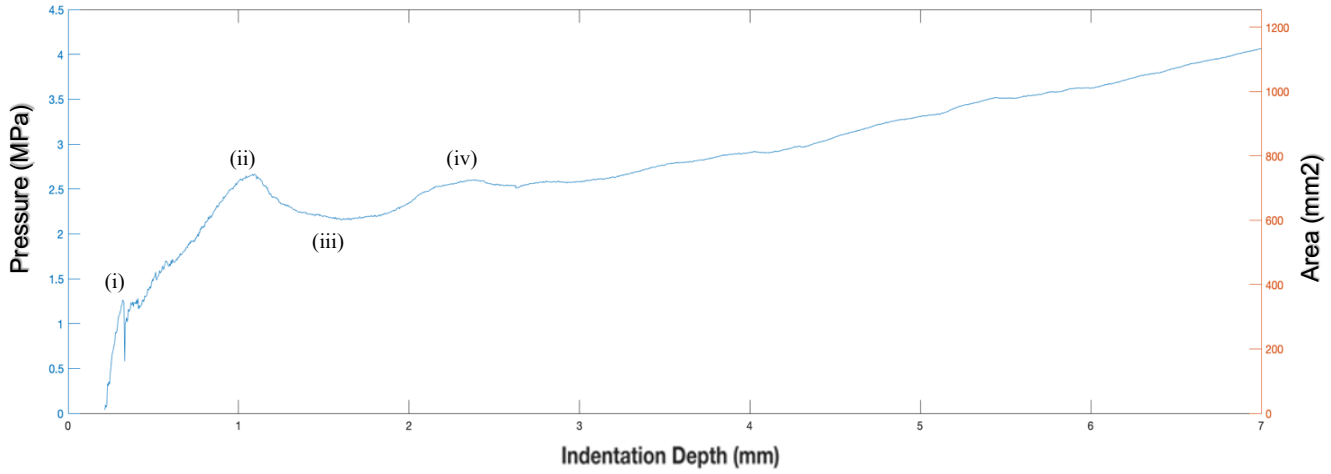

Figure 33 - Single particle pressure-indentation data completed at a rate of 0.5 mm//s to a depth of 7 mm for a 7D spacing case.

For the 7D (96 mm) spacing case at a moderate rate of 0.5 mm/s it can be observed that the load continuously increases, with one larger localized spall near the beginning of indentation as the sample experiences slow crushing failure and increases until the end of indentation; this is representative of a 'ductile' failure mode, and corresponds to a slow, continuous flow of crushed ice beneath the contact zone. Specifically, as can be seen in Figure 32 and Figure 33, the behaviour noted in event (i) shows an increasing trend of both load and pressure as indentation depth and effective area increase, which is followed by a localized spalling event. As the indentation progresses, it is noted in event (ii) damage enhanced creep and slow crushing failure is beginning to occur with a small load drop event occurring as can be seen in the force-depth plot while one of the peak pressure points can be observed on the pressure-depth plot. Smaller moderate load drops and decreases in pressure can be observed at events (iii), (iv) before continuing to increase steadily until the end of indentation. The data observed in the pressure-depth plot additionally corresponds to these observations from the force-indentation plots for the same denoted events. The load cell data and calculated pressure-depth data were in generally good agreement and compared well with the images taken after the tests were completed, as can be seen in Figure 34 below. Throughout

the process of indentation of the rock at the moderate rate, the rock particle indented fully and uniformly, with evidence of a slow, continuous flow of crushed ice beneath the contact zone, with some spalling and crushing events. As discussed previously, the images taken after indentation, shown in Figure 34, outlines that primarily ductile failure was observed with some spalling and crushing events occurring as well, with the overall failure being ductile in nature.

Figure 34 - Images taken after indentation of upper ice specimen (a) and lower ice specimen (b).

Photographs of the primary upper and lower ice specimens and rock particles can be seen above in Figure 34, depicting the crushed ice and indented rock particles immediately after the test was completed for experimental test runs completed at an indentation rate of 0.5 mm/s and a 7D spacing distances. These images taken after indentation in the case of the moderate speed test at a 7D spacing show primarily crushing in the lower ice specimen, with mild crushing and a small, confined indent on the upper primary ice specimen. There is also evidence of small cracks propagating away from the primary indentation area on the upper indentation surface.

4.2.5 5D Spacing Case (65 mm)

Results obtained from tests completed at a 5D (65 mm) spacing distance primarily presented behaviour which was again consistent with typical tests completed for the given conditions at the representative indentation rate of 0.5 mm/s, where ductile failure was observed throughout the indentation period. Despite a 60 second hold time being imposed throughout experimental runs; the initial indentation period was analyzed primarily for these tests in order to more accurately study the behaviour of compressive ice failure. Force-depth data collected from the MTS load cell and pressure-depth data are presented in Figure 35 and Figure 36. The maximum force for this ice sample was recorded as 5214 N and maximum pressure at full indentation was 6.94 MPa up to the indentation depth of 7 mm. The test referenced for the results in this section is denoted as Test 2021_28_06_(11)- 65-0.5.

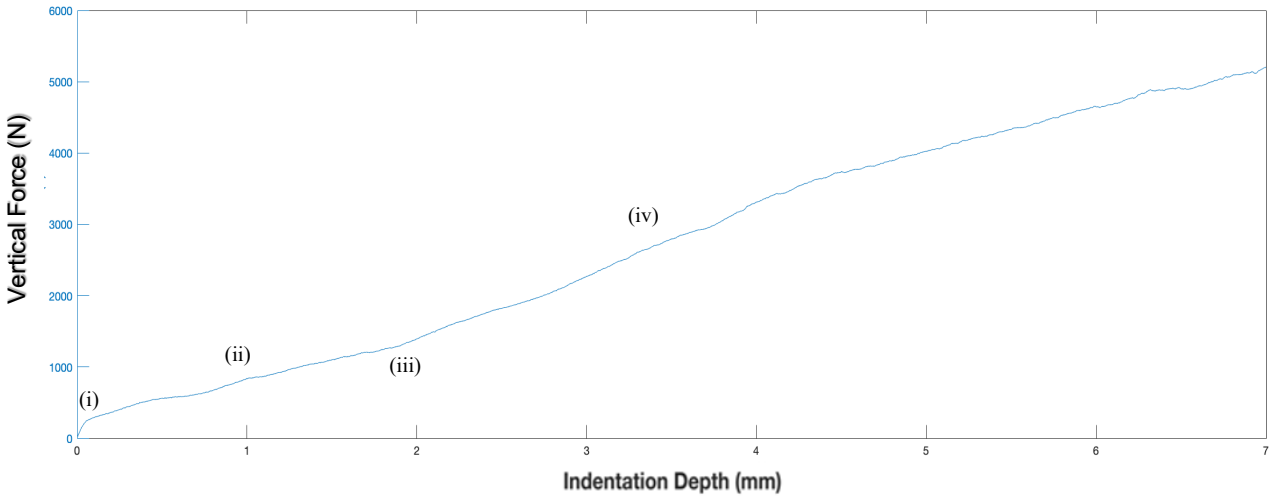

Figure 35 - Single particle force-indentation MTS load data completed at a rate of 0.5 mm//s to a depth of 7 mm for a 5D spacing case.

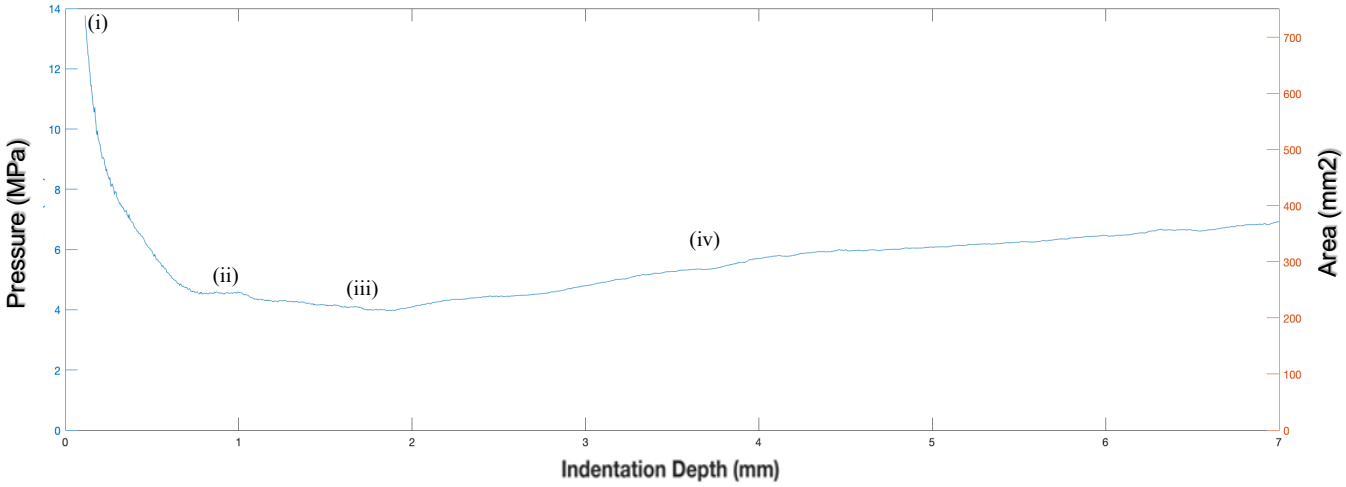

Figure 36 - Single particle pressure-indentation data completed at a rate of 0.5 mm//s to a depth of 7 mm for a 5D spacing case.

For the 5D (65 mm) spacing case at a moderate rate of 0.5 mm/s it can be observed that the load continuously increases, and the sample experiences slow crushing failure while increasing until the end of indentation; this is representative of a 'ductile' failure mode, corresponding to a slow, continuous flow of crushed ice beneath the contact zone. Specifically, as can be seen in Figure 35 the behaviour noted in event (i) shows a rapid initial increasing trend of both load and pressure as indentation depth and effective area increase. As the indentation progresses, it is noted in event (ii) damage enhanced creep and slow crushing failure is beginning to occur with a small load drop event occurring as can be seen in the force-depth plot while the pressure follows the same trend as can be observed on the pressure-depth plots. Smaller moderate load drops and decreases in pressure can be observed at events (iii), (iv) before continuing to increase steadily until the end of indentation. The data observed in the pressure-depth plot additionally corresponds to these observations from the force-indentation plots for the same denoted events. The load cell data and calculated pressure-depth data were in generally good agreement and compared well with the images taken after the tests were completed, as can be seen in Figure 37 below. Throughout the process of indentation of the rock at the moderate rate, the rock particle indented fully and

uniformly, with evidence of a slow, continuous flow of crushed ice beneath the contact zone. As discussed previously, the images taken after indentation, shown in Figure 37, outlines that primarily ductile failure was observed with some crushing events occurring as well, with the overall failure being ductile in nature.

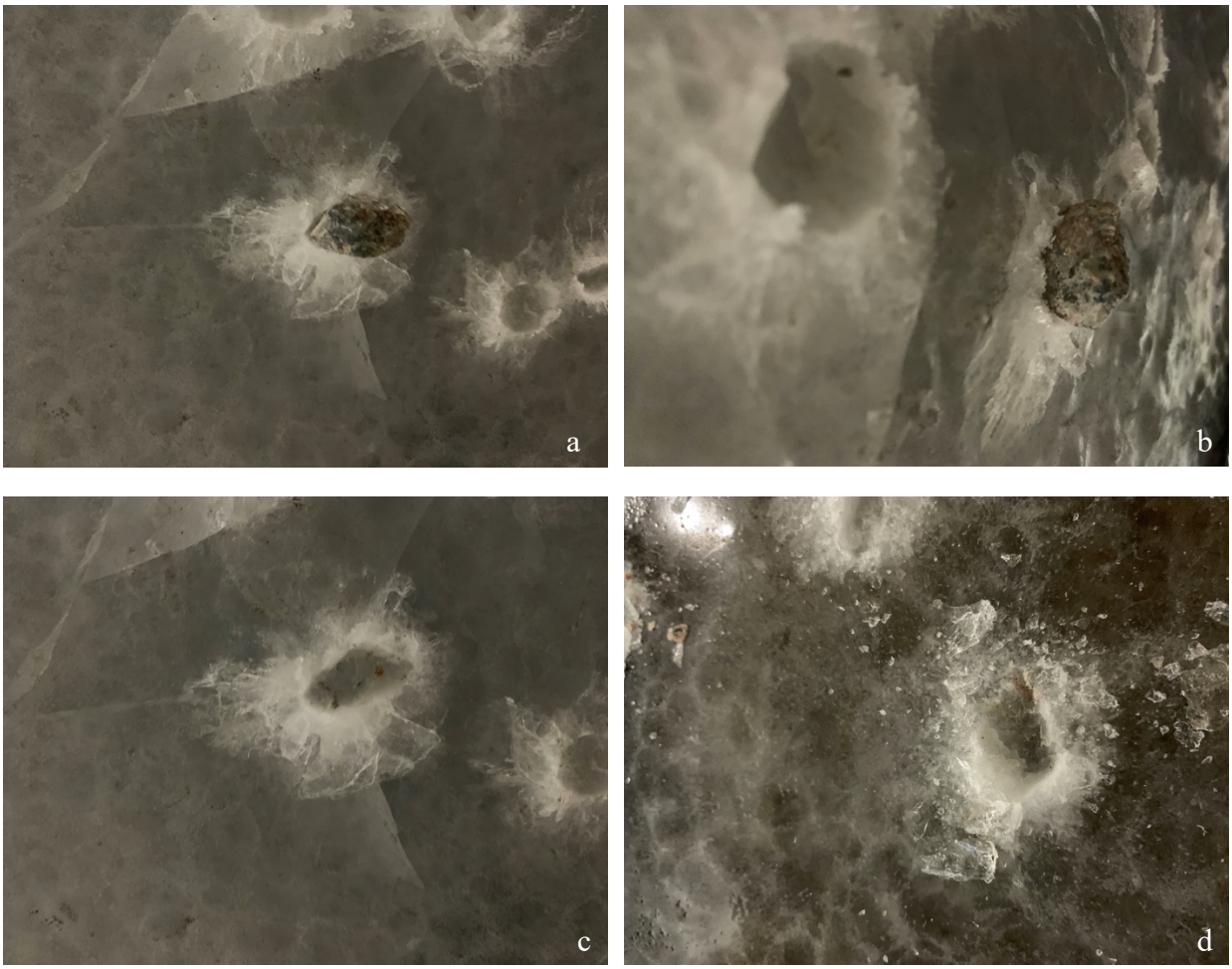

Figure 37 - Images taken after indentation of upper ice specimen (a)(b)(c) and lower ice specimen (d).

Photographs of the primary upper and lower ice specimens and rock particles can be seen above in Figure 37, depicting the crushed ice and indented rock particles immediately after the test was completed for experimental test runs completed at an indentation rate of 0.5 mm/s and a 5D spacing distances. These images taken after indentation in the case of the moderate speed test at a 5D

spacing show primarily crushing in the lower ice specimen, with mild crushing and a small, confined indent on the upper primary ice specimen. There is also evidence of small cracks propagating away from the primary indentation area on the upper indentation surface. Again, an additional point of particular interest is the rock which had embedded itself into the ice and stuck in place, which suggests localized pressure melting and refreezing during the indentation and holding process.

4.2.6 2D Spacing Case (26 mm)

Finally, results obtained from tests completed at a 2D (26 mm) spacing distance presented behaviour which was again consistent with typical tests completed for the given conditions at the representative indentation rate of 0.5 mm/s, where ductile failure was observed throughout the indentation period. Despite a 60 second hold time being imposed throughout experimental runs; the initial indentation period was analyzed primarily for these tests in order to more accurately study the behaviour of compressive ice failure. Force-depth data collected from the MTS load cell and pressure-depth data are presented in Figure 38 and Figure 39. The maximum force for this ice sample was recorded as 6492 N and maximum pressure was 6.17 MPa up to the indentation depth of 7 mm. The test referenced for the results in this section is denoted as Test 2021_29_06_(4)-26-0.5.

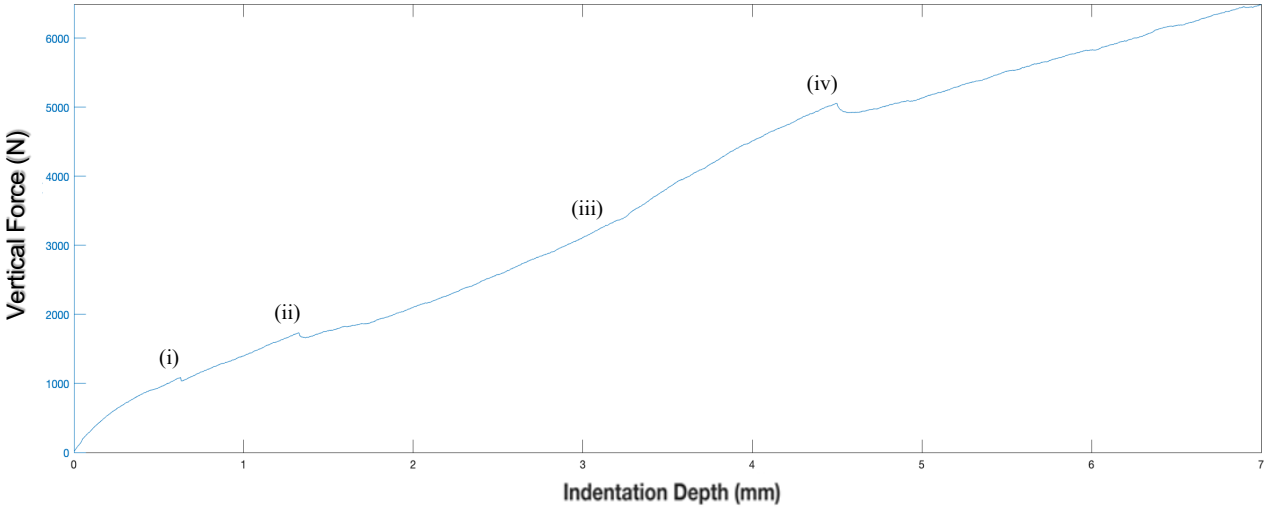

Figure 38 - Single particle force-indentation MTS load data completed at a rate of 0.5 mm//s to a depth of 7 mm for a 2D spacing case.

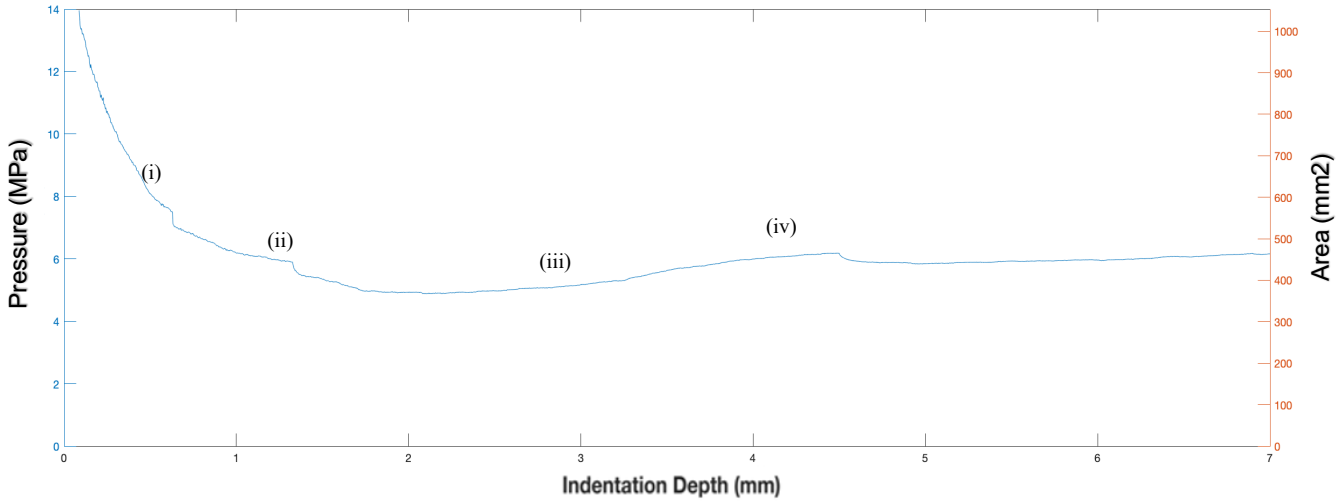

Figure 39 - Single particle pressure-indentation data completed at a rate of 0.5 mm//s to a depth of 7 mm for a 2D spacing case.

For the 2D (26 mm) spacing case at a moderate rate of 0.5 mm/s it can be observed that the load continuously increases, and the sample experiences slow crushing failure while increasing until the end of indentation; this is representative of a 'ductile' failure mode, corresponding to a slow, continuous flow of crushed ice beneath the contact zone. Specifically, as can be seen in Figure 38 and Figure 39, the behaviour noted in event (i) shows a rapid initial increasing trend of both load and pressure as indentation depth and effective area increase. As the indentation progresses, it is

noted in event (ii) damage enhanced creep and slow crushing failure is beginning to occur with a small load drop event occurring as can be seen in the force-depth plot while the pressure follows the same trend as can be observed on the pressure-depth plots. Smaller moderate load drops and decreases in pressure can be observed at events (iii), (iv) before continuing to increase steadily until the end of indentation. The data observed in the pressure-depth plot additionally corresponds to these observations from the force-indentation plots for the same denoted events. The load cell data and calculated pressure-depth data were in generally good agreement and compared well with the images taken after the tests were completed, as can be seen in Figure 40 below. Throughout the process of indentation of the rock at the moderate rate, the rock particle indented fully and uniformly, with evidence of a slow, continuous flow of crushed ice beneath the contact zone. As discussed previously, the images taken after indentation, shown in Figure 40, outlines that primarily ductile failure was observed with some crushing events occurring as well, with the overall failure being ductile in nature.

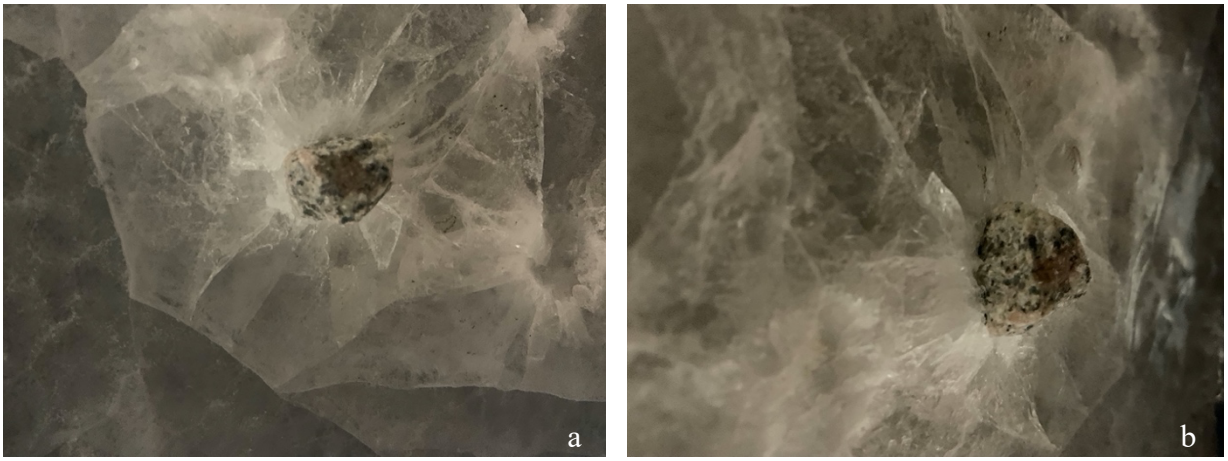

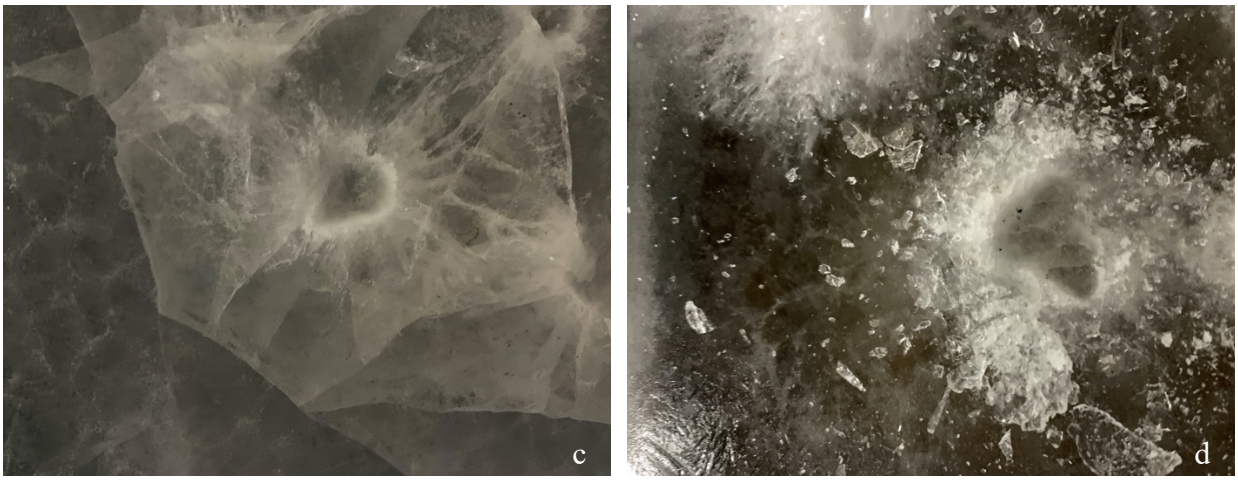

Figure 40 - Images taken after indentation of upper ice specimen (a)(b)(c) and lower ice specimen (d).

Photographs of the primary upper and lower ice specimens and rock particles can be seen above in Figure 40, depicting the crushed ice and indented rock particles immediately after the test was completed for experimental test runs completed at an indentation rate of 0.5 mm/s and a 2D spacing distances. These images taken after indentation in the case of the moderate speed test at a 2D spacing show primarily crushing in the lower ice specimen, with mild crushing and a small, confined indent on the upper primary ice specimen. There is also evidence of small cracks propagating away from the primary indentation area on the upper indentation surface. Again, a rock has embedded itself into the ice and stuck in place, which suggests the trend of localized pressure melting and refreezing during the indentation and holding process.

4.3 Results for Multiple Particle Embedment

Fifty-five (55) successful tests were completed for multiple particle embedment, including repetitions on non-pristine ice. Of these tests, twenty-five (25) were completed on pristine ice samples. Test were completed on a group of rock particles which were weighed out to a consistent weight of 170 grams, independent of the number of particles present in the samples to account for variability within the population. Initially, only vertical indentation was imposed on the rock samples, with horizontal motion being introduced later in tandem to an initial vertical indentation phase. Parameters varied included indentation depth and horizontal motion displacement. Of these 25 tests completed on pristine ice, three test were completed with a 1-minute hold time up to a 5 mm vertical indentation with no horizontal motion, four tests were completed with a 1-minute hold time to a 7 mm vertical indentation with no horizontal motion. Two tests were completed with a 30-minute hold time up to a 7 mm vertical indentation with no horizontal motion. Additionally, four tests were completed with a 1-minute hold time up to a 5 mm vertical indentation and 5 mm of horizontal motion, four were completed with a 1-minute hold times up to a 5 mm vertical indentation with 7 mm of horizontal motion. Finally, four tests were completed with a 1-minute hold time up to a 7 mm vertical indentation with 5 mm of horizontal motion, and four tests were completed with a 1-minute hold time up to a 7 mm vertical indentation with 7 mm of horizontal motion. All tests were completed with medium sized rocks ~ 3/4 - 3/8-inch samples, at setpoint temperatures of -10°C.

4.3.1 - 5 mm Indentation Depth

Results obtained from tests completed on a 170-gram sample of medium sized rocks up to an indentation depth of 5 mm primarily presented behaviour which was consistent with typical tests completed for the given conditions at the indentation rate of 0.5 mm/s, where ductile failure was observed throughout the indentation period. Despite a 60 second hold time being imposed throughout experimental runs; the initial indentation period was analyzed primarily for these tests in order to more accurately study the behaviour of compressive ice failure. Force-depth data collected from the MTS load cell is presented in Figure 41. The maximum force for this ice sample was recorded as 22157 N. Maximum pressure was determined based on a mean particle diameter of 13 mm and an indentation depth of 5 mm into the ice, where the total contact area for 55 particles may be estimated to be ~ 6.00 x 10^{-3} m^2; therefore, the maximum pressure was determined to be 3.66 MPa up to the indentation depth of 5 mm. The test referenced for the results in this section is denoted as Test 2020_13_11 (4)-5-0-1.

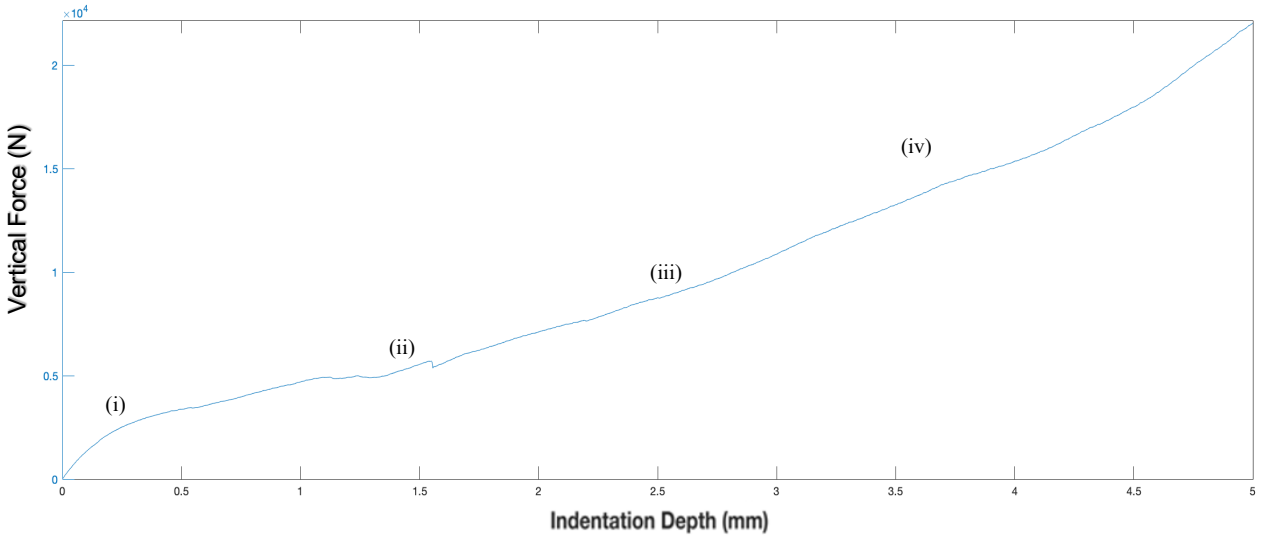

Figure 41 - Multiple particle force-indentation MTS load data completed at a rate of 0.5 mm//s to a depth of 5 mm.

For the 5 mm multi-particle indentation test at a moderate rate of 0.5 mm/s it can be observed that, similarly to the trends observed in the single particle tests, the load continuously increases, and the sample experiences slow crushing failure while increasing until the end of indentation; representative of a 'ductile' failure mode, corresponding to a slow, continuous flow of crushed ice beneath the contact zone. Specifically, as can be seen in Figure 41, the behaviour noted in event (i) shows a moderate initial increasing trend of applied load as indentation depth increases. As the indentation progresses, it is noted in event (ii) damage enhanced creep and slow crushing failure is beginning to occur with a small spall and drop in load occurring as can be seen in the force-depth plot. This trend continues as the force begins to increase more rapidly (iii), (iv) before continuing to increase steadily until the end of indentation. The load cell data compared well with the images taken after the tests were completed, as can be seen in Figure 42 below. Throughout the process of indentation of the rock at the moderate rate to the indentation depth of 5 mm, the rock particle indented fully and uniformly, with evidence of a slow, continuous flow of crushed ice beneath the contact zone. As discussed previously, the images taken after indentation, shown in Figure 42, outlines that primarily ductile failure was observed with some crushing events occurring as well, with the overall failure being ductile in nature.

Figure 42 - Image taken after indentation of upper ice specimen, 5mm indentation.

4.3.2 - 7 mm Indentation Depth

Results obtained from tests completed on a 170-gram sample of medium sized rocks up to an indentation depth of 7 mm primarily presented behaviour which was consistent with typical tests completed for the given conditions at the indentation rate of 0.5 mm/s, where ductile failure was observed throughout the indentation period. Despite a 60 second hold time being imposed throughout experimental runs; the initial indentation period was analyzed primarily for these tests in order to more accurately study the behaviour of compressive ice failure. Force-depth data collected from the MTS load cell is presented in Figure 43. The maximum force for this ice sample was recorded as 82008 N. Maximum pressure was determined based on a mean particle diameter of 13 mm and an indentation depth of 7 mm into the ice, where the total contact area for 55 particles may be estimated to be ~ 6.00 x 10^{-3} m^2; therefore, the Maximum pressure was determined to be 13.6 MPa up to the indentation depth of 7 mm. The test referenced for the results in this section is denoted as Test 2020_19_11_(1)- 7-0-1.

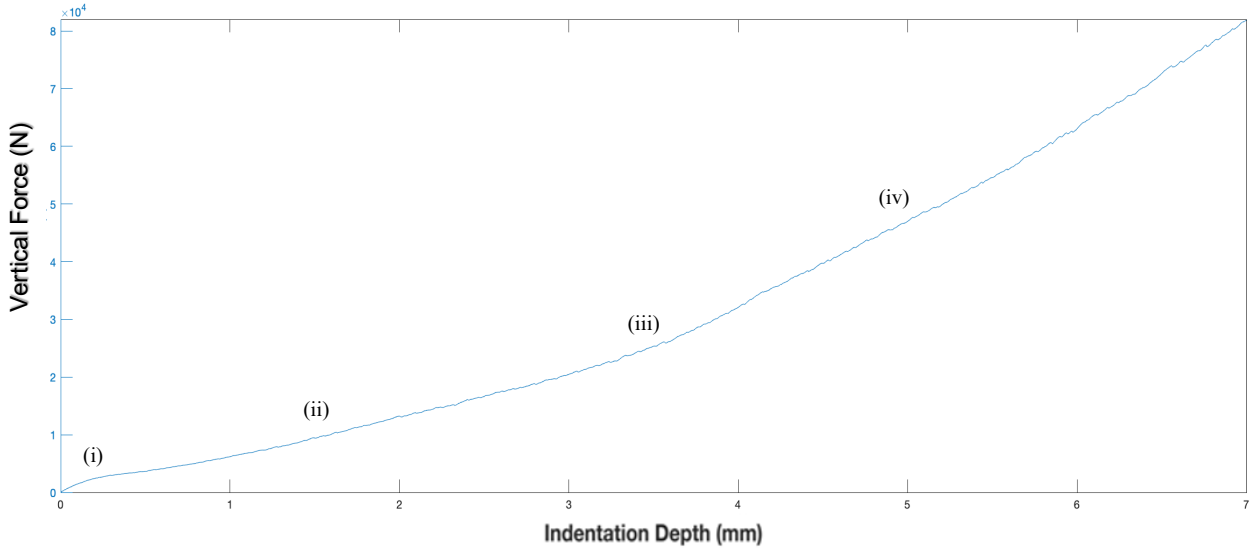

Figure 43- Multiple particle force-indentation MTS load data completed at a rate of 0.5 mm//s to a depth of 7 mm.

For the 7 mm multi-particle indentation test at a moderate rate of 0.5 mm/s it can be observed that, similarly to the trends observed in the single particle tests, the load continuously increases, and the sample experiences slow crushing failure while increasing until the end of indentation; representative of a 'ductile' failure mode, corresponding to a slow, continuous flow of crushed ice beneath the contact zone. Specifically, as can be seen in Figure 43, the behaviour noted in event (i) shows a moderate initial increasing trend of applied load as indentation depth increases. As the indentation progresses, it is noted in event (ii) damage enhanced creep and slow crushing failure is beginning to occur with small fluctuations in load occurring as can be seen in the force-depth plot. This trend continues as the force begins to increase more rapidly (iii), (iv) before continuing to increase steadily until the end of indentation. The load cell data compared well with the images taken after the tests were completed, as can be seen in Figure 44 below. Throughout the process of indentation of the rock at the moderate rate to the indentation depth of 7 mm, the rock particle indented fully and uniformly, with evidence of a slow, continuous flow of crushed ice beneath the contact zone. As discussed previously, the images taken after indentation, shown in Figure 44, outlines that primarily ductile failure was observed with some crushing events occurring as well, with the overall failure being ductile in nature.

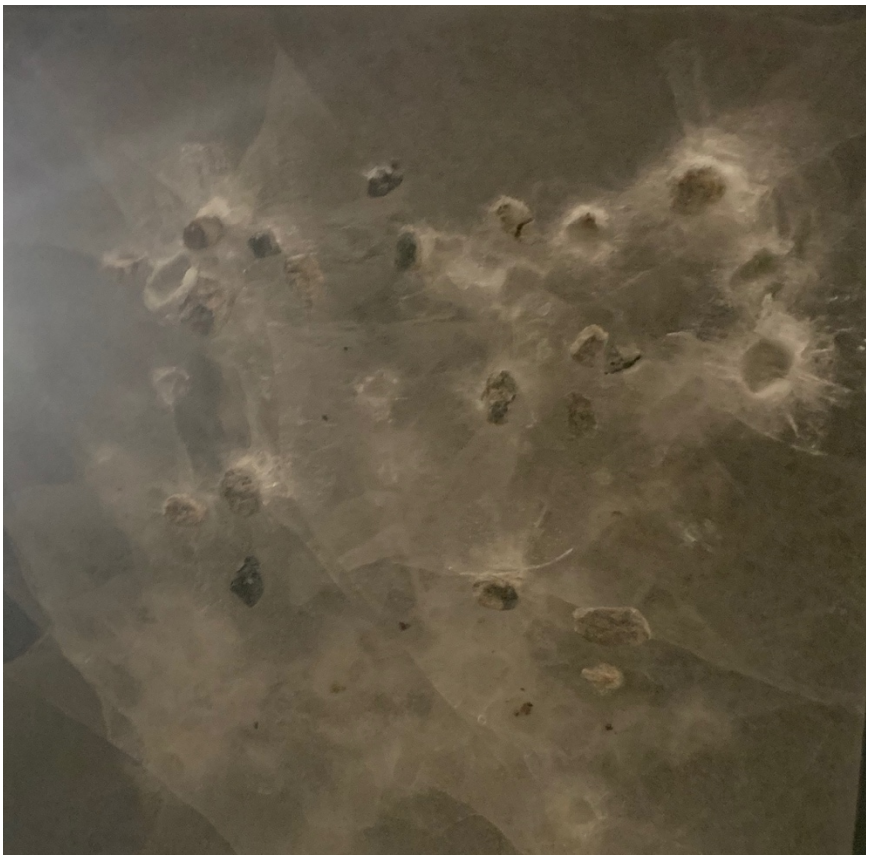

Figure 44 – Image taken after indentation of upper ice specimen, 7mm indentation.

An image depicting of the primary upper ice specimen and rock particles can be seen above in Figure 44, depicting the crushed ice and indented rock particles immediately after the test was completed for experimental test runs completed at an indentation rate of 0.5 mm/s and a 7 mm indentation depth. These images taken after indentation in the case of the moderate speed test at a 7 mm indentation depth show primarily mild crushing and small, confined indents on the upper primary ice specimen. There is also evidence of cracks propagating away from the primary indentation area on the upper indentation surface. Additionally, multiple rocks have embedded into the ice and stuck in place, which suggests the trend of localized pressure melting and refreezing during the indentation and holding process.

4.4 Summary of Results

Eight selected representative test events were discussed in this chapter. Six corresponded to single particle tests conducted at a set distance away from a previously formed damage zone, and two were completed on samples of multiple rock particles subjected to vertical indentation.

From the load cell data cyclic loading patterns were observed to be directly dependent on the indentation rate. Ductile failure was observed to dominate for moderate loading rates of 0.5 mm/s, while a combination of both ductile and brittle failure was observed throughout tests completed with a fast-loading rate of 10 mm/s. For slow rate tests of 0.01 mm/s a combination of brittle and ductile failure was also observed. For test completed at slow rates, it was observed that less dynamics loading patterns were observed. Conversely highly dynamic loads were observed for the tests completed at fast loading rates. Results completed at a constant loading rates of 0.01 mm/s, 0.5 mm/s, and 10 mm/s across different relative spacings of 2D, 5D, and 7D produced load cell data, which agreed with previously reported trends, independent of the spacing distance.

Multi-particle tests at a constant loading rate of 0.5 mm/s produced load cell data which were in agreement with the single-particle tests. Primarily ductile failure was observed for all indentation depths of 7 mm and 5 mm, with larger overall forces and pressures observed for tests completed with an indentation depth of 7 mm, compared to those completed to a depth of 5 mm.

Finally, it was observed from photographs taken after completion of testing that studying the images and comparing them to the recorded force and pressure data allowed for good correlation between loading events and different modes of failure at specific points in the testing process.

5.0 Analysis

5.1 Overview

In this chapter results and data collected from both single particle and multi-particle small-scale indentation tests are presented, discussed, and compared. For the purposes of these analyses, the test results have been grouped to allow for the appropriate comparisons of tests having the same factors, except for the parameter of interest. The influence of factors such as indentation rate, spacing from previously formed damage zones, indentation depth, and number of particles were considered.

To provide a further assessment of the influence of these factors, a qualitative evaluation of the ice failure mechanisms, and a deeper analysis of images taken after test completion are also presented in this chapter.

5.2 General Test Results

Based on the completed tests and results presented above, all experimental runs have been examined individually in order to effectively investigate the different behaviours of the ice failures and the interaction effects of rocks compressed between two ice specimens. One of the primary focuses of this thesis document is to investigate the interaction effects of rock particles, with consideration of the relative distance from previously formed damage zones. Special attention was paid to analysis of maximum force and pressure data against relative spacing distances, indentation rate, and indentation depth. Images taken after indentation were compared with the load cell data to assess the different types of ice failures and associated load drops. In the following section a detailed description of the observed failure processes associated with crushing and spalling for

representative sample events is provided, along with a detailed comparison between the effects of particle spacing, number or particles, and indentation rates.

5.3 Effects of Indentation Rate on Single Particles

Testing was completed at three different indentation rates, as programmed in the MTS controls, to investigate the effects of rate on particle indentation. These rates were chosen as 0.01 mm/s (slow), 0.5 mm/s (moderate) and 10 mm/s (fast). Plots representing three separate tests completed at these three indentation rates for 5D spacing can be seen below in Figure 45. For this spacing at an indentation rate of 0.01 mm/s, the curve can be seen to exhibit evidence of combined ductile and brittle failure, which gives way to two repeated crushing events as the indentation depth increased. Irregularities in the ice-particle contact geometry arising from asperities on the natural rock particles is a likely contributor which triggers localized spalling under conditions where more damage-enhanced creep behaviour would typically be expected from smooth indenter tests, as described by Wells et al. (2011). For the moderate rate of 0.5 mm/s it can be observed that the load continuously increases, with one localized spall near the beginning of indentation as the sample experiences slow crushing failure; this corresponds with a failure mode which is typically referred to as a ‘ductile’ failure, and corresponds to a slow, continuous flow of crushed ice beneath the contact zone. For the 10 mm/s test, the load builds steadily and undergoes typical phases of dynamic loading, with larger spalls and associated load drops being observed near the end of indentation.

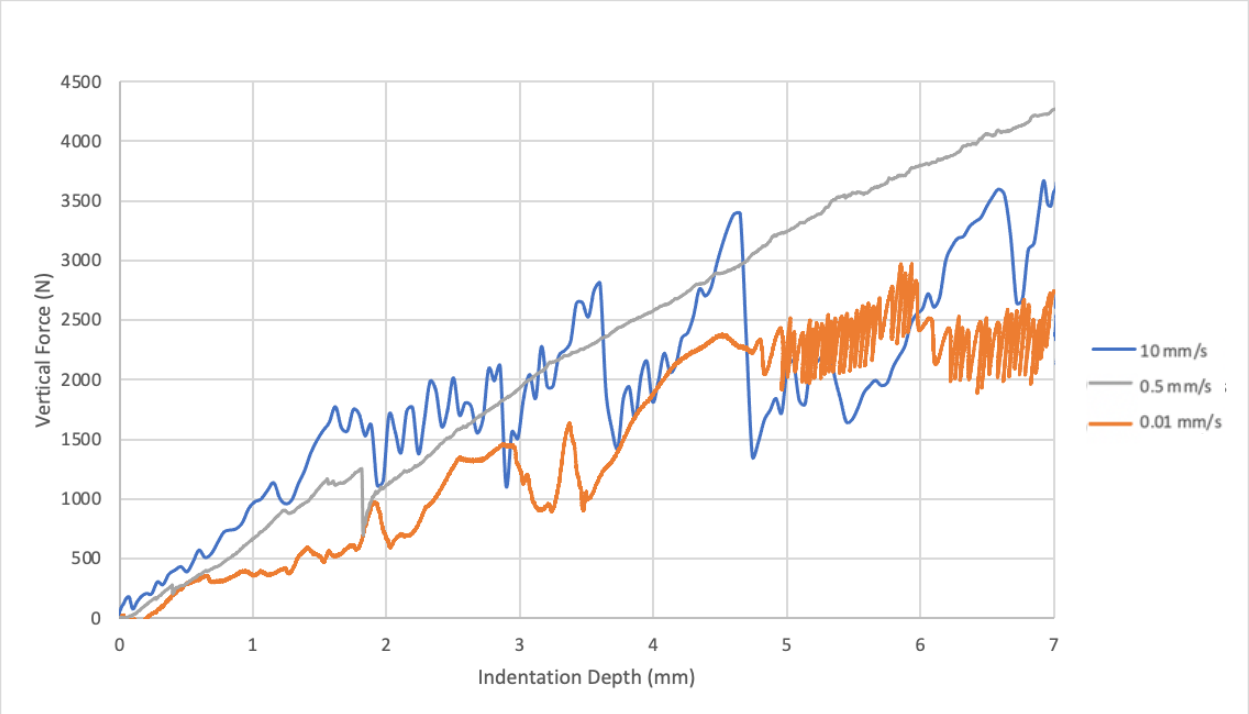

Figure 45 – MTS load cell data for 3 tests: Slow speed (Orange); Moderate speed (Grey); Fast speed (Blue) completed at 5D (65 mm) spacings.

To examine trends in these results, the maximum observed forces were compiled for all separate tests completed at 0.01 mm/s, 0.5 mm/s, and 10 mm/s for all three spacing cases of 7D, 5D, and 2D. The forces were taken directly from the force trace data obtained from the MTS. Plots representing an aggregate of tests completed at 0.01 mm/s, 0.5 mm/s, and 10 mm/s for all three spacing cases of 7D, 5D, and 2D can be seen in Figure 46, Figure 47, and Figure 48 below. For the first set of tests at the 2D case, in Figure 46, the maximum forces were recorded as being the lowest for slow speed tests at 0.01 mm/s, while increasing to the largest values which are observed at moderate rates of 0.5 mm/s. For the fast speed tests at 10 mm/s the forces observed trended down. Similar trends in the behaviour were observed for the sets of tests completed at the 5D and 7D spacing cases as shown in Figure 47 and Figure 48, respectively. Observed peak forces were smallest at slow rates of 0.01 mm/s, moderately higher but remaining lower overall at fast rates of 10 mm/s, and highest for the moderate rate case of 0.5 mm/s. This behaviour is consistent with

reported ice strain rate behavior from Wells et al. (2011) wherein slow rates result in ductile failure for which peak forces increase as rate increases, which then transition to mixed mode failure characterized by higher peak loads, and ultimately brittle failure at higher rates that exhibit lower peak forces.

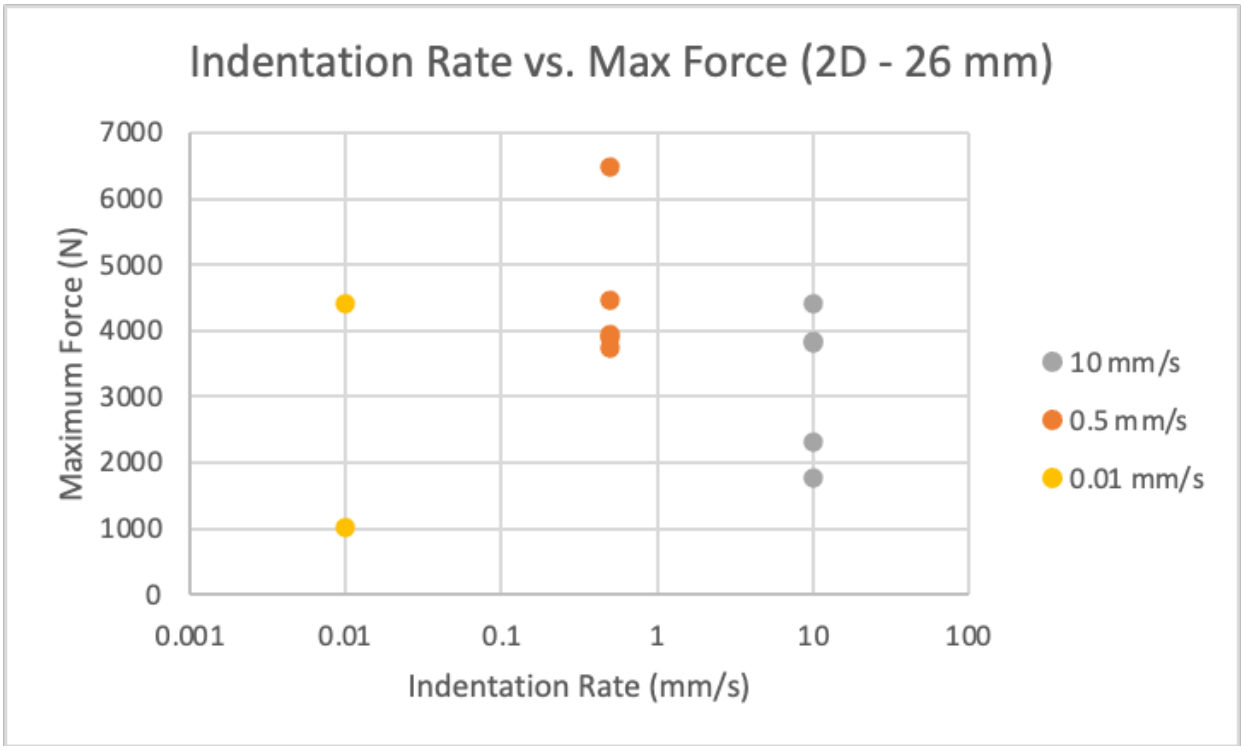

Figure 46 – Aggregate maximum observed MTS load data from tests done at a spacing of 2D (26 mm) for slow (Yellow), moderate (Orange), and fast (Grey) tests.

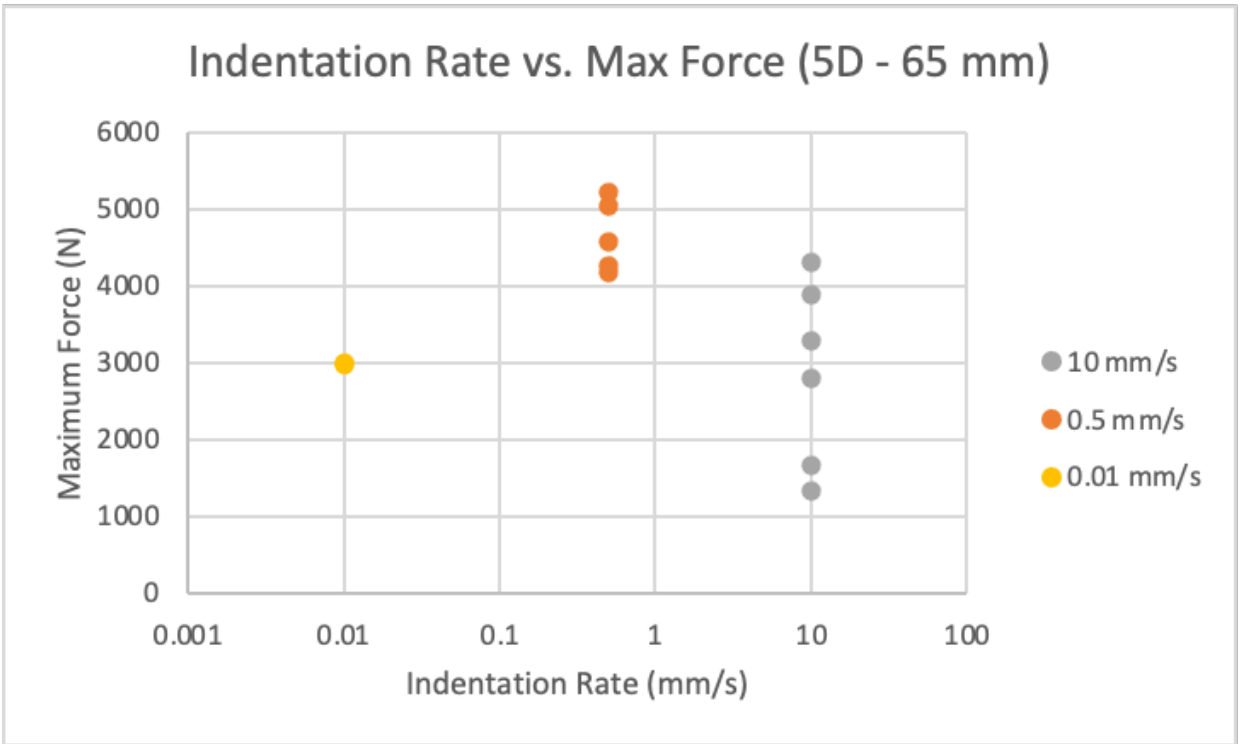

Figure 47 - Aggregate maximum observed MTS load data from tests done at a spacing of 5D (65 mm) for slow (Yellow), moderate (Orange), and fast (Grey) tests.

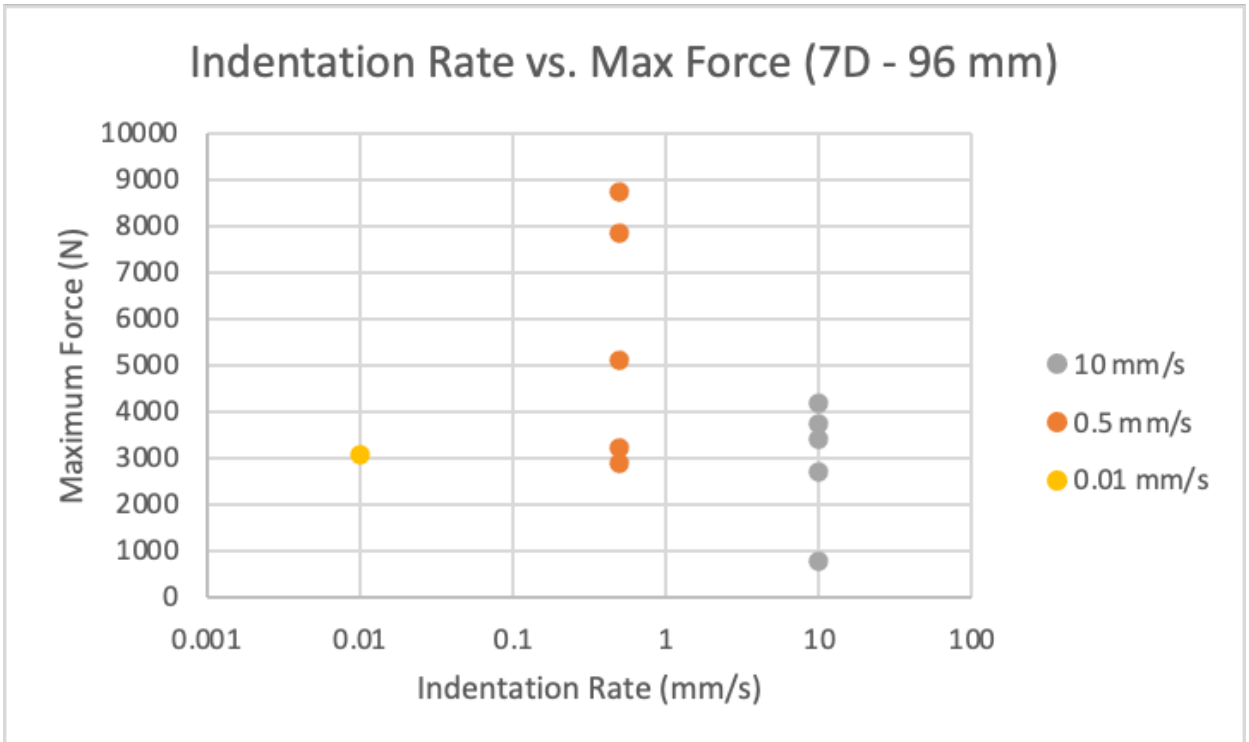

Figure 48 - Aggregate maximum observed MTS load data from tests done at a spacing of 7D (96 mm) for slow (Yellow), moderate (Orange), and fast (Grey) tests.

Similarly, the maximum observed pressures were compiled for tests completed at 0.01 mm/s, 0.5 mm/s, and 10 mm/s for all three spacing cases of 7D, 5D, and 2D. The pressures were calculated based on the nominal projected area of the rock particle assuming maximum indentation, which can be seen by the shaded area in Figure 49 below.

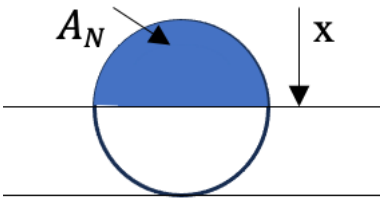

Figure 49 – Schematic showing the nominal projected area of a rock during indentation to a given depth x.

Plots representing an aggregate of all tests completed at 0.01 mm/s, 0.5 mm/s, and 10 mm/s for all three spacing cases are shown in Figure 50, Figure 51, and Figure 52 respectively. For the 2D case seen in Figure 50, the maximum pressures were lower for slow speed tests and increased for moderate rates tests of 0.5 mm/s. For the 10 mm/s tests, there was significant spread in the pressure data due to differences in ice-particle contact areas, but the mean trends are in general agreement with those observed for the force data.

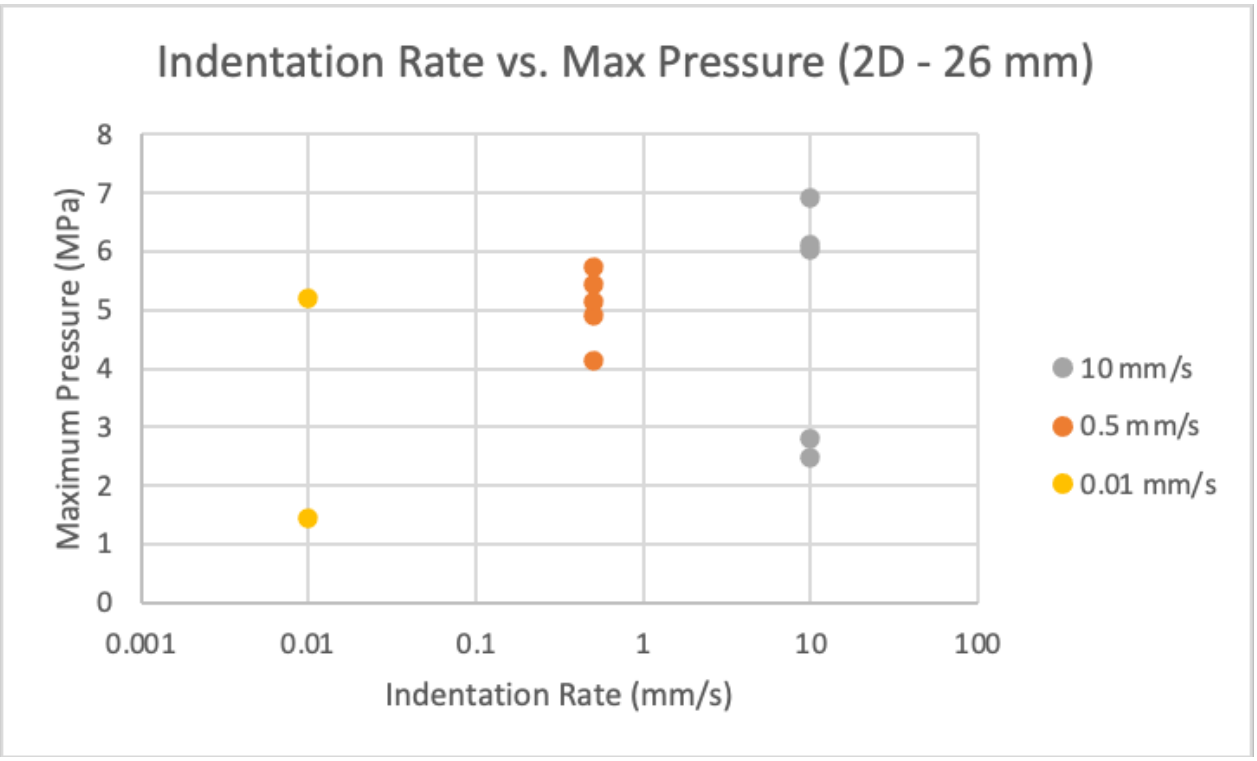

Figure 50 - Aggregate maximum observed pressure data from tests done at a spacing of 2D (26 mm) for slow (Yellow), moderate (Orange), and fast (Grey) tests.

For the 5D and 7D spacing tests, seen in Figure 51 and Figure 52 respectively, the observed pressures were smallest at slow rates of 0.01 mm/s, moderately higher at fast rates of 10 mm/s, with the maximum pressures occurring for moderate rates of 0.5 mm/s. This behaviour is consistent with the trends observed for the force trace data.

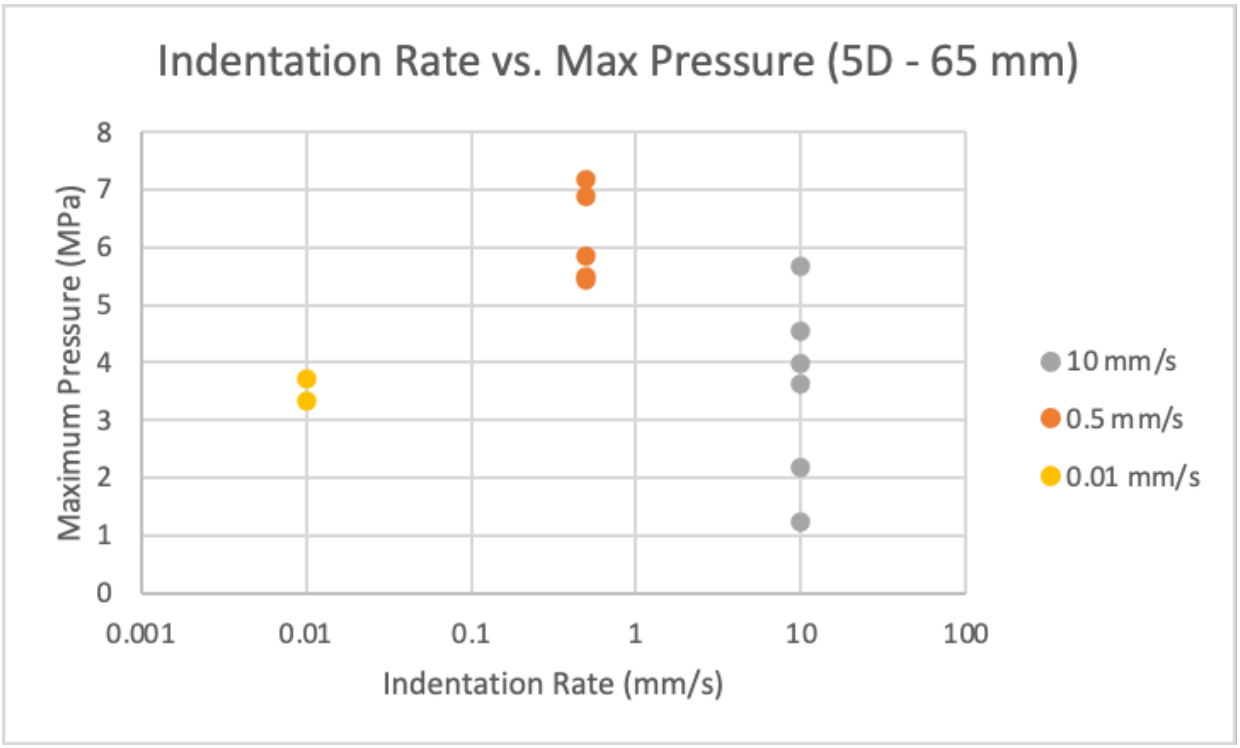

Figure 51 - Aggregate maximum observed pressure data from tests done at a spacing of 5D (65 mm) for slow (Yellow), moderate (Orange), and fast (Grey) tests.

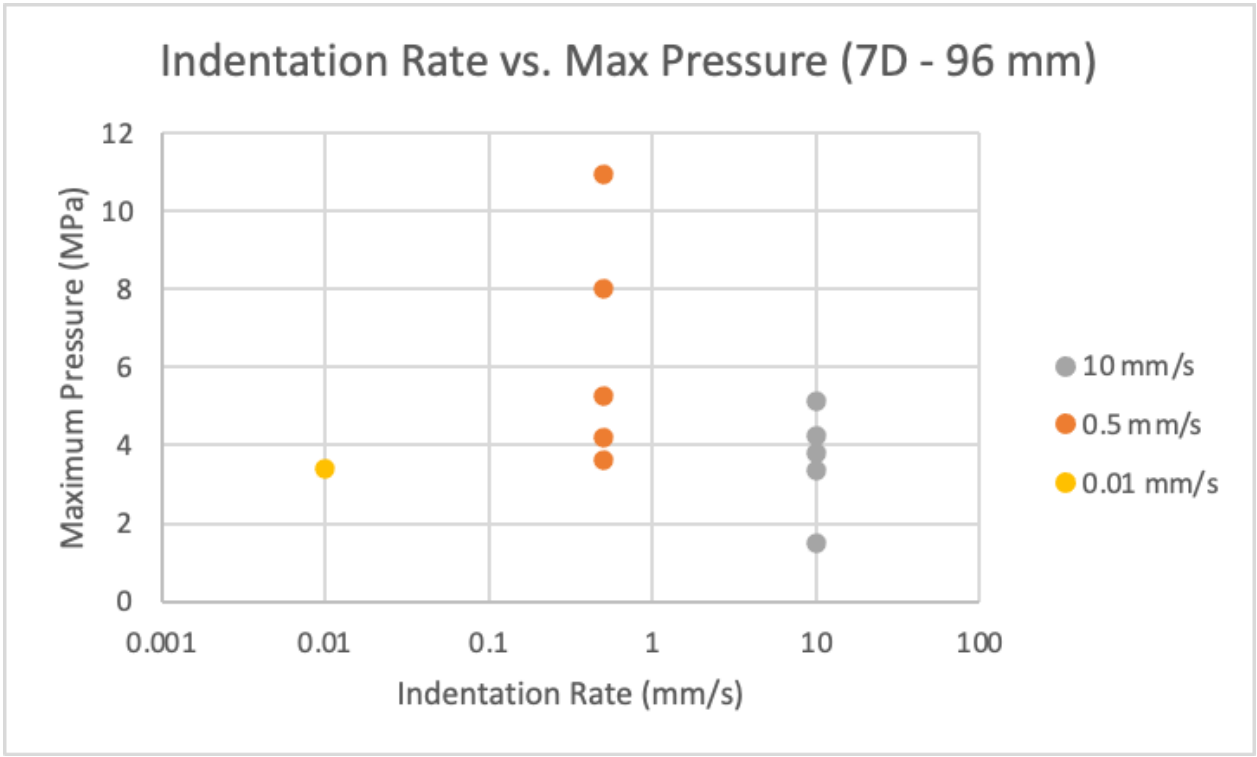

Figure 52 - Aggregate maximum observed pressure data from tests done at a spacing of 7D (96 mm) for slow (Yellow), moderate (Orange), and fast (Grey) tests.

Photographs of the ice specimens and rock particles can be seen depicting the undamaged ice with a rock particle placed before indentation (Figure 53) as well as the crushed ice and indented rock particles immediately after the tests were completed (Figure 54). The images taken before testing show the placement of the rock relative to the previously indented zones.

Figure 53 – Image taken before testing showing rock placement relative to prior test indentation locations.

In Figure 54 the images taken following the fast tests (a./b.) show evidence of crushing with extensive spalling, which is characteristic of brittle failure. Such failures exhibited small zones of localized damage with much of the local material removed by fractures resulting from cracks propagating from beneath the ice-particle interface. For moderate speeds, images taken after the test (Figure 54 c./d.) there is more evidence of slow crushing and damage enhanced creep on both surfaces, with a few cracks propagating away from the center of the damage zone on the upper ice specimen, but clear evidence the shape of the rock embedded into the ice as the crushed ice extruded and solidified around the particle. The images shown in Figure 54 (e./f.) were taken following a slow speed indentation test. These specimens exhibit some crushing on the bottom ice specimen, with crushing and embedment of the ice particle in a localized indent on the upper ice specimen. These observations of differences between indentation patterns in top and bottom ice specimens for different indentation rates highlight the importance of the rock particle geometry in influencing the nature of the embedment process.

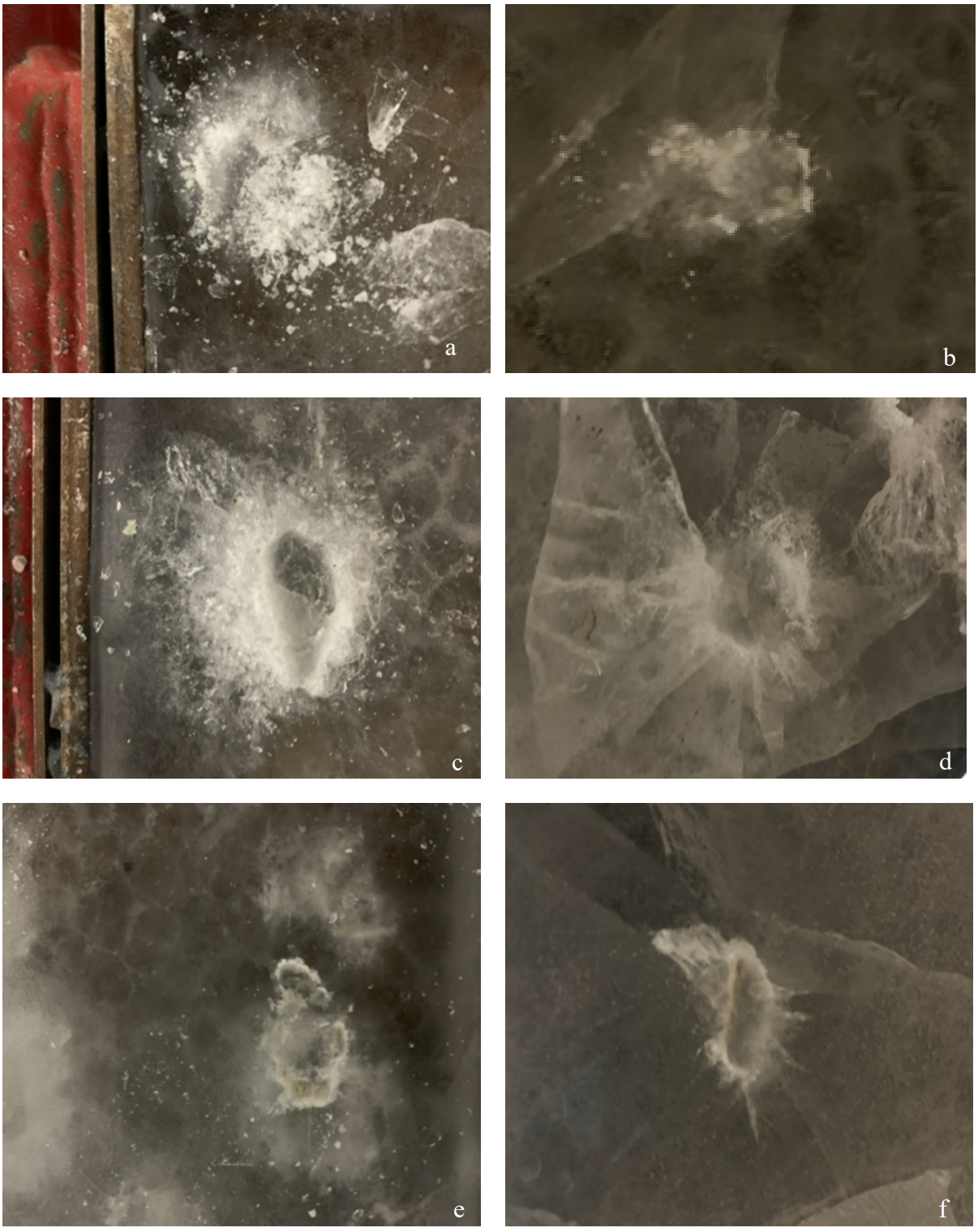

Figure 54 - Images of bottom (left) and top (right) ice surfaces taken after testing for fast (a./b.), moderate (c./d.), and slow (e./f.) speed cases.

5.4 Effects of Particle Spacing on Single Particles

To effectively investigate the effects of the relative spacing of a rock particle from a previous damage zone on indentation, testing was completed at three different spacing setpoints based on a mean rock diameter of 13 mm. These relative spacings were chosen as 2D (26 mm), 5D (65 mm) and 7D (96mm). Plots representing three separate tests completed at 7D, 5D, and 2D for an indentation rate of 0.5 mm/s can be seen below in Figure 55.

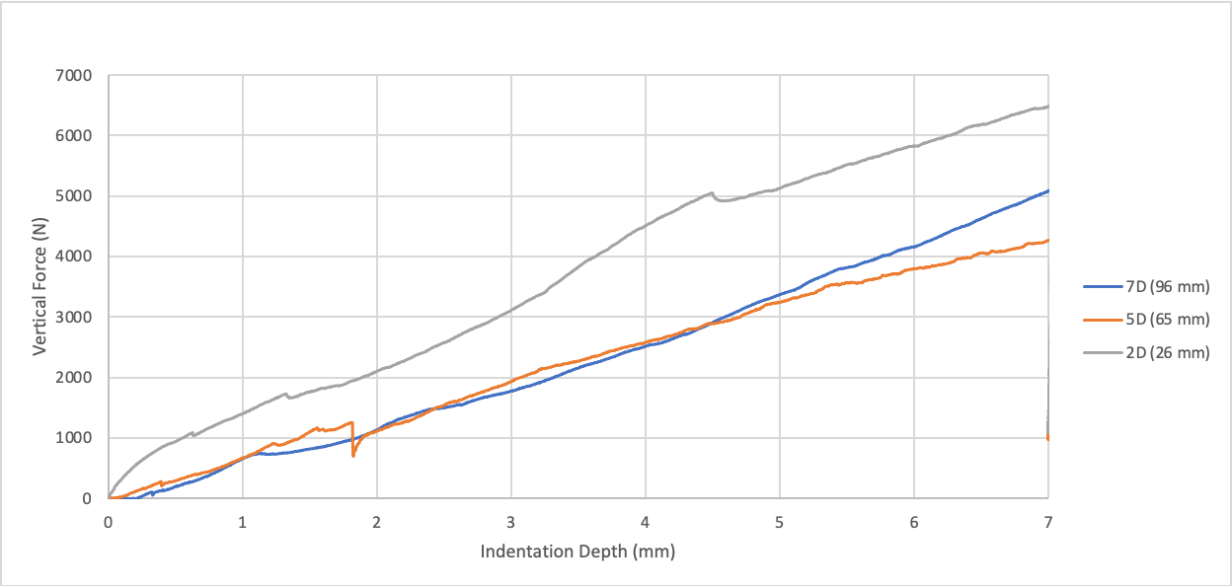

Figure 55 - MTS load cell data for 3 tests: 7D spacing (Blue); 5D spacing (Orange); 2D spacing (Grey) completed at a rate of 0.5 mm/s.

For a rate of 0.5 mm/s the force time traces follow typical ductile failure curves for all spacings. For spacings of both 7D and 5D, similar curve and peak forces can be seen, with a small spalling event occurring near the beginning of indentation for the 5D test. Finally, for the 2D, or 26 mm, spacing case it can be seen from the curve that ductile failure is again consistent, with this indentation test a slightly higher overall level of force.

Similarly, maximum forces were compiled for tests completed at 7D, 5D, and 2D and plotted for all indentation cases in Figure 56 (10 mm/s), Figure 57 (0.5 mm/s) and Figure 58 (0.01 mm/s). For the 10 mm/s case shown in Figure 56, it may be observed that the lowest maximum forces correspond to the 7D spacing, with the forces measured for 5D and 2D spacing generally being higher in magnitude, although this is not a strong trend.

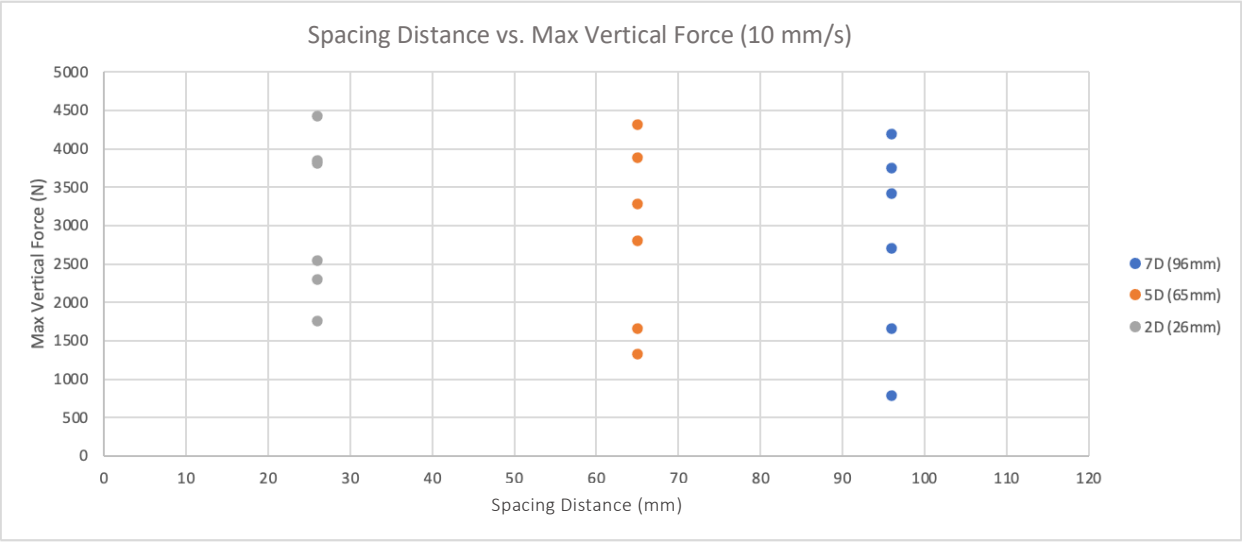

Figure 56 - Aggregate maximum MTS load data from tests done at a rate of 10 mm/s for 7D (Blue), 5D (Orange), and 2D (Grey) spacings.

For the 0.5 mm/s case shown in Figure 57, the force distributions are similar, but with the forces observed for the 5D spacing case more tightly distributed in the middle of the force range. In this case, a slight upward trend is observed, but this is not a strong trend given the significant scatter in the data.

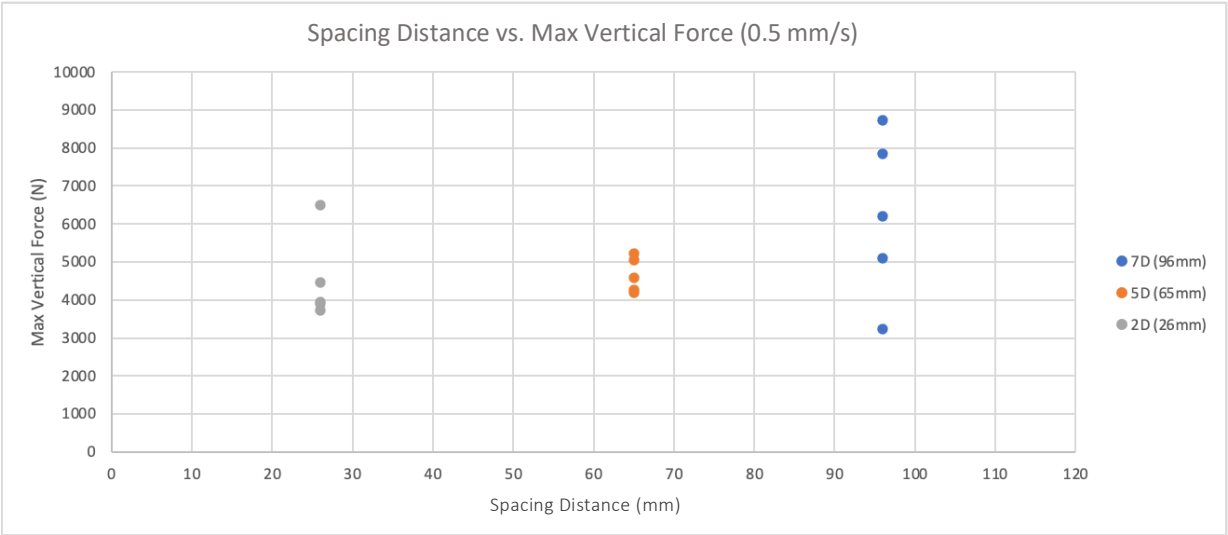

Figure 57 - Aggregate maximum MTS load data from tests done at a rate of 0.5 mm/s for 7D (blue), 5D (Orange), and 2D (Grey) spacings.

For the 0.01 mm/s case shown in Figure 58, while there are too few data to draw meaningful conclusions, these limited data are consistent with the general observation of weak dependence of peak force on particle spacing for the 2D, 5D, and 7D cases considered. The collection of additional data for low indentation rates would be beneficial in enabling more statistically significant assessments and is recommended in the future.

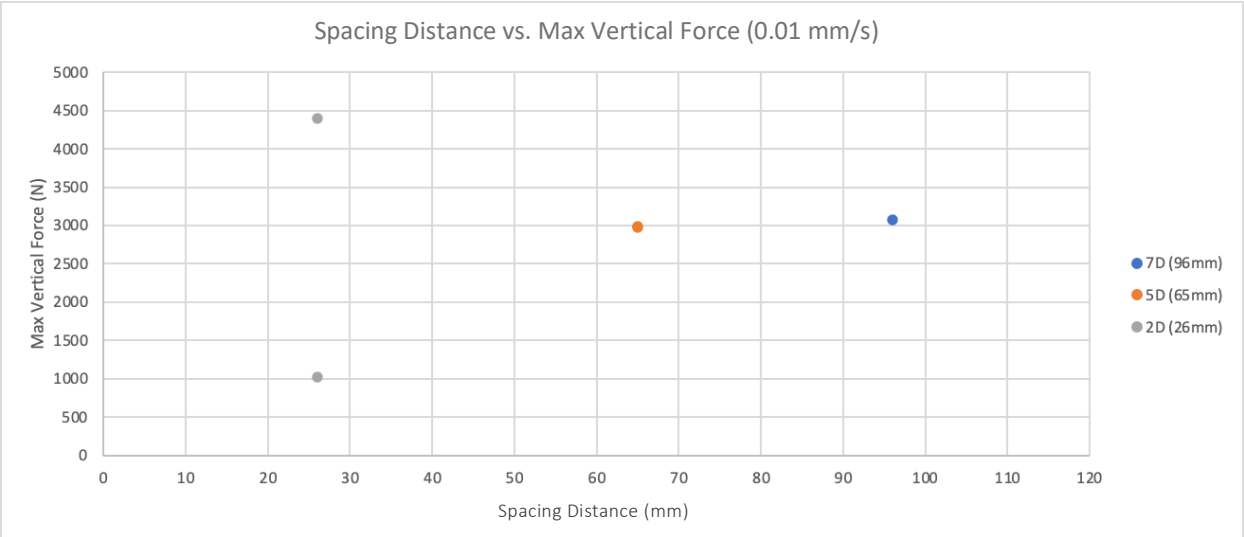

Figure 58 - Aggregate maximum MTS load data from tests done at a rate of 0.01 mm/s for 7D (blue), 5D (orange), and 2D (grey) spacings.

Similarly, maximum pressures were compiled for all tests completed at 7D, 5D, and 2D for the three indentation rates considered. These aggregate results are plotted in Figure 59 (10 mm/s), Figure 60 (0.5 mm/s), and Figure 61 (0.01 mm/s) below.

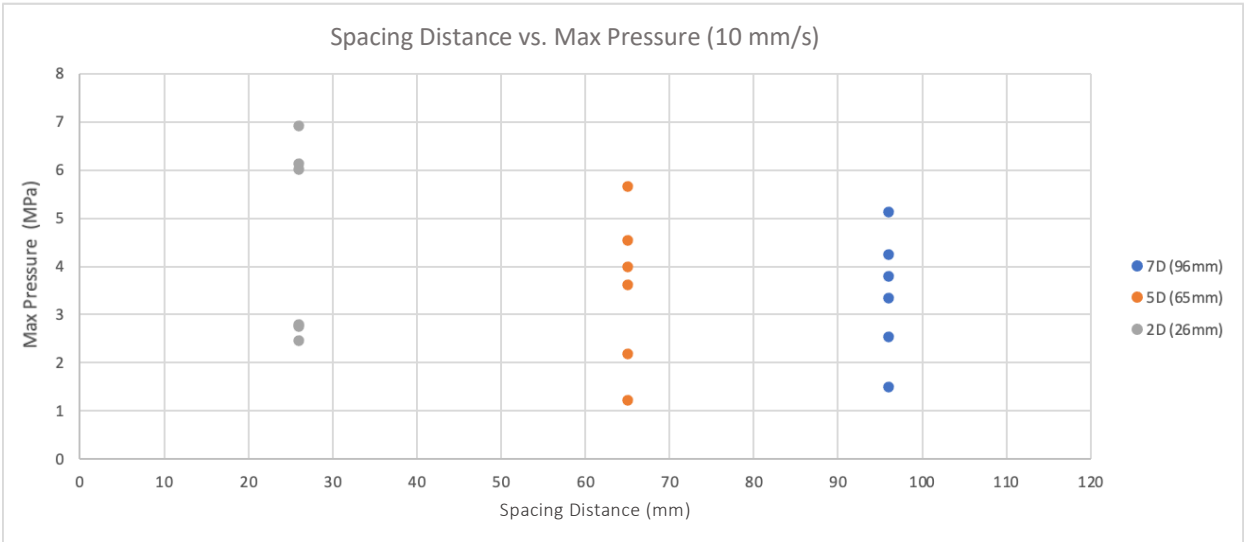

Figure 59 - Aggregate maximum pressure data from tests done at a rate of 10 mm/s for 7D (Blue), 5D (Orange), and 2D (Grey) spacing.

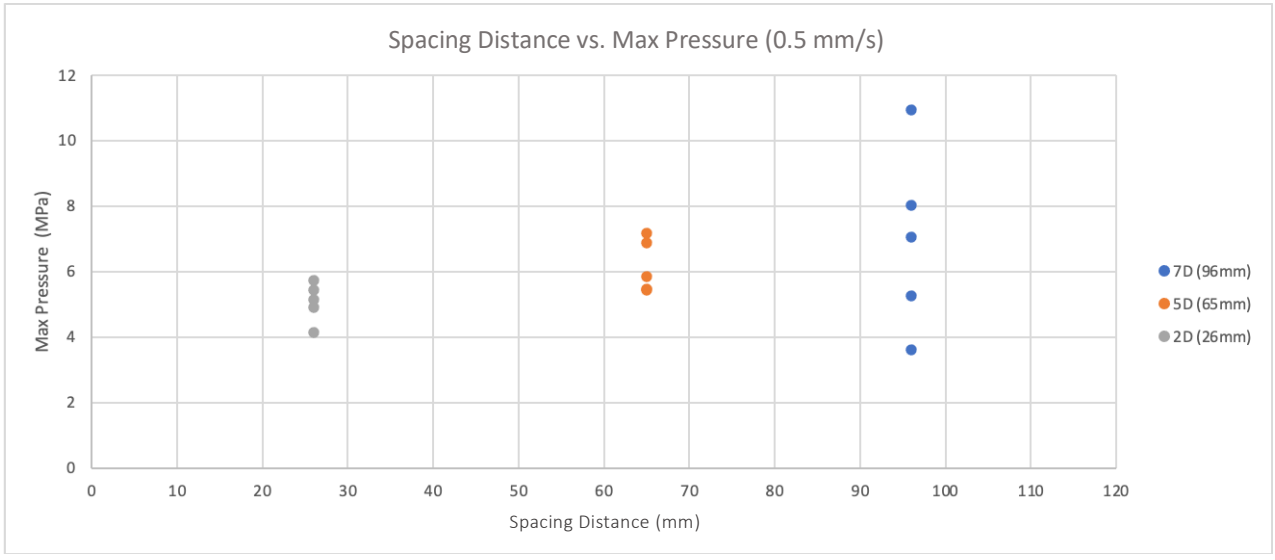

Figure 60 - Aggregate maximum pressure data from all tests done at a rate of 0.5 mm/s for 7D (Blue), 5D (Orange), and 2D (Grey) spacing.

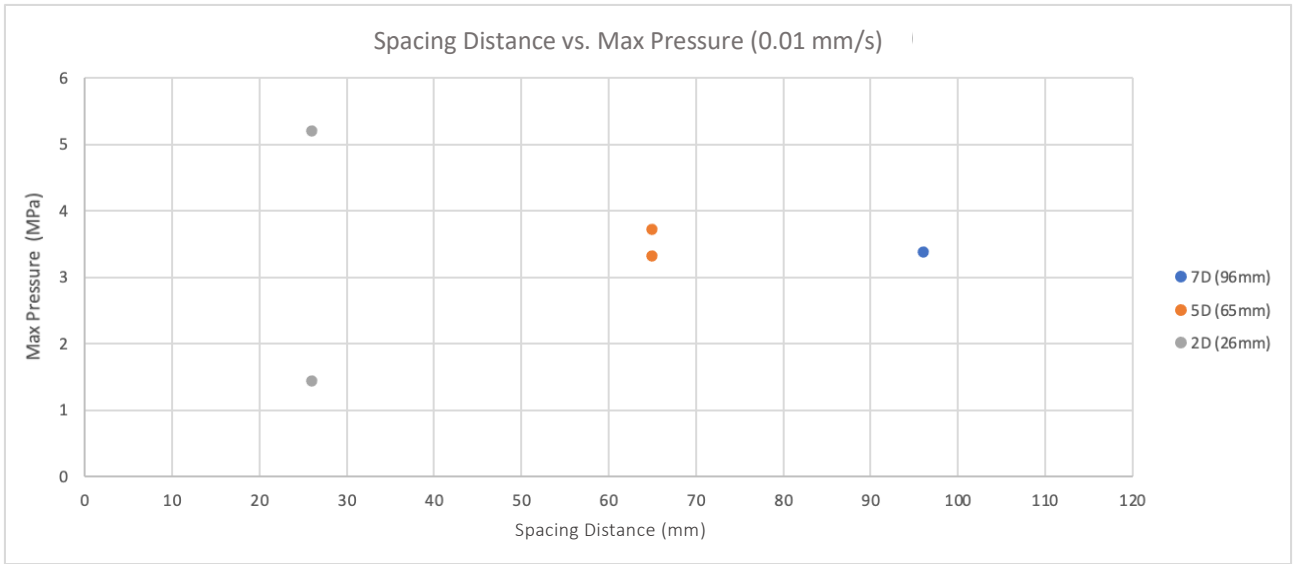

Figure 61 - Aggregate maximum pressure data from tests done at a rate of 0.01 mm/s for 7D (Blue), 5D (Orange), and 2D (Grey) spacing.

The above results show trends that are consistent with Figure 51, Figure 52, and Figure 53, which suggests that the maximum force and maximum pressure do not exhibit a significant dependence on particle spacing for the range of spacings considered.

Photographs of the ice specimens and rock particles show rock particle placement before indentation (Figure 62), as well as the crushed ice and indented rock particles immediately after the 0.5 mm/s tests were completed (Figure 63). The images taken before testing show the placement of individual rock particles relative to the damaged ice surrounding the site of the previous indentation tests.

Figure 62 - Images before testing for 7D (a), 5D (b) and 2D (c) spacing.

From the images taken after indentation shown in Figure 63, it is evident that a mix of spalling and crushing are observed. It is important to note that these observations of ice failure processes are very similar to the observed damaged zones formed during steel spherical indentation tests completed by Barrette et al. (2002), Wells et al. (2011), and Browne et al. (2013). Of particular interest from an ice mechanics standpoint, is Figure 63 (c), which exhibits similar characteristics to crushed and extruded ice that forms due to localized pressure melting and refreezing. Moreover, it is noted that such ice indentation conditions also correspond to the embedment and bonding of the ice particle in the upper ice specimen, as shown in Figure 63 (d). These observations provide valuable insights into the interaction mechanics between the ice and individual rock particles that will serve to guide future experiments and modelling directions.

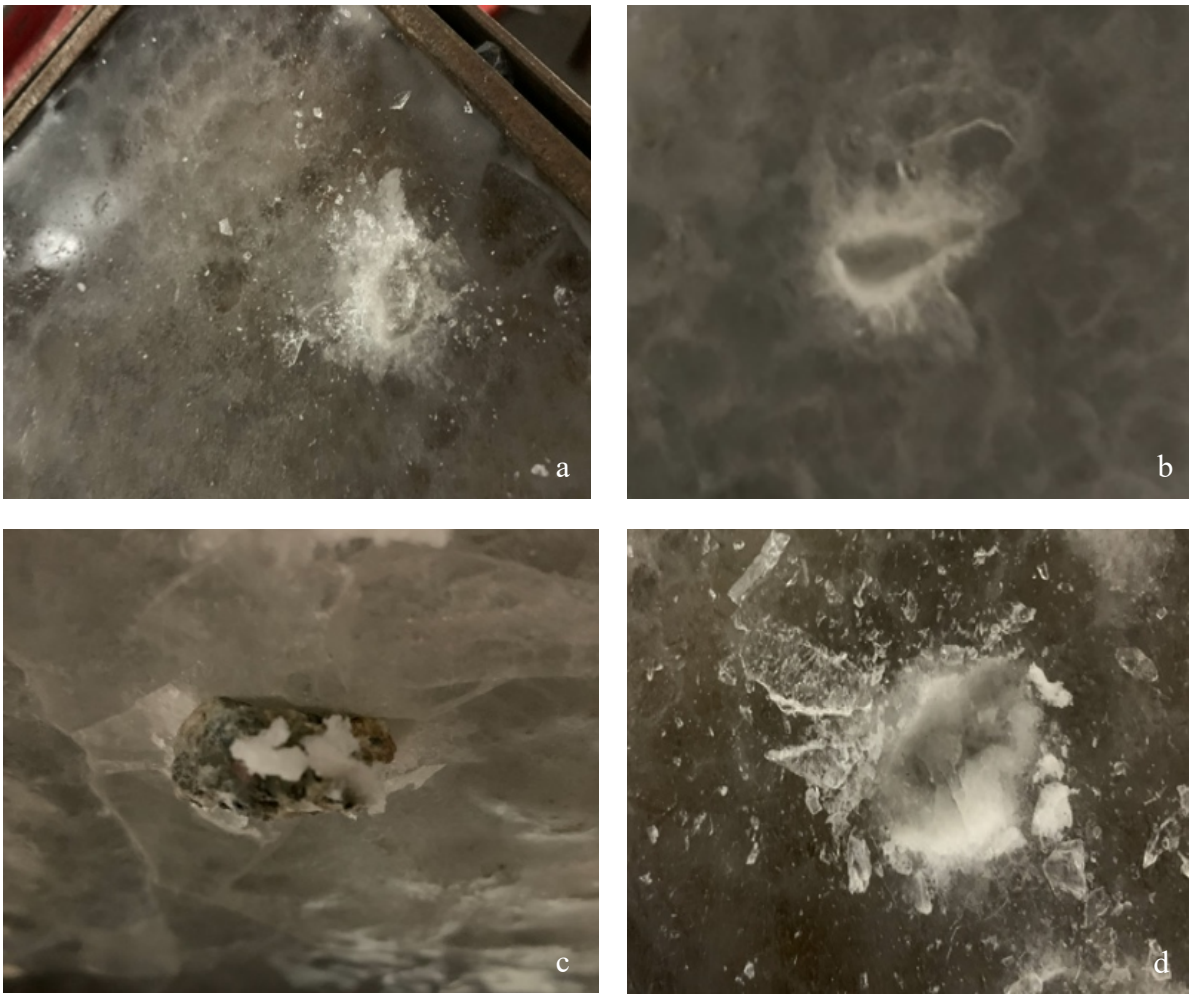

Figure 63 - Images of bottom (left) and top (right) ice surfaces taken after testing for 7D (a./b.) and 2D (c./d.).

5.5 Comparison Between Single Particle and Spherical Steel Indentation Tests

Based on the analysis completed for single unconstrained rock particle indentation, particular interest was paid to the nature of indentation rate effects. The trends observed in the analysis of the indentation of single unconstrained rock particles was observed to be similar in nature to typical trends identified in research from spherical steel indentation tests.

For the typical ranges of indentation rates implemented of 0.01 mm/s (slow rate), 0.5 mm/s (moderate rate), and 10 mm/s (fast rate) similar ice indentation research has been completed historically with spherical steel indenters of various geometries. Based on noted observed similarities between indentation of single unconstrained rock particles and these spherical steel indenter tests, a more direct comparison can be made in order to draw potential comparisons between the two testing scenarios.

Research completed by Wells et al. (2011) presented Total Force versus Time graphs for indentation tests with a steel indenter of 20 mm in diameter for a range of indentation rates. Shown below in Figure 64 (a) and (b), are plots for indentation tests completed at 0.2 mm/s, and 10 mm/s. Similarities can be clearly seen between the force trace data patterns in these experiments completed by Wells et al. (2011) as those shown below in Figure 64 (c) and (d), which were observed for similar indentation rates of 0.5 mm/s and 10 mm/s tests using single unconstrained rock particles which were completed in this thesis research program.

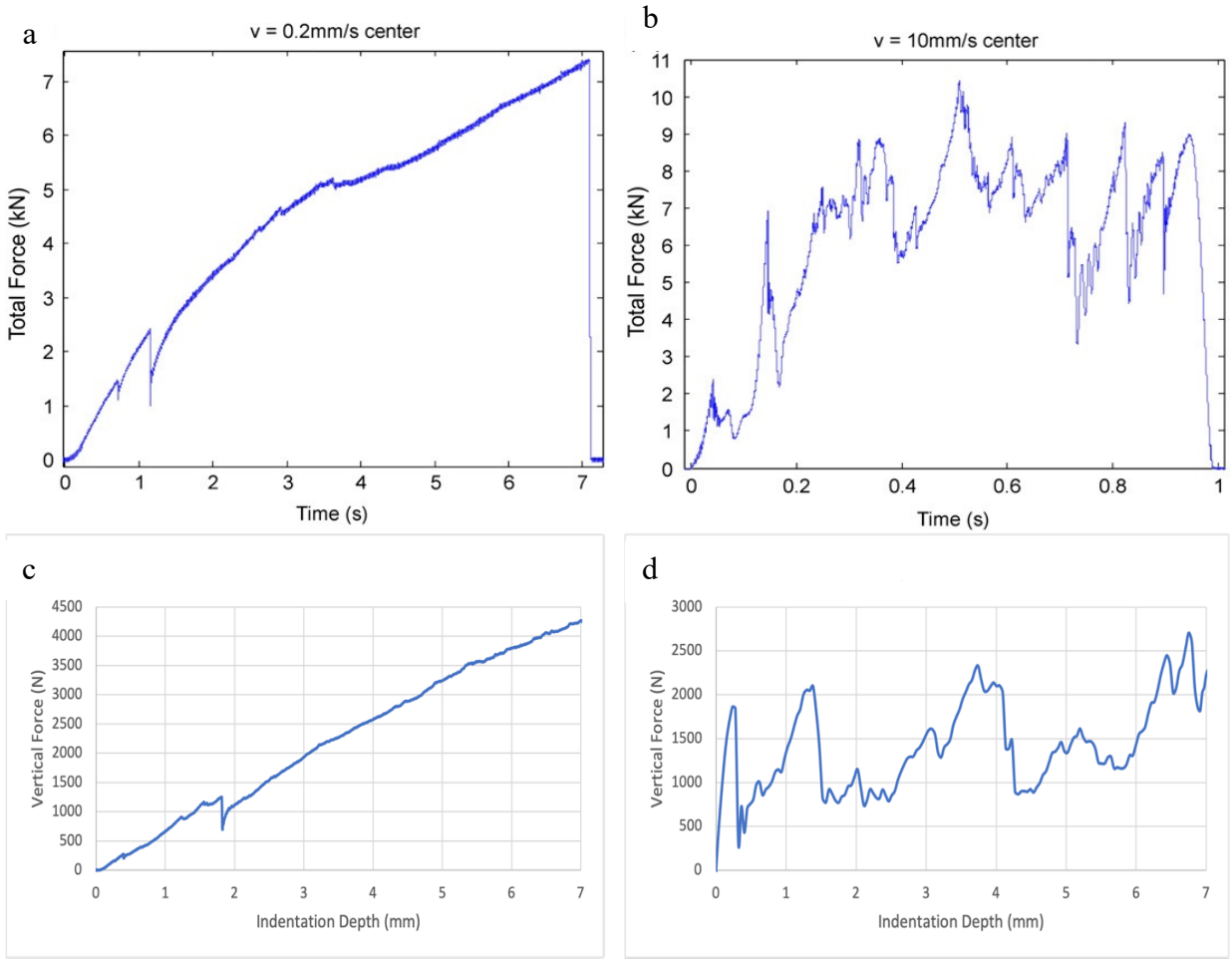

Figure 64 – Force-Time plots from spherical steel indenter tests completed by Wells et al. (2011) *at 0.2 mm/s (a) and 10 mm/s (b) compared with tests completed on single unconstrained rock particles 0.5 mm/s (c) and 10 mm/s (d).*

Direct comparison between the moderate rate test at 0.2 mm/s completed by Wells et al. (2011) shown in Figure 64 (a) with tests completed in this thesis with an unconstrained rock particle at the moderate rate test of 0.5 mm/s shown in Figure 64 (c), it can be seen that both plots exhibit typical phases of ductile failure, where the load continuously increases, with localized spalling occurring near the beginning of indentation as the sample experiences slow crushing failure; this corresponds with a failure mode which is typically referred to as a 'ductile' failure, and corresponds to a slow, continuous flow of crushed ice beneath the contact zone. Direct comparison between the fast rate test at 10 mm/s completed by Wells et al. (2011) show in Figure 64 (b) with tests completed in this thesis with an unconstrained rock particle at the fast rate test of 10 mm/s

shown in Figure 64 (d), both plots can be seen to undergo typical phases of dynamic loading which is expected at this rate, where the load builds steadily and undergoes typical phases of dynamic loading, with larger spalls and associated load drops being observed near the end of indentation in both plots.

Similarly, research presented in Sanderson (1988) shows Total Pressure versus Indentation Rate graphs for different indentation tests for a wide range of indentation rates. Shown below in Figure 65, are three plots for indentation tests completed from a range of indentation rate from 10^{-7}mm/s to over 10 mm/s. Similarities can be clearly seen between the scatter plot data patterns in these experiments presented in Sanderson (1988) as those shown below in Figure 66, which were observed for similar indentation rates in the range of 0.01 mm/s, 0.5 mm/s, and 10 mm/s in tests using single unconstrained rock particles which were completed in this thesis research program.

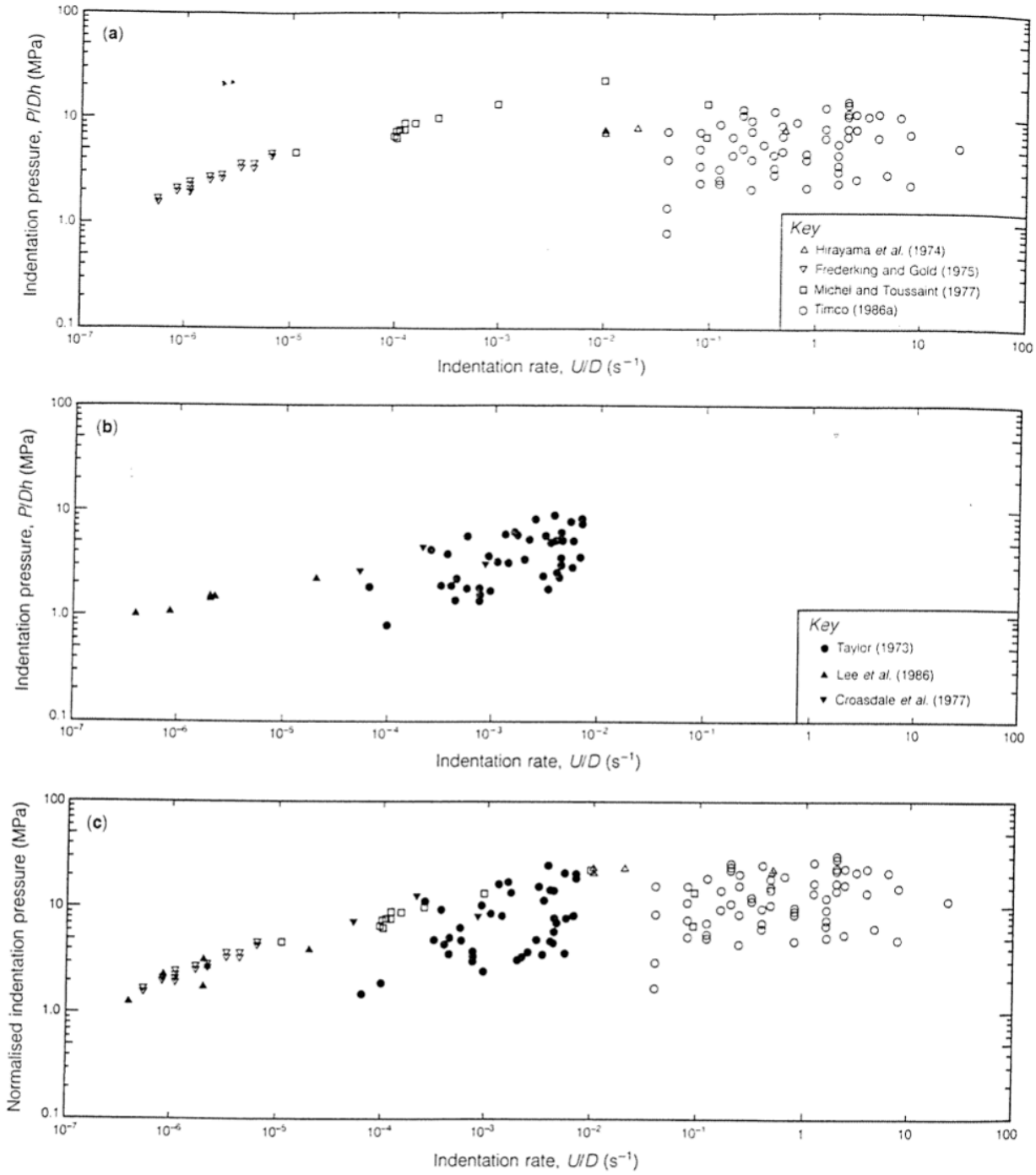

Figure 65 - Indentation data of indentation pressure (P/Dh) versus indentation rate (U/D) for (a) small-scale data measured in the laboratory for a number of experiments, (b) medium scale ice tests, and (c) combined small-scale and medium scale tests from (a) and (b) normalized to zero salinity and temperature of -10°C (Sanderson, 1988).

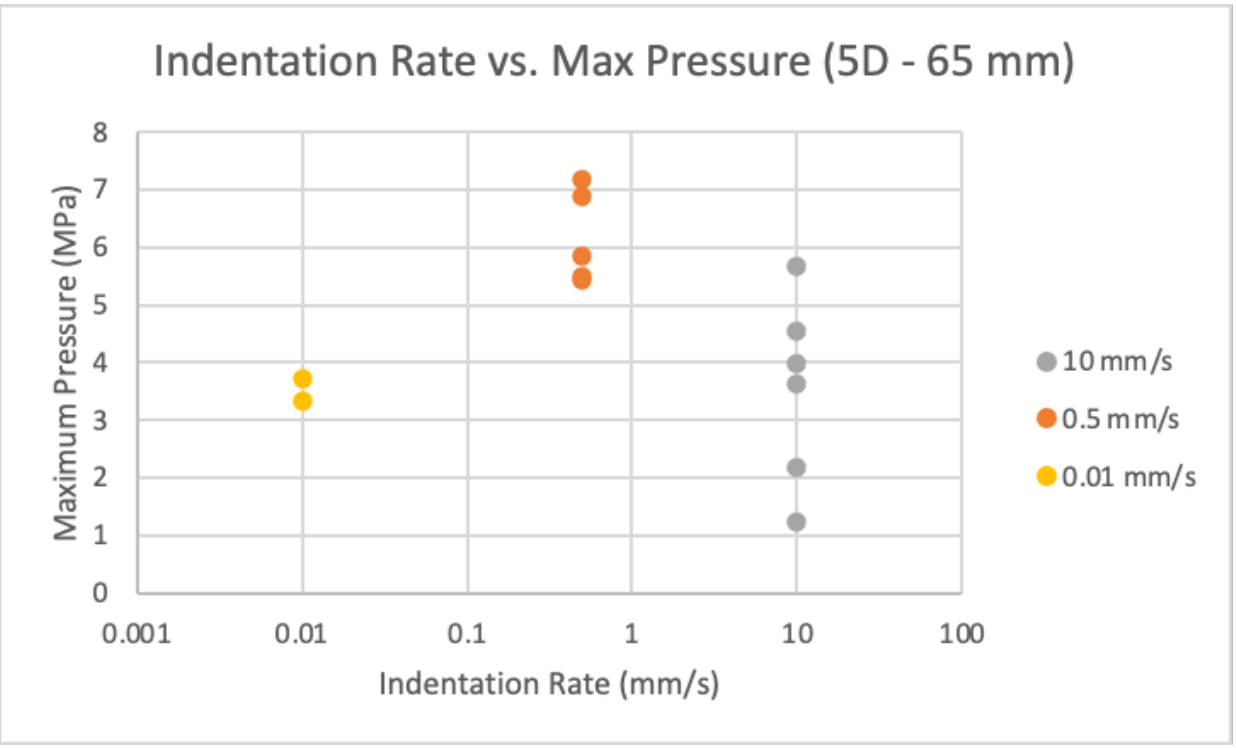

Figure 66 - Aggregate maximum observed pressure data from tests done at a spacing of 5D (65 mm) for slow (Yellow), moderate (Orange), and fast (Grey) tests.

Similarities in pressures were investigated between the multi-particle tests and spherical steel indenters. Using a mean particle diameter of 13 mm and an indentation depth of 7 mm into the ice, the total contact area for 55 particles may be estimated to be ~ 6.00 x 10^{-3} m^2. For a total indentation force of 82,000 N, this gives a peak indentation pressure of about 13.6 MPa. These pressures are lower than the indentation pressures reported for spherical steel indenter tests e.g., mean peak indentation pressure reported by Wells et al. (2011) for similar conditions was about 23.9 MPa.

Considering nominal pressures, which is calculated as the total peak force over the nominal area of the ice surface of 0.065m^2, the nominal pressure would be about 1.46 MPa. This nominal local pressure is significantly lower than local ice crushing pressure expected for an area of this size

(Jordaan., 2001), highlighting that the particles appear to serve as stress concentrators that promote local failure of the ice.

The analysis results presented here suggest that the peak indentation pressures during these multi-particle experiments was between 13.2 MPa and 19.8 MPa, which is lower than the mean indentation pressure of 23.9 MPa reported by Wells et al. (2011) for spherical steel indenter tests under similar conditions. Similarly, nominal pressures were calculated to be between 1.43 MPa and 2.14 MPa for the conditions considered, which is considerably lower than the nominal local pressure expected for an area of this size (Jordaan., 2001). These preliminary results suggest that the rock particles appear to serve as stress concentrators that promote local failure of the ice at pressures below those reported in the literature for ice-structure interactions with steel structures. Additional research is needed to further explore this topic and better understand the associated mechanics.

5.6 Comparison Between Single and Multiple Particle Indentation

Testing was completed on 170-gram weighted populations of medium sized rocks to effectively investigate the effects of multiple particle indentation on the compressive failure of ice, and to draw comparison to tests completed with only single particle indentation. The representative indentation rate case of 0.5 mm/s (moderate) was chosen as the comparison case, with an indentation depth setpoint of 7 mm. Plots representing tests completed at this indentation rate and indentation depth for the three different spacing cases of 7D, 5D, and 2D spacings are compared with tests completed at the same setpoints for tests completed with 170 grams of medium sized rocks. For the moderate rate of 0.5 mm/s it can be observed that the load continuously increases,

with one localized spall near the beginning of indentation as the sample experiences slow crushing failure; this corresponds with a failure mode which is typically referred to as a 'ductile' failure, and corresponds to a slow, continuous flow of crushed ice beneath the contact zone. This is consistent across all three different spacing cases of 7D, 5D, and 2D spacings and are seen to be consistent with the trends in the multiple particle tests completed with 170-grams of medium sized rocks. Based on previous observations of independence of single rock particle indentation events from other previously formed damage zones, and investigation of an empirical model is completed to compare single rock particle indentation to the multiple particle indentation.

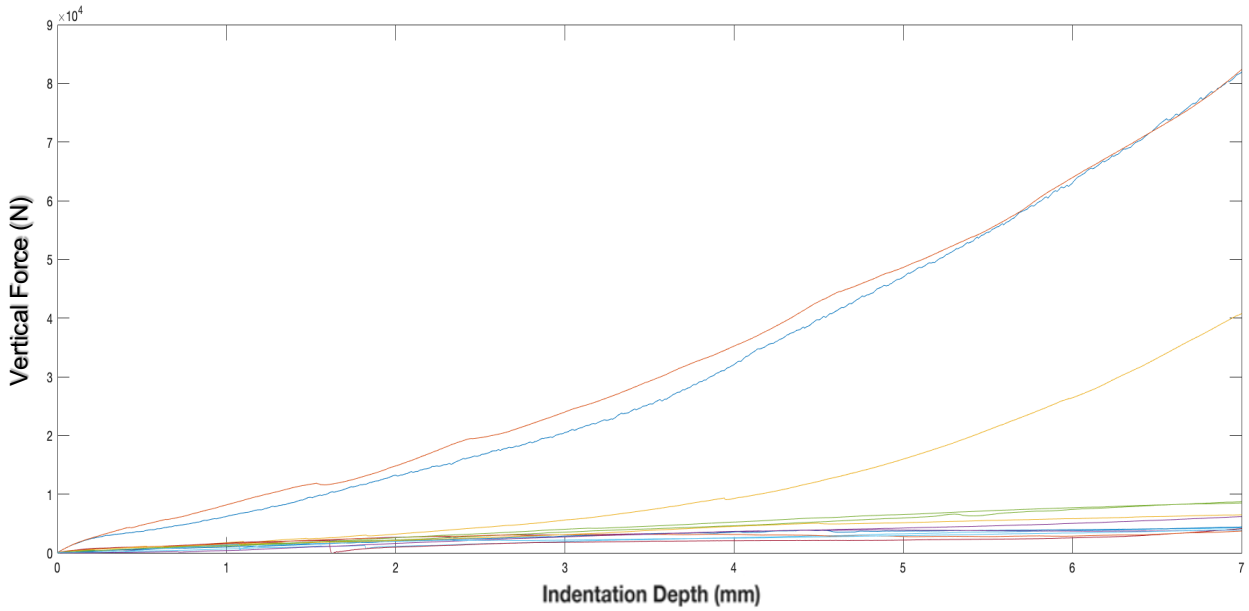

Figure 67 – Force-Indentation plot of aggregate single-particle indentation tests (Tests under $4x10^4N$) resulting in overall multi-particle simulation force trace (Orange). Also compared with laboratory multi-particle tests (Yellow/Blue).

A model relating each rock of the roughly 55 total particles in the 170-gram population transmits the same force as a single rock from the independent single rock indentation test. The average maximum force from independent tests completed on a single rock particle was observed to be 4657 N, and similarly for a separate independent test completed on a population of roughly 55

rocks, the maximum force was observed to be 82 000 N. Based on a simple linear scale model, the test completed on a population of roughly 55 rocks should transmit a maximum force of roughly the maximum force from the single particle test multiplied by the total number of rocks in the population which gives a total maximum force from the multiple particle test of 256,135 N. This predicted value of 256,135 N is observed to be about 3 times larger than the actual maximum force for a multiple particle test, which could be due to a number of factors.

One such factor is that since indentation is completed based off an initial position just before contact with the largest rock, despite 55 rocks being in an average population for a 170-gram sample multiple particle test, not all rocks would fully indent 7 mm; similarly, some rocks would not contact at all. For example, of the 55 rocks, the diameter and relative size of each rock differed, on average, between 9.5-19.1 mm; therefore, one rock which is 19.1 mm would not observe the same level of indentation as another which is 9.5 mm. Therefore, the implementation of a probabilistic model would be expected to give results much more in line with the typically observed maximum force for these tests. In order to more effectively investigate this hypothesis, a probabilistic model using empirical data in MATLAB was developed.

5.7 Empirical Model Development

Based on the assumption of independence from the single-particle indentation tests and data obtained from the multi-particle testing, further analysis was completed using MATLAB. The purpose of this model is to simulate multi-particle rock indentation for larger and different shaped interaction areas to allow scaling of the analysis to different cases based on empirical data from

single-particle tests. The overall function of the MATLAB model code is described in the flowchart shown in Figure 68 below.

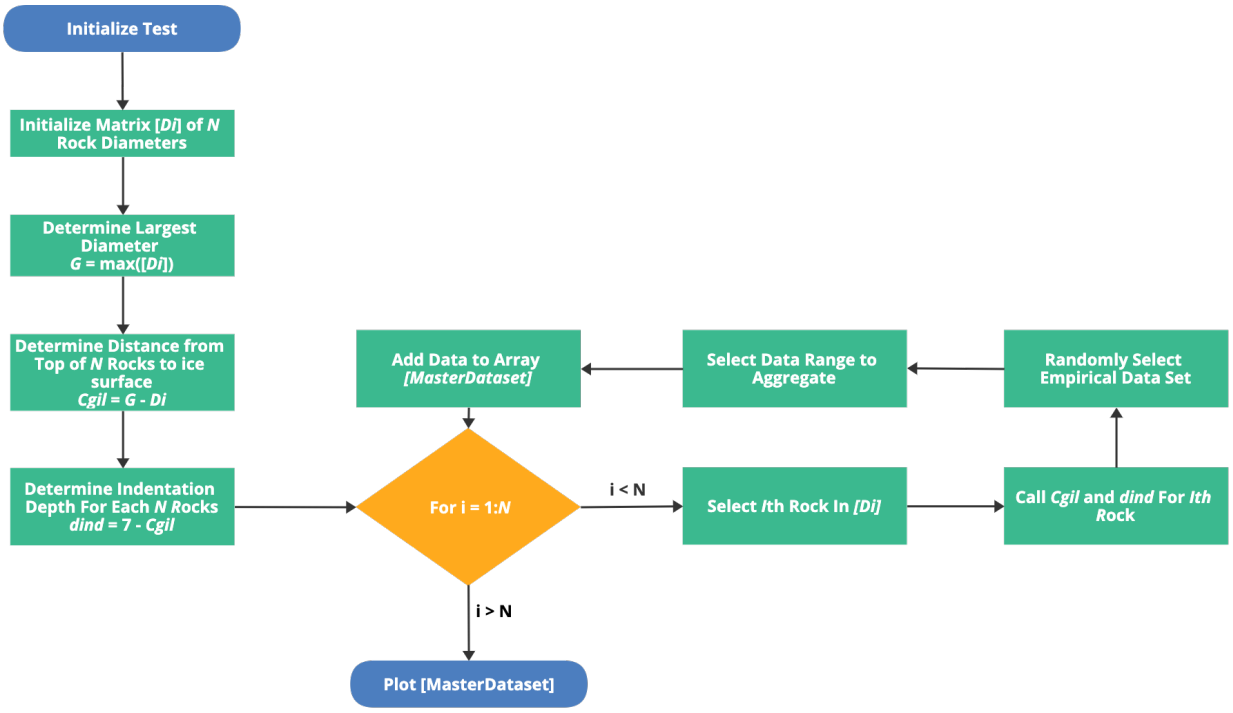

Figure 68 – Flowchart describing the overall function and process of the MATLAB multi-point simulation model.

The flowchart shown in Figure 68 above, provides a high-level outline and describes the overall flow of the code. Full details of the algorithm's procedures are described fully below with the aid of an example simulation.

To model multi-particle interactions, the MATLAB script is set-up to sample a user-prescribed number of rocks, n. In the present case, this number was matched to the corresponding experiments (n = 55). Rock size distributions used in these simulations were derived from statistical image analysis of rock particles used in the experiments. For a given simulation, a sample of n particles is randomly drawn from the rock population based on a uniform distribution of diameters with a lower bound of 9.5 mm and an upper bound of 19.1 mm, based on statistical analysis of the rock

population. These randomly generated rock diameters are saved into an array, denoted as Di. A histogram showing a sample group of 55 rocks from one simulation case is shown in Figure 69.

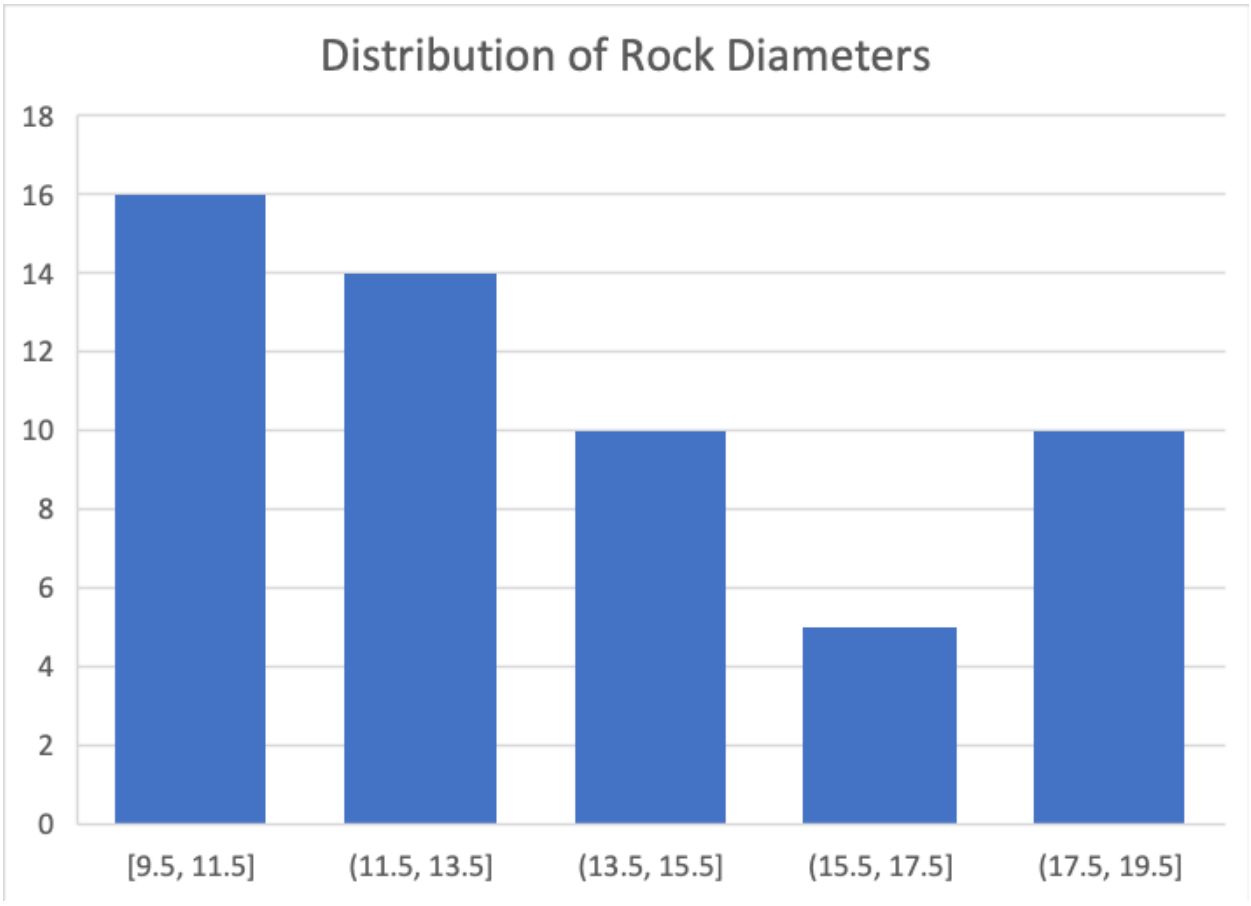

Figure 69 - Randomly sampled population distribution of (n=55) rock diameters (mm) at initial condition.

Empirical force-depth data from the single-particle test have been compiled in a database. For each of the particles in a simulated sample, a corresponding empirical force-depth dataset is randomly extracted from the single-particle database.

To determine the initial point of indentation from which the simulated indentation depth (here chosen to be 7 mm) will be calculated, the maximum rock diameter in the sample array of *n* rocks is identified, as indentation starts when the gap between the two ice surfaces is equal to the

maximum rock diameter. From Figure 69 it is noted that the largest rock for this set of sample data is 18.9 mm. This process also reflects the procedure followed during laboratory indentation experiments and gives a common starting point for the simulated upper ice surface as would be used in the experiment. This position is the point where the ice is in first contact with any rock particle, and the total indentation depth follows from that point.

With the initial position of the simulated indentation model defined, further operations are completed to determine the relative distance from this position to the first contact for each rock based on the gap between each rock and the upper ice specimen. This is calculated by subtracting the diameter of each rock in the array from the largest diameter in the population, per Equation 9 below.

$$C_{g_{i,I}} = G - Di \qquad \textit{Equation 9}$$

Where, G, is the largest rock diameter in the population, Di, is the diameter of the ith rock in the array and, *Cgi,I,* is the resulting distance from the upper ice specimen to each ith rock. An example of the output array for a sample calculation of *Cgi,I* values is shown in Figure 70 below.

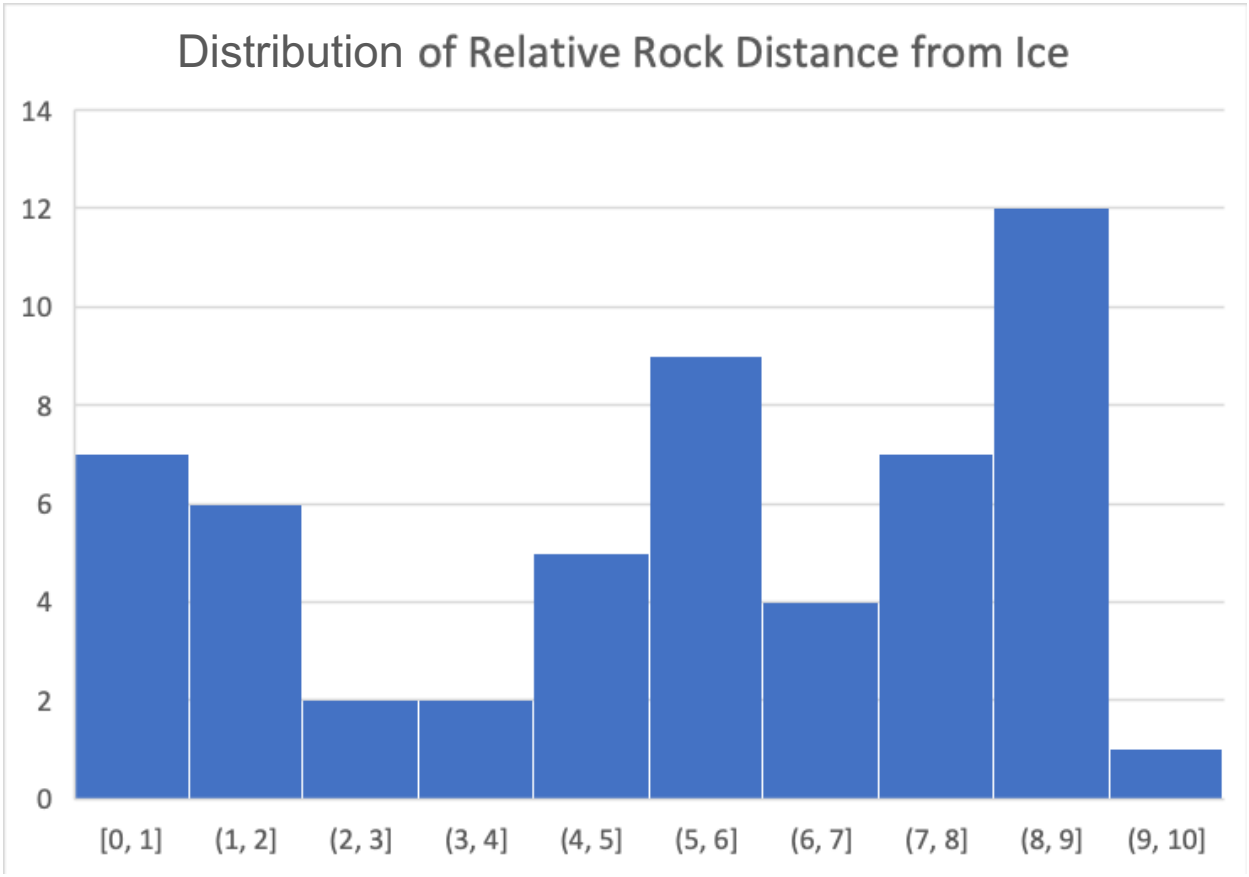

Figure 70 – Distributions of relative distance Cgi,I (mm) from the upper ice surface at first contact to the top of each randomly sampled rock.

The above data provides insight into the relative distance that the indentation must proceed before each individual particle begins to contact and indent into the ice. In the empirical model, this information is used to determine the point in the overall indentation at which each single particle force-depth trace commences. In other words, each individual rock will only begin to transmit force to the ice once it comes into contact, which corresponds to a specified indentation depth for each sampled rock. This indentation depth *dind* each *i*th rock indents into the ice specimen is calculated as shown in Equation 10 below.

$$d_{ind} = 7\ mm - C_{g_{i,l}} \qquad \textit{Equation 10}$$

Where, $C_{g_{i,l}}$, is the distance from each ith rock to the upper ice specimen and 7 mm is the constant indentation depth. Sample indentation data shown are shown in Figure 71.

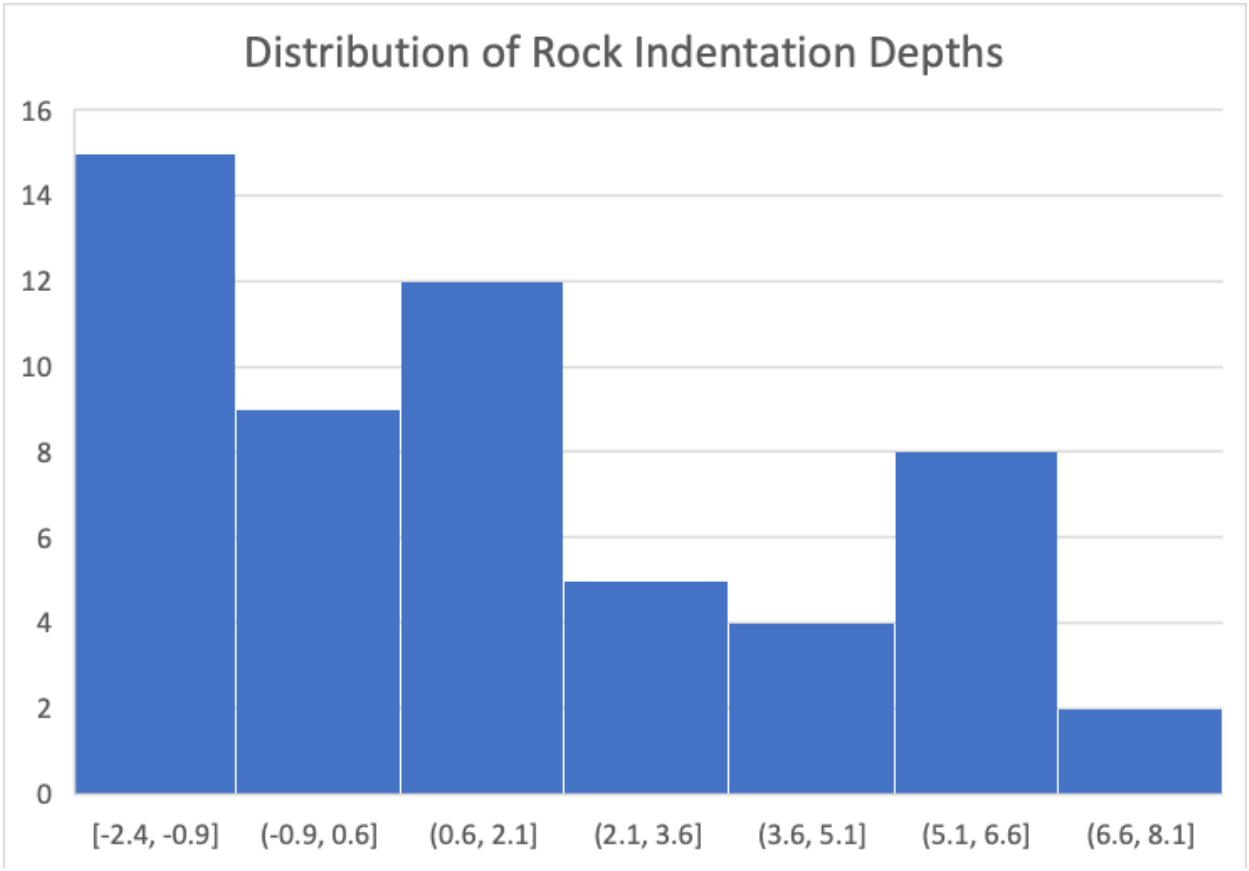

Figure 71 – Distribution of relative indentation depth (mm) experienced by each rock after the full 7 mm indentation test is completed.

Any value that is denoted as negative indicates that the indentation stops before coming into contact with that particular rock (e.g., the respective rock remains that distance away from the upper ice specimen at the end of the simulated 7 mm indentation). Correspondingly, such rocks would contribute no force data to the aggregate loads on the ice for that particular case. A schematic is shown below as an illustrative example of the physical meaning behind the above discussed parameters and equations. Sample equations are also provided.

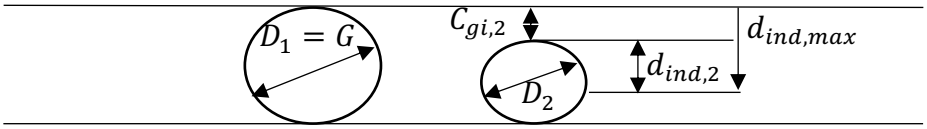

$$G = \max(D_i) = D_1$$
$$C_{gi,2} = D_2 - G$$
$$D_{ind,2} = 7\ mm - C_{gi,2}$$

Using the above-described indentation depth data, the force-depth data are compiled for all n particles with the initiation point for each of the *i*th rocks corresponding to its calculated *Cgi,I* value and continuing until it has indented *dind*. Thus, the simulation starts with the largest rock (e.g., at depth = 0 mm) and data from each randomly selected rock test is added to the aggregate set sequentially as the simulated indentation proceeds. For example, the first force-depth data added starts at the beginning of indentation (0 mm) and proceed until the end of the indentation (7 mm), with data added for the entire individual test added to the aggregate set. If the second largest particle is 0.5 mm smaller in diameter than the largest particle, only data ranging for indentation depths from 0 mm to 6.5 mm for the corresponding single-particle force data would be added, starting at 0.5 mm from the beginning of the indentation. This process is repeated for each *i*th rock and sequentially added to the master data set to create an aggregate plot derived from the experimental data for individual indentation tests. A sample single-particle force-depth plot for an individual indentation tests used to calculate the aggregate force plot is shown in Figure 72.

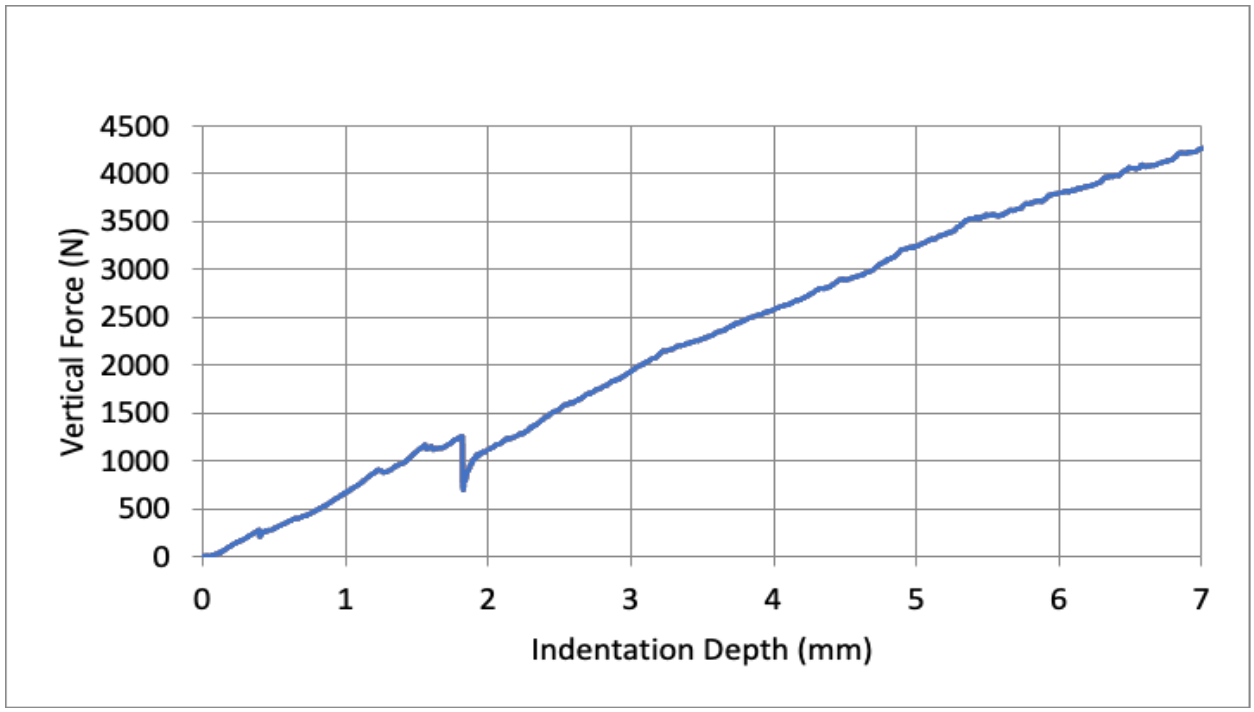

Figure 72 – Single particle indentation MTS load data completed at a rate of 0.05 mm//s to a depth of 7 mm.

Once this calculation has been completed for all *n* rocks in the sample and all force data have been compiled, the overall simulated multi-point indentation force can be calculated. The aggregate force plot output for the MATLAB simulation for a 7 mm indentation is shown for $n = 55$ in Figure 73.

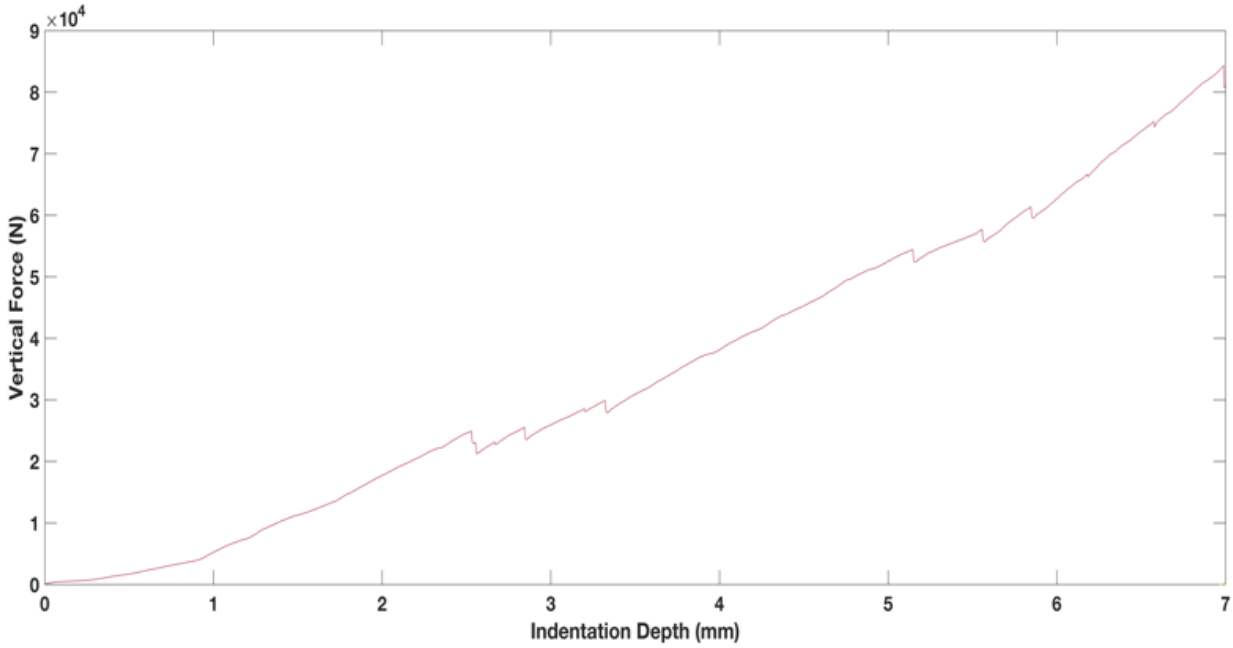

Figure 73 - Plot of simulated multi-point indentation at 0.5 mm/s to a depth of 7 mm for n = 55 rocks randomly sampled from individual rock particle tests.

As can be seen from Figure 73, the trends generated for multi-point (n = 55) indentation to a depth of 7 mm at a rate of 0.5 mm/s shows a steadily increasing load, paired with localized load drops during the indentation. This behavior is typical of indentation tests at this rate and is consistent with multi-point indentation tests. The maximum simulated force was 81,596 N, which agrees closely with the maximum observed forces of 82,000 N for the corresponding laboratory experiments shown in Figure 74 and Figure 75 below. Differences, such as the presence of more frequent load drops in the simulated data is primarily due to the nature of sampled individual indentation data.

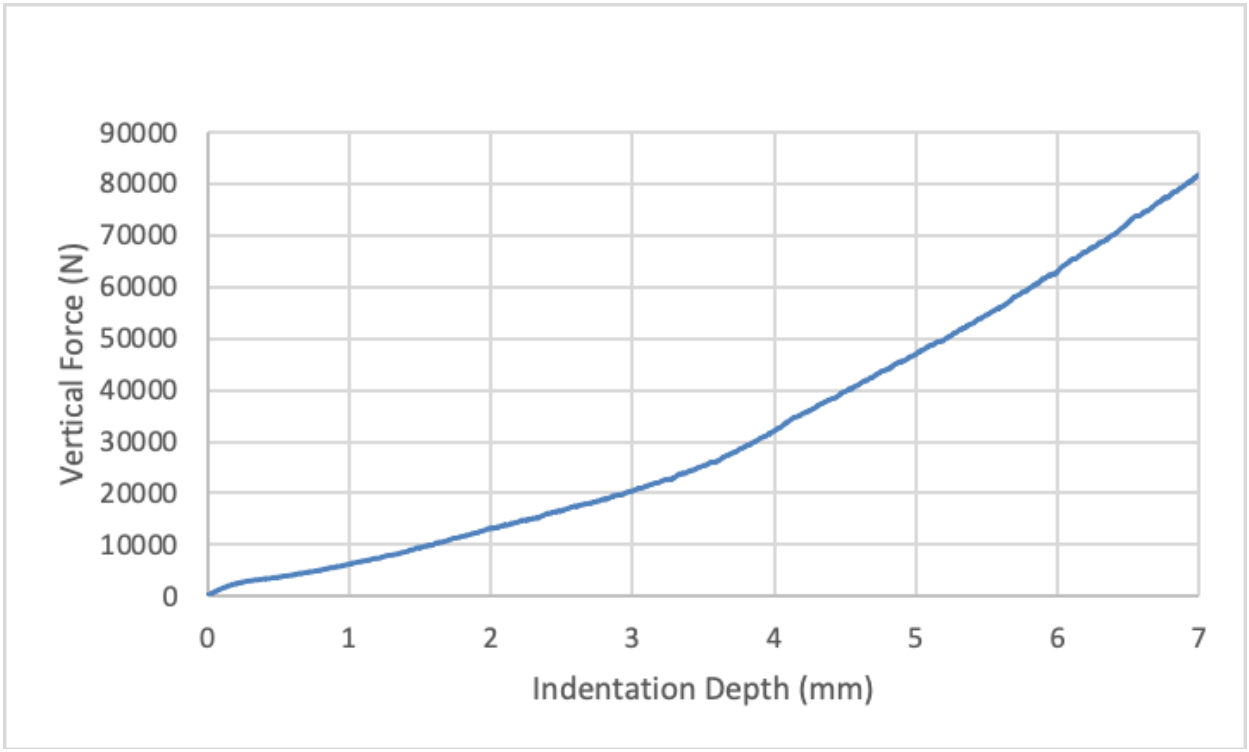

Figure 74 - Multi-point laboratory indentation MTS load data for 170-gram sample indented 7 mm at a rate of 0.5 mm/s.

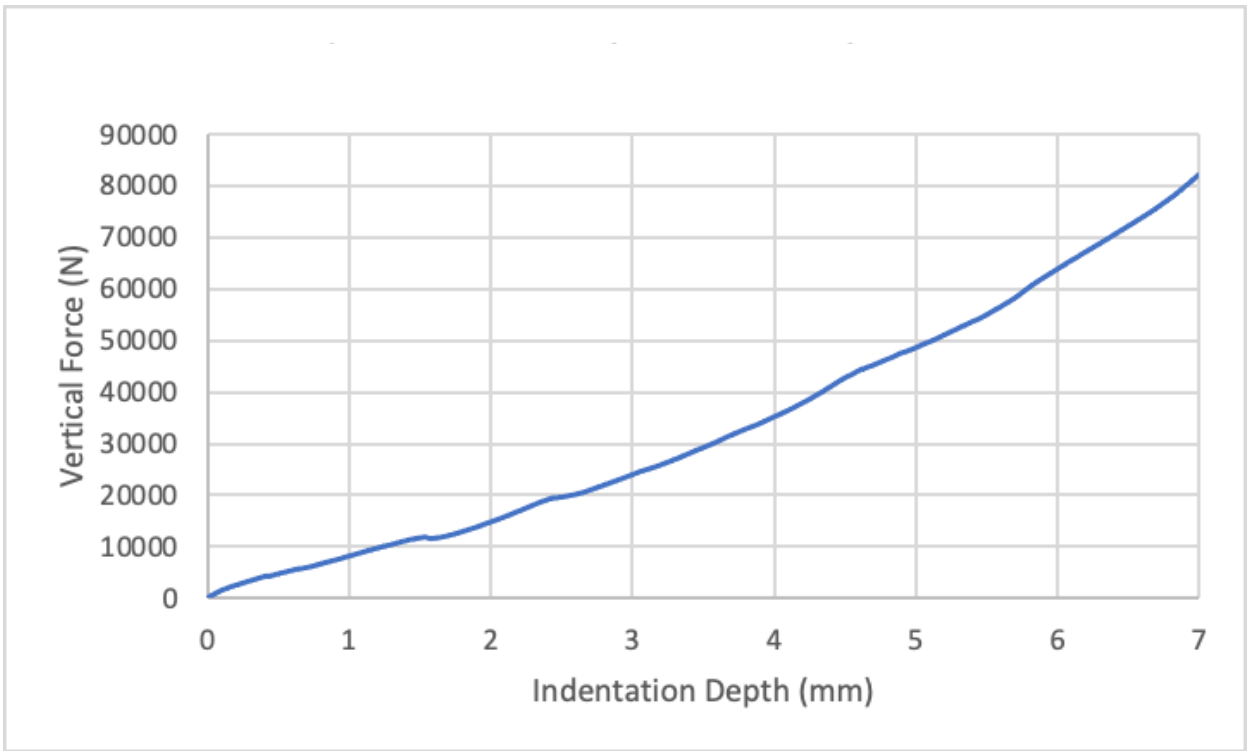

Figure 75 - Multi-point indentation MTS load data for 170-gram sample indented 7 mm at a rate of 0.5 mm/s.

To assess the range of simulated forces produced by the MATLAB simulations, a series of simulation cases were run, and the observed maximum forces were found to range from 80,000 N to 120,000 N. Variation in maximum forces in these simulations is noted to be primarily attributed to differences in sampled rock populations between simulations.

It is noted that while the above result corresponds to the specific conditions considered in the multi-particle experiments, this model can also be used to model aggregate loads for different numbers and sizes of independent, randomly sampled single particles based on chosen indentation depth, while accounting for local differences in indentation depth associated with differences in individual particle sizes.

5.8 General Model Comparison

A comparison of two cases of simulated ice failure loads compared with corresponding experimental results are shown in Figure 76 and Figure 77. These comparisons show very good agreement between the experimental and simulated results, suggesting that the underpinning assumptions of independence between individual particles is reasonable. Moreover, fluctuation in aggregate loads may be linked back to individual ice failure events at the scale of individual rock particles.

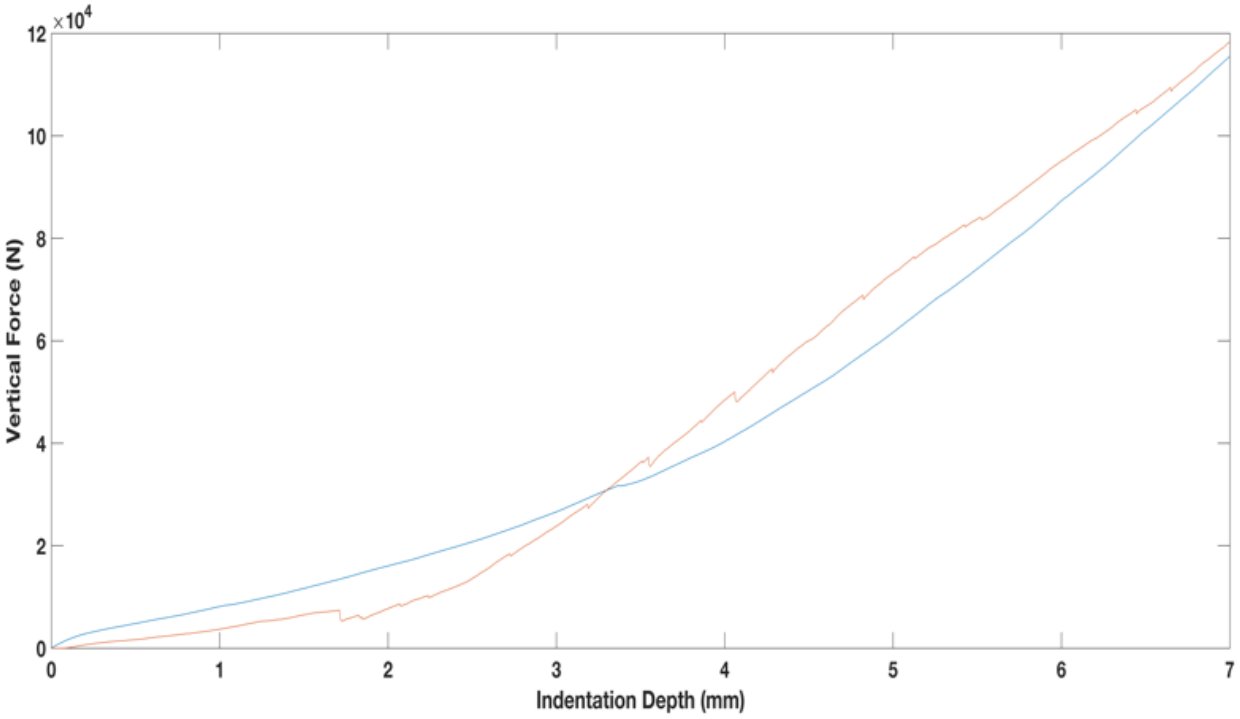

Figure 76 – Comparison plot of simulated model data (orange) and laboratory test 2020_25_11 (4) (blue).

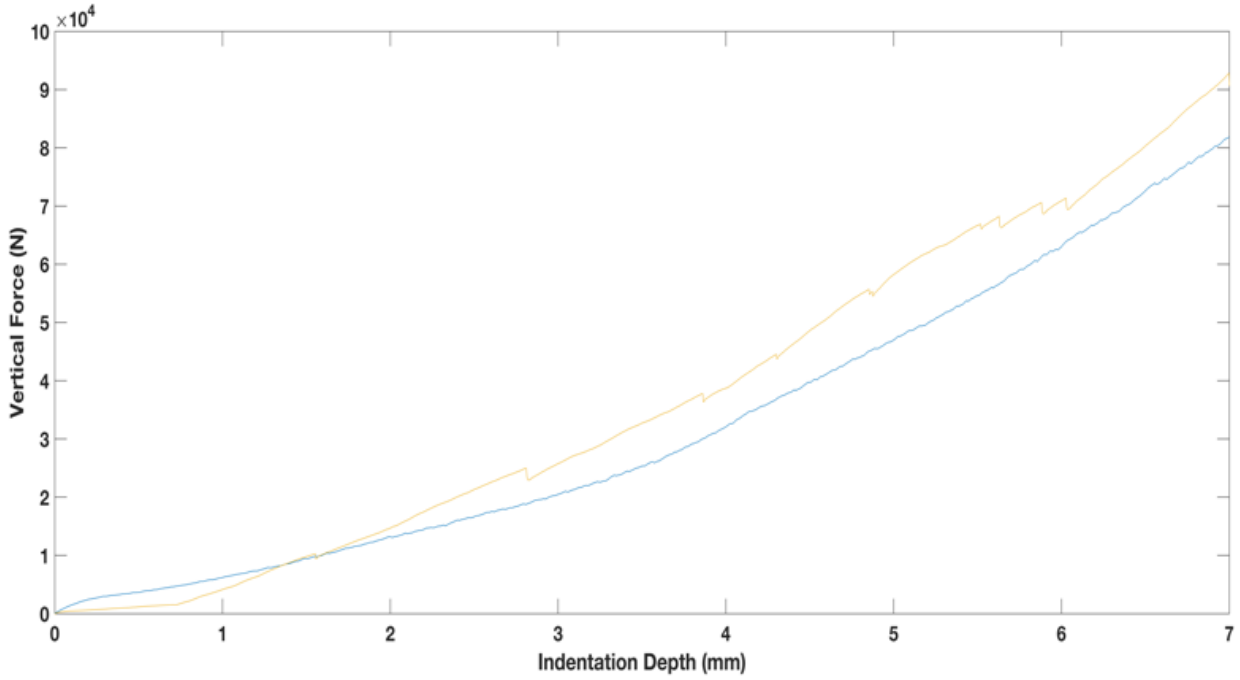

Figure 77 - Comparison plot of simulated model data (orange) and laboratory test 2020_19_11 (1) (blue).

Close agreement between the experimental results and the simulated indentation plots obtained from the MATLAB routines can be seen from both plots shown in Figure 76 and Figure 77 above. While there are some minor differences in the force traces, the general trends for the force and overall maximum observed forces agree strongly between experiments and simulations.

5.9 Discussion of Implications for Subsea Infrastructure

Marine and Offshore operators may rely on seafloor infrastructure such as cables and pipelines. When these operations are located in ice prone regions which may see deep draft ice features present in the area, there is a risk these structures may interact with ice features which may impinge and gouge the seafloor. One protection strategy against such events is to bury the pipeline below the seafloor so that a collision does not have the potential to occur. This situation is further complicated if this collision takes place with an ice feature which has embedded rock or soil particles, as described by Barrette (2011).

Results obtained for both single particle and multiple particle indentation tests provided interesting insights related to the ice failure mechanics due to the indentation of rock particles. The question remained, will localization of contact by the rocks cause the ice to fail more easily, resulting in reduced ice pressures, or will rocks transmit high ice pressures through smaller contact areas between the rock and structure resulting in more intense contact stresses on the surface of the structure. Based on initial pressure considerations discussed above, these preliminary results suggest that the rock particles appear to serve as stress concentrators that promote local failure of the ice at pressures below those reported in the literature for ice-structure interactions with steel structures. Additional research is needed to further explore this topic and better understand the

associated mechanics; however, initial considerations are presented to assess the potential consequences of contact between an ice feature with embedded objects and steel structures.

As previously discussed in consideration of the similarities between particle indentation and spherical steel indenters, using a mean particle diameter of 13 mm and an indentation depth of 7 mm into the ice, the total contact area for 55 particles may be estimated to be ~ 6.00 x 10^{-3} m^2. For a total indentation force of 82,000 N, this gives a peak indentation pressure of about 13.6 MPa. Additionally, considering these nominal pressures, which are calculated as the total peak force over the nominal area of the ice surface of 0.065 m^2, the nominal pressure would be about 1.46 MPa. This nominal local pressure is significantly lower than local ice crushing pressure expected for an area of this size (Jordaan., 2001), highlighting that the particles appear to serve as stress concentrators that promote local failure of the ice. If these pressures are implemented as a comparison case for potential pressures observed on a steel structure, simple preliminary considerations can be investigated for the results of localized indentation during contact between an ice feature with embedded rock particle and a steel subsea pipe or structure.

Currently, steel grades X60, X65 and X70 according to API 5L (American Petroleum Institute, 2018) are mainly used in pipeline applications. For the purposes of this brief analysis piping of grade X65 is implemented for the considered steel subsea pipeline. The X65 piping material possesses a 448 MPa Yield Strength, and 530 MPa Tensile Strength, based on API 5L (American Petroleum Institute, 2018). While detailed analysis of ice-rock-pipe interactions is beyond the scope of this work, it is evident that local pressures are significantly below levels needed to cause local plastic deformation. Further analysis is recommended in future work.

5.10 Summary

Sixty-six (66) single particle tests were conducted with up to ten (10) repetitions per setpoint, and fifty-five (55) multi-particle tests were conducted including repetitions with twenty-five (25) being completed on pristine ice specimen. These small-scale laboratory tests as well as the development of the empirical model, allowed for an in-depth study of the compressive failure process which are observed during ice subsea interaction due to indentation by rock particles. For single-particle indentation tests the effects of indentation rate were found to have a significant effect on the failure processes of rock indentation. Slower rates of 0.01 mm/s exhibiting evidence of combined ductile and brittle failure, which gives way to two repeated crushing events. For the moderate rate of 0.5 mm/s it was observed that one localized spalling and slow crushing failure occurred which is described as a failure mode that is typically referred to as a 'ductile' failure, and corresponds to a slow, continuous flow of crushed ice beneath the contact zone. For the fast tests at 10 mm/s, typical phases of dynamic loading and larger spalls as well as associated load drops were observed. Different spacing distances of 2D, 5D, and 7D, were found to have little effect on the failure mechanics of compressive ice failure due to rock indentation, with similar trends being observed at the slow, moderate, and fast indentation setpoints for each spacing. Based on the analysis completed for single unconstrained rock particle indentation, the trends observed in the analysis of the indentation of single unconstrained rock particles was observed to be similar in nature to typical trends identified in research from spherical steel indentation tests. The effects of indentation rates for multi-particle tests were investigated and compared with those observed in single-particle indentation tests. For these multi-particle tests, it was observed that for the moderate rate of 0.5 mm/s localized spalling and slow crushing failure occurred. This is consistent across all three different spacing cases of 7D, 5D, and 2D spacings for the single particle indentation tests.

These similarities in the compressive failure mechanisms between the two tests, as well as the established independence of indentation events at spacing distances as small as 2D (26mm), an empirical model was developed to simulate multi-particle tests based on an empirical set of single particle indentation tests. This model showed close agreement between the experimental results and the simulated indentation plots obtained from the MATLAB routines.

6.0 Discussion and Conclusion

6.1 Summary and Conclusion

In this thesis, the effects of indentation rate and relative spacing of a single unconstrained rock particle under compressive ice loading were investigated, with multi-particle indentation test being considered for comparison. For single particle testing, an analysis of force and pressure data collected during a series of experiments including three spacing distances and three indentation rates has been conducted. For multi-particle testing, an analysis of force data collected during a series of experiments has been conducted and compared with results from single particle indentation tests.

From this analysis, it has been concluded that indentation rate effects observed during ice-particle interactions correspond closely to effects previously observed for indentation tests on ice with spherical steel indenters. The main contributor to observed differences between ice-rock and ice-steel indentation is believed to be local geometric variation in rock particle shape, which was observed to influence dominant ice failure mechanism and contribute to variability in measured forces and pressures. From a fundamental standpoint, perhaps of greatest interest was the observation that the greatest degree of embedment and adhesion of rock particles into the ice tended to correspond to conditions that generate the highest loads ($v = 0.5$mm/s) and have the most damaged ice around the indentation site ($S = 2D$). Observed damaged ice immediately beneath the rock indentation site for those test conditions exhibited characteristics that correspond closely with observations of crushed/extruded ice associated with localized pressure melting and refreezing observed during steel indentation tests. These observations provide valuable insights into the underpinning mechanics of the interactions and suggests that these mechanisms may be important to the embedment and bonding of rock in ice during ice interactions with gravelly soils.

Given the high degree of scatter in the force/pressure vs spacing distance data, it may be concluded that the effect of spacing distance on local ice-rock indentation is not strong. The implications of these findings are that for modelling purposes it is reasonable to assume as a first order approximation that individual ice-rock indentation processes may be treated as independent events. The present data suggests that this approximation may be assumed if particle densities are sufficiently low such that the mean spacing distance is greater than twice the mean particle diameter. Future work to extend this analysis to study and model multi-contact ice-particle interactions, better characterize embedded ice-rock bond strength, and consider different particle and interaction conditions was completed through comparisons with multi-particle indentation tests and the development of an empirical model.

Results from this series of multi-particle experiments have been presented, along with an empirical model for multi-particle ice indentation under compression. An analysis of force and pressure data collected during a series of experiments and plots produced from the MATLAB simulation model was presented. From this analysis, it has been concluded that the aggregation of local ice loads based on the summation of independent individual particle interactions appears to be a reasonable approach. This represents a promising direction for modelling interactions over larger areas of interest in assessing design implications, although additional research is needed for a broader range of temperature, rate, scale, and loading conditions.

Overall, sixty-six (66) single particle tests were conducted with up to 10 repetitions per setpoint, and fifty-five (55) multi-particle tests were conducted including repetitions with twenty-five (25) being completed on pristine ice specimen. These small-scale laboratory tests as well as the

development of the empirical model, allowed for an in-depth study of the compressive failure process which are observed during ice subsea interaction. The main findings from these experiments are given below.

6.1.1 Effects of Indentation Rate on Single Particles

From this analysis, it has been concluded that indentation rate effects observed during ice-particle interactions correspond closely to rate effects previously observed for indentation tests on ice with spherical steel indenters. The main contributor to observed differences between ice-rock and ice-steel indentation and primary source of uncertainty in these experiments is believed to be local geometric variation in rock particle shape, which was observed to influence dominant ice failure mechanism and contribute to variability in measured forces and pressures.

6.1.2 Effects of Particle Spacing on Single Particles

Given the high degree of scatter in the force/pressure vs spacing distance data, it may be concluded that the effect of spacing distance on local ice-rock indentation is not strong. The implications of these findings are that for modelling purposes it is reasonable to assume as a first order approximation that individual ice-rock indentation processes may be treated as independent events. The present data suggests that this approximation may be assumed if particle densities are sufficiently low such that the mean spacing distance is greater than twice the mean particle diameter.

6.1.3 Effects of Normal Loading on Multiple Particles

Consistent with tests completed for single particle indentation, this analysis of normal loading on multiple particles indicates that it can be concluded that indentation rate effects observed during ice-particle interactions correspond closely to effects previously observed for indentation tests on

ice with spherical steel indenters. The main contributor to observed differences between ice-rock and ice-steel indentation is believed to be local geometric variation in rock particle shape and potential interaction between rocks in the population, which was observed to influence dominant ice failure mechanism and contribute to variability in measured forces and pressures.

6.1.4 Comparison Between Single Particle and Spherical Steel Indentation Tests

The analysis results presented here suggest that the peak indentation pressures during these multi-particle experiments was lower than the mean indentation pressure reported by Wells, et al. (2011) for spherical steel indenter tests under similar conditions. Similarly, nominal pressures were calculated to be considerably lower than the nominal local pressure expected for an area of this size (Jordaan, 2001). These preliminary results suggest that the rock particles appear to serve as stress concentrators that promote local failure of the ice at pressures below those reported in the literature for ice-structure interactions with steel structures. Additional research is needed to further explore this topic and better understand the associated mechanics, and how these effect scale over larger interactions and compare with nominally flat or cylindrical structures.

6.1.5 Comparison Between Single and Multiple Particle Indentation

From this analysis, it has been concluded that the aggregation of local ice loads based on the summation of independent individual particle interactions appears to be a reasonable approach. This represents a promising direction for modelling interactions over larger areas of interest in assessing design implications, although additional research is needed for a broader range of temperature, rate, scale, and loading conditions. Additional single-particle tests are recommended to better understand the effects of particle shape, size, and other factors.

6.2 Recommendations for Future Work

The indentation of rock particles into ice and associated ice failure processes are highly complicated, necessitating in-depth analysis. The analysis presented in this work provided valuable new insights into these processes but also highlights that there is room for further investigation and extension of the present research. Limitations such as time, practicality, and experimental setup have resulted in a number of recommendations based on the outcomes of this research.

From the multi-particle testing program, the data suggest that the approximation of independence of indentation events may be assumed if particle densities are sufficiently low such that the mean spacing distance is greater than twice the mean particle diameter. Therefore, future work to better characterize embedded ice-rock bond strength and consider different particle and interaction conditions is recommended.

The development of an empirical model to simulate multi-particle indentation represents a promising direction for modelling interactions over larger areas of interest in assessing design implications. Additional research is recommended for a broader range of temperature, rate, scale, and loading conditions. As testing was only completed for single-particle indentation at a slow rate of 0.01 mm/s, moderate rate of 0.5mm/s, and fast rate of 10 mm/s and only at the moderate rate of 0.5mm/s for multi-particle tests, additional experiments are recommended at a wider range of conditions between 0.001 mm/s and 100 mm/s for both single and multi-particle indentation. Similarly, as tests were completed at a nominal setpoint temperature between -10℃ and -12℃ tests at warmer temperatures closer to 0℃ and much colder temperatures trending towards -20℃ are recommended to better investigate temperature effects. Additionally, since the empirical model suggests that each single-particle test is reasonably representative of individual ice failure events during a multi-particle test, additional single-particle tests are recommended to better understand

the effects of particle shape, size, and other factors related to the particle indentation. Finally, it is recommended that more testing with both single and multiple particles be competed with the imposition of horizontal motion and combined loading in order to more realistically understand the failure mechanics associated with all aspects of realistic ice feature scouring. It is recommended that these expanded test results may then be used to improve the empirical set and serve to provide more avenues for analysis and comparison. This expanded model would prove to be a useful tool for simulating realistic results for rock indentation into ice features, and their associated failure forces, for a wider range of conditions. Considering this, additional work is recommended to expand the model further in order to use previously simulated and present empirical data to predict an approximation for how the failure would progress past the observed indentation depth. This estimated failure trend would inform the types of peak forces or pressures that could be observed in tests completed at larger indentation depths and serve as another valuable comparison case for future testing programs. Preliminary results from indentation experiments for both single and multiple particles suggest that the rock particles appear to serve as stress concentrators that promote local failure of the ice at pressures below those reported in the literature for ice-structure interactions with steel structures. Additional research is needed to further explore this topic and better understand the associated mechanics. The question of how these embedded particles may affect the failure mechanics of contact between an ice feature and subsea pipeline or structure remains; these observed pressures are recommended to be used to guide deeper analysis of failure stresses and interaction effects with subsea structures. The implementation of Finite Element Analysis is recommended to fully investigate these interactions. Through continued development, this work can help inform future research on the nature of subsea interactions of icebergs with the ocean floor and how this may affect potential risks related to subsea installations.

Bibliography

American Petroleum Institute. (2018). *API 5L.* American Petroleum Institute.

Barrette, P. (2011). Offshore pipeline protection against seabed gouging by ice: An overview. *Cold Regions Science and Technology. Volume 69, Issue 1.*, 3-20.

Barrette, P., & Timco, G. (2009). Sliding resistance of grounded ice on clay in a laboratory: Potential implications for offshore design. *Cold Regions Science and Technology, Volume 58, Issues 1–2*, 1-14.

Barrette, P., Pond, J., & Jordaan, I. (2002). Ice damage and layer formation in small scale indentation experiments. *Ice in the Environment, Proceedings of the 16th internation Symposium on Ice, IAHR*, *3*, pp. 246-253. Dunedin, New Zealand.

Barrette., P., Timco, G. W., Palmer, A., & . (2008). Laboratory study on the sliding resistance of level ice and rubble on sand. *Cold Regions Science and Technology Volume 54, Issue 2*, 73-82.

Bridgman, P. V. (1912). Water in the liquid and five solid forms, under pressure. *ArtsSci., Proc.*(47), 441-558.

Browne, T. (2012). *Analysis of Compressive Ice Failure during Ice-structure Interaction.* St. John's: Memorial University of Newfoundland.

Browne, T., Taylor, R., Jordaan, I., & Gürtner, A. (2013). Small-scale indentation tests with variable sturctural compliance. *Cold regions science and technology*(88), 2-9.

Cammaert, A. B., & Muggeridge, D. B. (1988). *Ice interaction with offshore structures. Van Nostrand Reinhold.*

Dillenburg, A. K. (2012). *Rate dependency in conical ice indenter failure.* University of Duisburg-Essen, Institute of Ship Technology, Ocean Engineering and Transport Systems.

Duval, P., Ashby, M., & Anderman, I. (1983). Rate-controlling processes in the creep of polycrystalline ice. *J Phys. Chem.*(87), 4066-4074.

Frederking, R., Jordaan, I., & McCallum, J. (1990). Field tests of ice indentation at medium scale: Hobson's Choice ice island 1989. *Proceedings of 10th International Symposium on Ice, IAHR' 90*, (pp. Vol. 2, pp. 931-944). Espoo, Finland.

Geonautics. (1989). Regional Ice Scour Data Base Studies. *Environmental Studies Research Funds, Report No. 105*, J68 pp.

Habib, B. K. (2014). *Experimental Investigation of Compressive Failure of Truncated Conical Ice Specimens.* St. John's: Memorial University of Newfoundland, Faculty of Engineering and Applied Science. .

Hallam, S., & Ashby, M. (1986). The failure of brittle solids containing small cracks under compressive stress states. *Acta Metallurgica, Volume 34*, 497-510.

Hobbs, P. (1974). *Ice Physics.* Oxford: Clarendon Press.

ISO 19906. (2019). *Petroleum and natural gas industries - Arctic offshore structures, Internationad Organization for Standardization.* ISO.

Jordaan, I. (2001). Mechanics of ice-structure interaction. *Engineering Fracture Mechanics, 68*, 1923-1960.

Jordaan, I., Li, C., Sudom, D., Stuckey, P., & Freeman, R. (2005). PRINCIPLES FOR LOCAL AND GLOBAL ICE DESIGN USING PRESSURE- AREA RELATIONSHIPS. *Int.*

Conf. on Port and Ocean Eng. Under Arctic Conditions. I, pp. 375-386. Postdam: The National Academies of Sciences, Engineering, and Medicine.
Jordaan, I., Wells, J., Xiao, J., & Derradji-Aouat, A. (2008). Ice crushing and cyclic loading in compression. *Proceedings 19th IAHR Symposium on Ice.* Vancouver, British Columbia, Canada.: IAHR.
Jordaan., I. (2001). Mechanics of ice-structure interaction. *Engineering Fracture Mechanics, 68*, 1923-1960.
King, D. A. (2002). *Iceberg Scour Risk Analysis for Pipelines on The Labrador Shelf.* St. John's: Memorial University of Newfoundland, Faculty of Engineering and Applied Science.
Kollmeyer, R. (1977). West Greenland glaciers: iceberg sources. *Iceberg Utilization: Proceedings of the First International Conference* (pp. pp. 25-28). Ames, Iowa,: A.A. Husscіny (cd.).
Linch., L. D., Van Der Meer., J. J., Menzies., J., & . (2012). Micromorphology of iceberg scour in clays: Glacial Lake Agassiz, Manitoba, Canada. *Quaternary Science Reviews, Volume 55*, Pages 125-144.
Lockett, F. J. (1972). *Nonlinear Viscoelastic Solids.* London and New York.: Academic Press.
Means, W. D. (1983). Microstructure and micromotion in recrystallization flow of octachloropropane, a first look. *Geol. Rundscha*(72), 511-528.
Mellor, M. (1983). *Mechical behaviour of sea ice. CRREL Report 83-1.* U.S. Army Cold Region Research and Engineering Lab, Honover: CRREL.
Murray, J. (1969). The drift, deterioration and distribution of icebergs in the North Atlantic Ocean. *ClM Special Vol. 10, The Ice Seminar*, (pp. pp. 3-18).
Nadreau, J., & Michel, B. (1984). Ice properties in relation to ice forces. Proceedings of 2nd State-of-the-Art IAHR Working Group on Ice Forces. *IAHR.* Hamburg: IAHR.
Nordell, B. (1990). Measurement of P-T coexistencecurve for ice-water mixture. *Cold Regions Science and Technology*(19), 83-88.
Poirier, J. (1985). *Creep of crystals.* London: Cambridge University Press.
Poirier, J., & Guillope, M. (1979). Deformation induced recrystallization of minerals. *Bull. Mineral.*(102), 67-74.
Sanderson, T. (1988). *Ice mechanics: risks to offshore structures.* London: Graham & Trotman.
Schapery, R. (1997). Nonlinear viscoelastic and viscoplastic constitutive equations based on thermodynamics. *Mechanics of Time-Dependent Materials, Vol. 1* , 209- 240.
Schulson, E. M. (2001). Brittle Failure of Ice. *Engineering Fracture Mechanics 68*, 1839-1887.
Schulson, E. M., & Duval, P. (2009). Creep and fracture of ice. *Cambridge University Press*, 416.
Schulson, E. M., Lim, P. N., & Lee, R. W. (1984). A brittle to ductile transition in ice under tension.
Sinha. (1979). Grain boundary sliding in polycrystalline materials. *Phil. Mag. A, Vol. 40*, 825-842.
Sinha., N. (1989). Elasticity of natural types of polycrystalline ice. *Cold Regions Science and Technology 17*, 127–135.
Tammann, G. (1903). *A contribution to the science of phase changes.(Kristallisieren und Schmeltzen. Ein Beitrag zur Lehre der Änderungdes Aggregatzustande).* Leipzig.
Tammann, G. (1910). On the behavior of water at high pressure and low temperature (Über das Verhalten des Wassers bei hohen Drucken und tiefern Temperaturen. *Z. Phys. Chem.*(72), 609-630.

Taylor, R. S., & Richard, M. (2014). Development of a probabilistic ice load model based on empirical descriptions of high pressure zone attributes. *International Conference on Offshore Mechanics and Arctic Engineering. 45561*, p. V010T07A049. American Society of Mechanical Engineers.

Taylor, R., Frederking, R., & Jordaan, I. J. (2008). The nature of high-pressure zones in compressive ice failure. *Proceedings 19th IAHR Symposium on Ice.* Vancouver, British Columbia, Canada.: IAHR.

Taylor, R., Frederking, R., Jordaan, I. J., & . (2008). The nature of high-pressure zones in compressive ice failure. *Proceedings 19th IAHR Symposium on Ice.* Vancouver, British Columbia, Canada.: IAHR.

Taylor., R. (2010). *Analysis of Scale Effect in Compressive Ice Failure and Implications for Design.* St. John's: Memorial University.

Urai, J. L., Means, W. D., Lister, G. S., Hobbs, B., & Heard, H. W. (1986). Dynamic Recrystallization of Minerals. In *Mineral and Rock Deformation* (pp. p.161-199). Washington, D. C:: American Geophysical Union.

Vernon, R. H. (1981). Optical microstructure of partly recrystallized calcite in some naturally deformed marbles. *Tectonophysic*(72), 601-612.

Wells, J., Jordaan, I., Derradji-Aouat, A., & Taylor, R. (2011). Small-scale laboratory experiments on the indentation failure of polucrystalline ice in compression: Main results and pressure distribution. *Cold Regions Science and Technology, 65*(3), 314-325.

Woodworth-Lynas, C. (1992). *The Geology of Ice Scour.* University of Wales.

APPENDIX A – Additional Single Particle Test Results: Total Load and Pressure, Images Taken After Indentation.

0.01 mm/s

2021_13_07_(1)-96-0.01

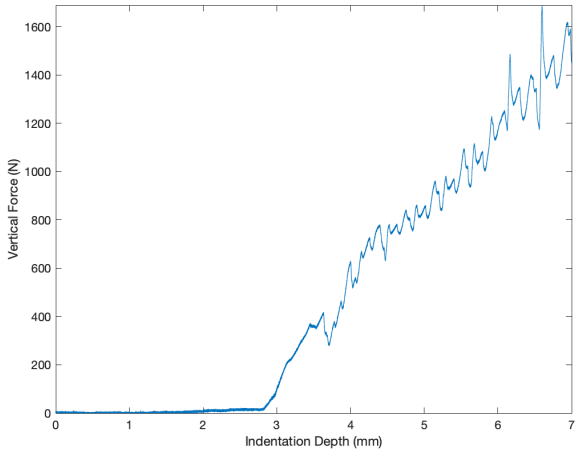

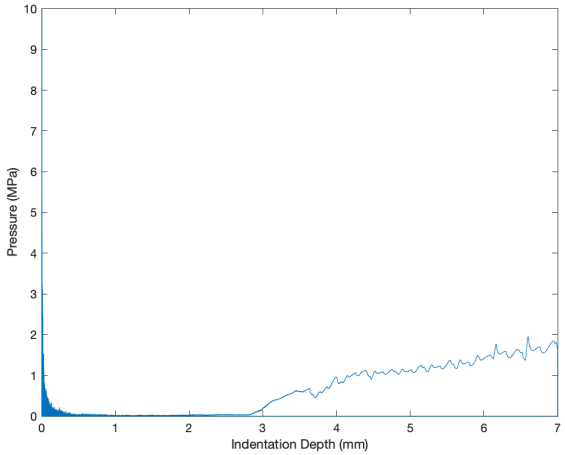

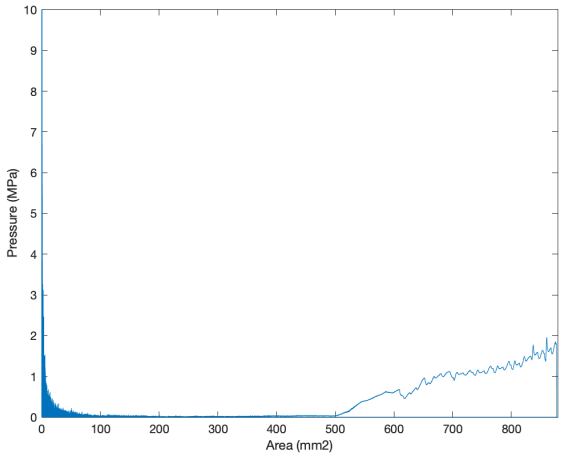

Upper Ice Surface

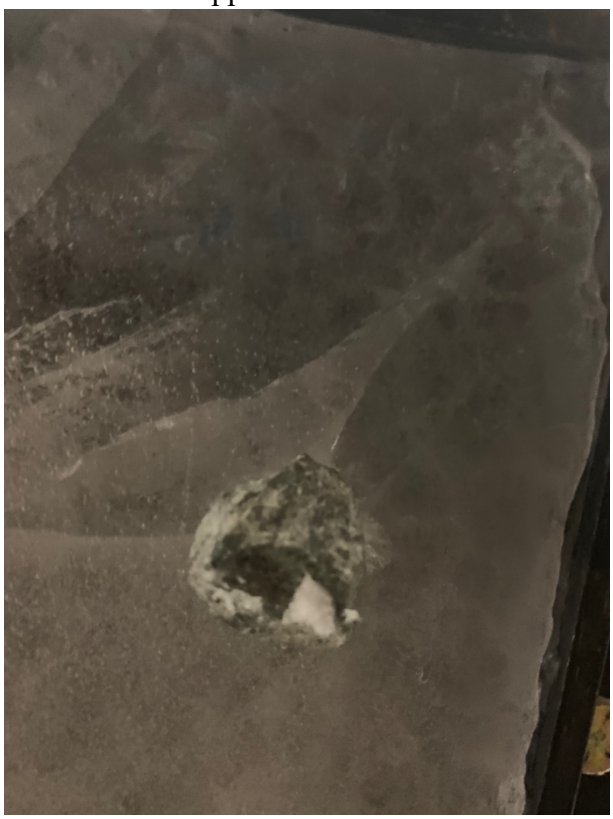

Lower Ice Surface

2021_13_07_(2)-65-0.01

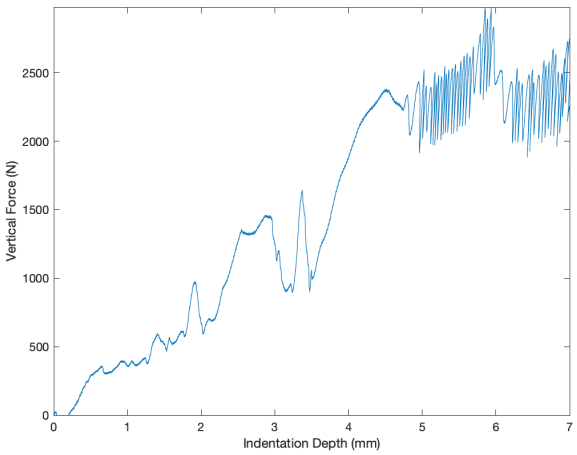

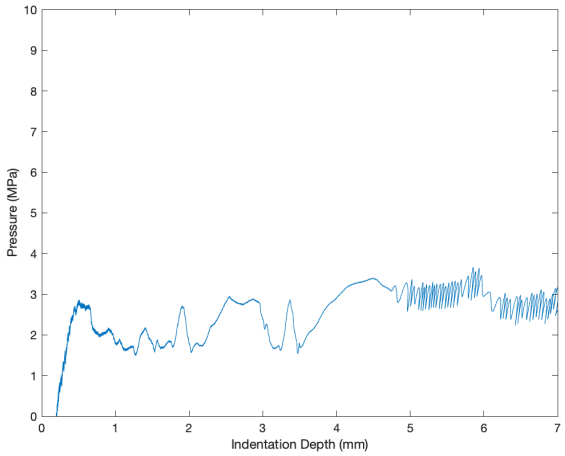

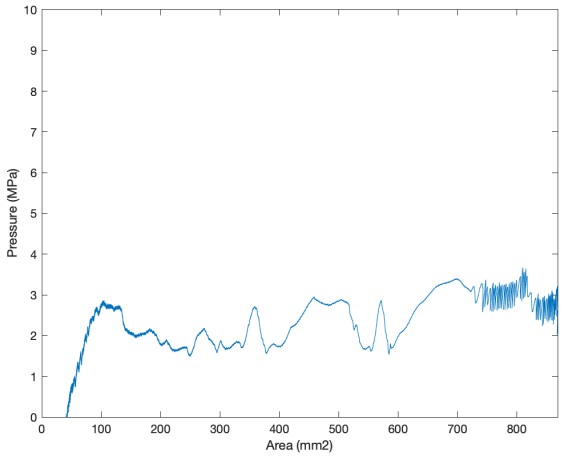

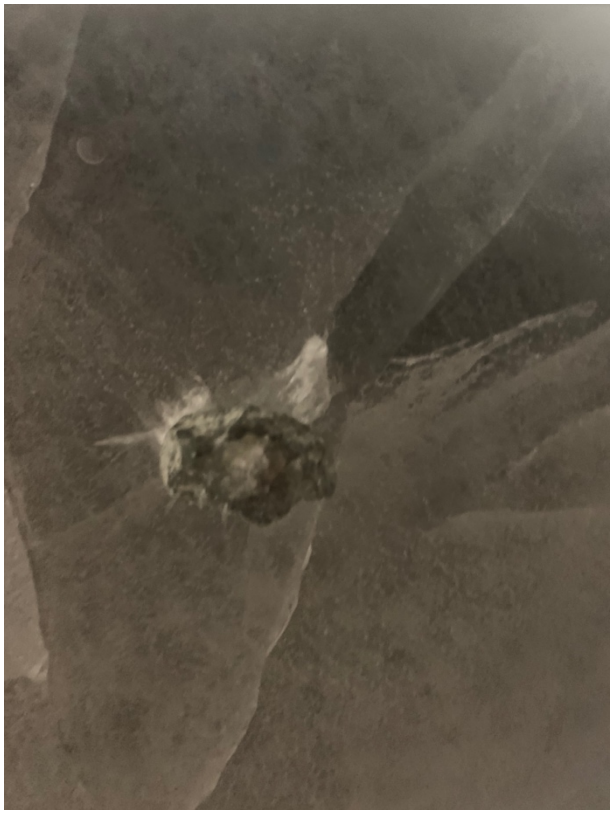

2021_13_07_(3)-26-0.01

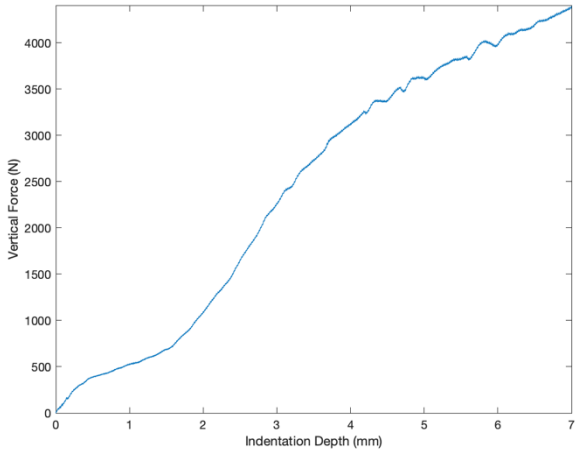

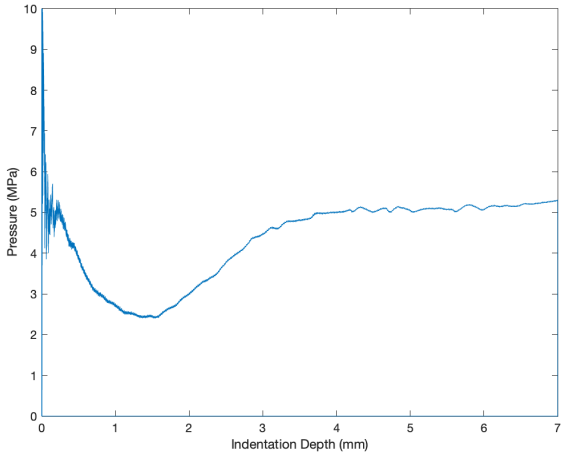

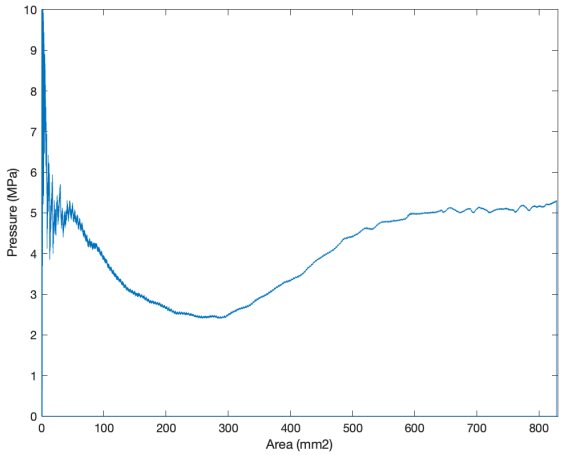

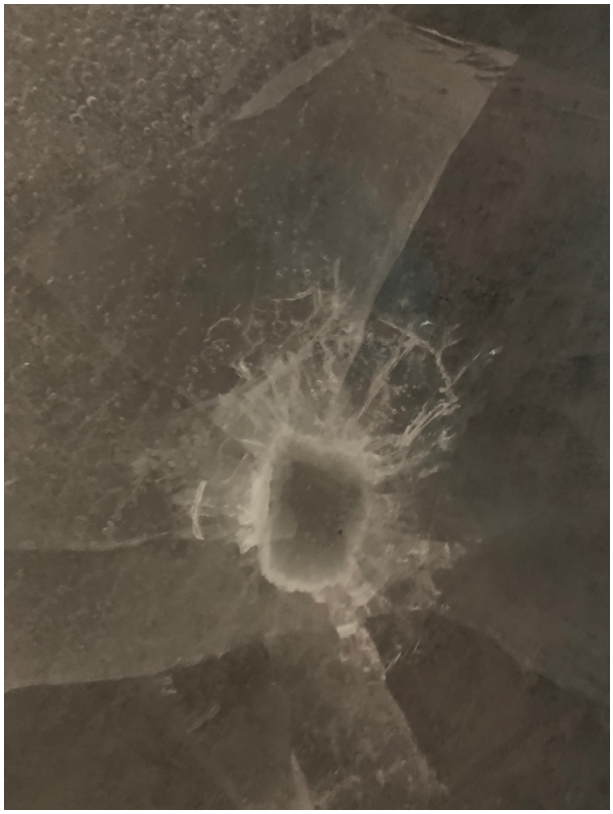

2021_13_07_(4)-96-0.01

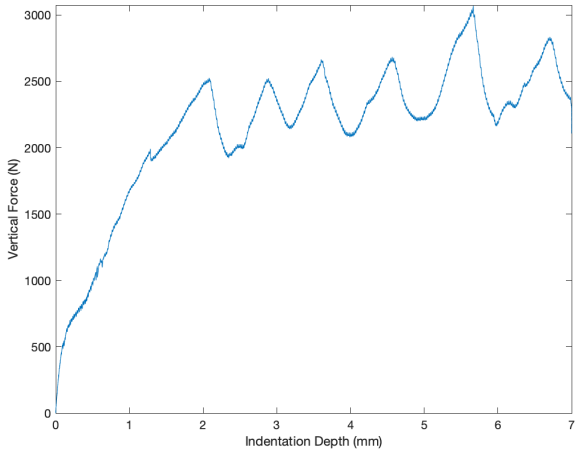

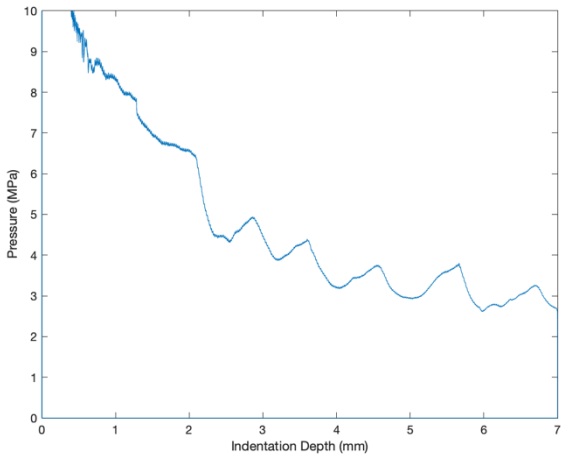

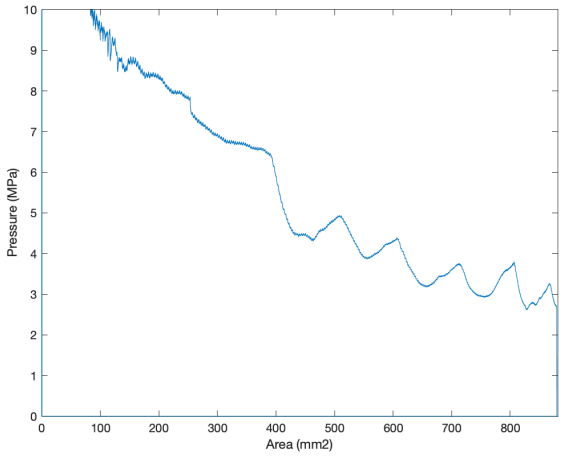

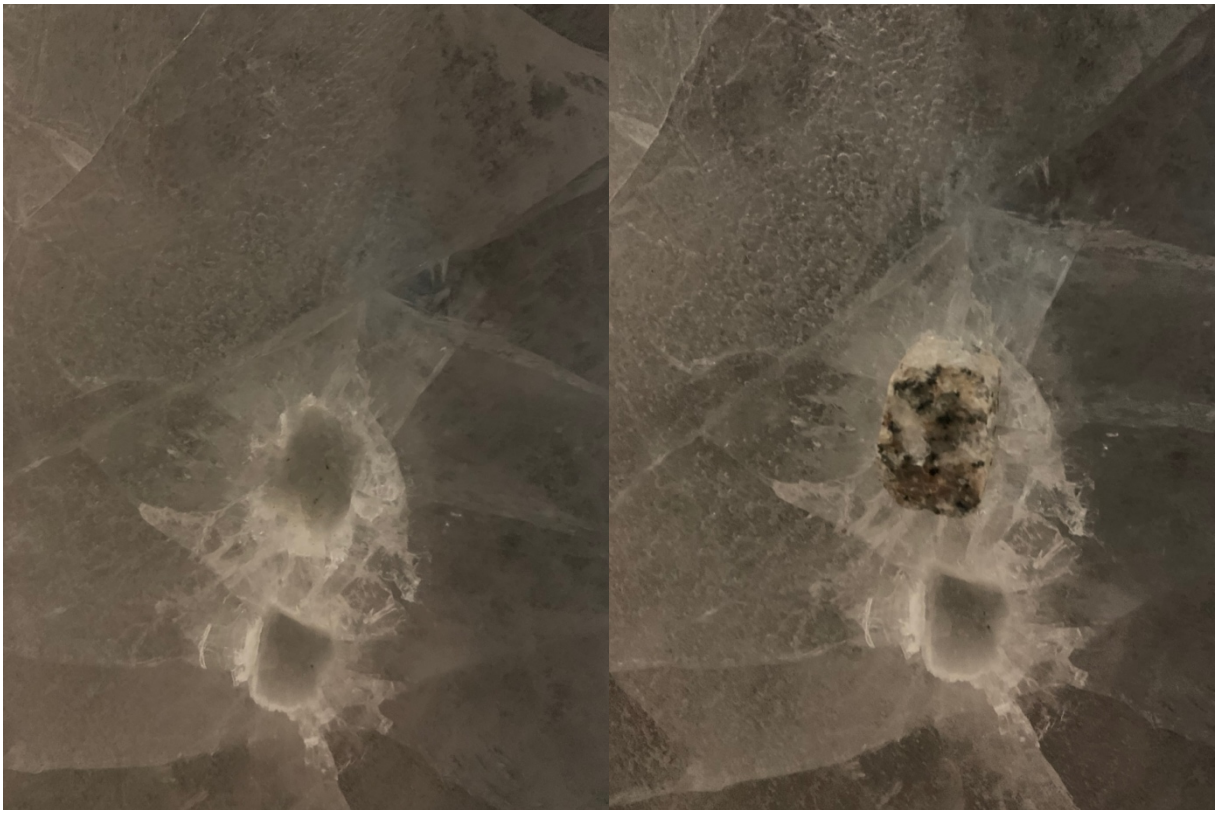

Lower ice image omitted

2021_13_07_(5)-65-0.01

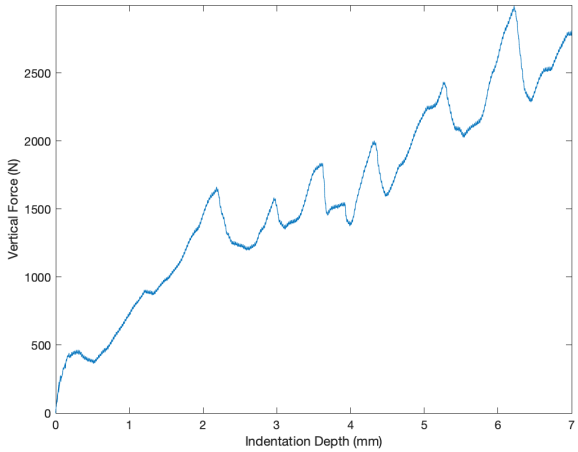

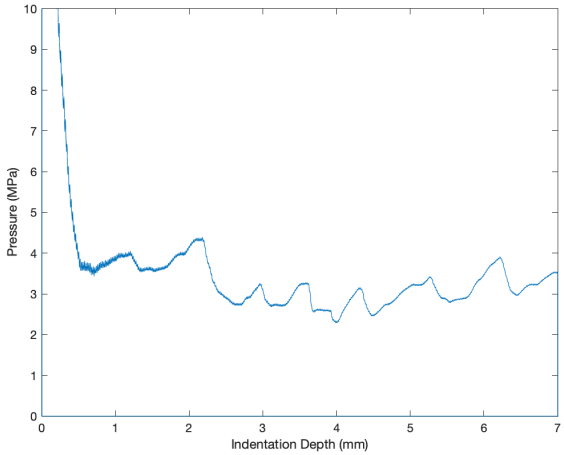

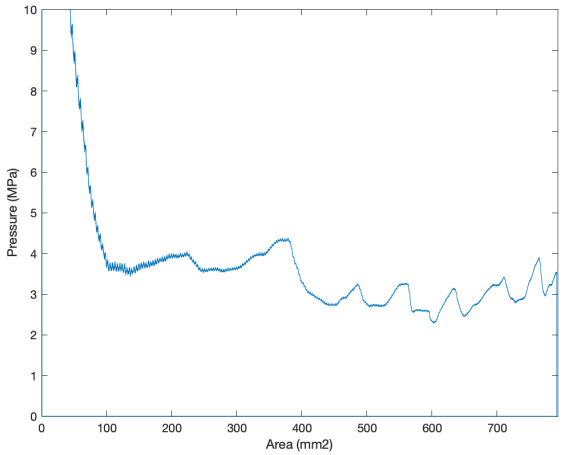

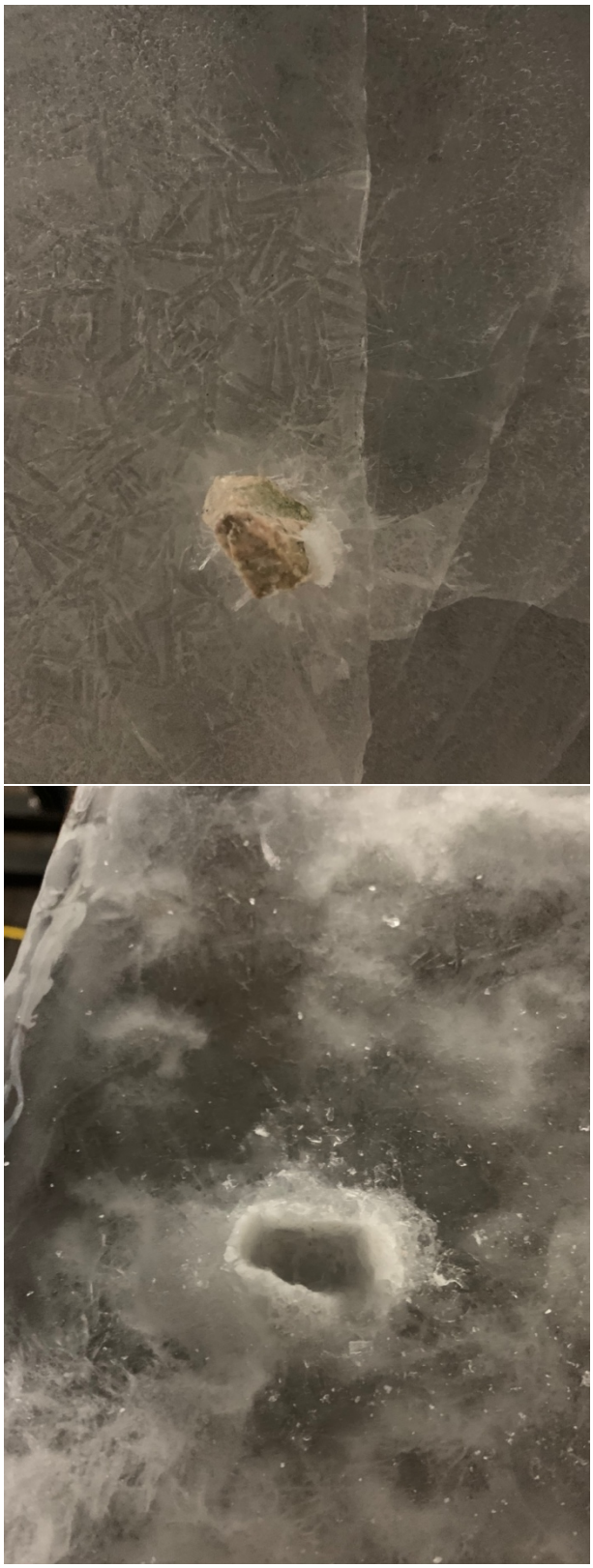

2021_13_07_(6)-26-0.01

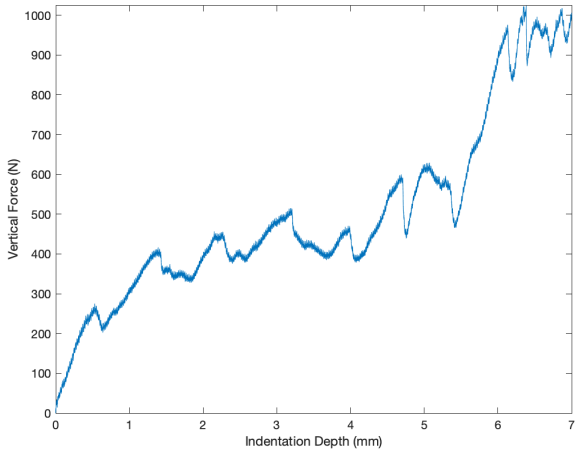

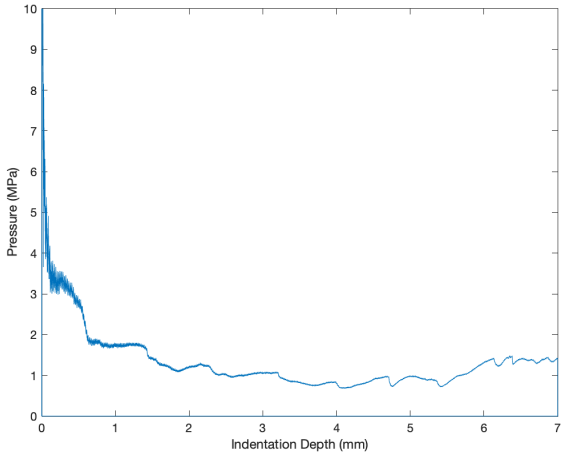

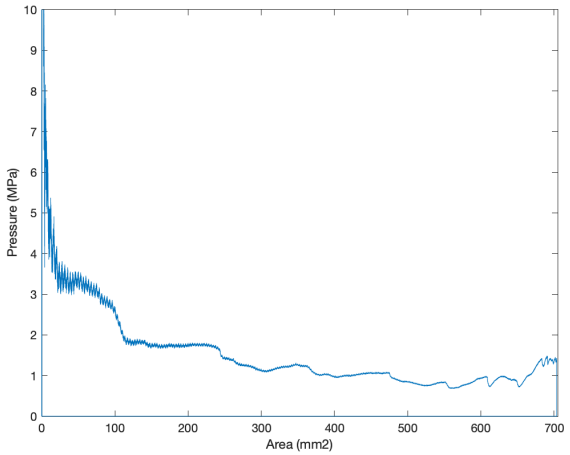

0.5 mm/s
2021_28_06_(1)-96-0.5

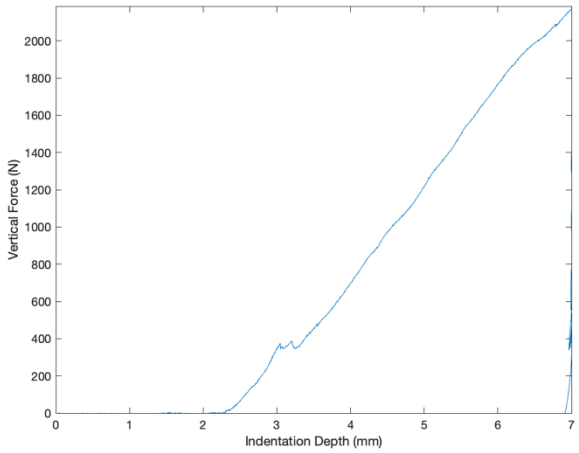

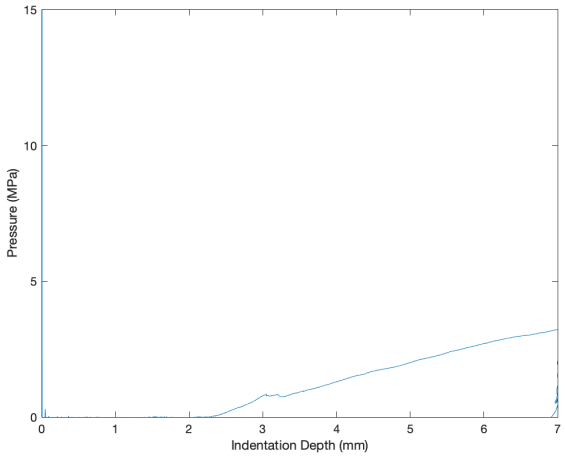

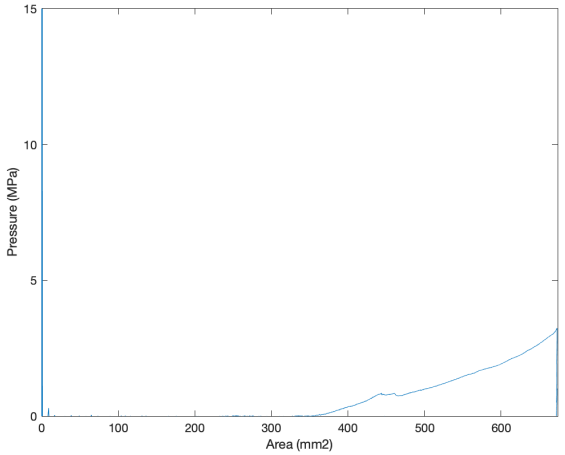

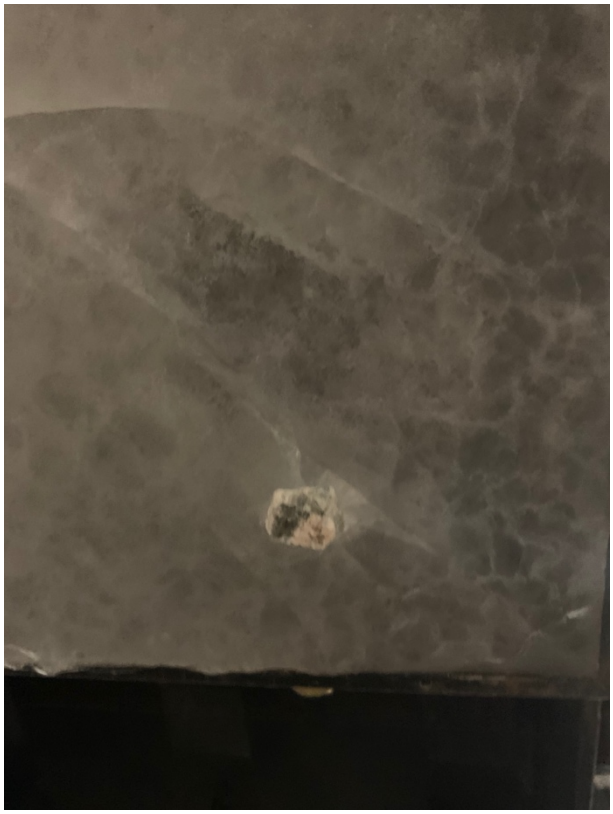

2021_28_06_(2)-96-0.5

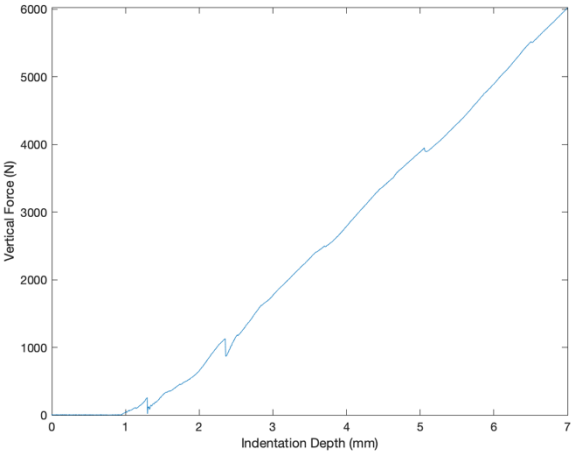

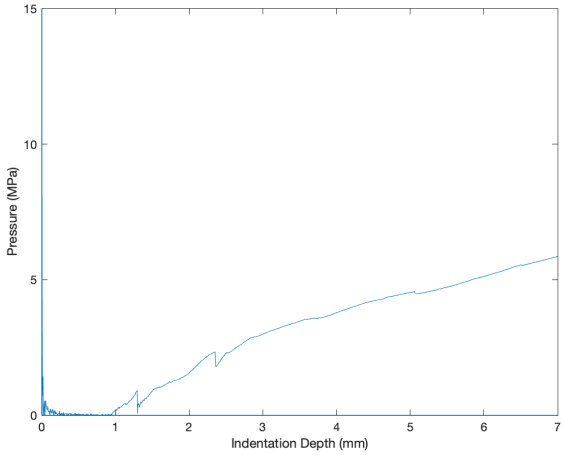

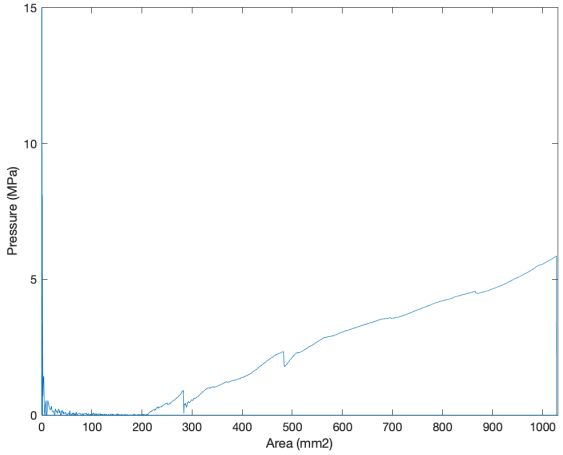

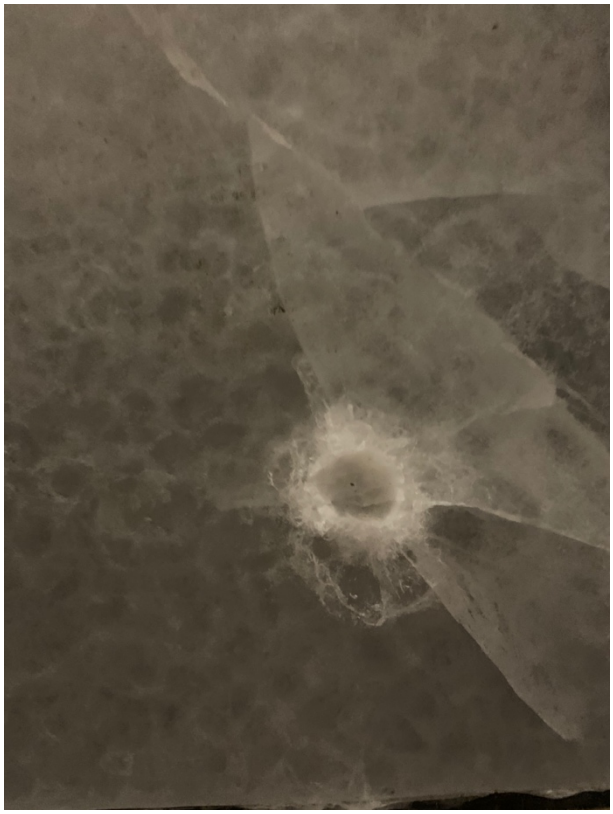

2021_28_06_(3)-96-0.5

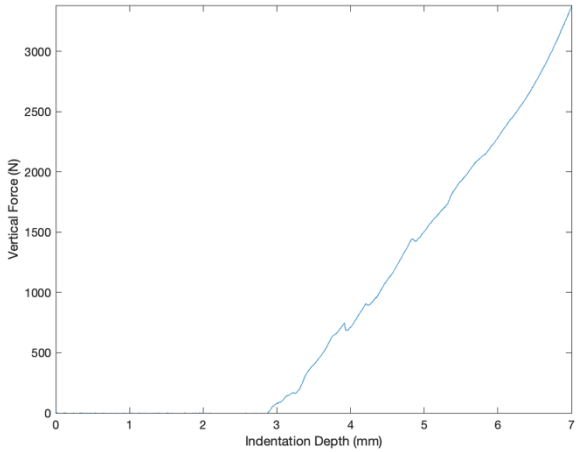

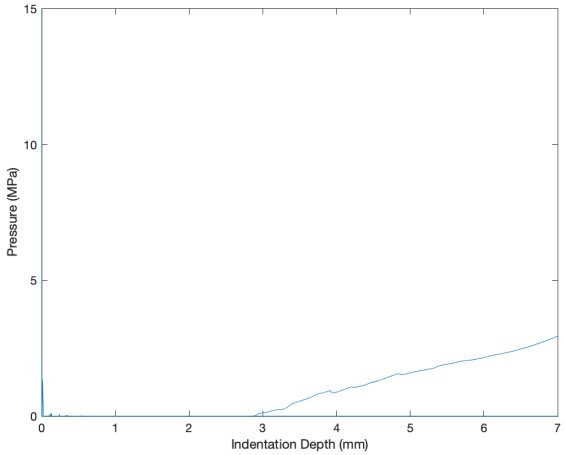

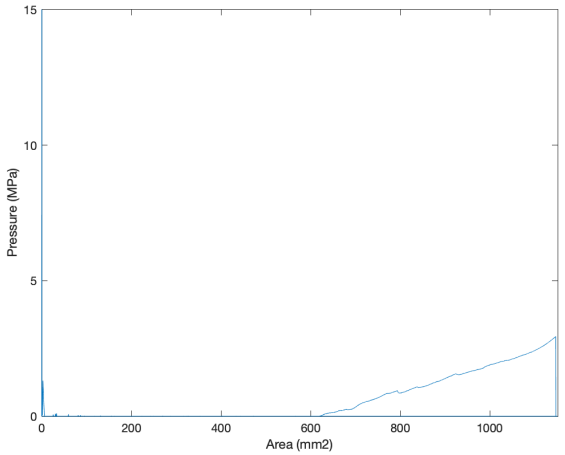

2021_28_06_(4)-96-0.5

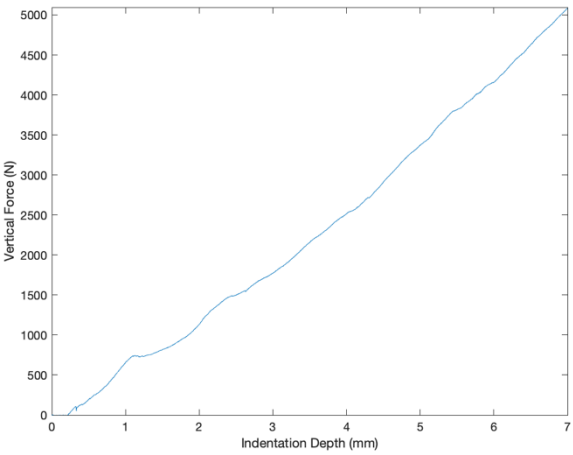

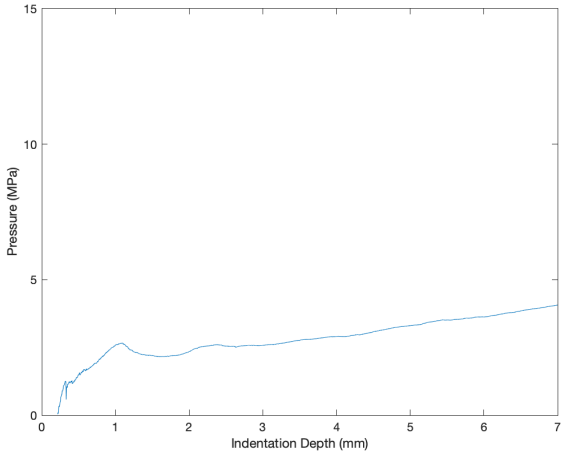

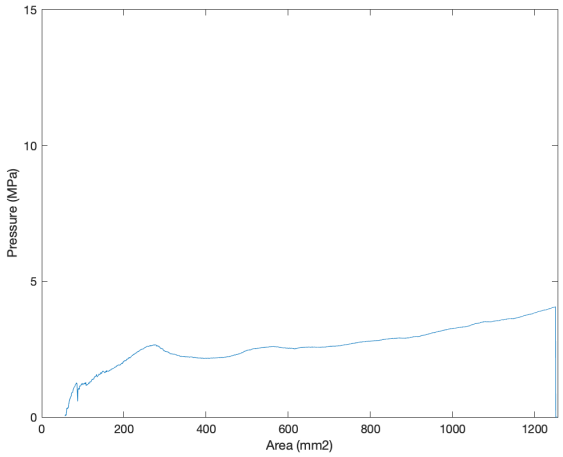

2021_28_06_(5)-96-0.5

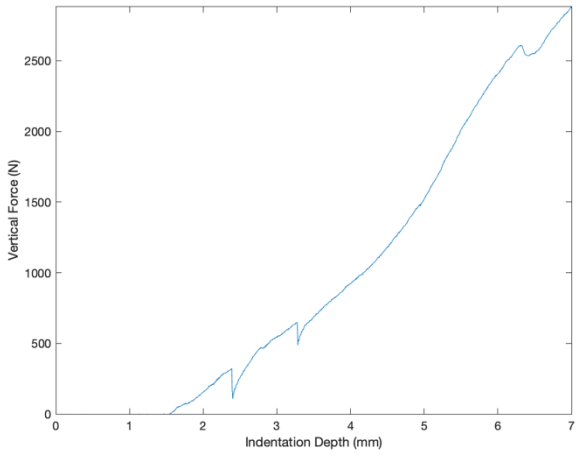

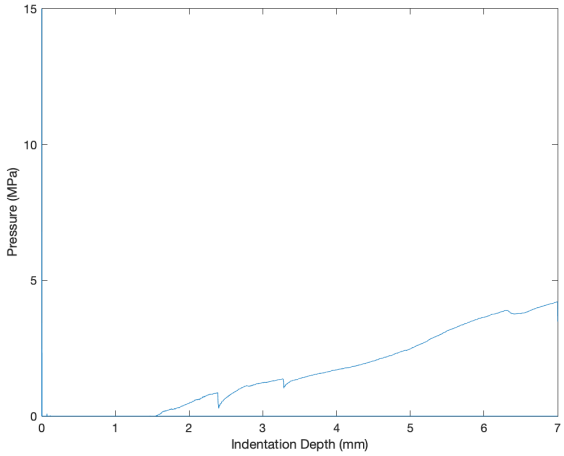

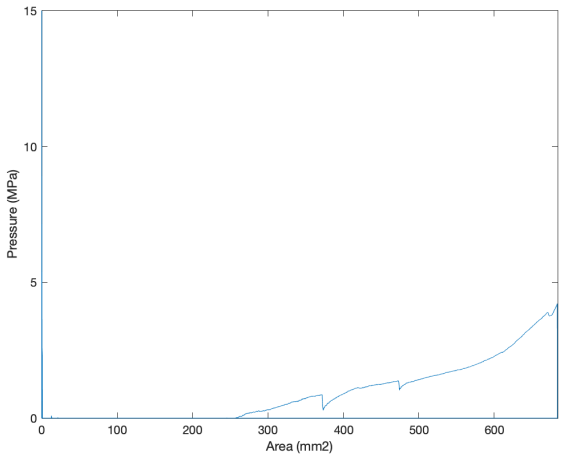

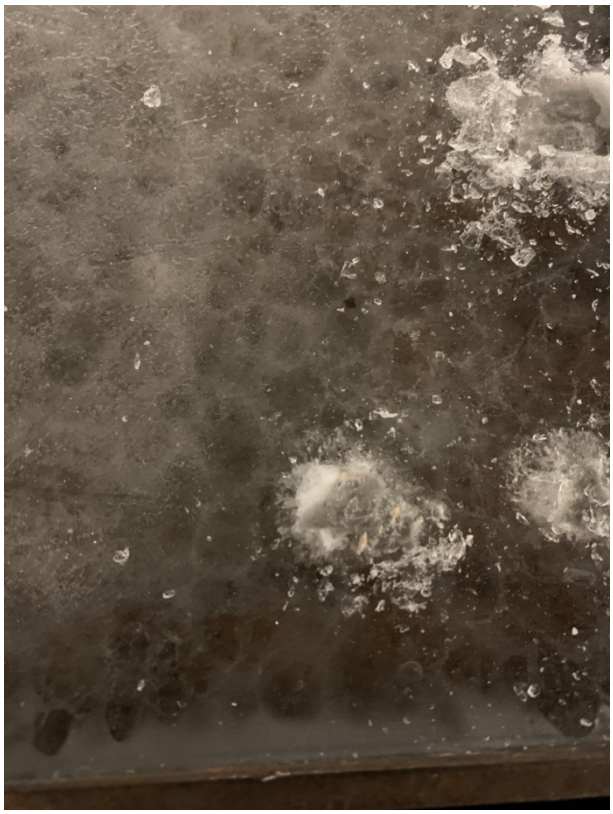

2021_28_06_(6)-96-0.5

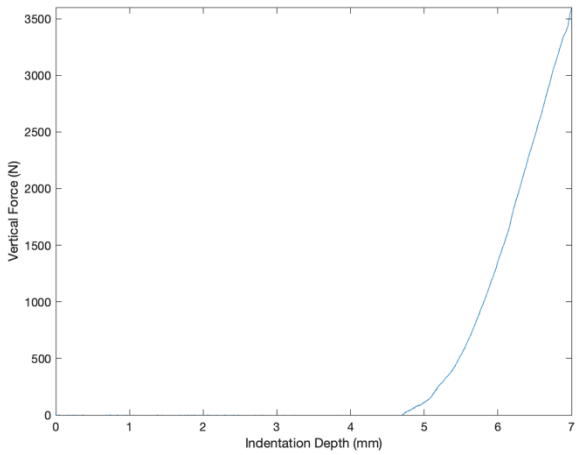

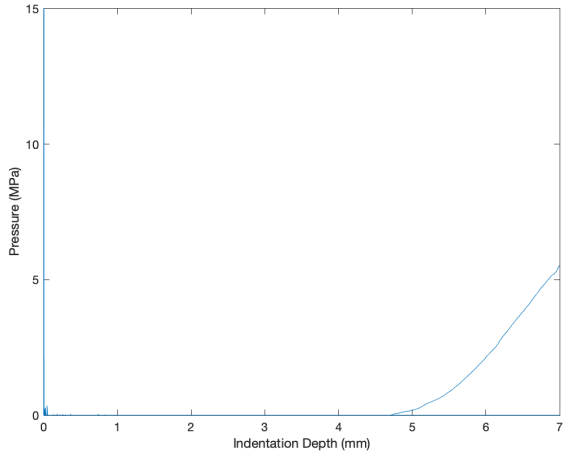

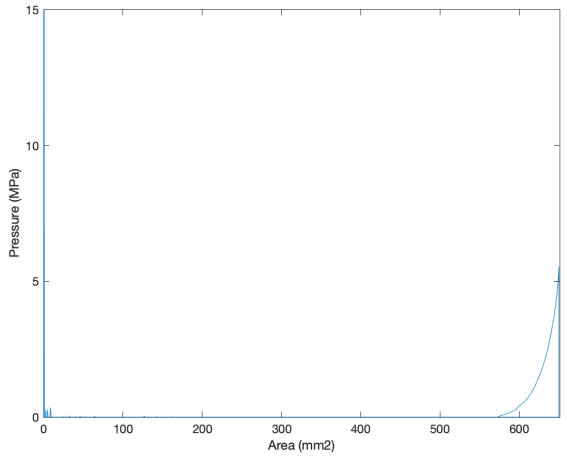

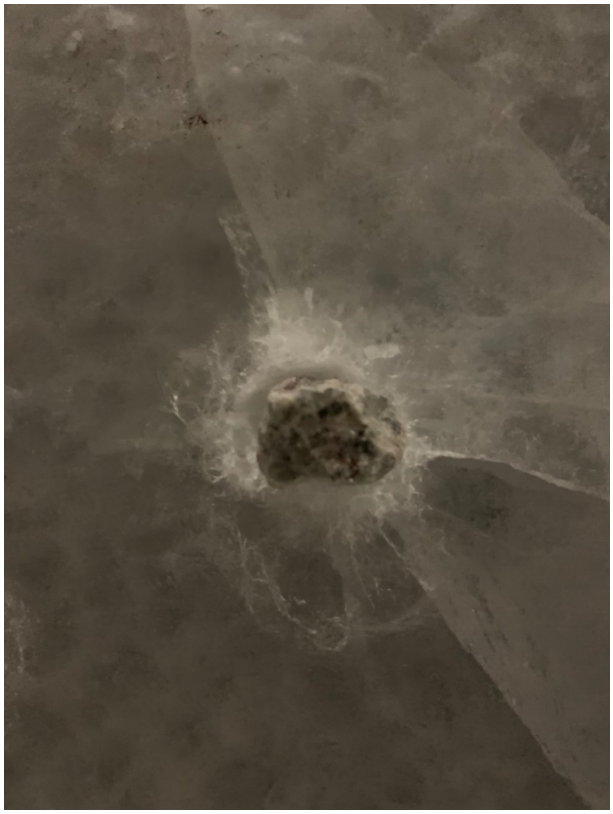

2021_28_06_(7)-96-0.5

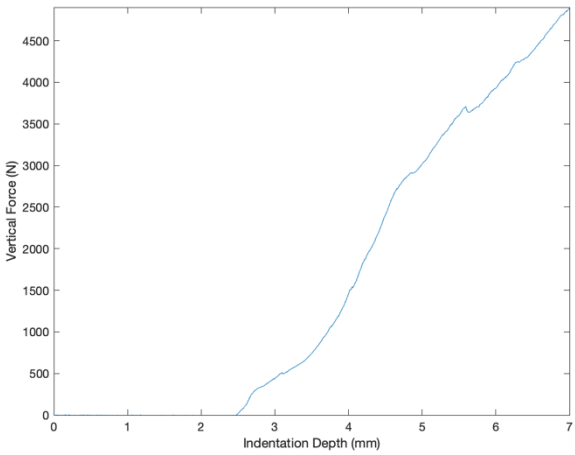

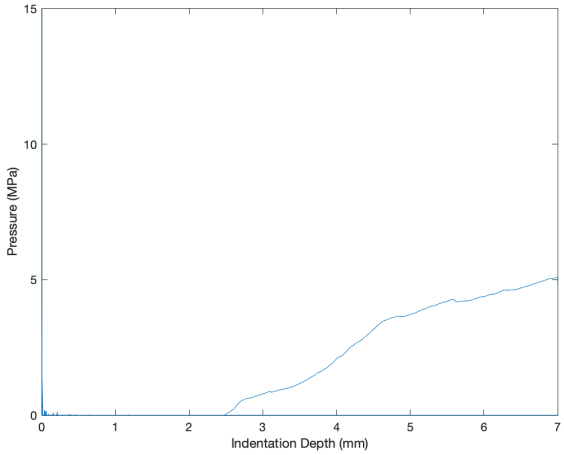

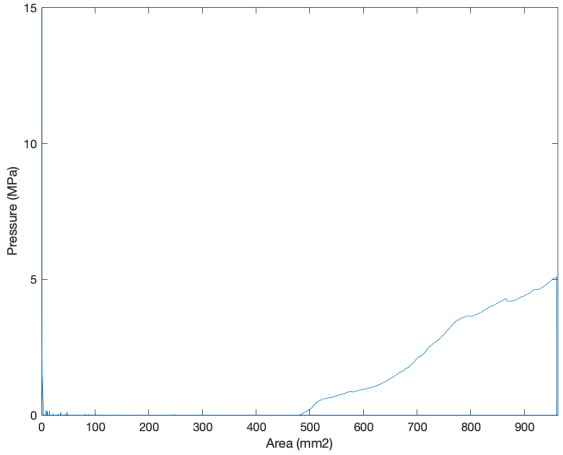

2021_28_06_(8)-96-0.5

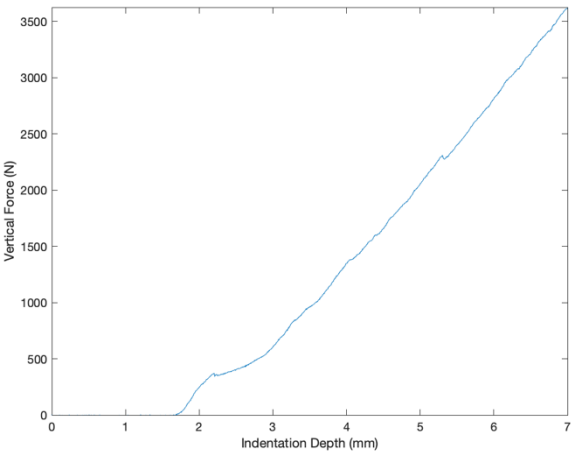

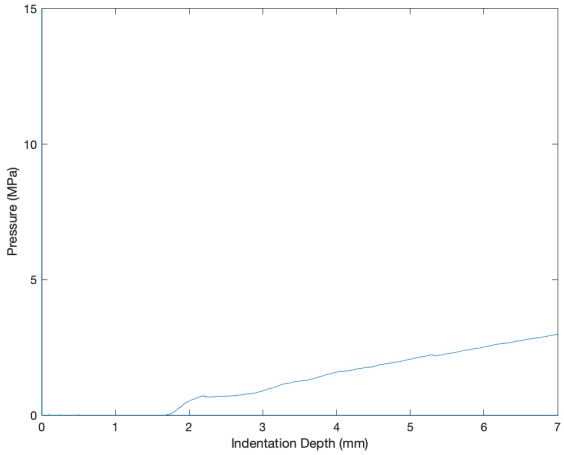

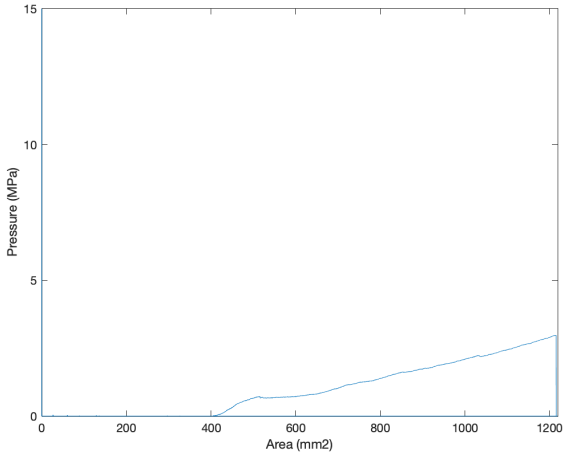

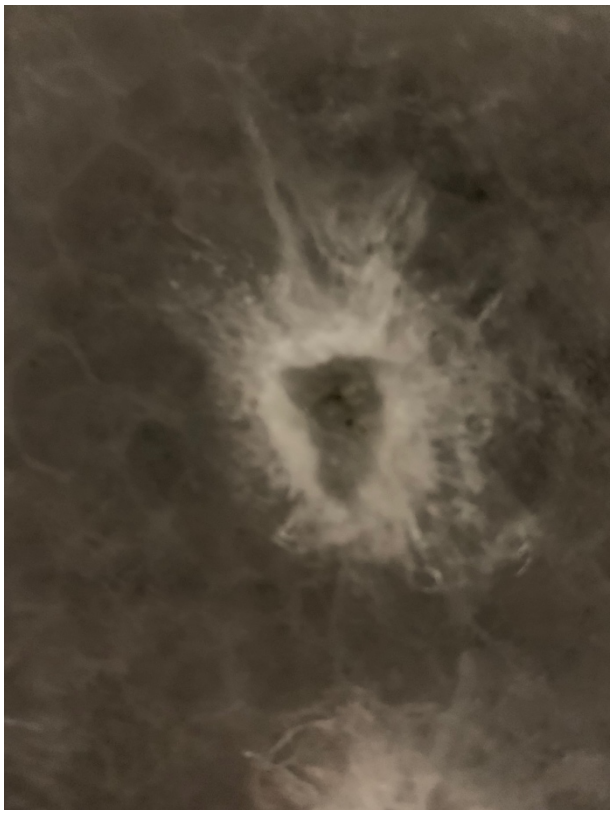

2021_28_06_(9)-96-0.5

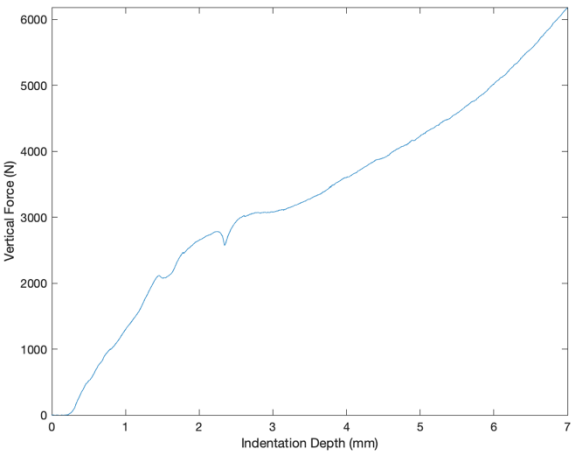

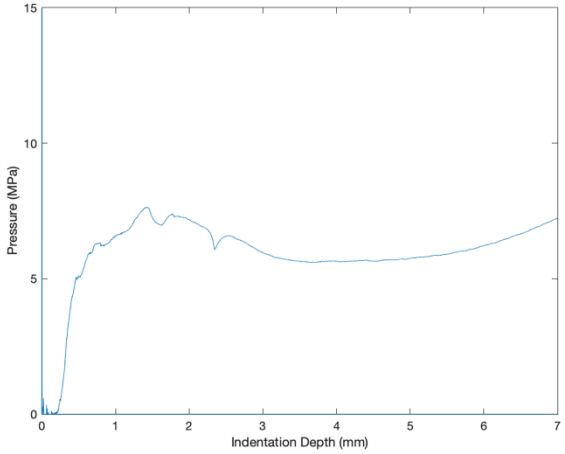

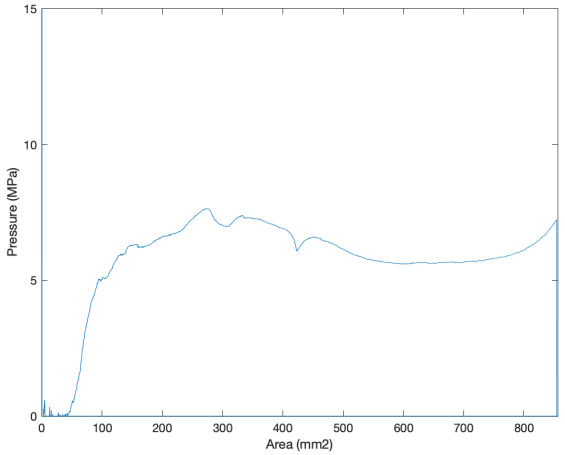

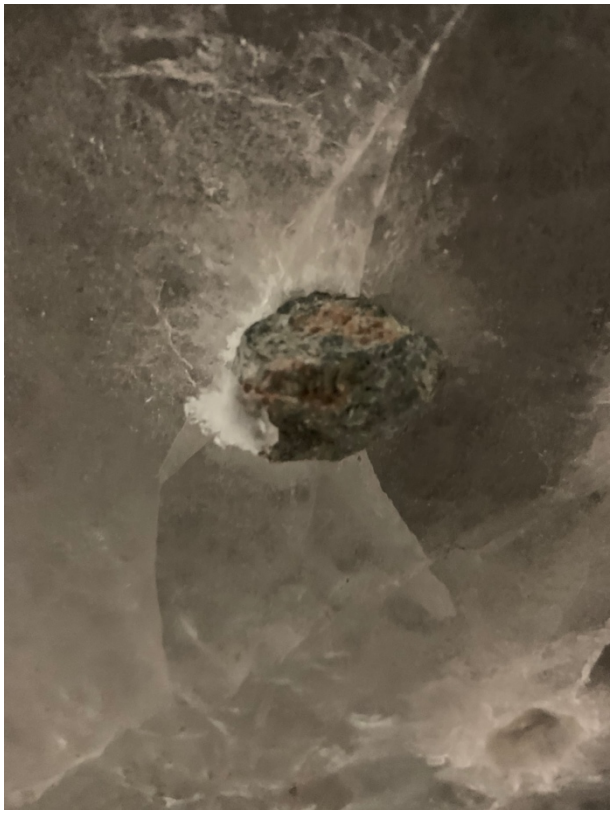

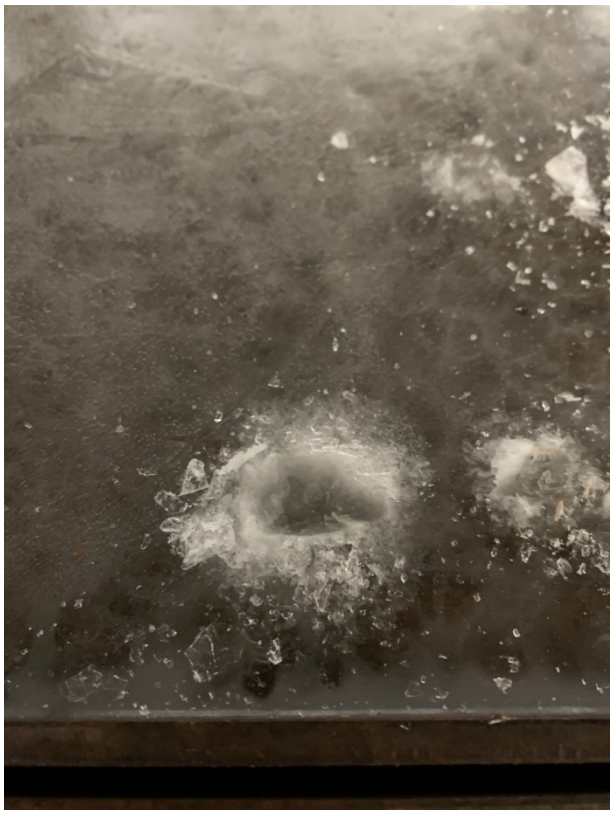

2021_28_06_(10)-96-0.5

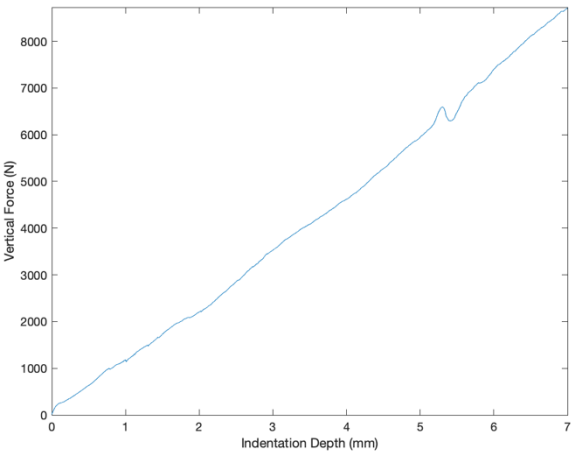

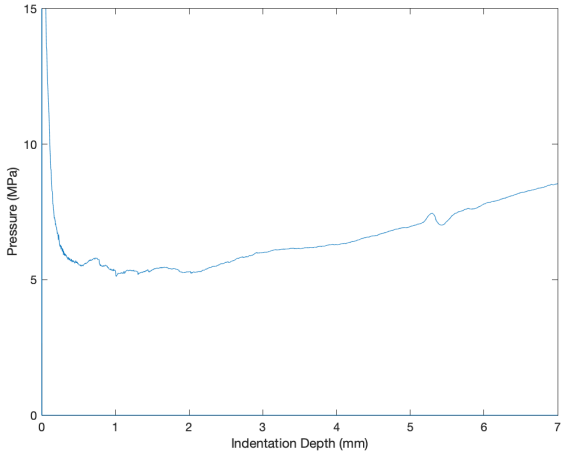

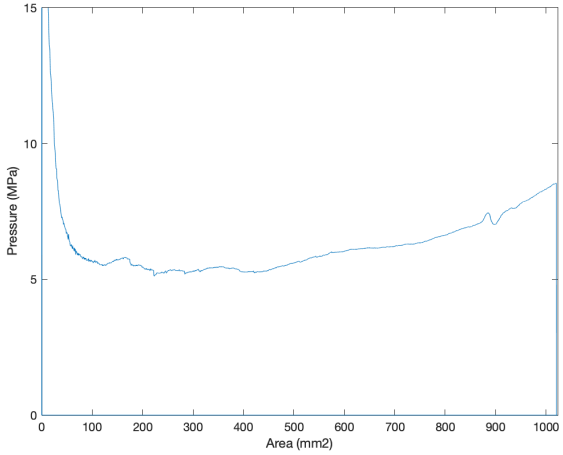

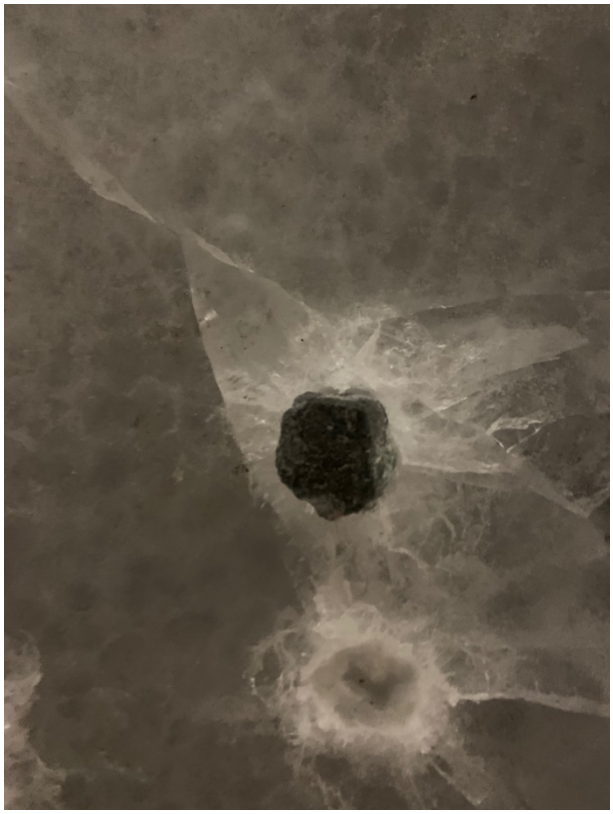

2021_28_06_(11)-65-0.5

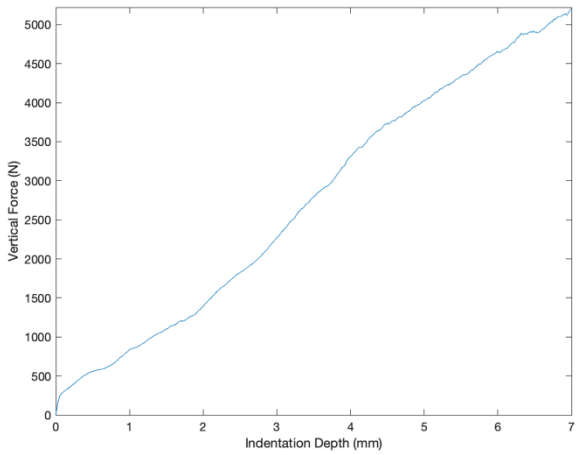

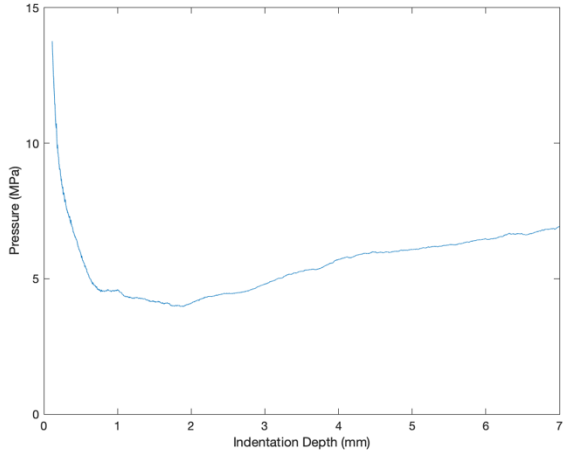

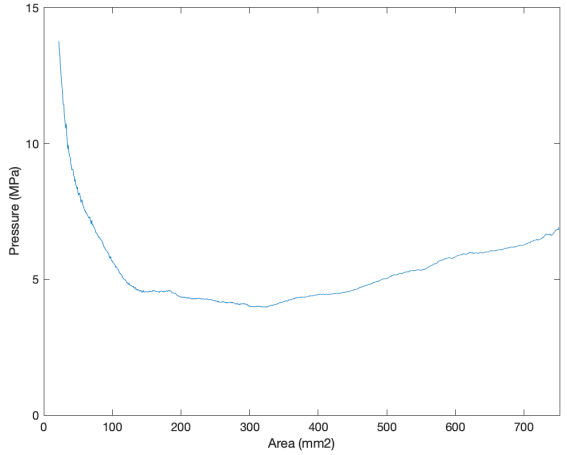

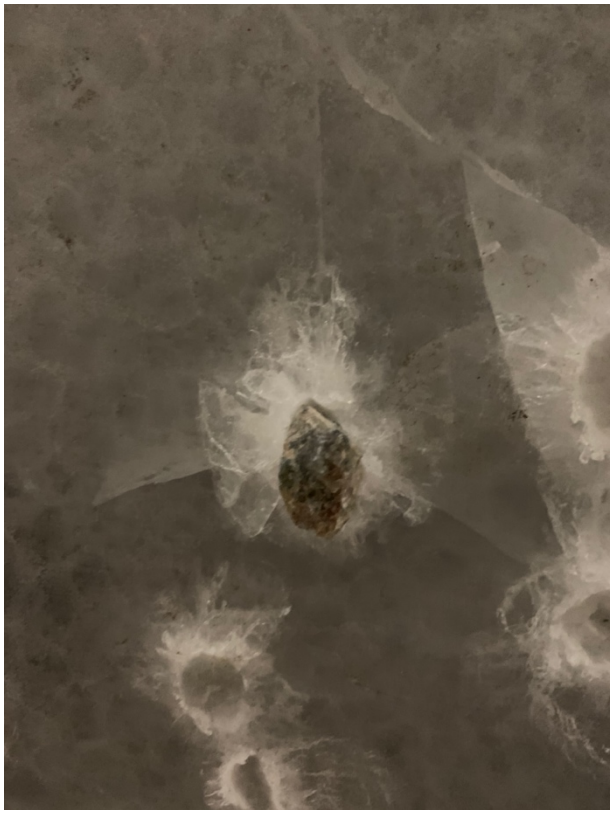

2021_28_06_(12)-65-0.5

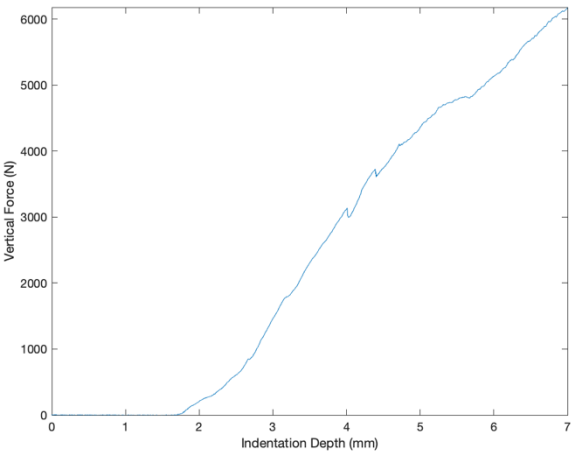

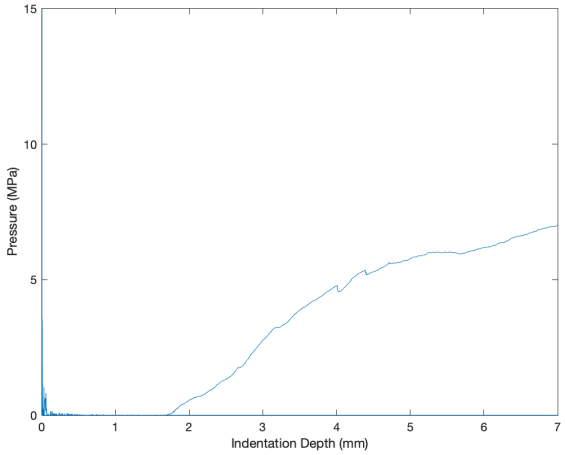

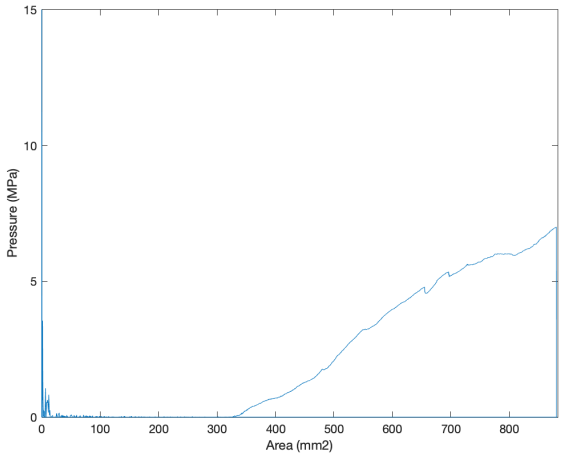

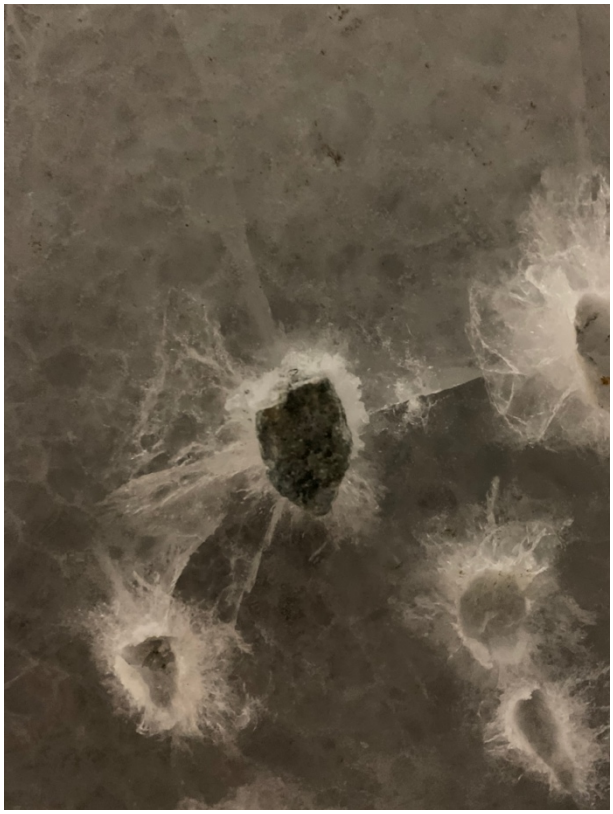

2021_28_06_(13)-65-0.5

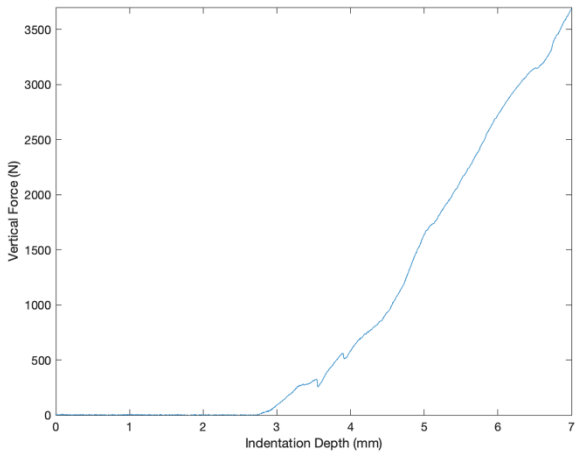

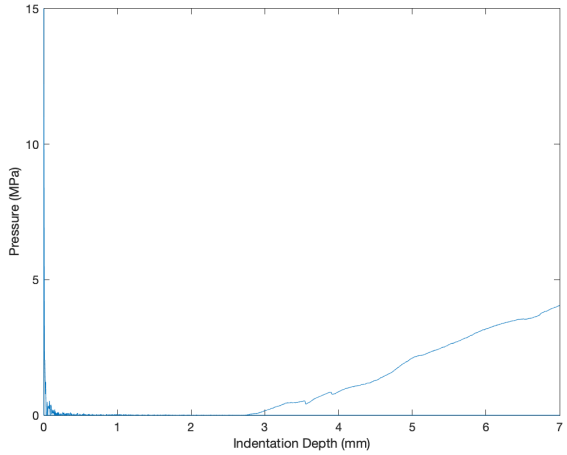

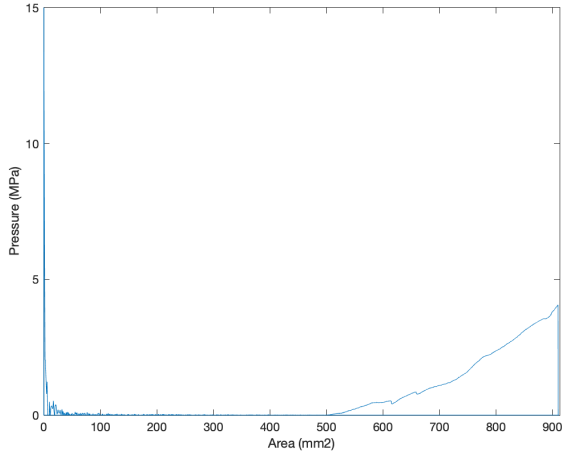

2021_28_06_(14)-65-0.5

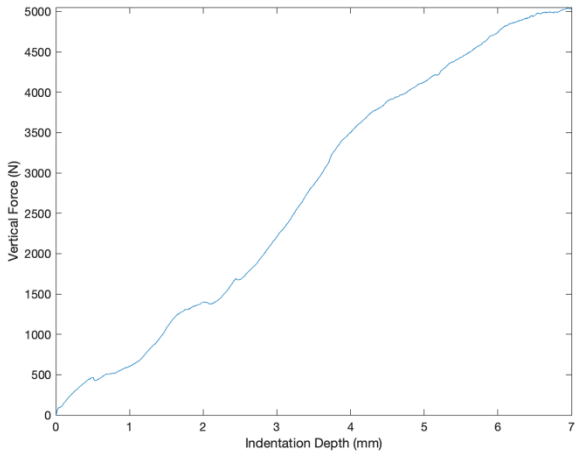

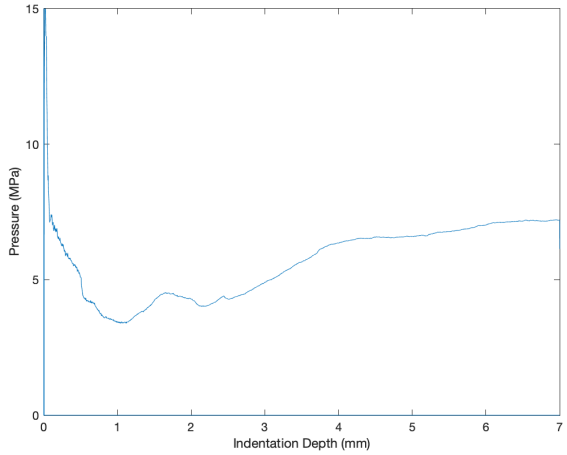

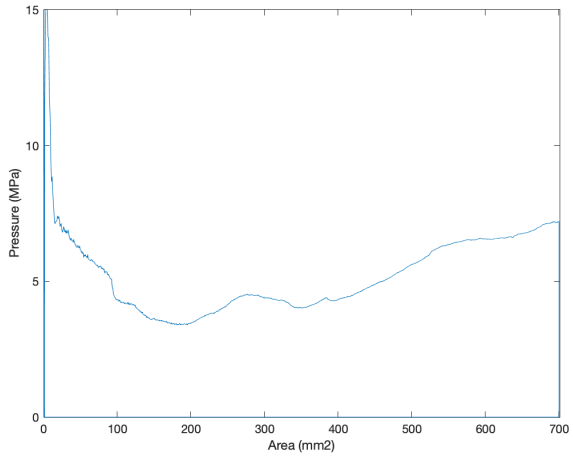

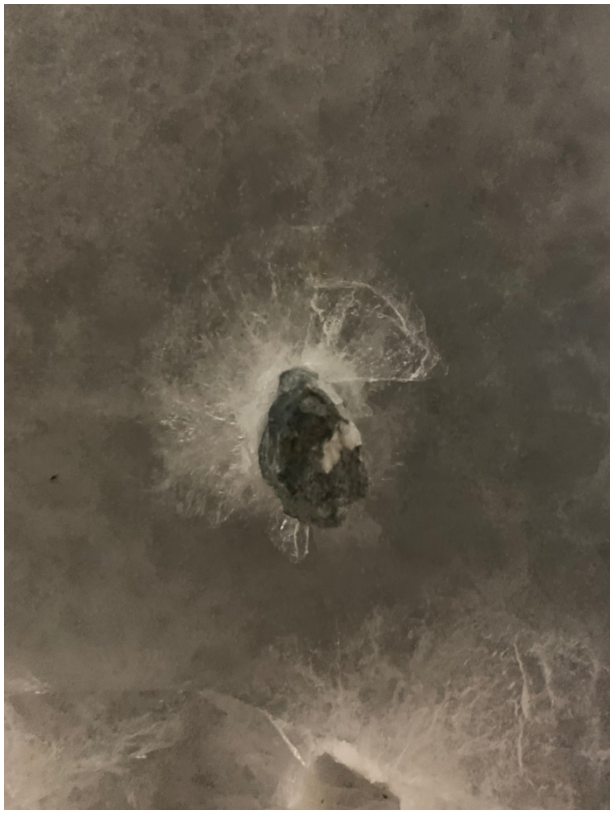

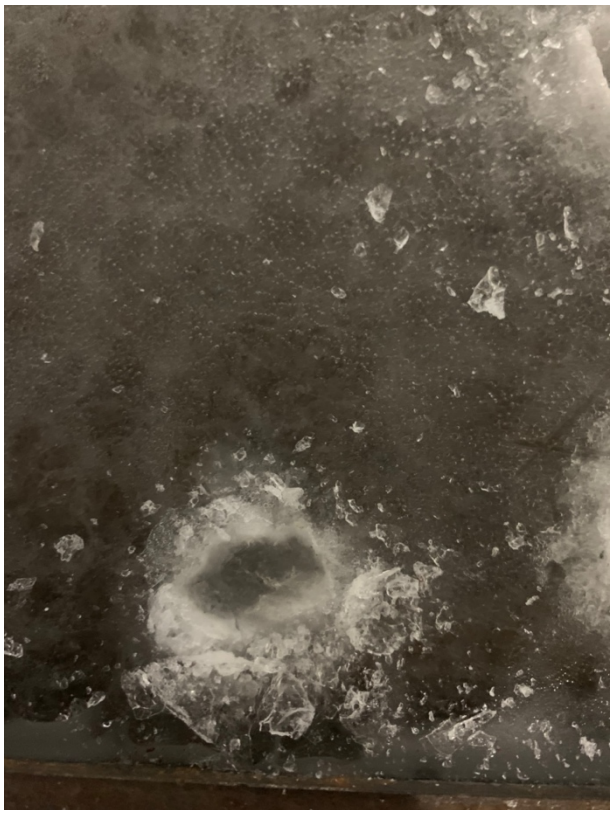

2021_28_06_(15)-65-0.5

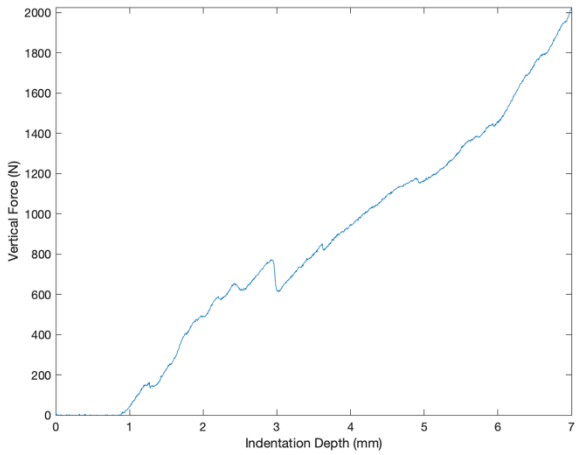

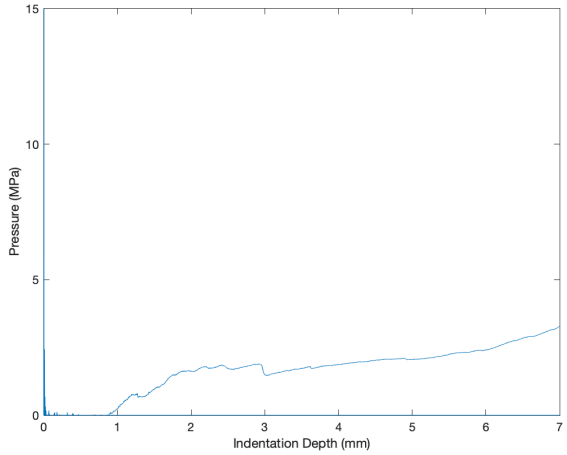

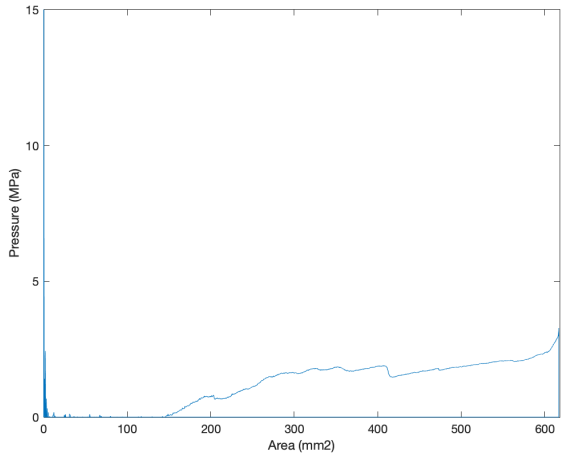

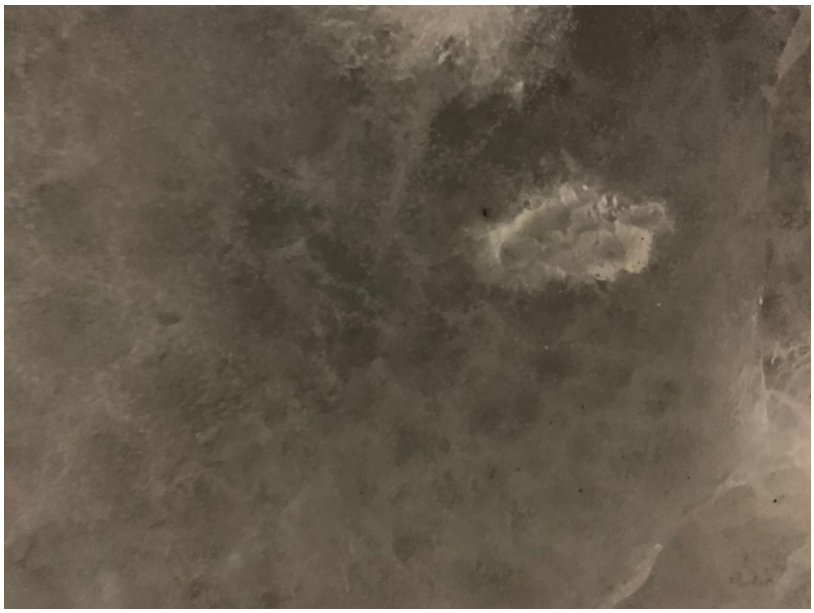

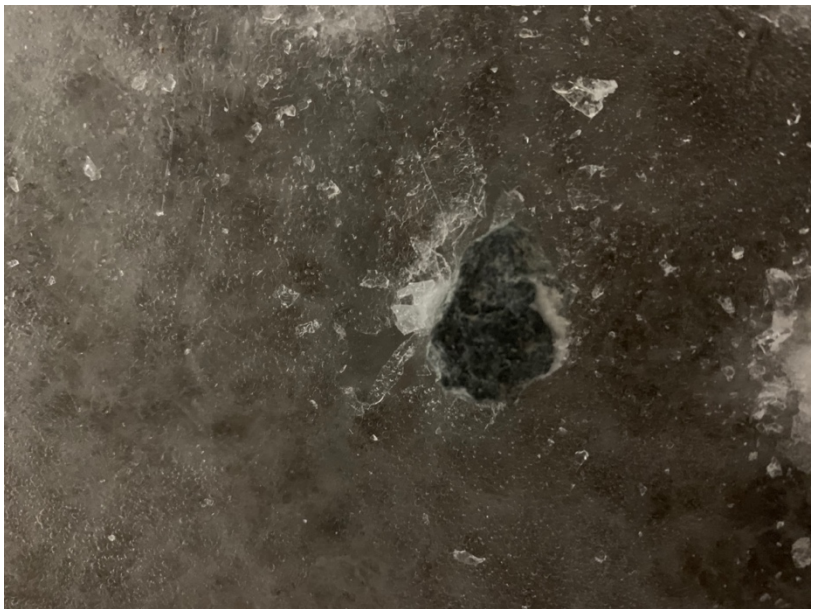

2021_28_06_(16)-65-0.5

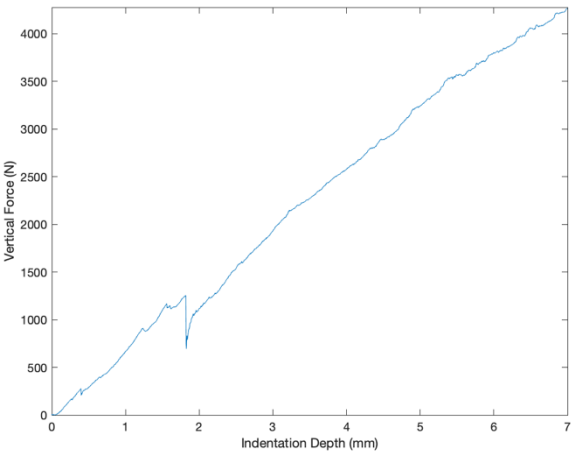

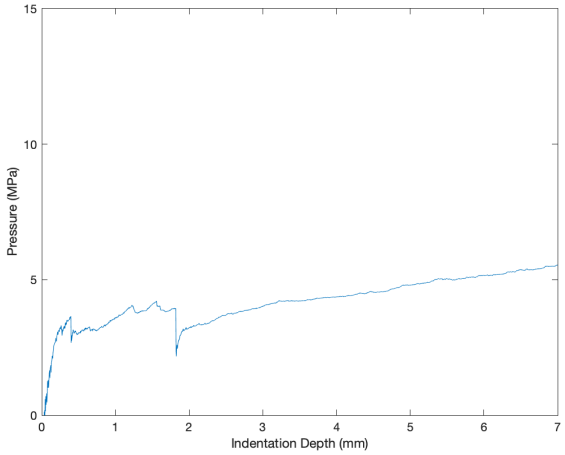

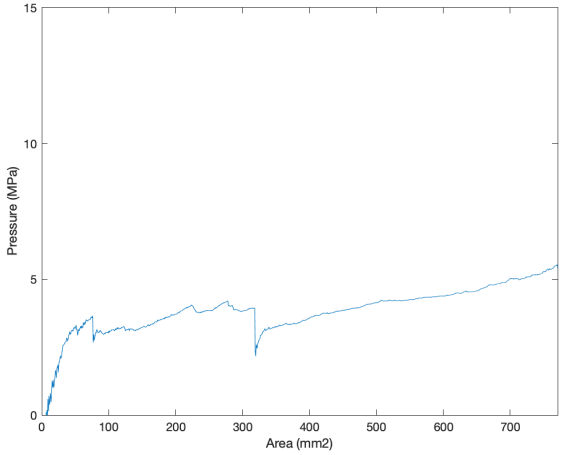

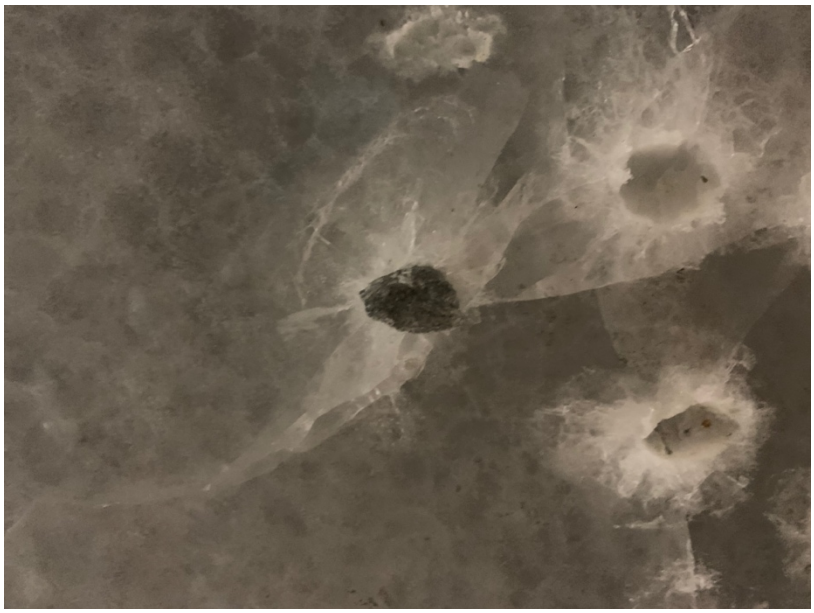

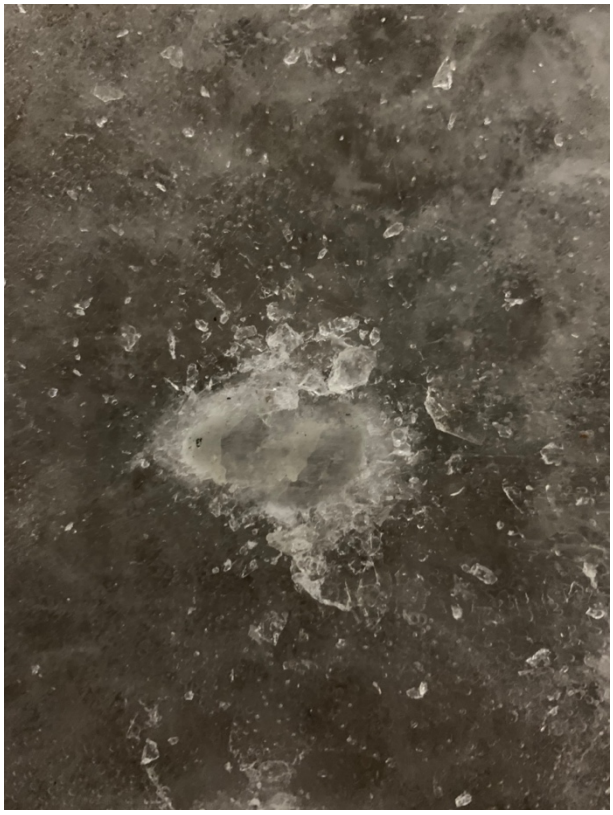

2021_28_06_(17)-65-0.5

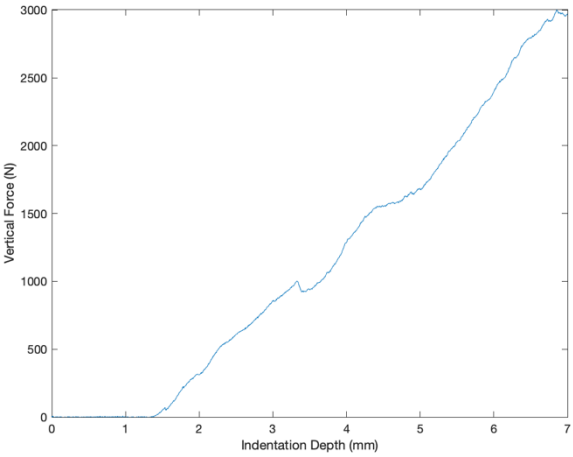

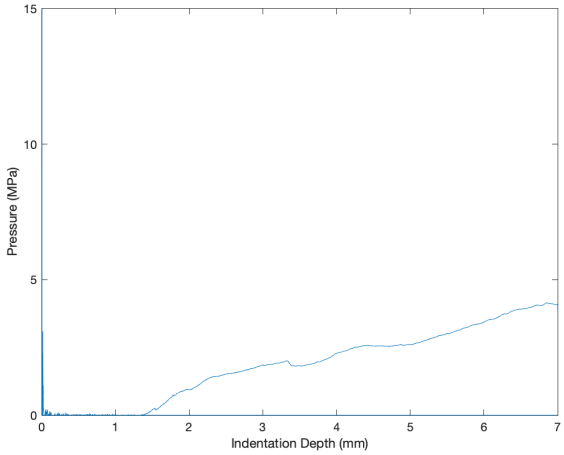

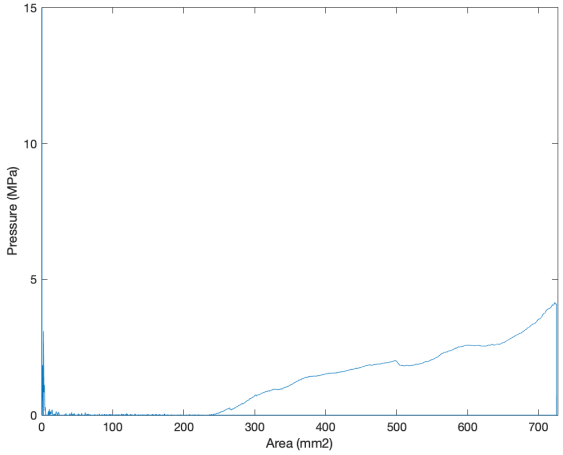

2021_28_06_(18)-65-0.5

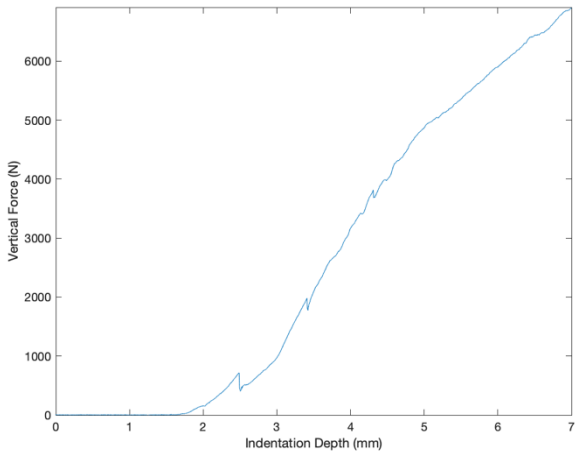

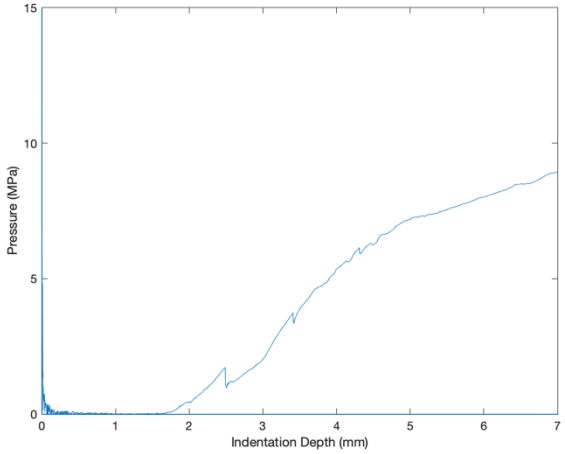

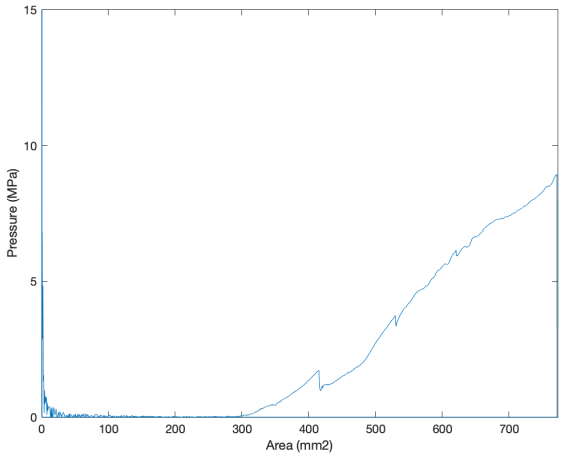

2021_28_06_(19)-65-0.5

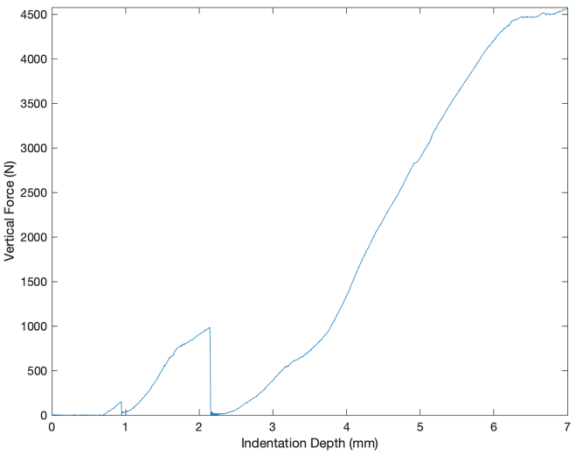

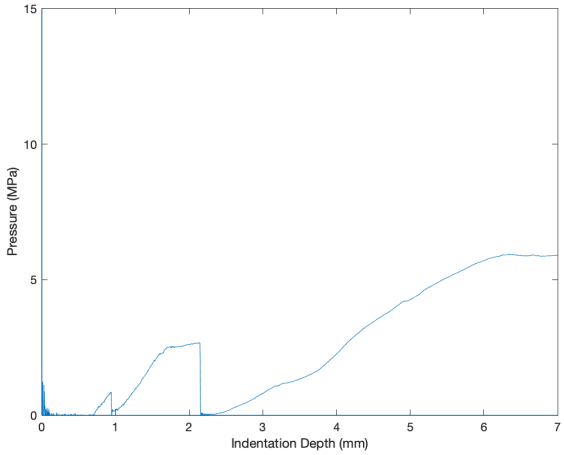

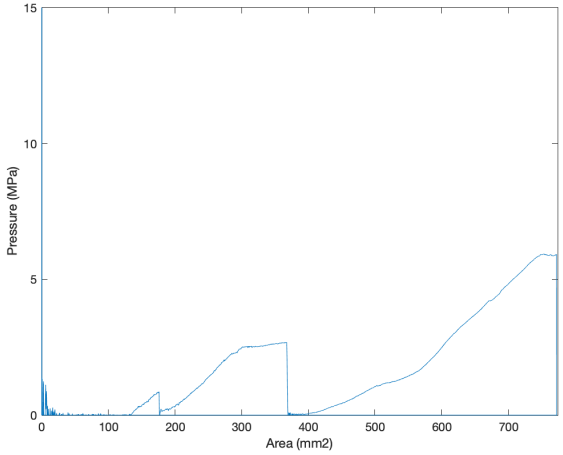

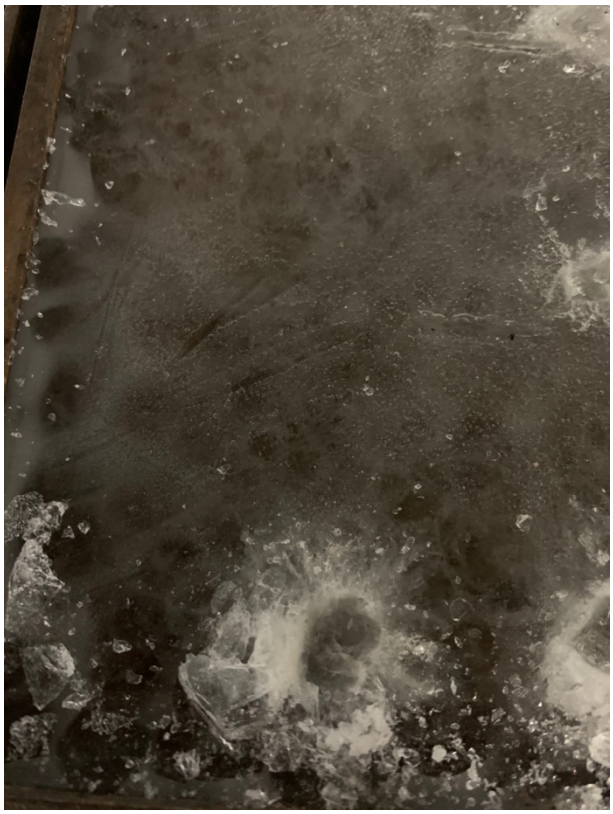

2021_28_06_(20)-65-0.5

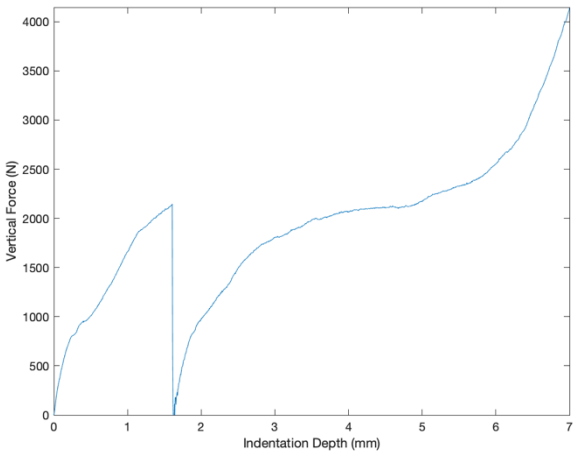

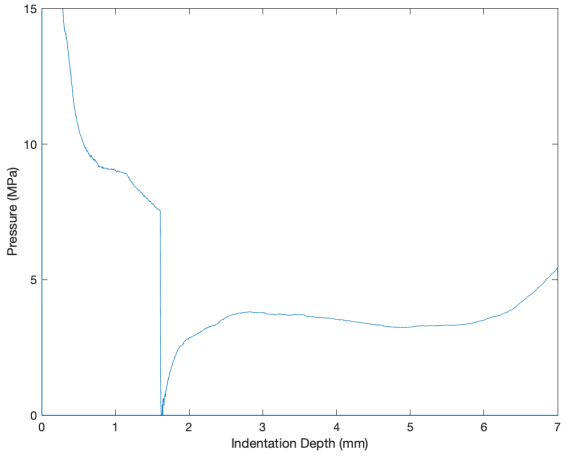

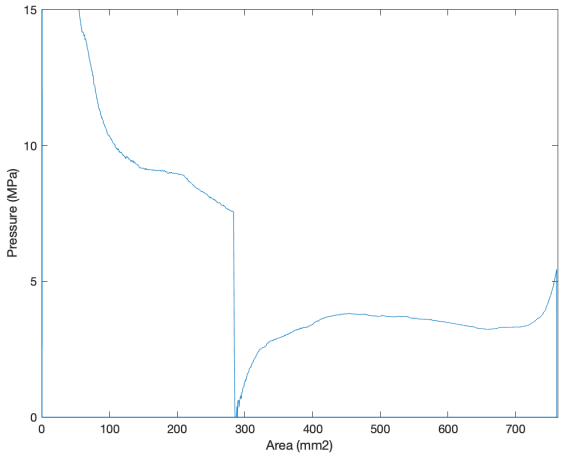

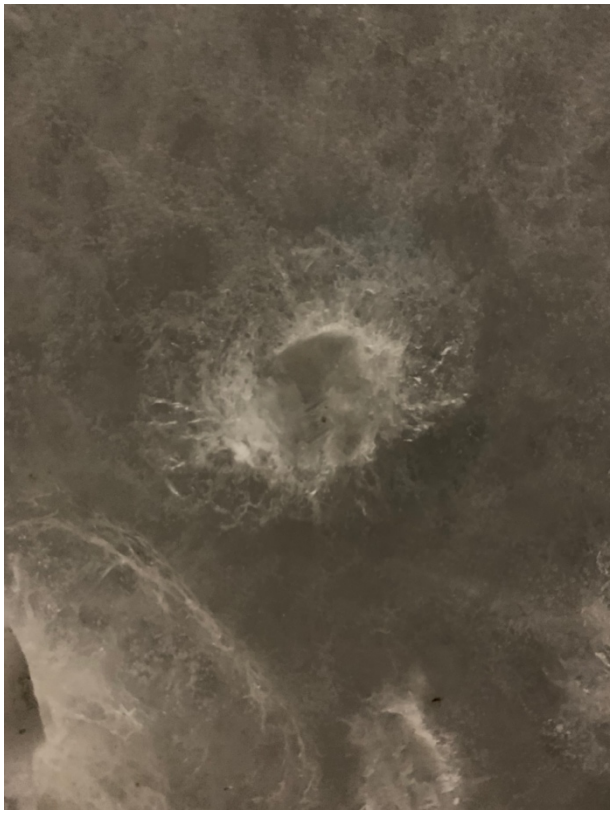

2021_29_06_(1)-26-0.5

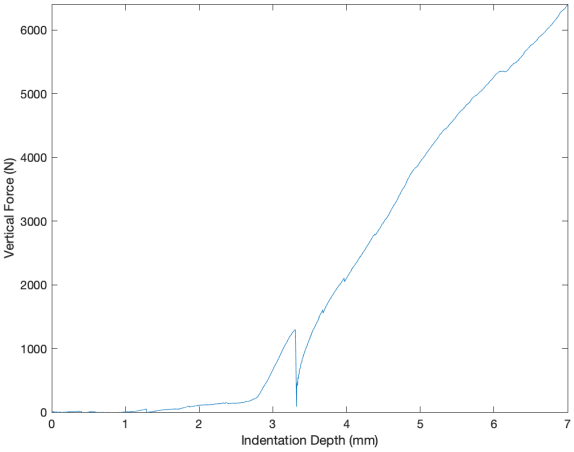

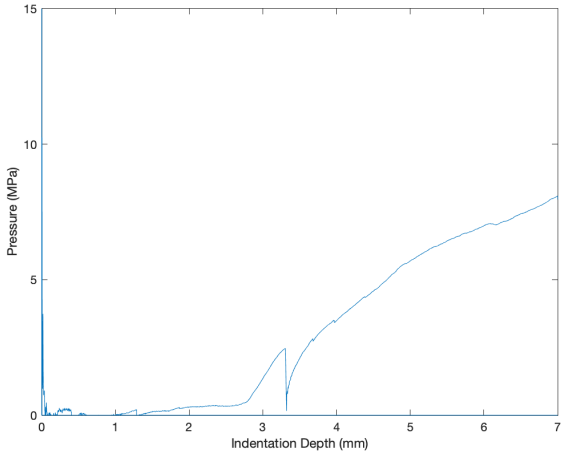

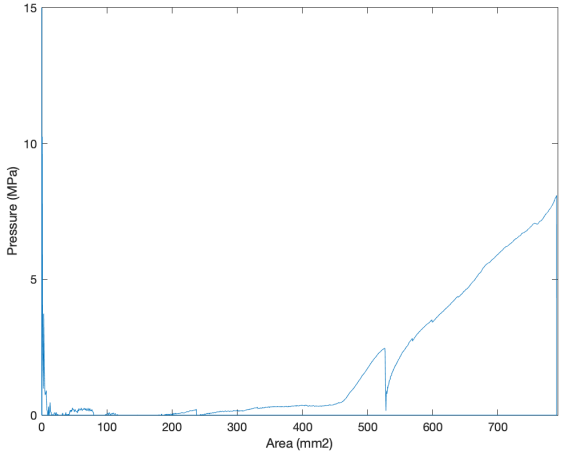

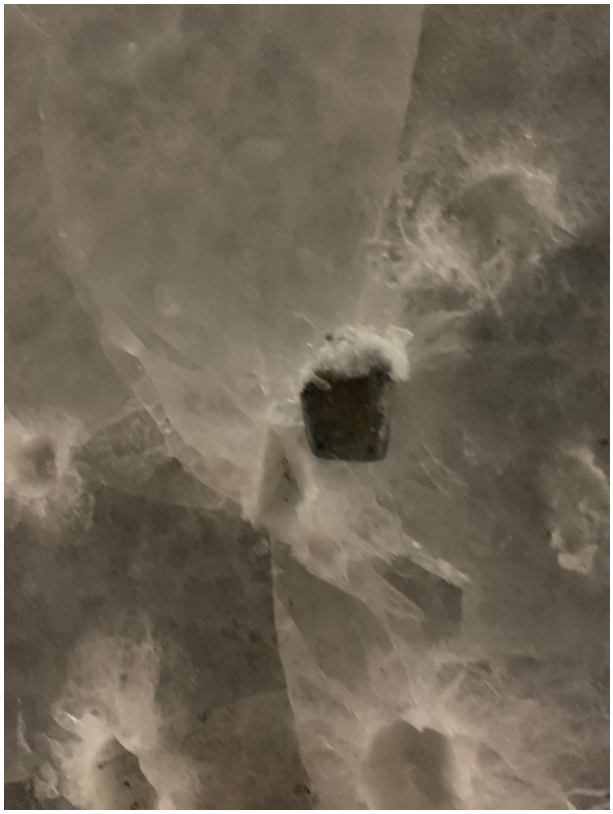

2021_29_06_(2)-26-0.5

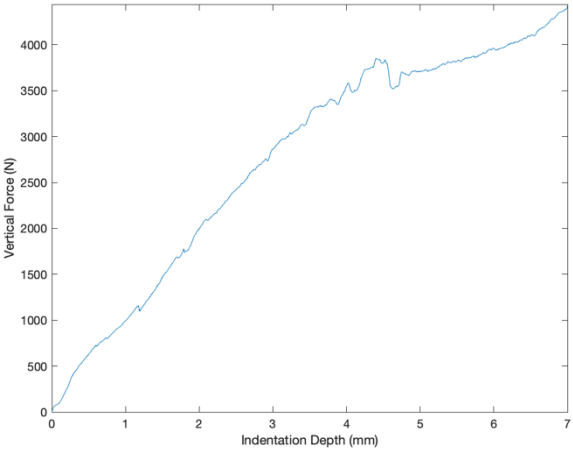

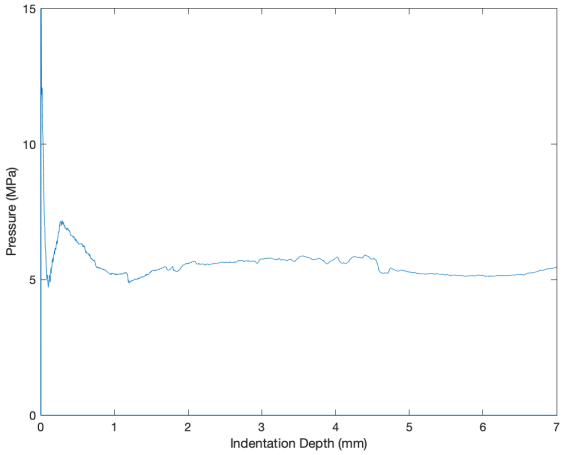

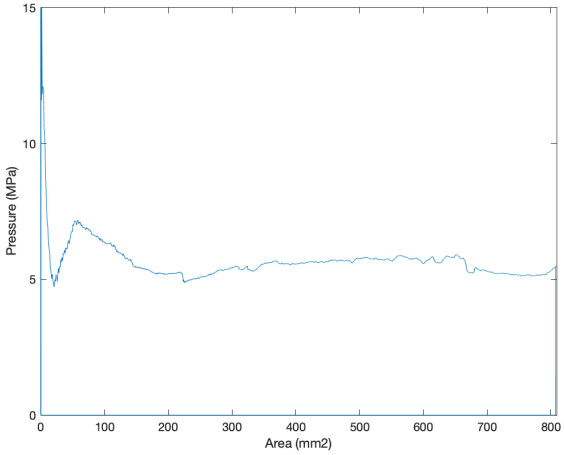

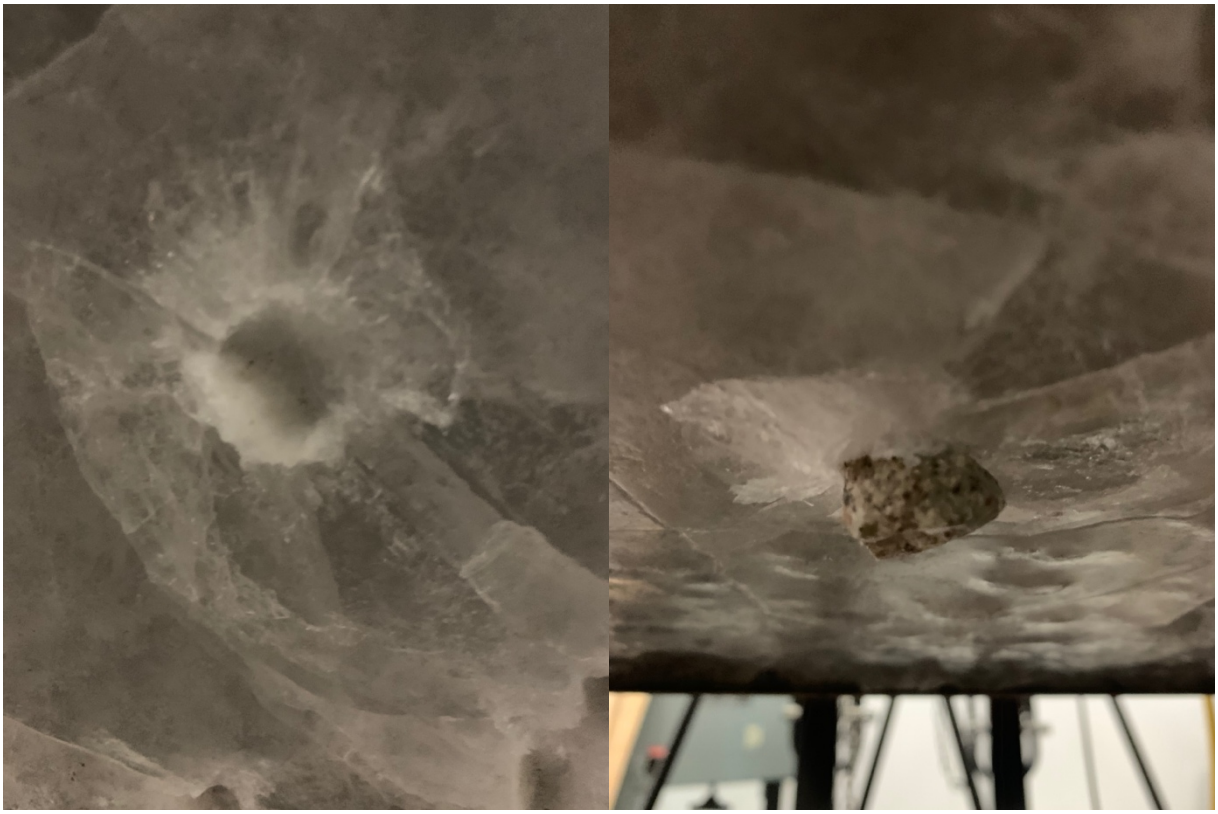

2021_29_06_(3)-26-0.5

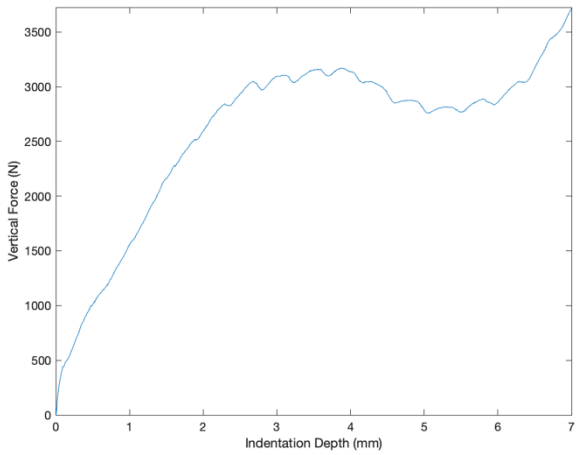

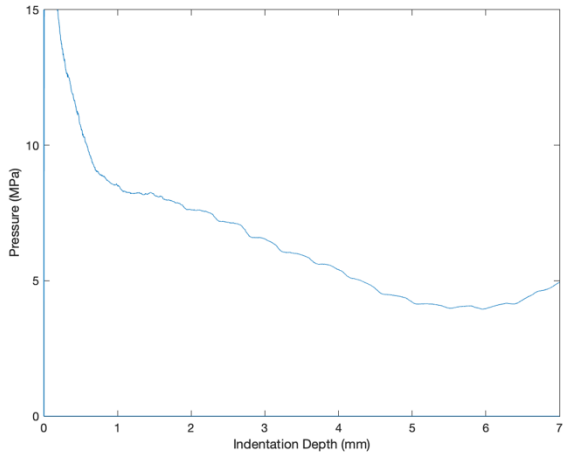

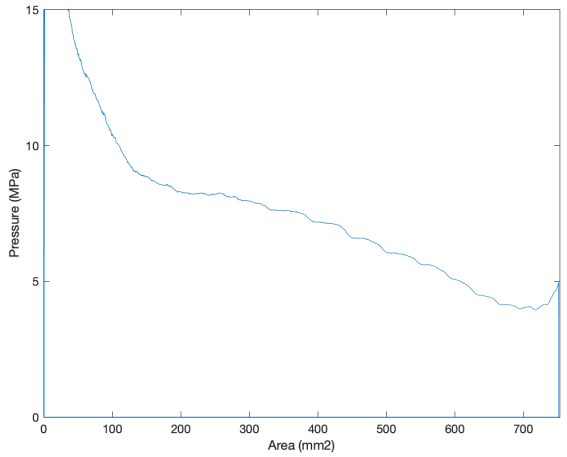

2021_29_06_(4)-26-0.5

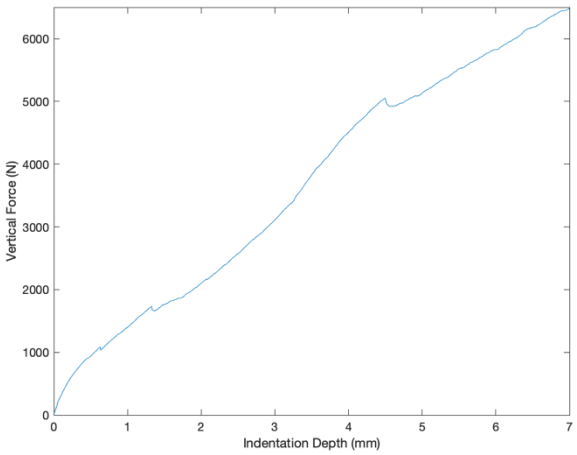

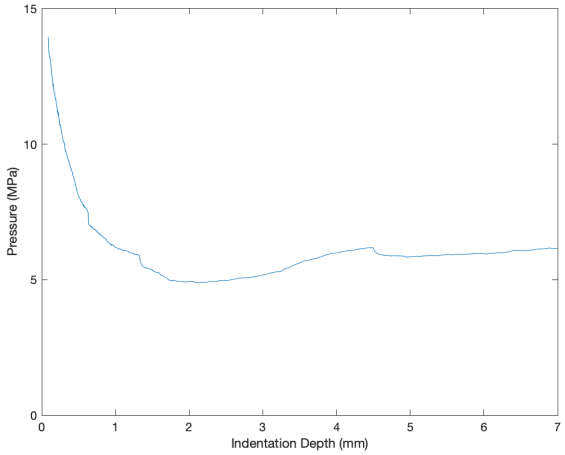

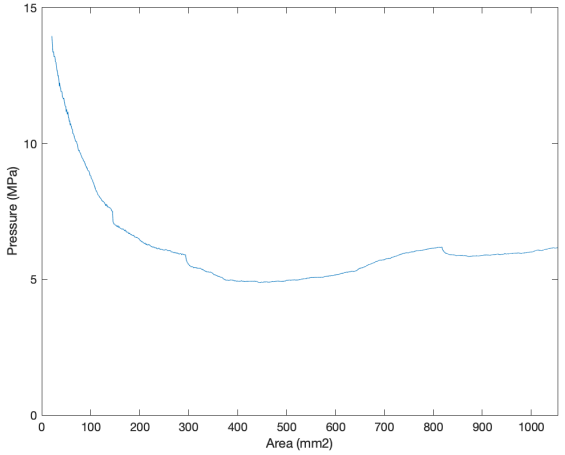

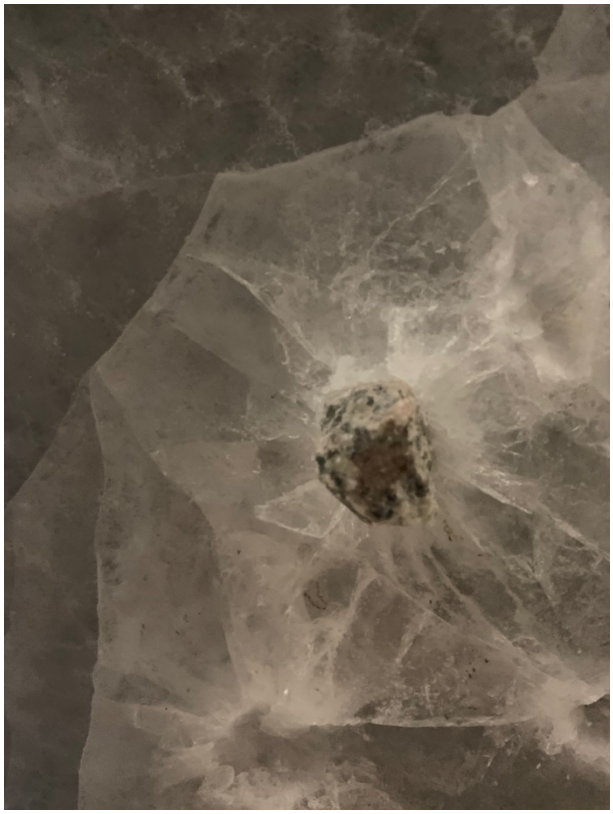

2021_29_06_(5)-26-0.5

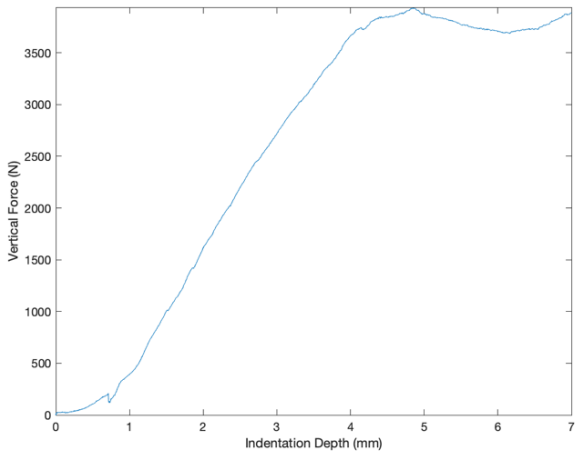

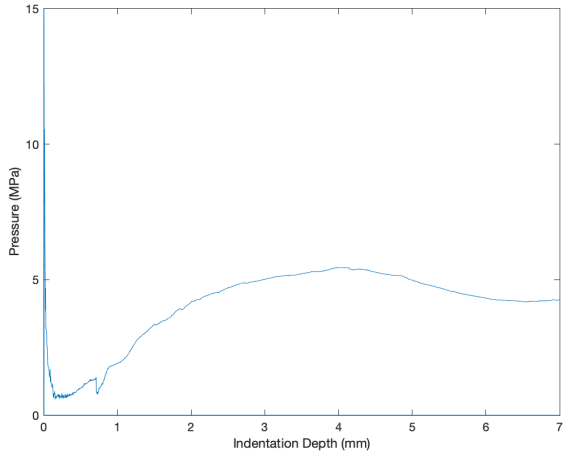

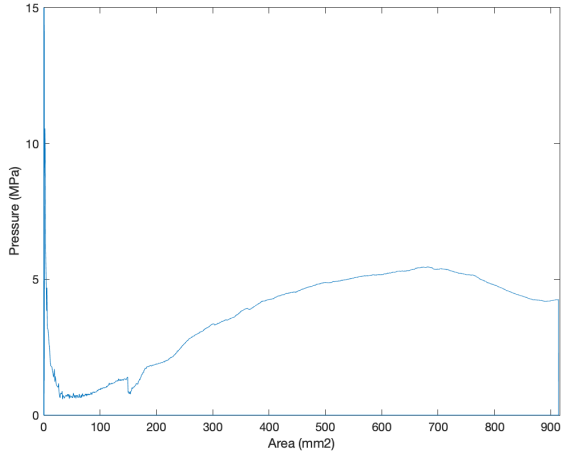

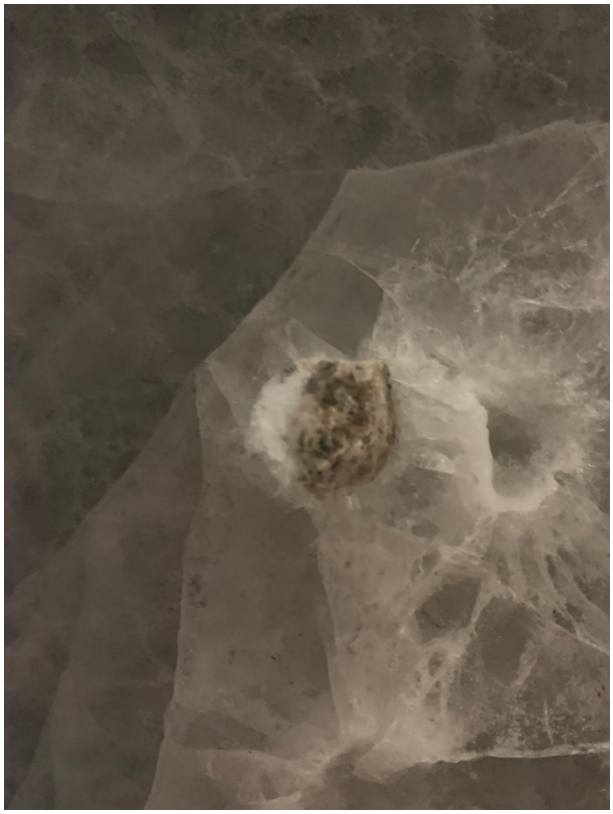

2021_29_06_(6)-26-0.5

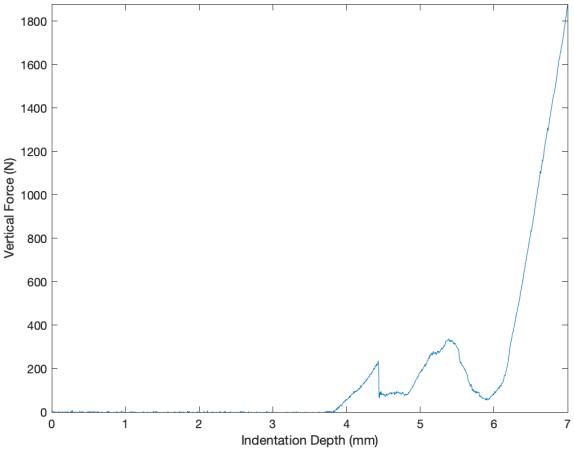

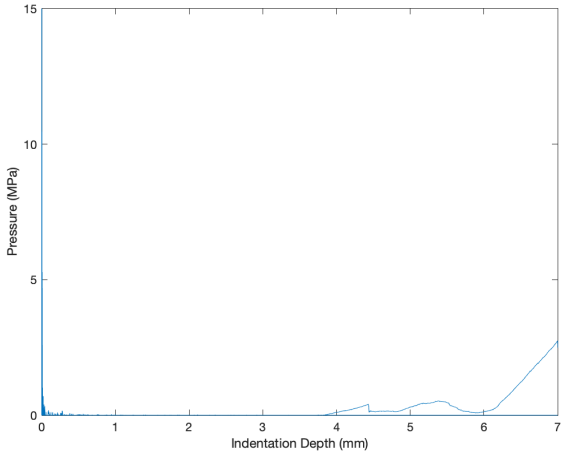

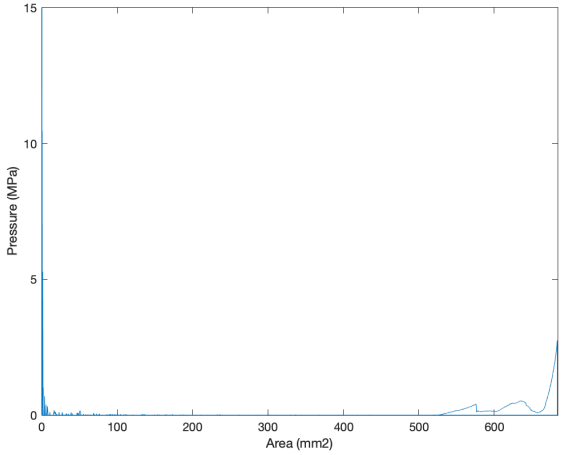

2021_29_06_(7)-26-0.5

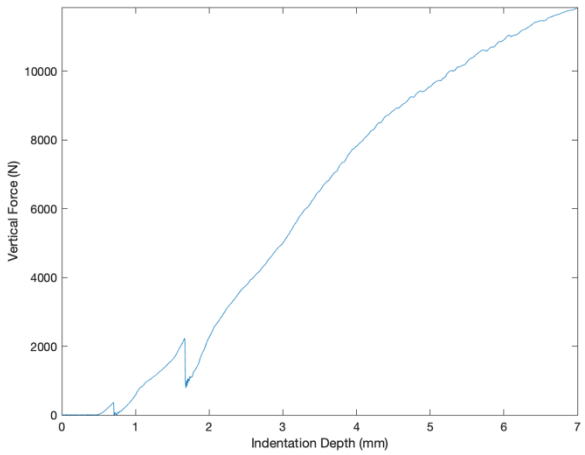

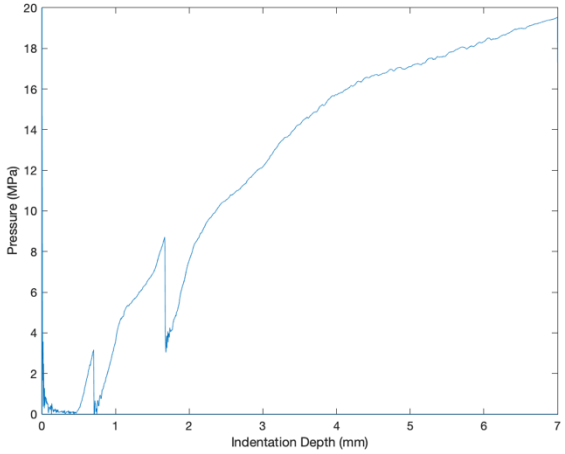

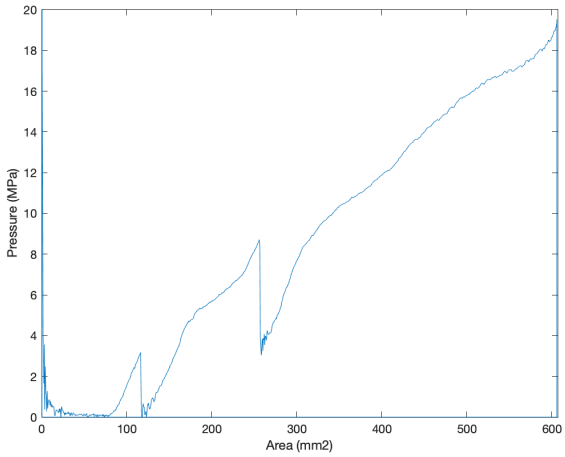

Images taken after indentation omitted due to poor quality.

2021_30_06_(1)-26-0.5

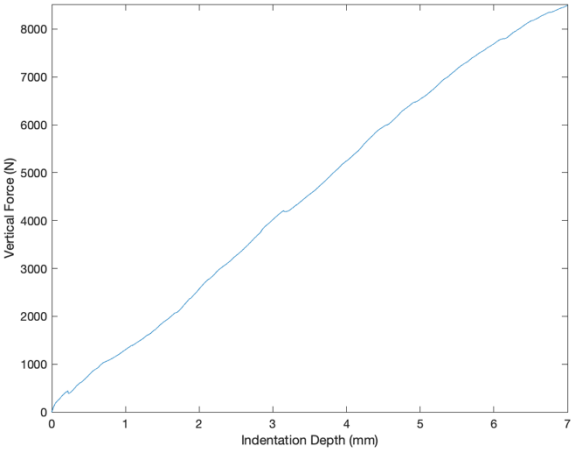

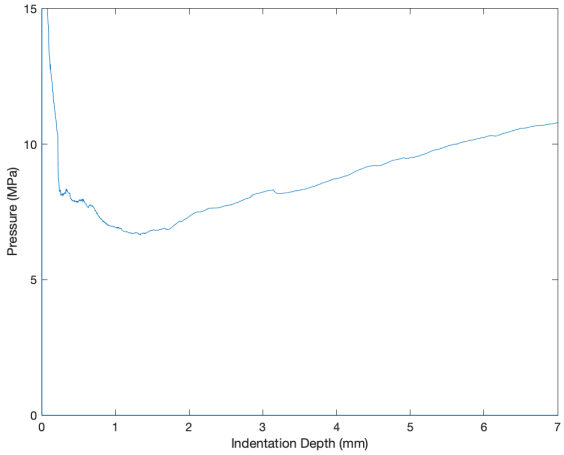

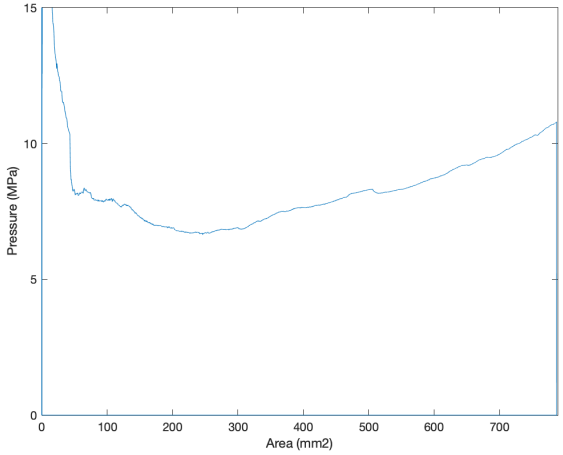

2021_30_06_(2)-26-0.5

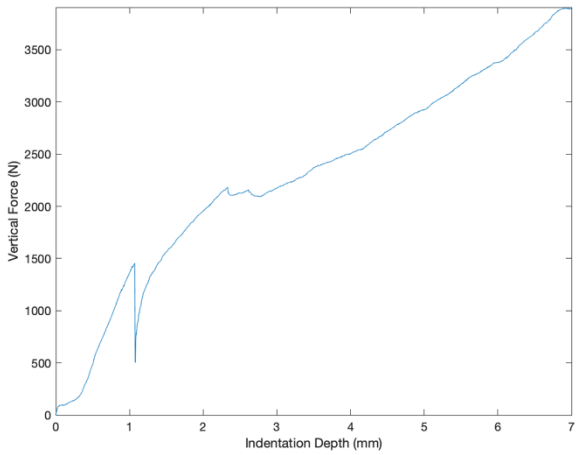

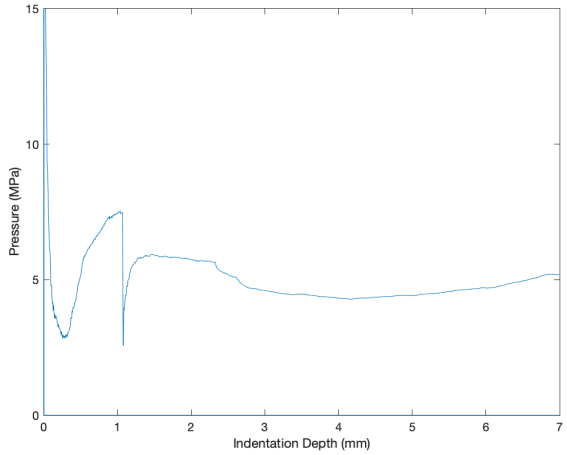

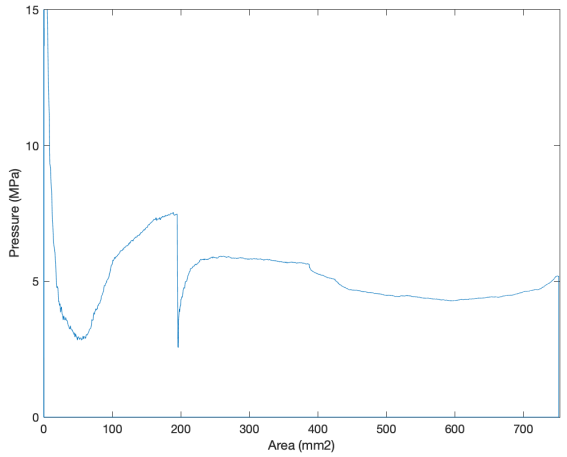

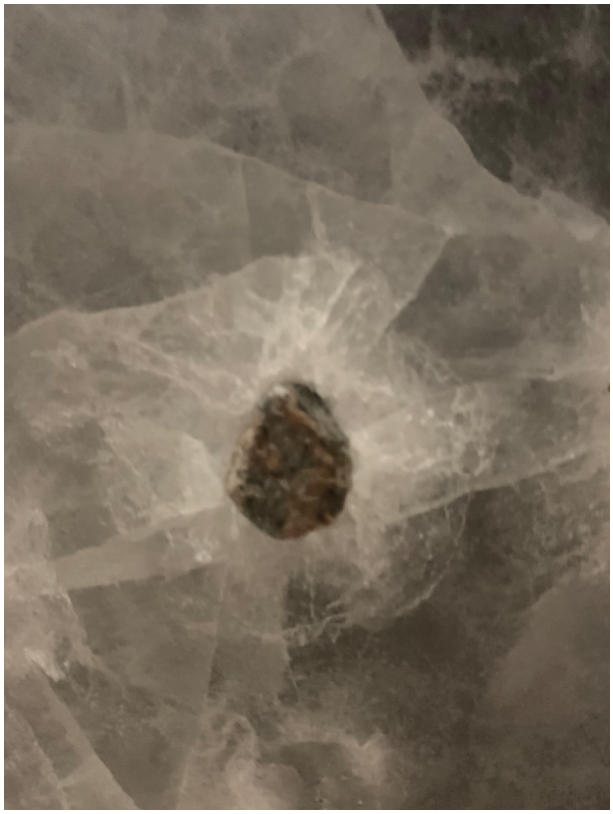

2021_30_06_(3)-26-0.5

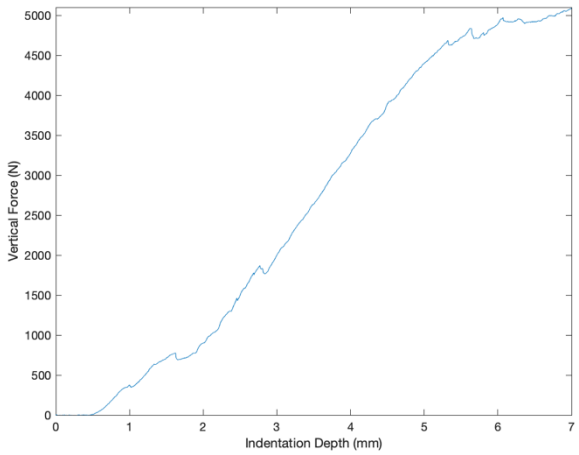

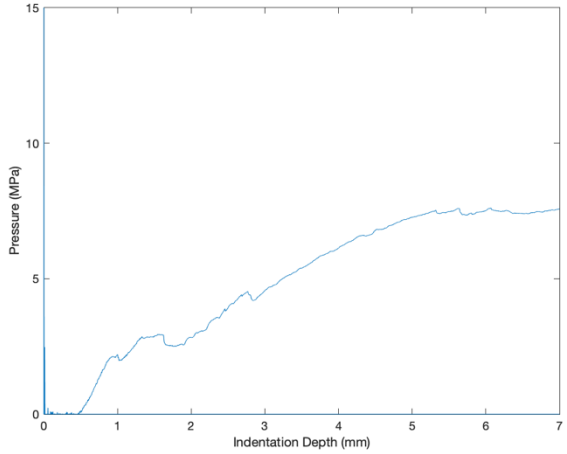

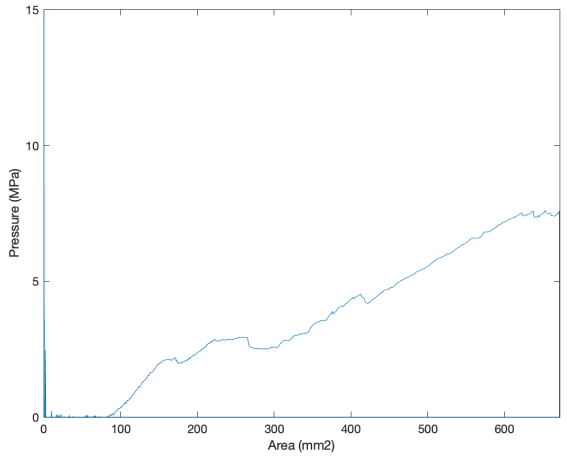

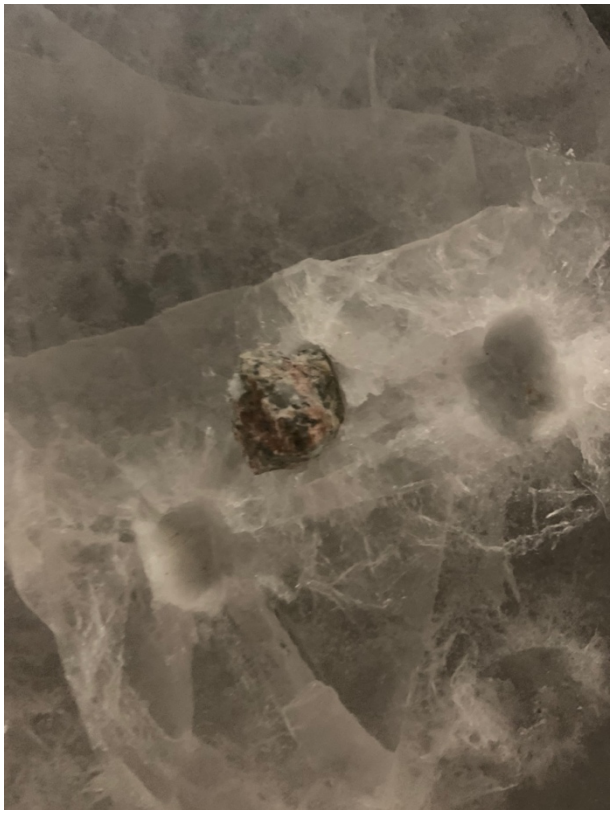

2021_30_06_(4)-96-0.5

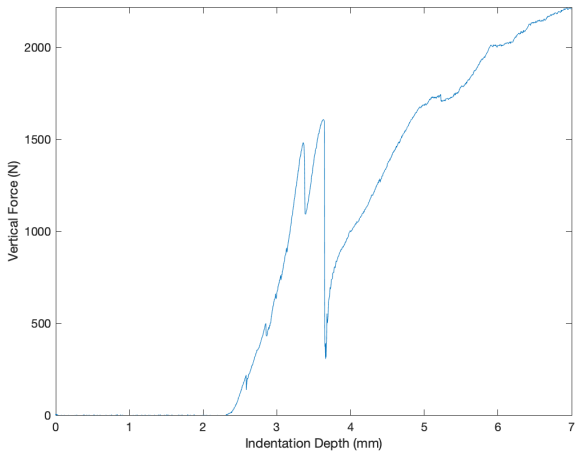

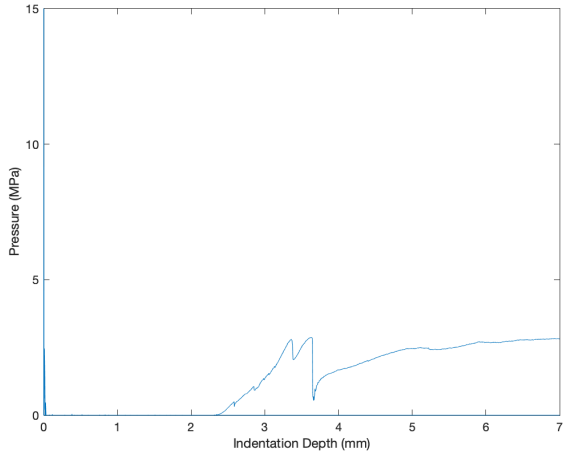

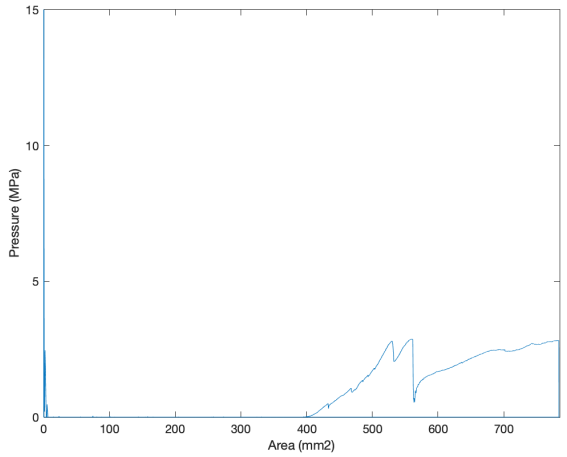

2021_30_06_(5)-96-0.5

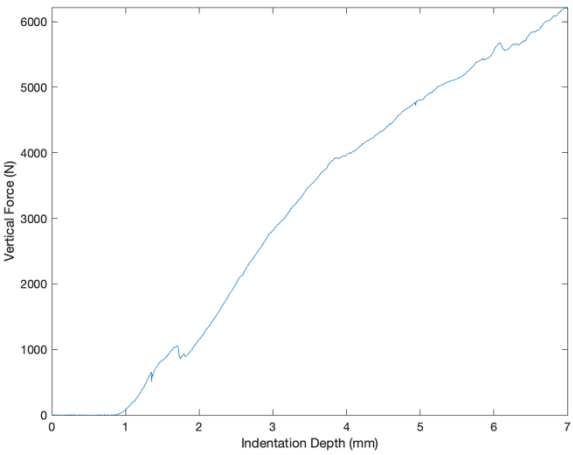

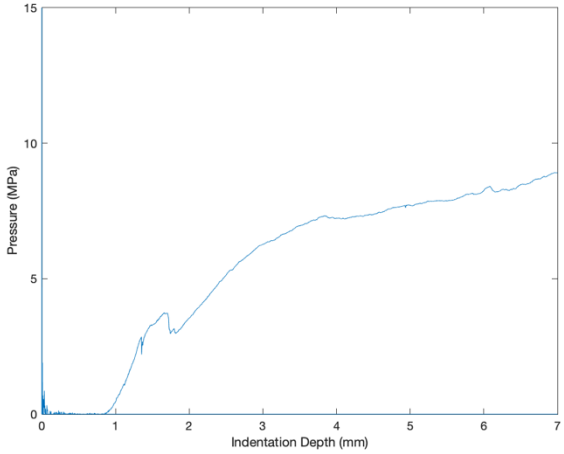

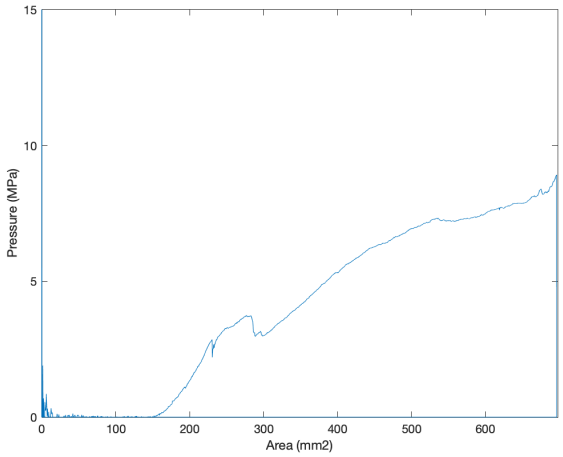

Upper image omitted due to poor quality

2021_30_06_(6)-96-0.5

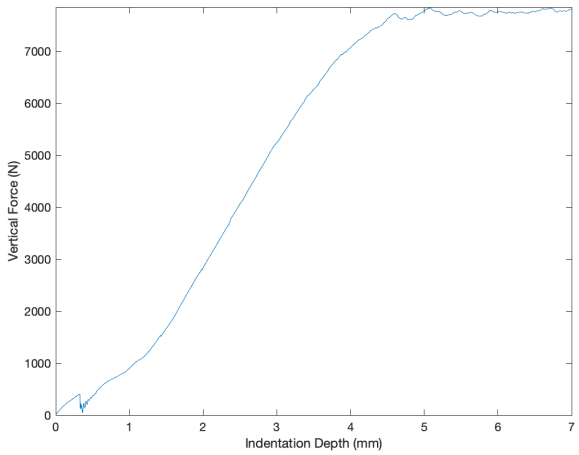

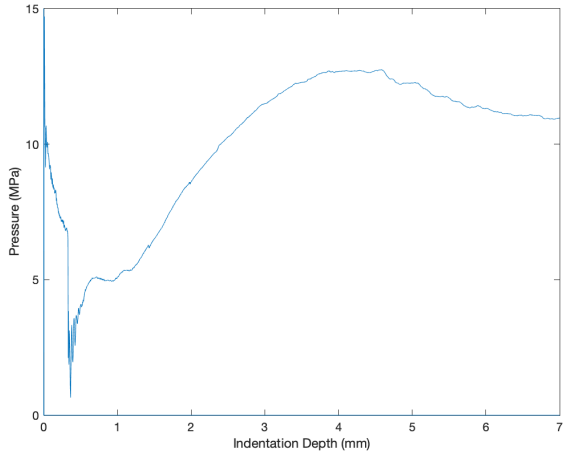

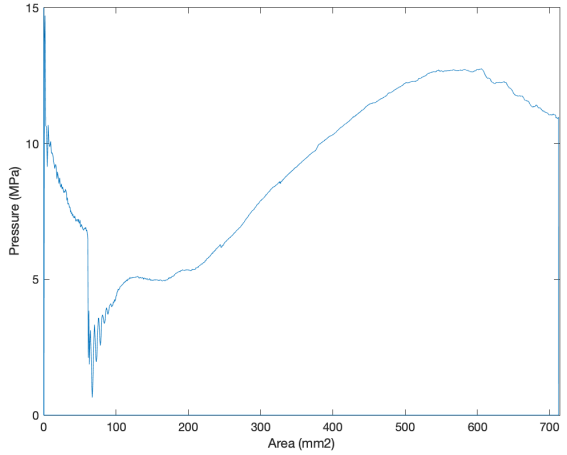

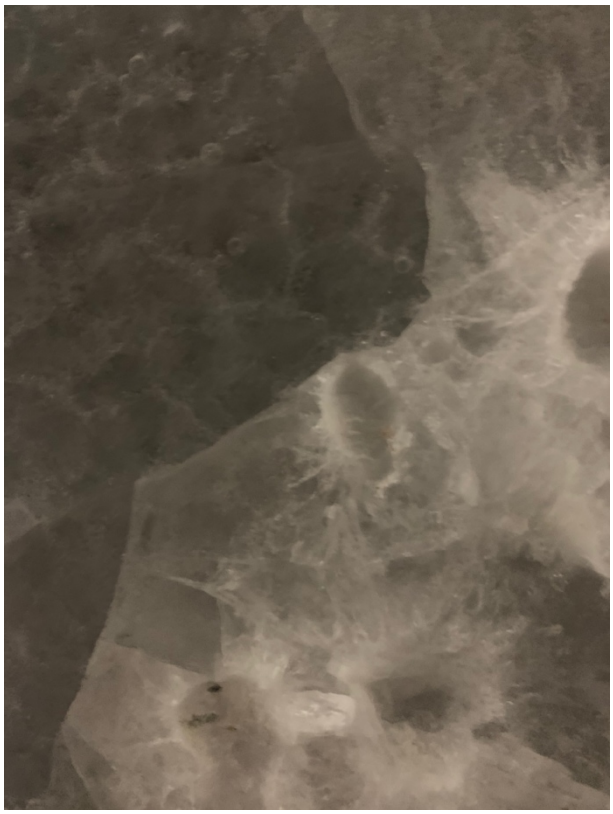

2021_30_06_(7)-96-0.5

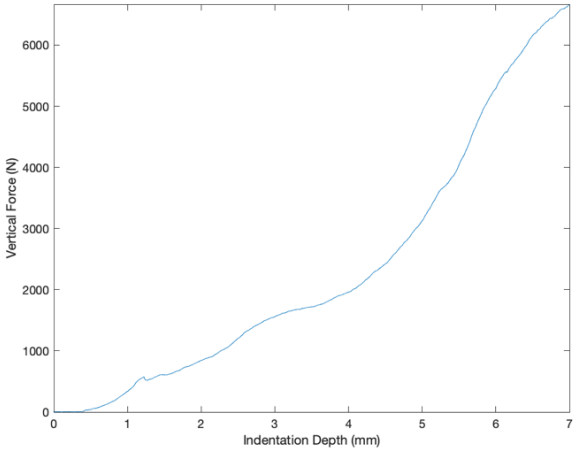

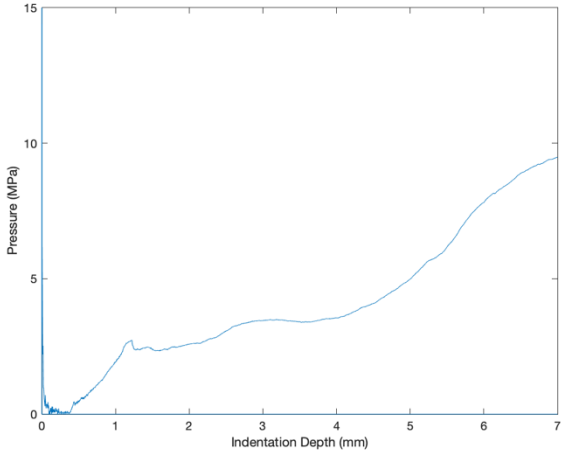

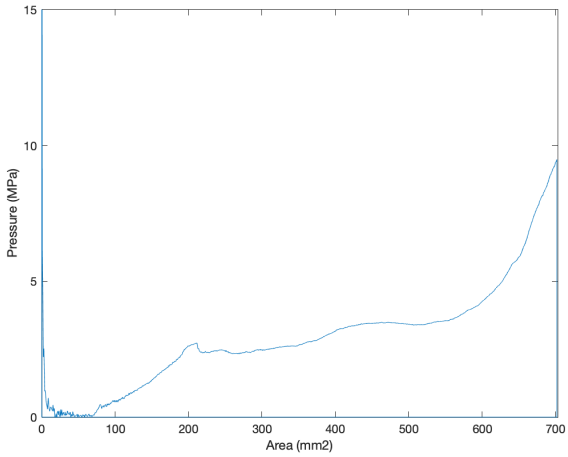

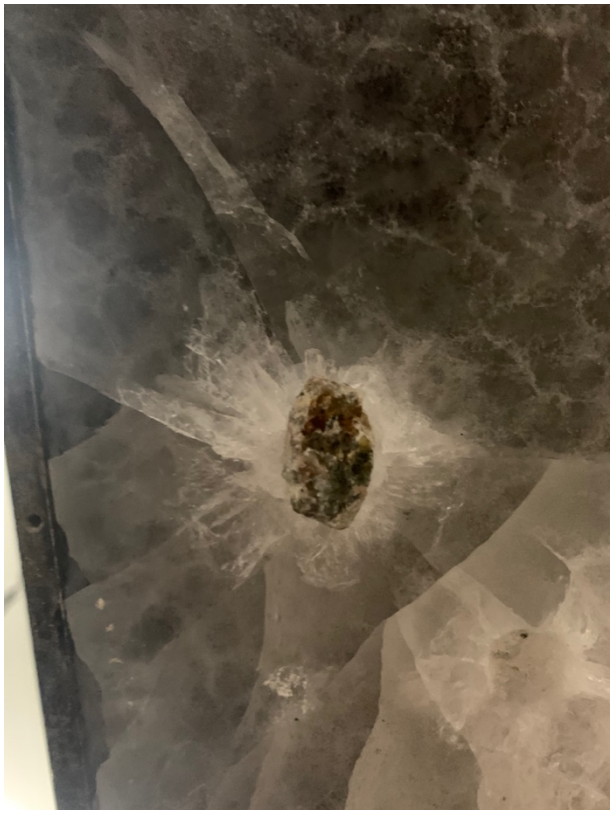

2021_30_06_(8)-96-0.5

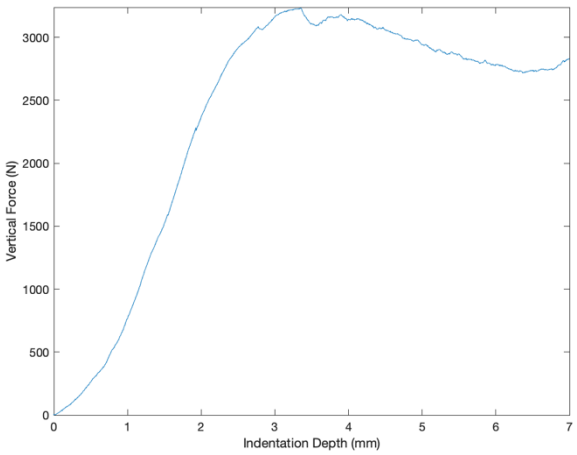

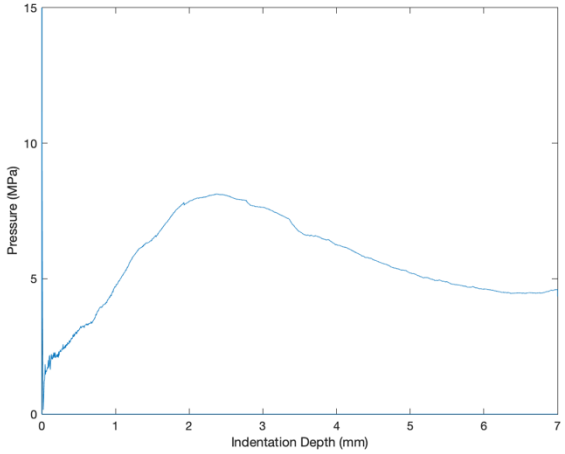

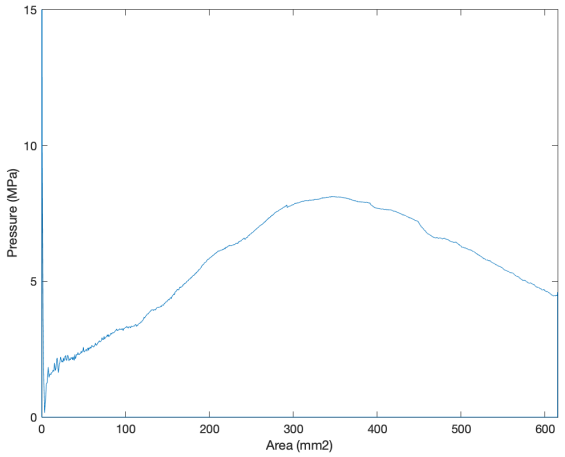

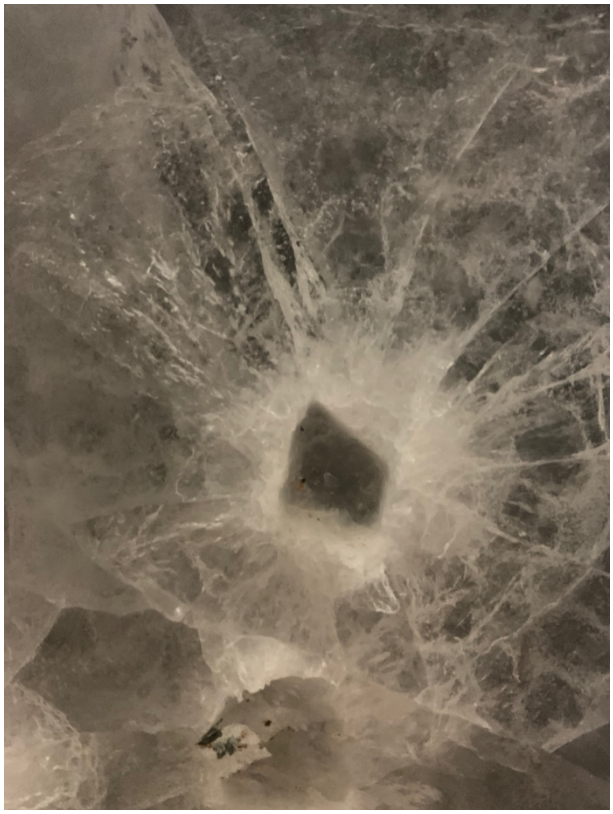

2021_30_06_(9)-96-0.5

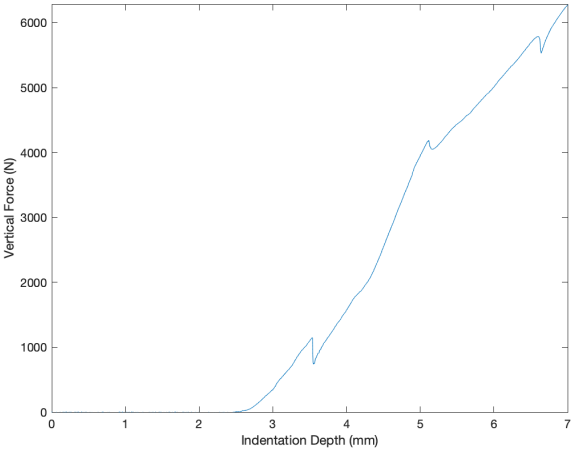

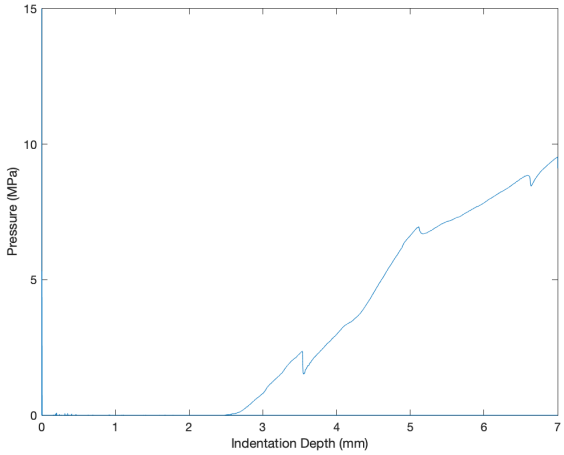

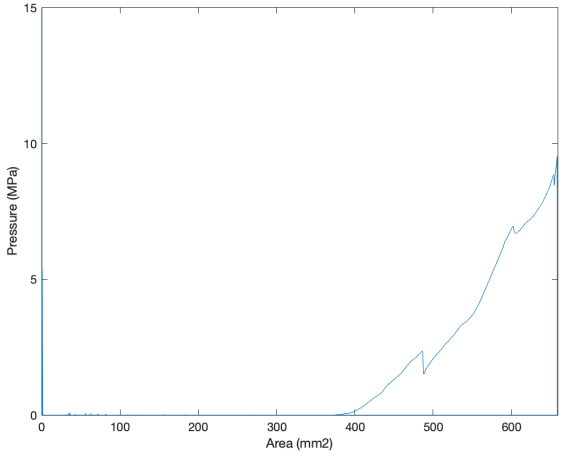

10 mm/s
2021_06_07_(1)-96-10

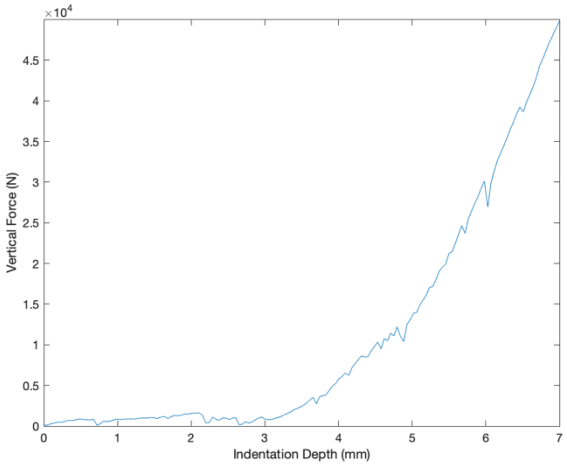

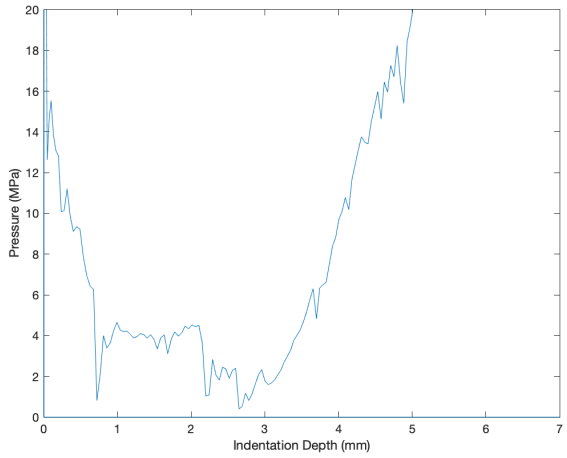

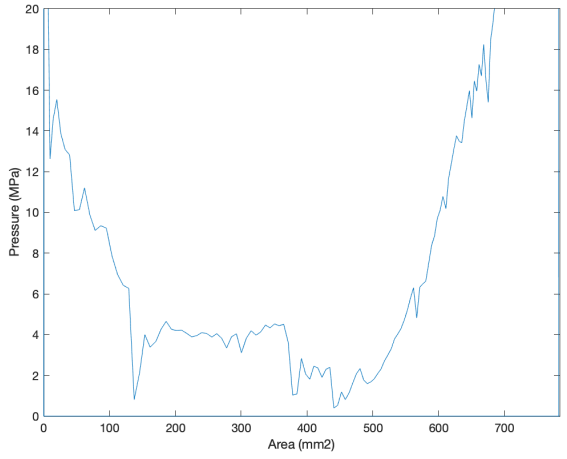

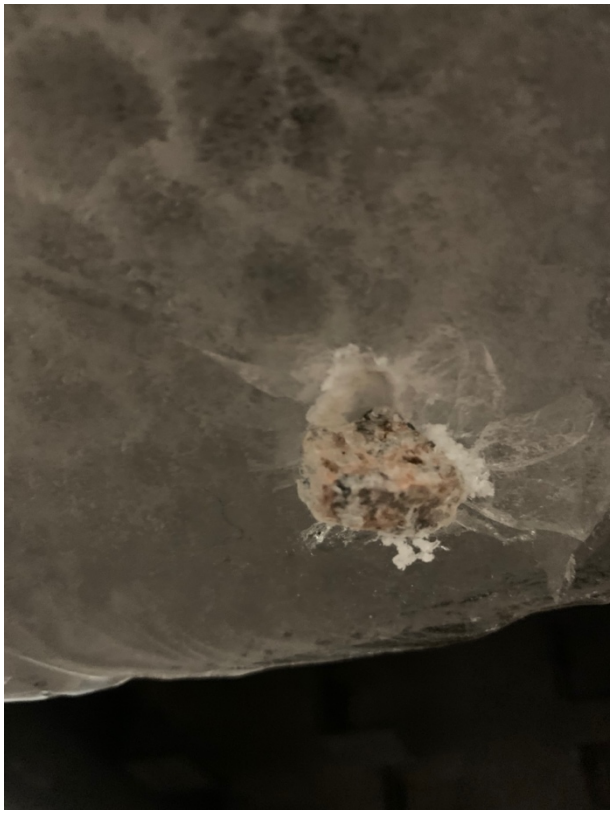

2021_06_07_(2)-96-10

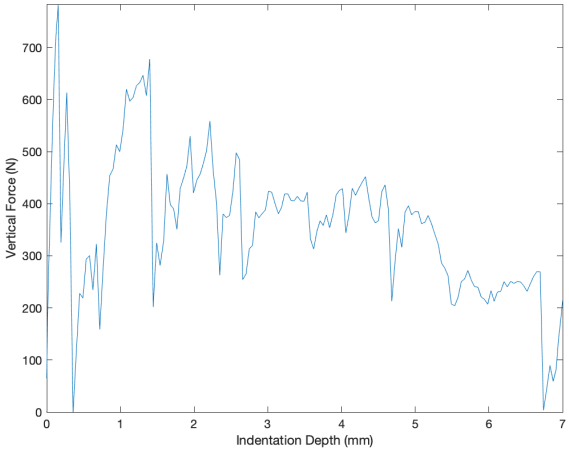

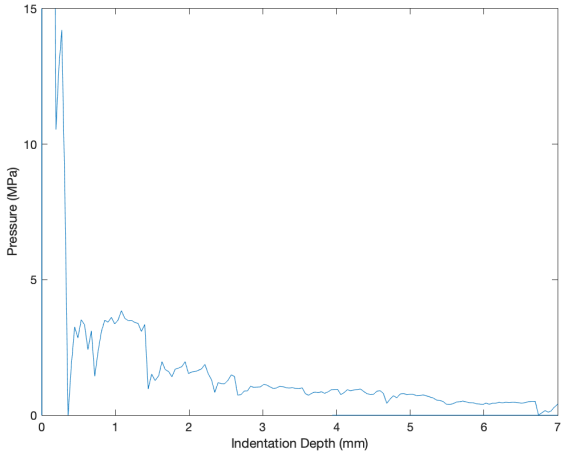

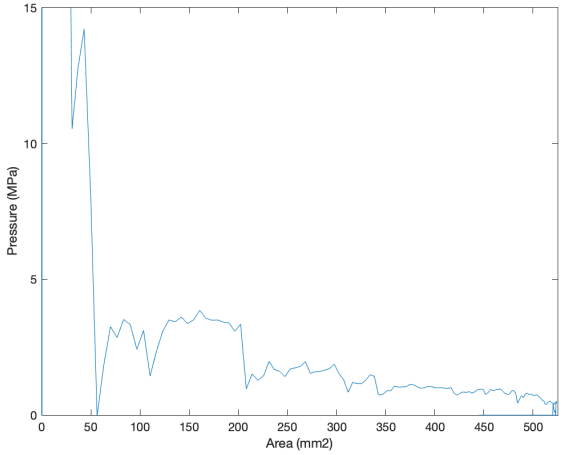

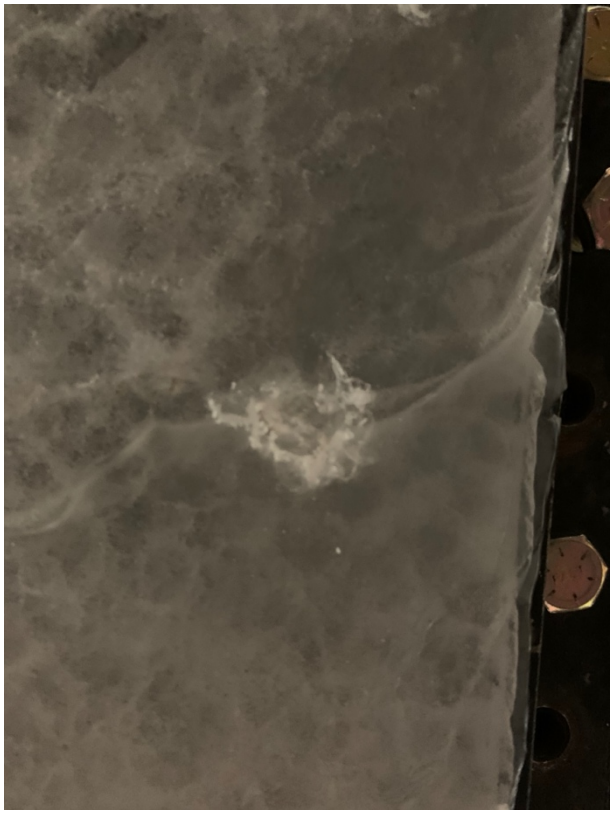

2021_06_07_(3)-96-10

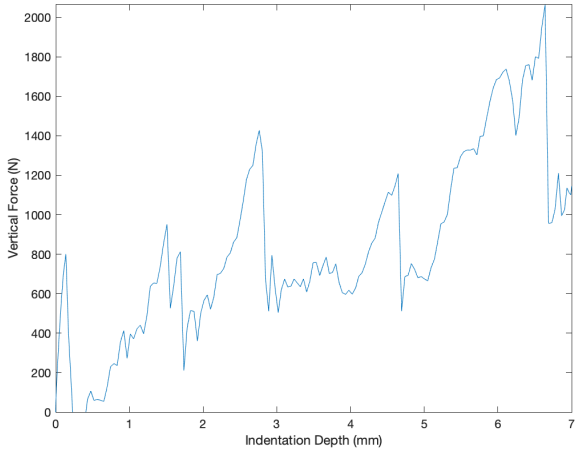

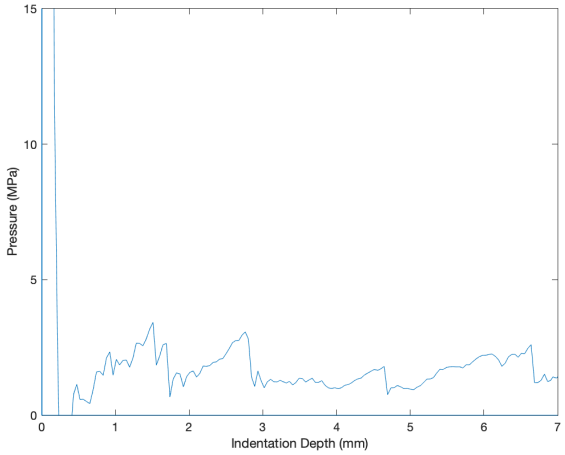

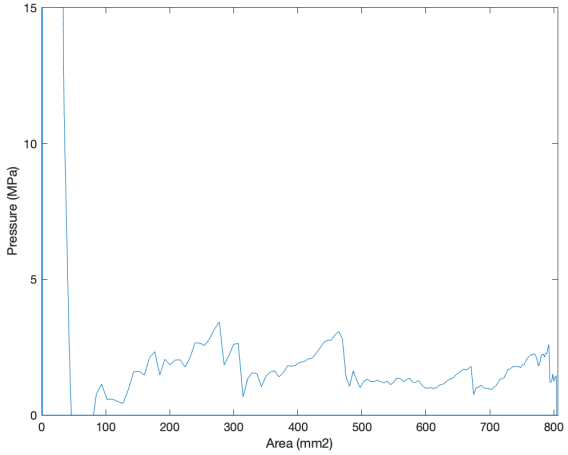

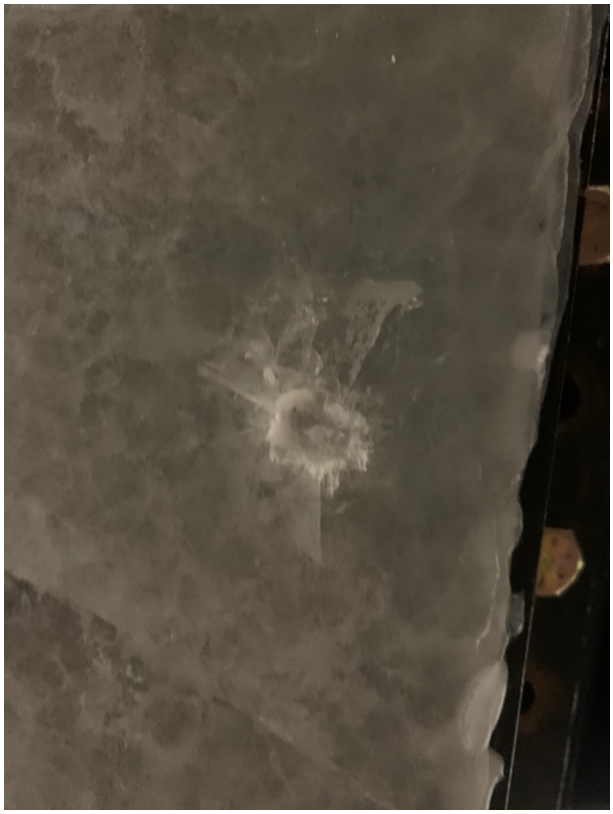

2021_06_07_(4)-96-10

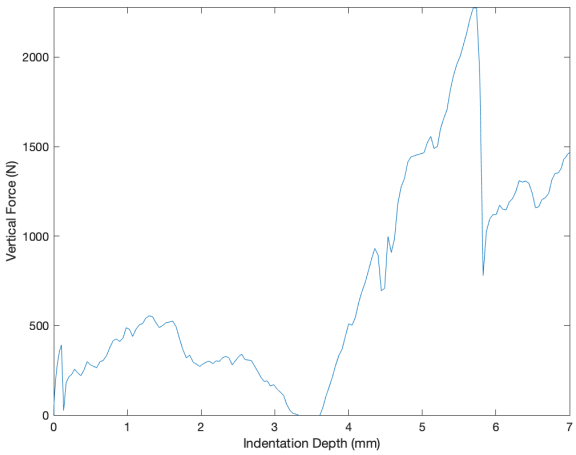

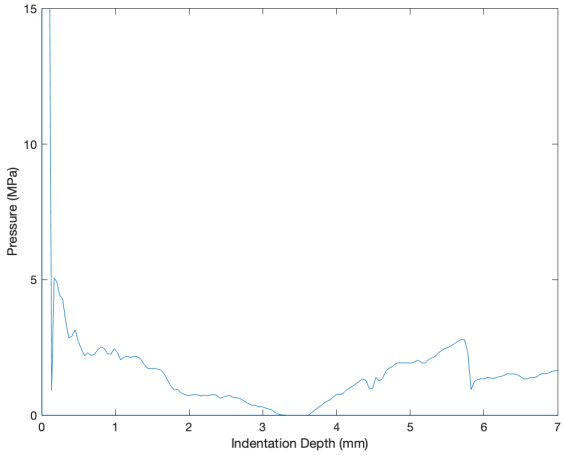

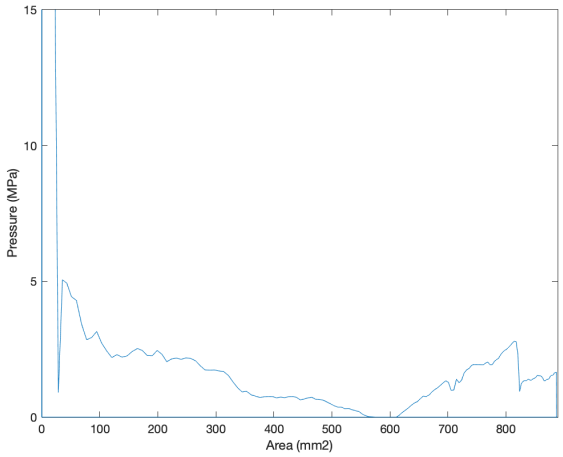

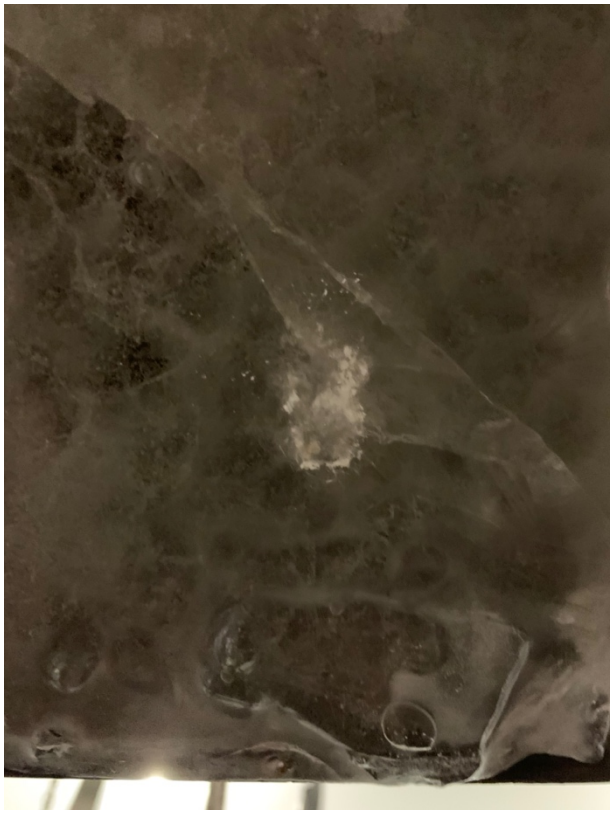

2021_06_07_(5)-96-10

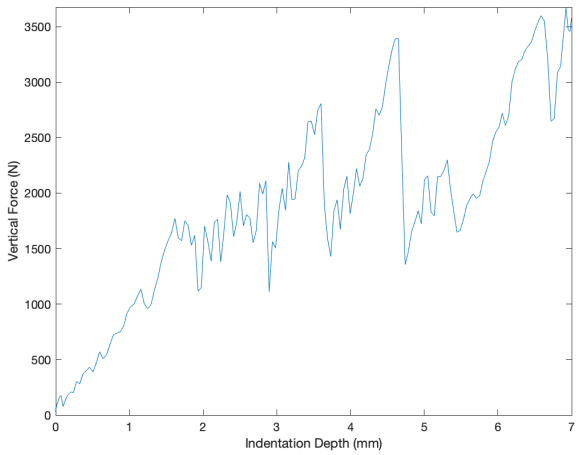

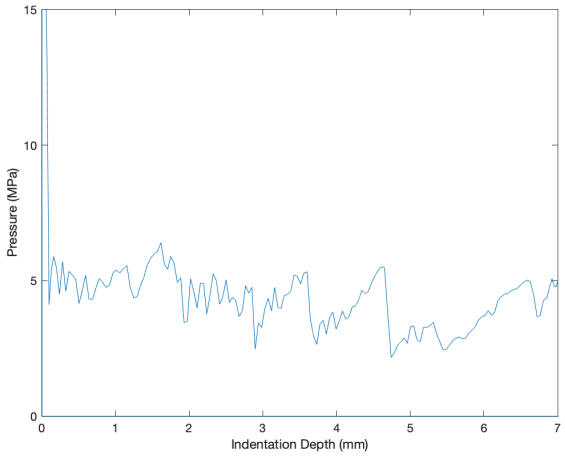

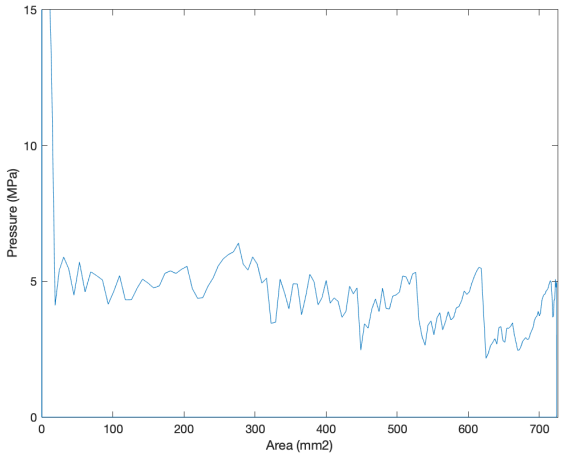

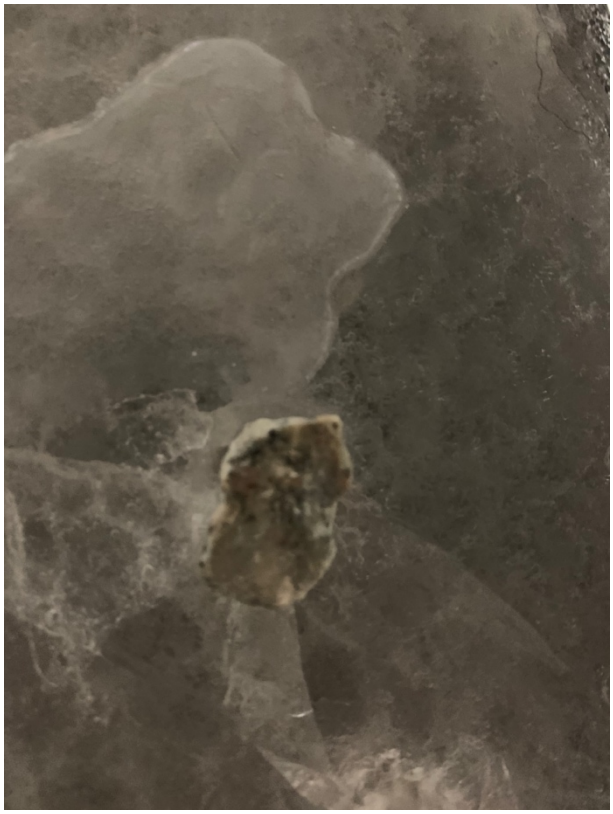

2021_06_07_(6)-96-10

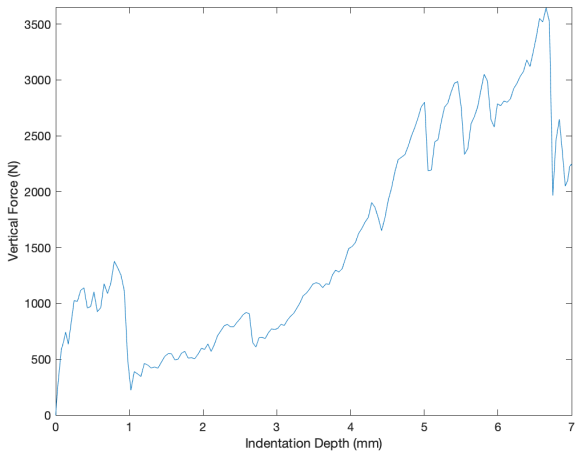

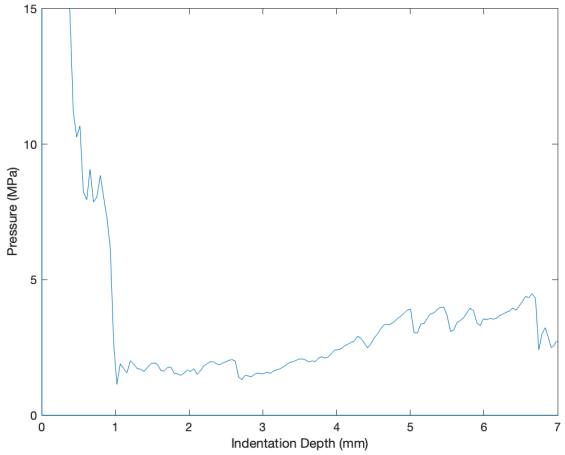

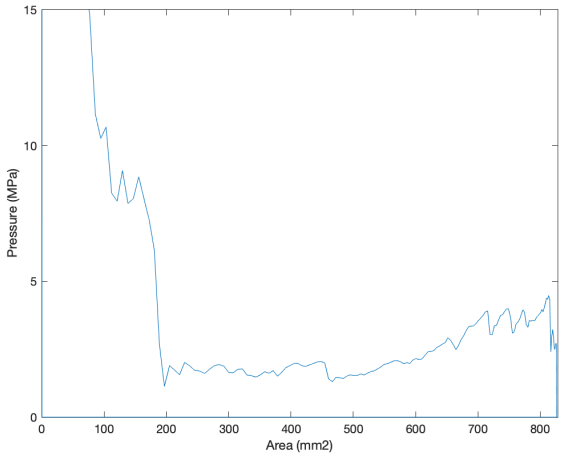

2021_06_07_(7)-96-10

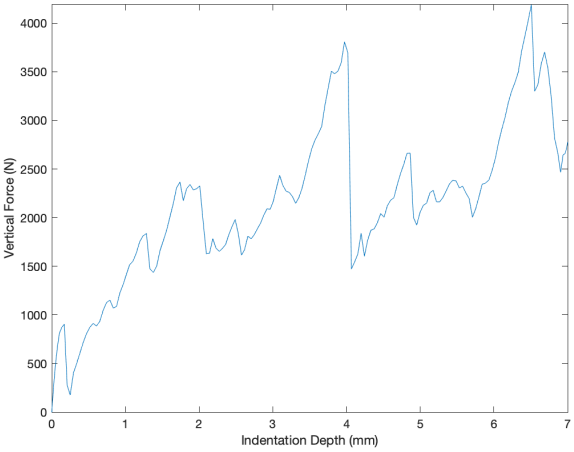

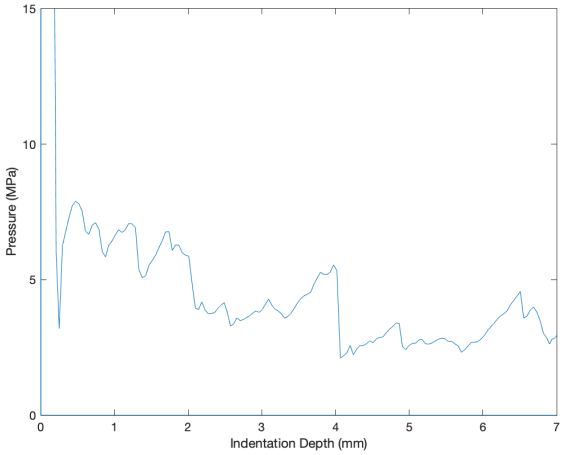

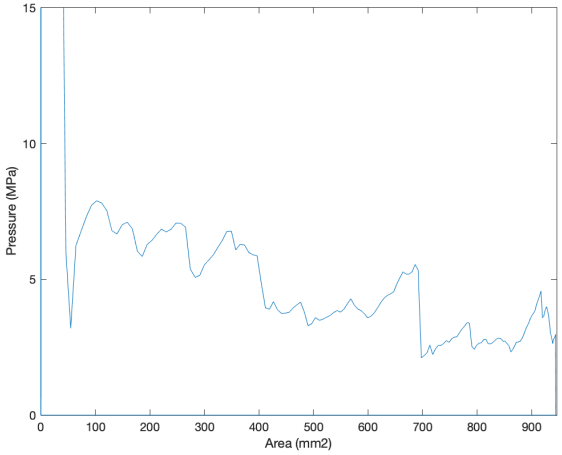

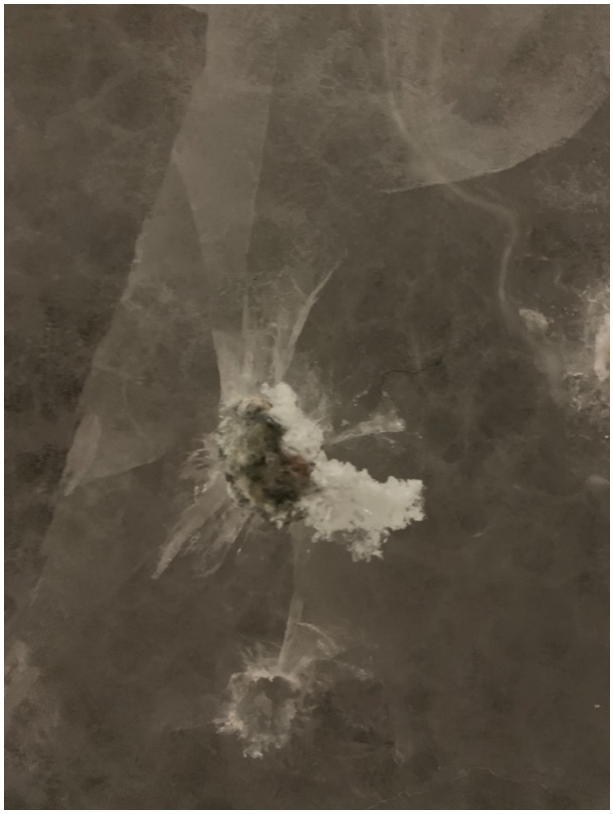

2021_06_07_(8)-96-10

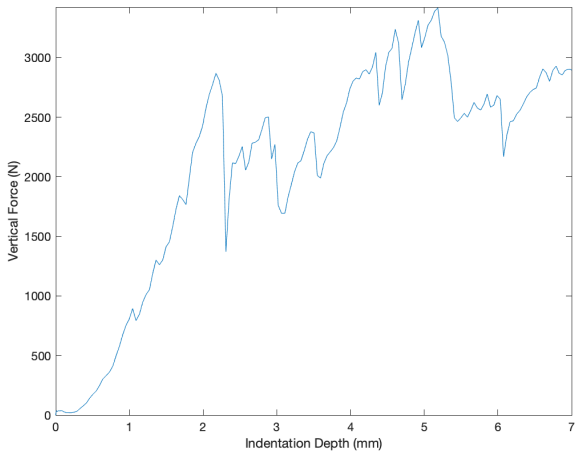

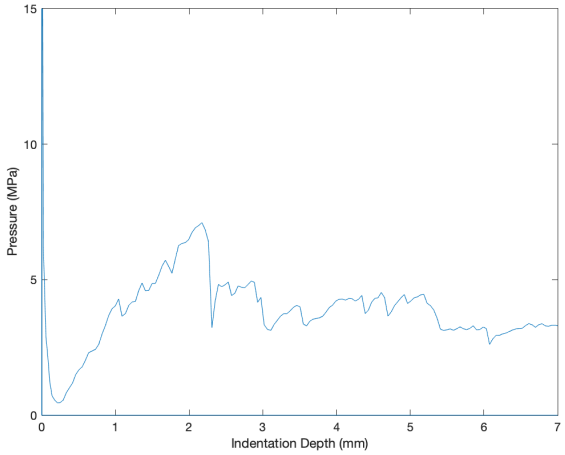

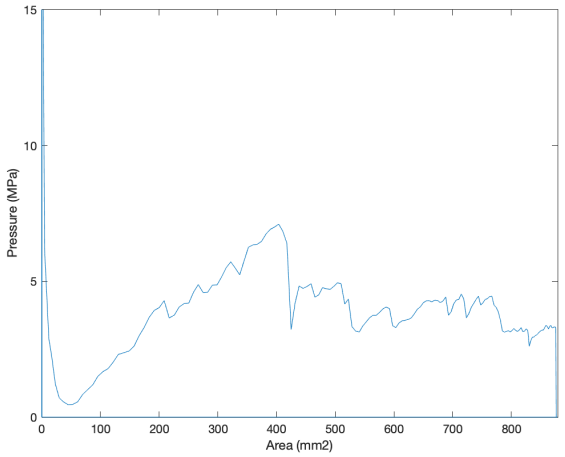

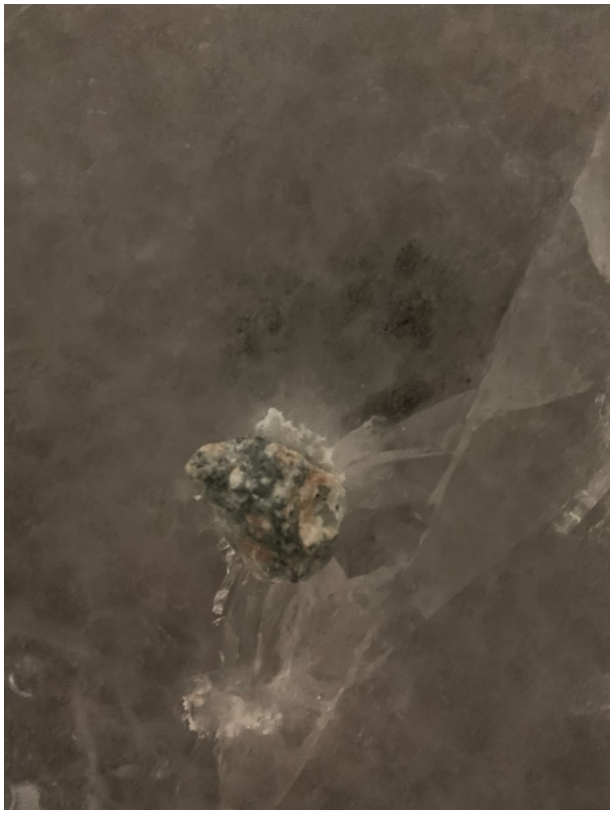

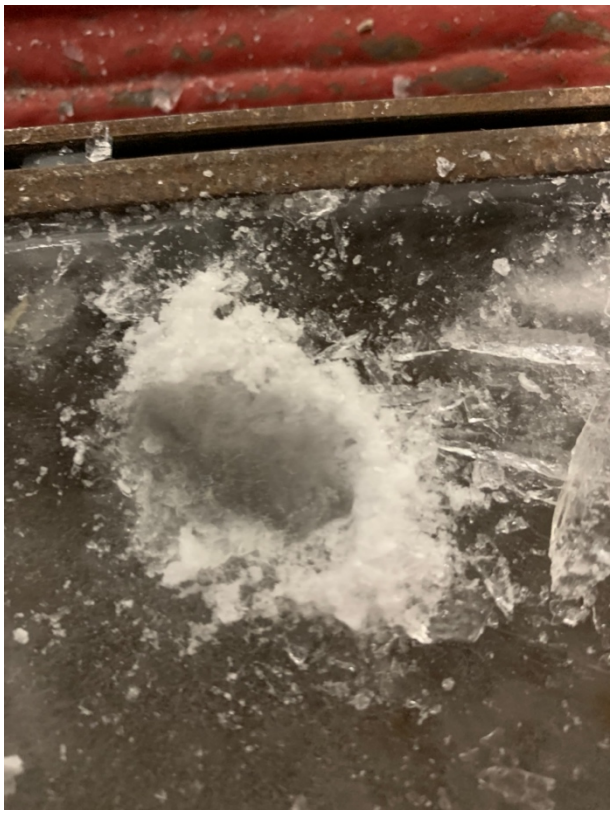

2021_06_07_(9)-96-10

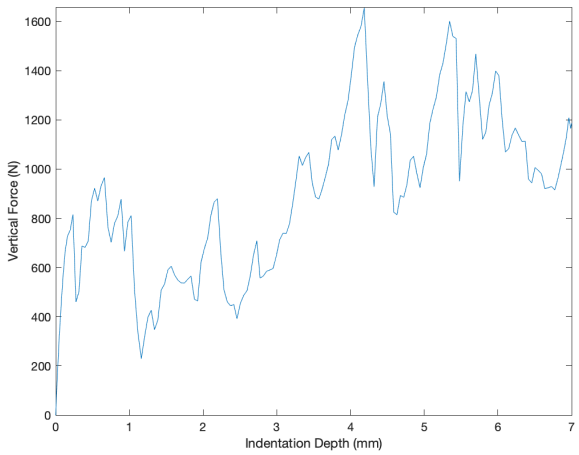

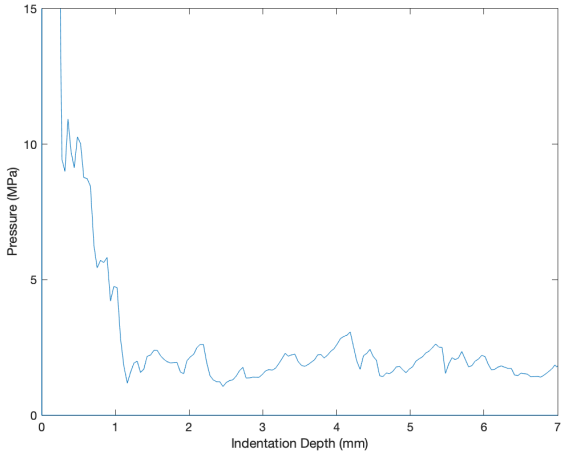

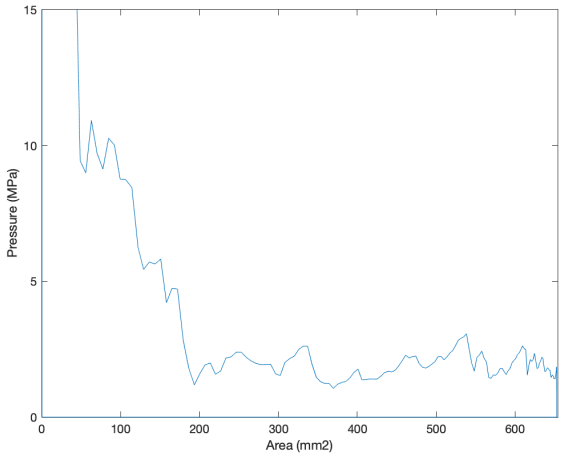

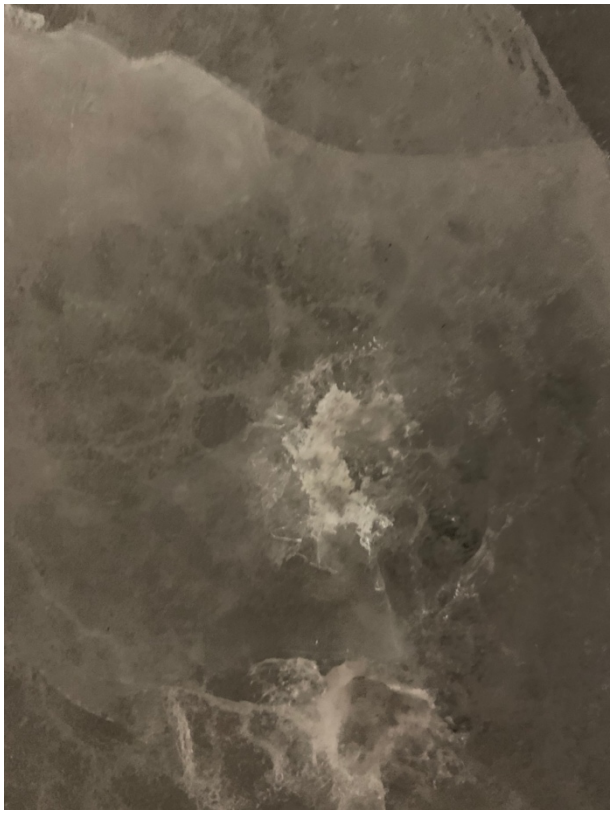

2021_06_07_(10)-96-10

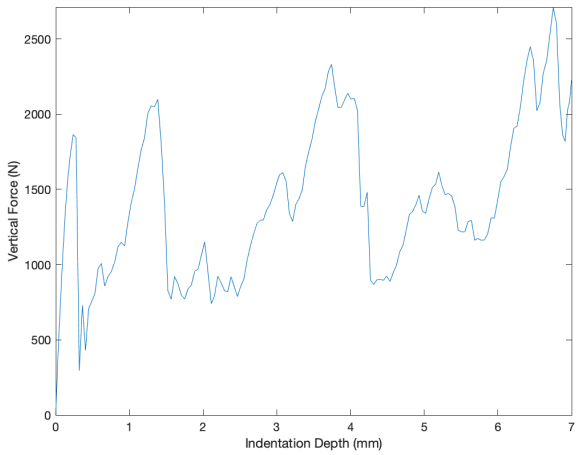

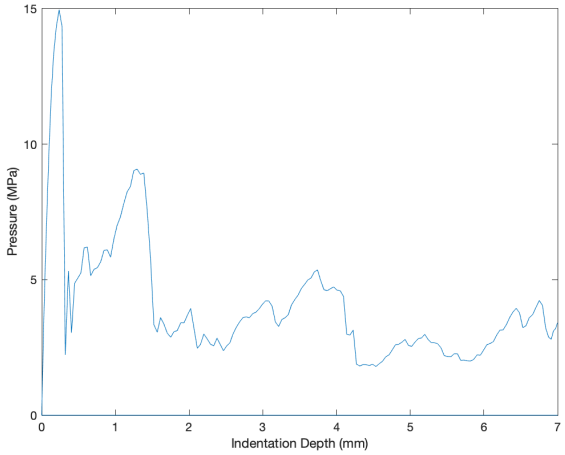

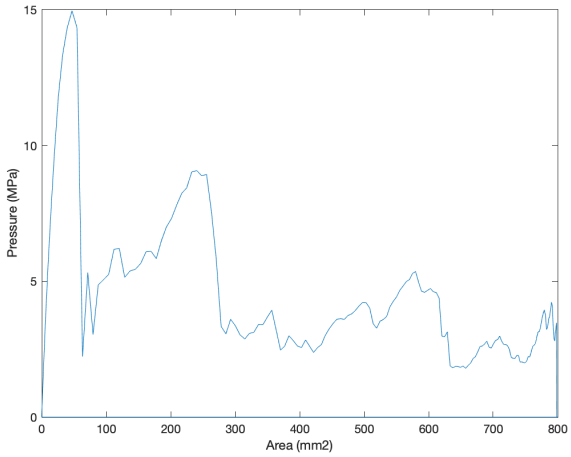

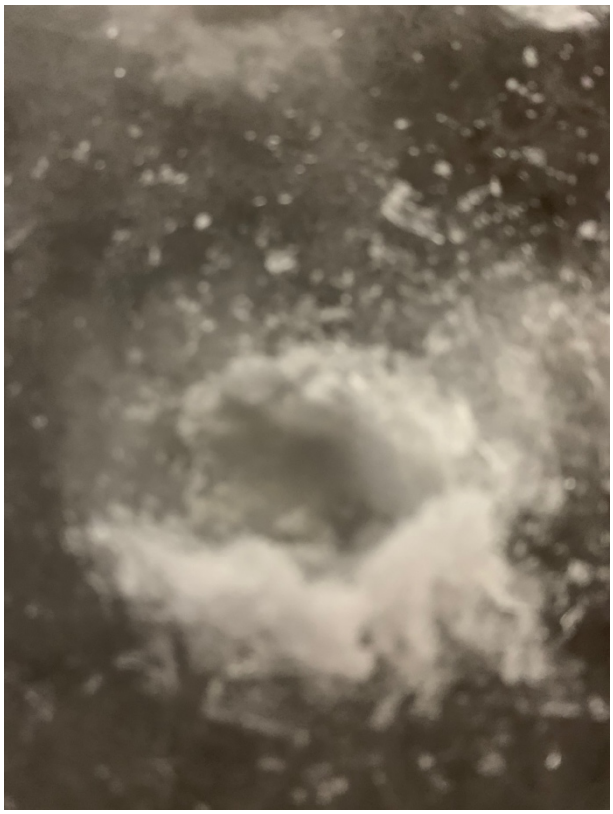

2021_07_07_(1)-65-10

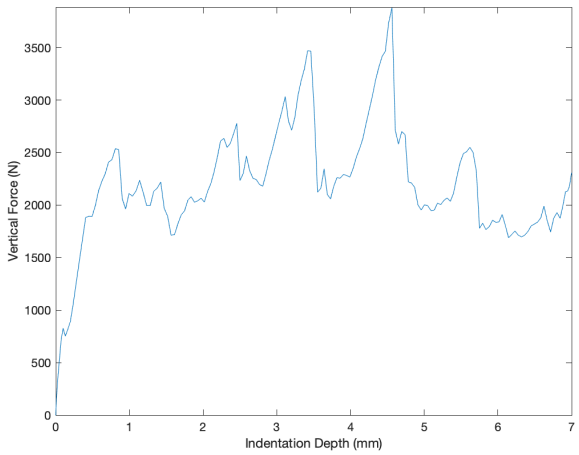

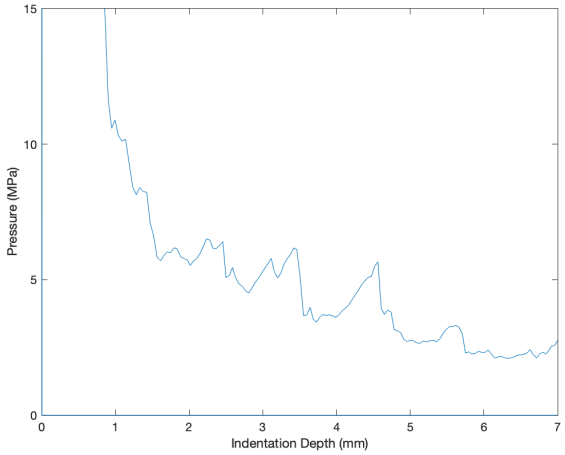

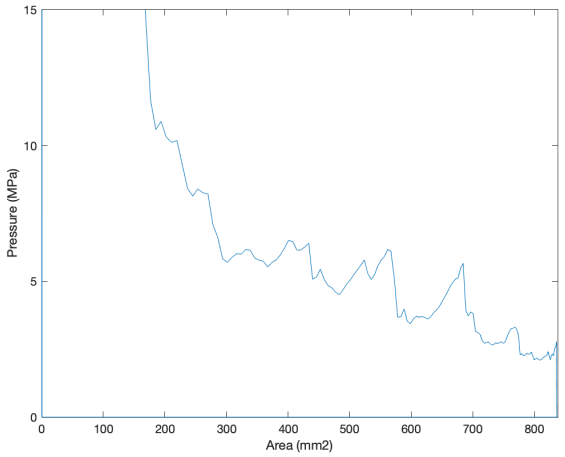

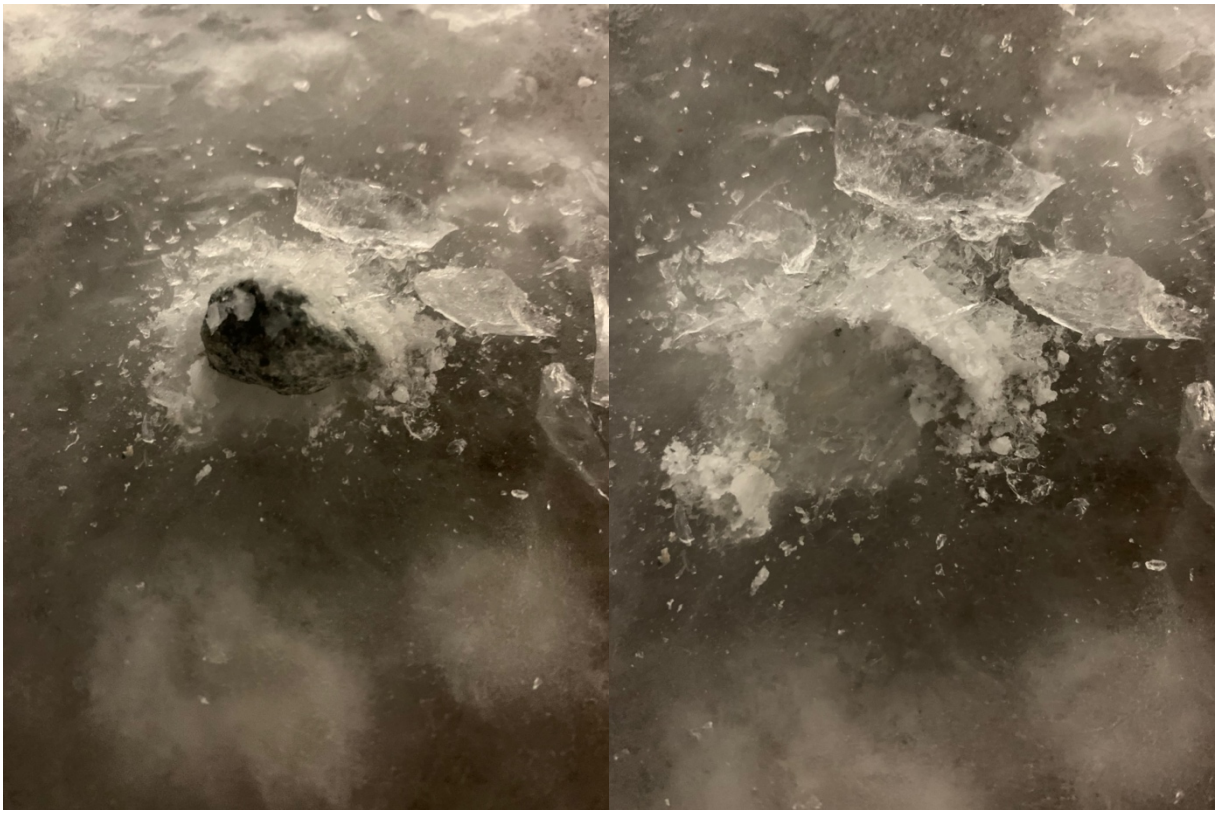

Upper image omitted due to poor quality.

2021_07_07_(2)-65-10

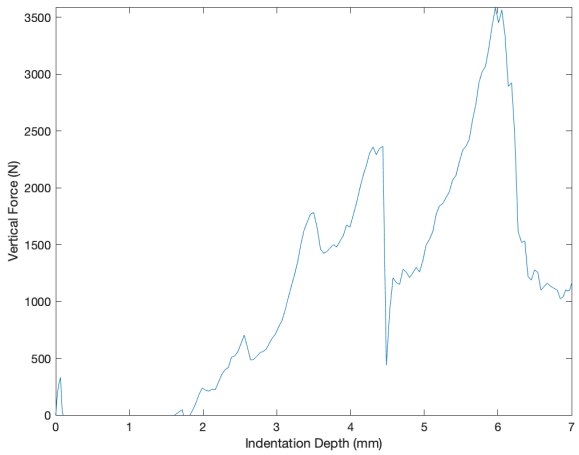

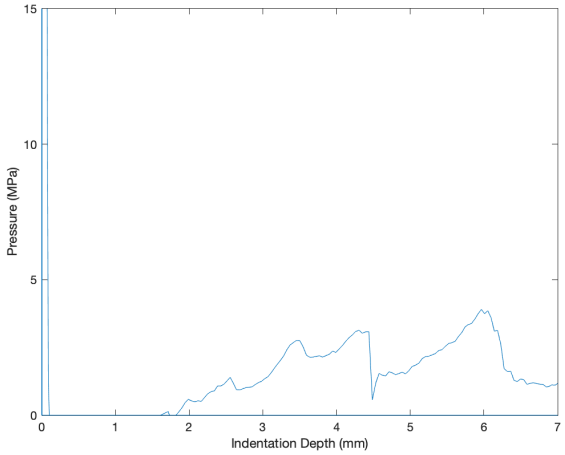

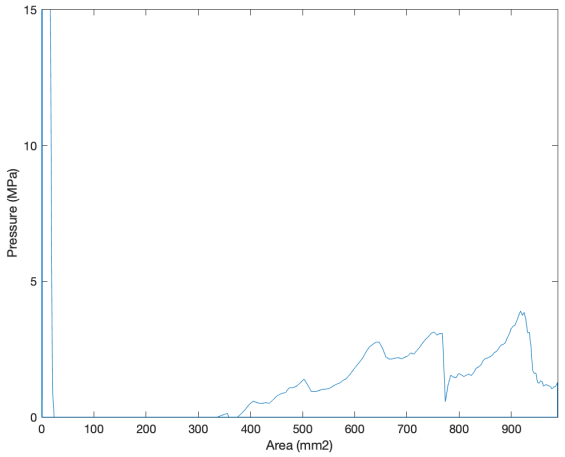

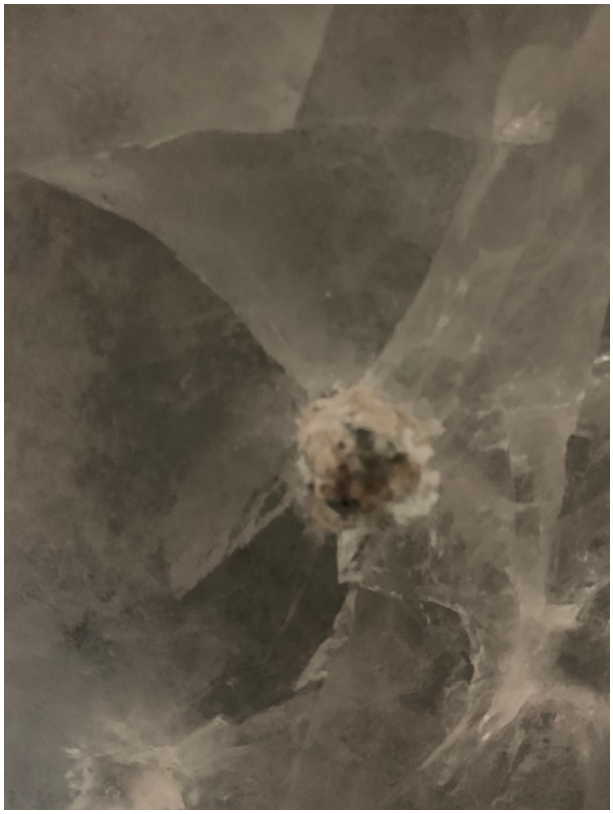

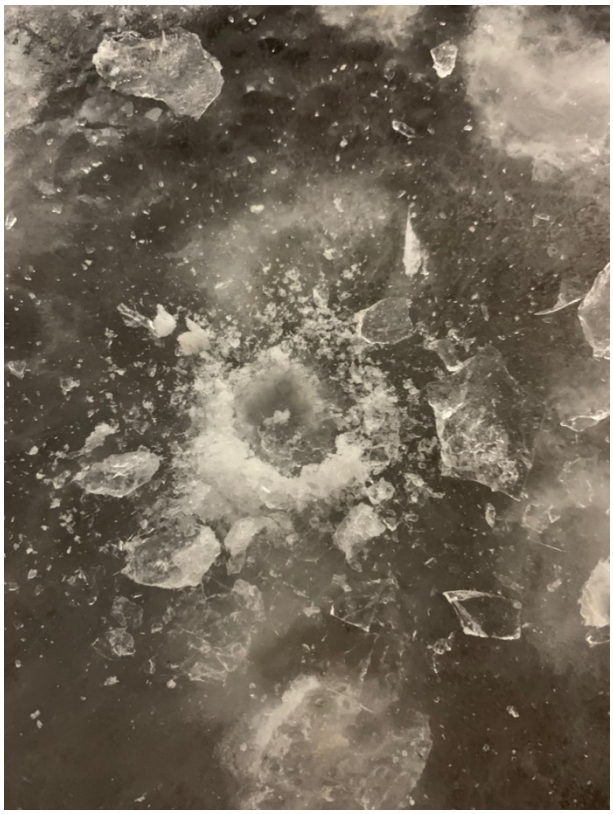

2021_07_07_(3)-65-10

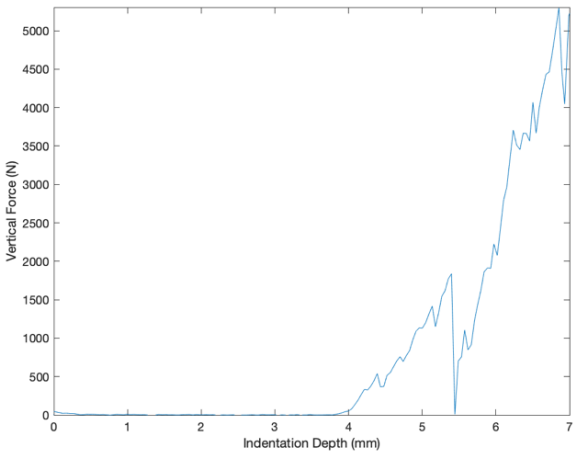

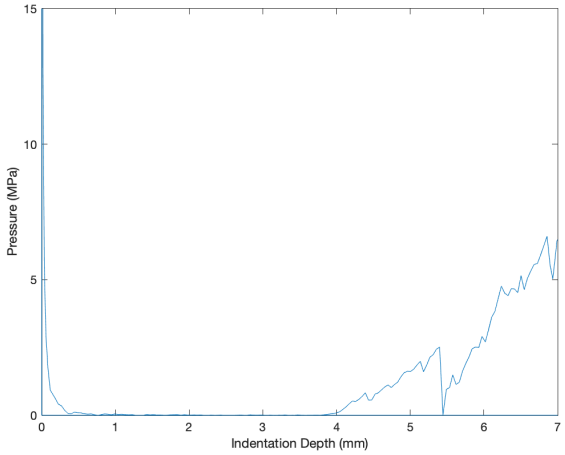

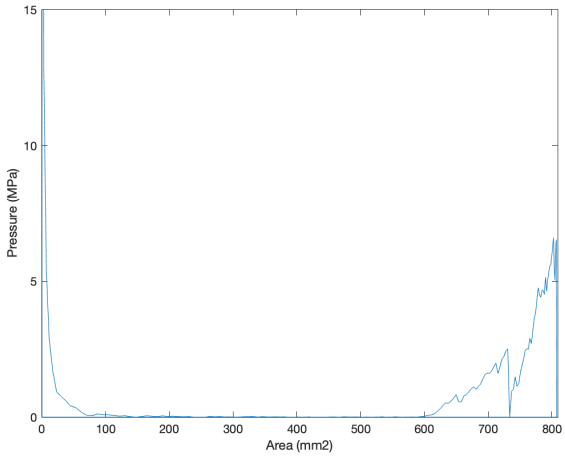

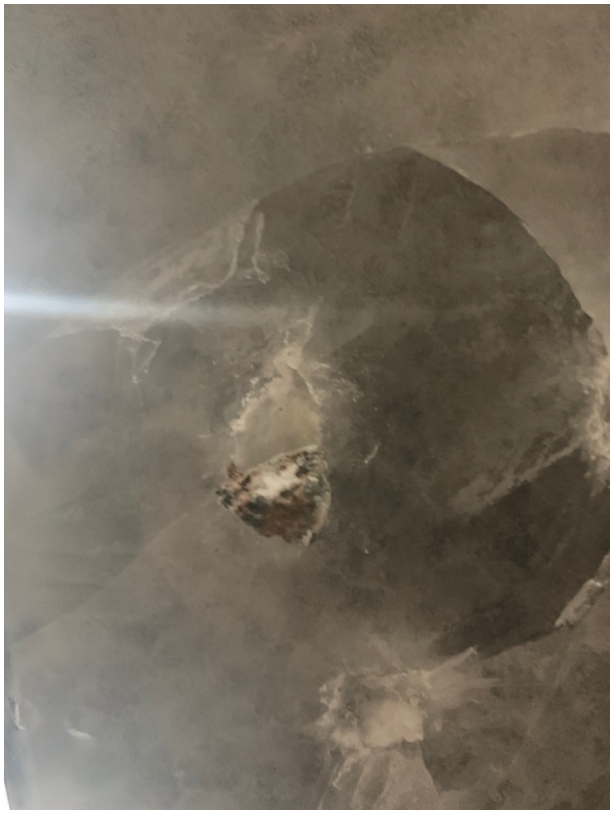

2021_07_07_(4)-65-10

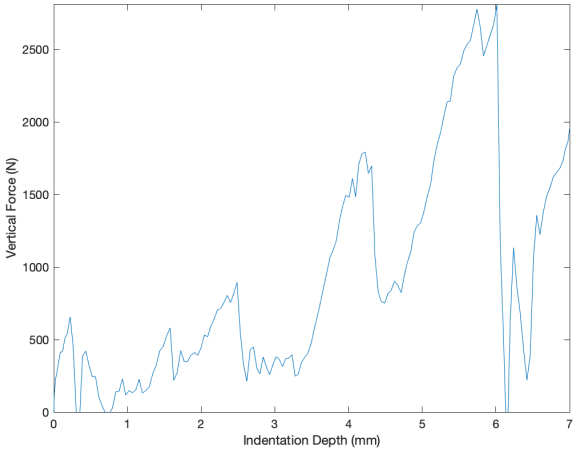

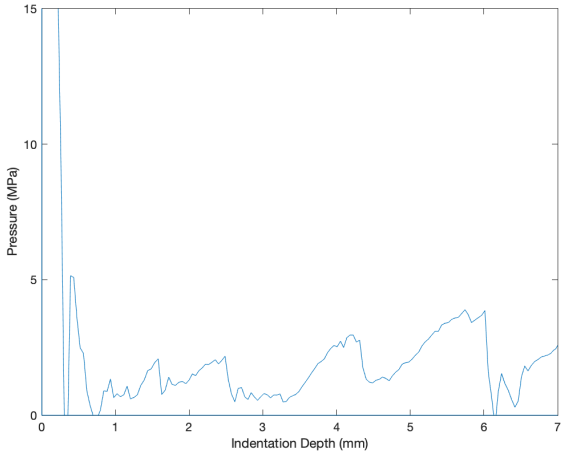

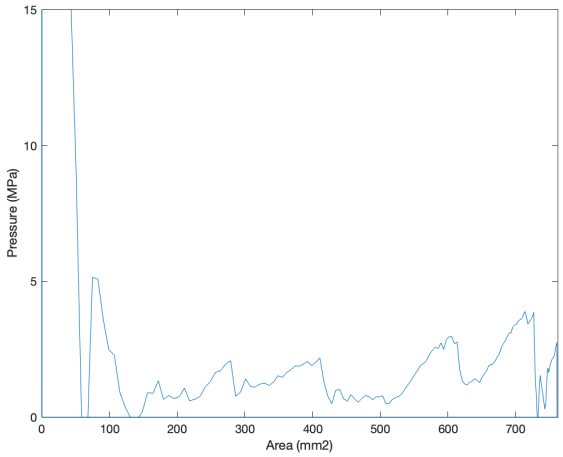

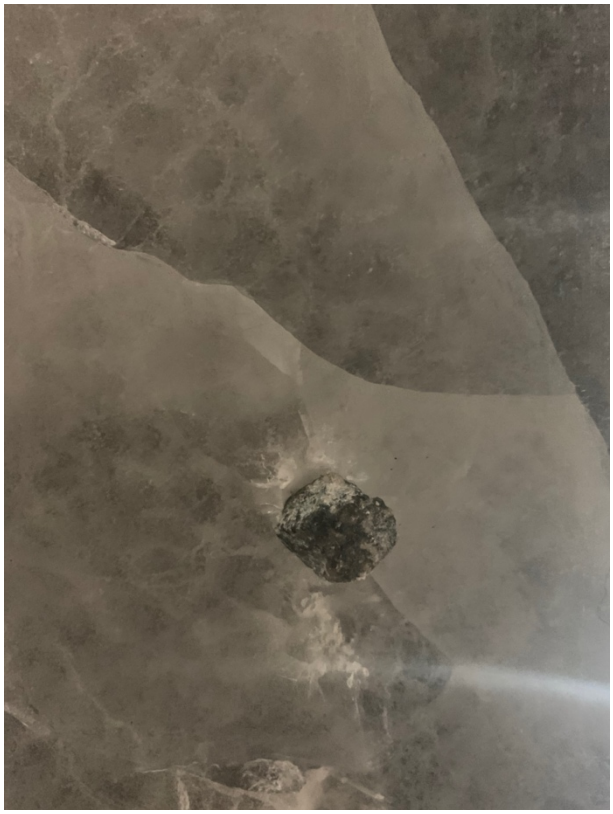

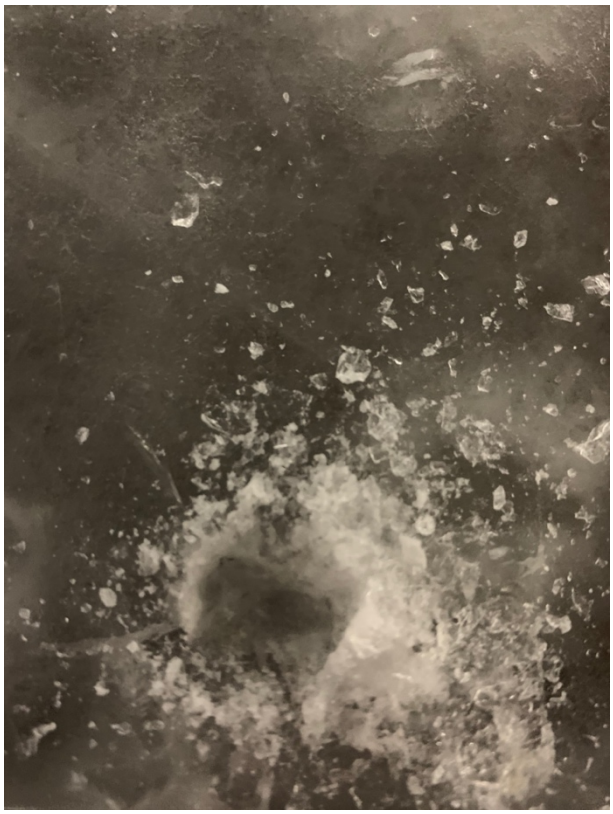

2021_07_07_(5)-65-10

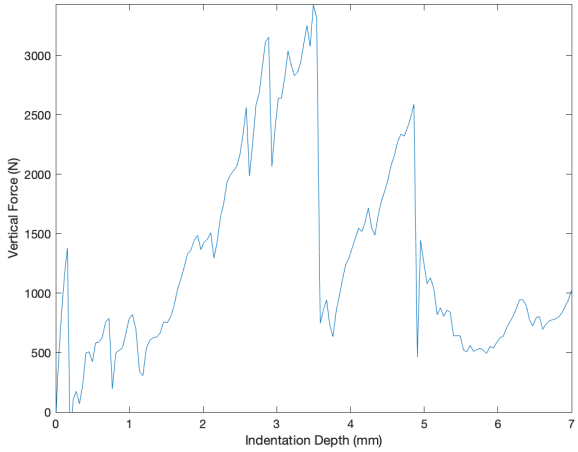

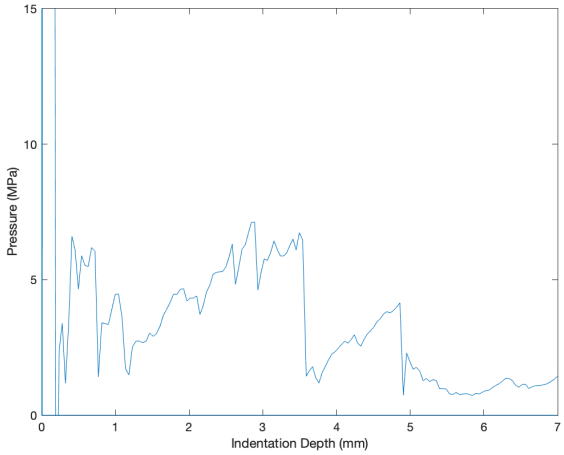

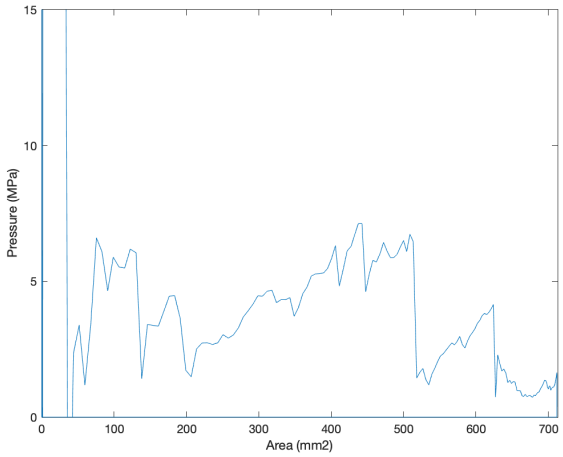

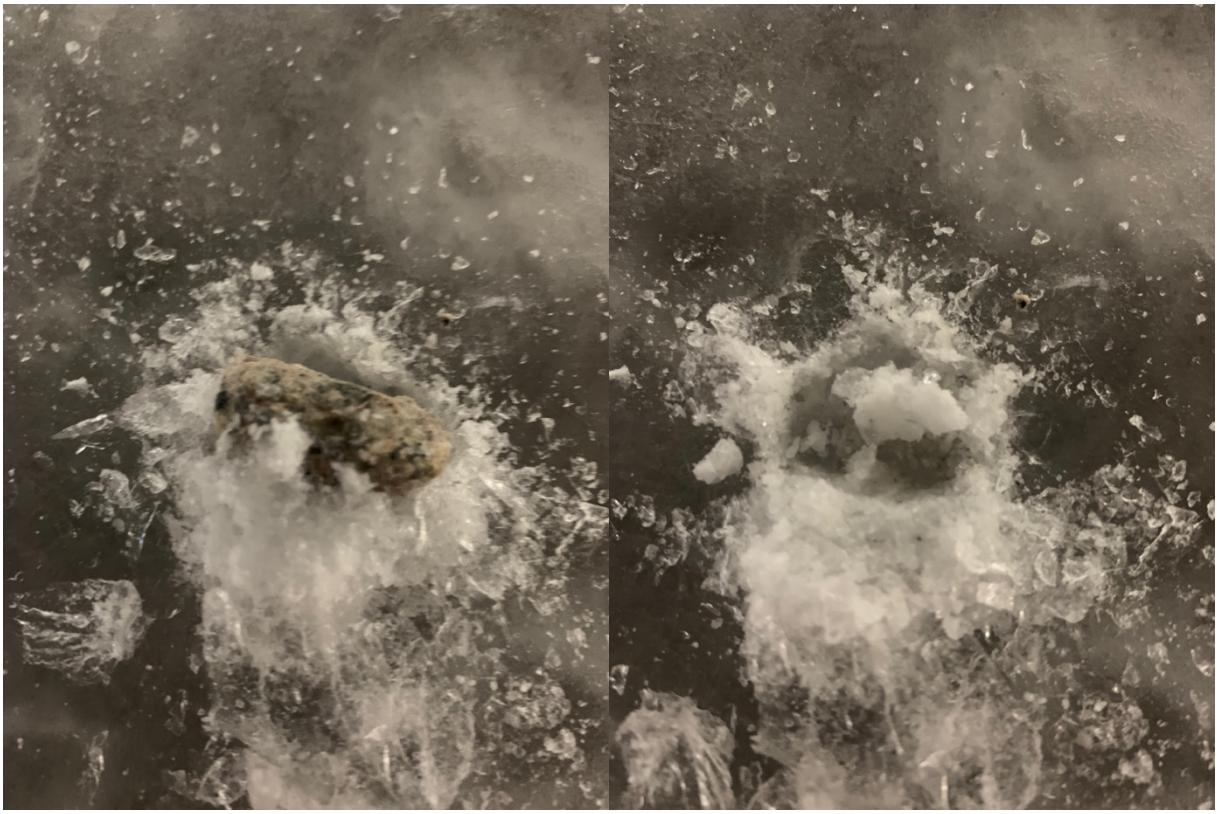

Upper image omitted due to poor quality.

2021_07_07_(6)-65-10

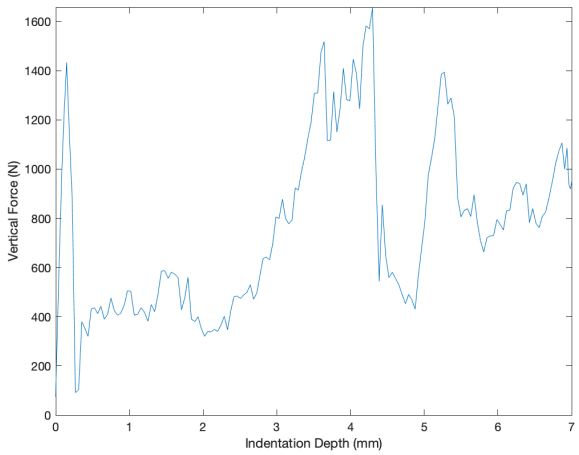

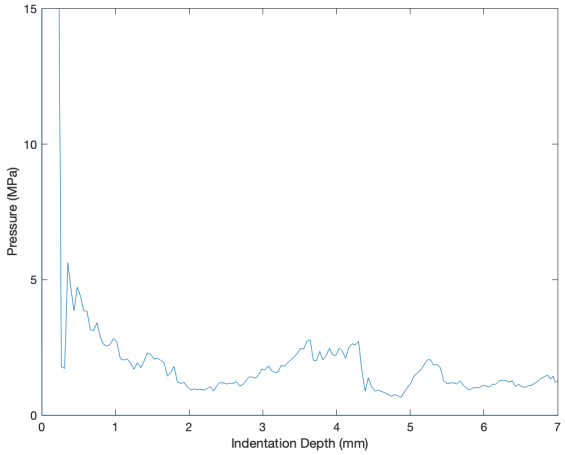

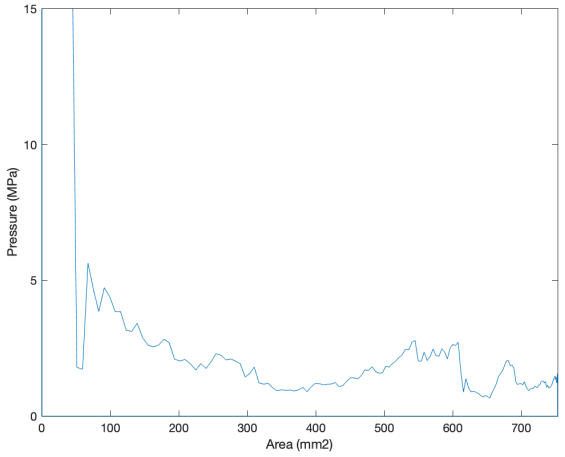

2021_07_07_(7)-65-10

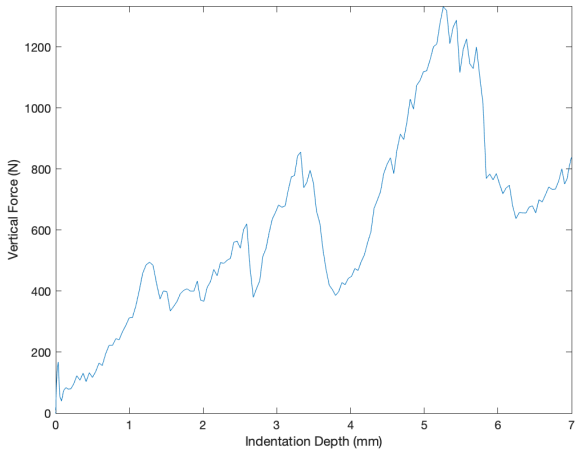

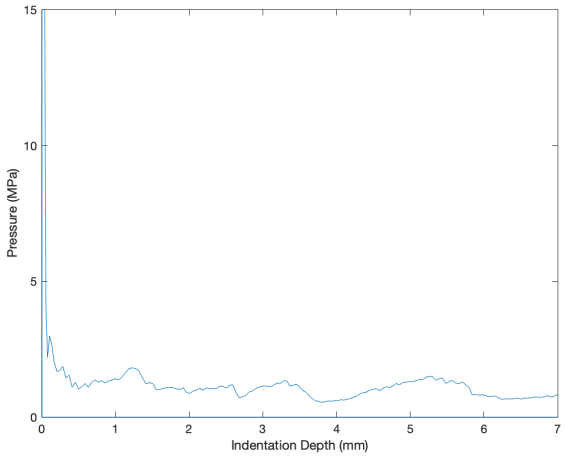

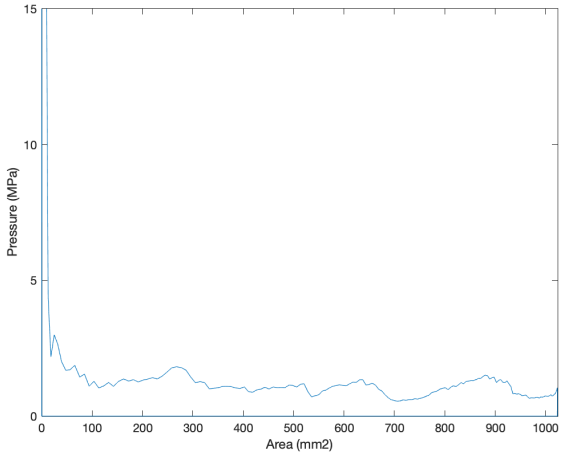

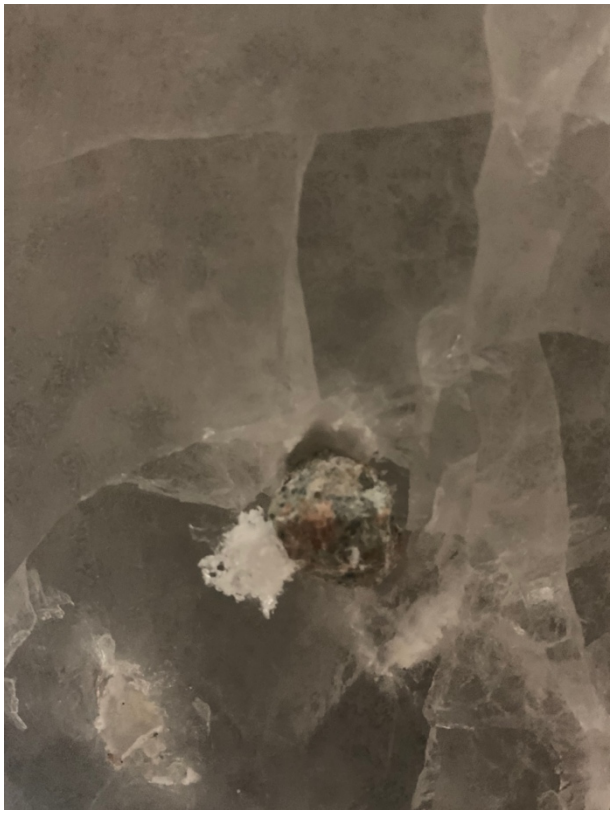

2021_07_07_(8)-65-10

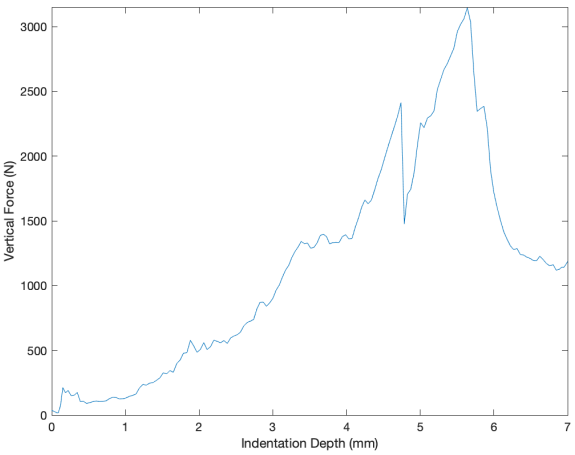

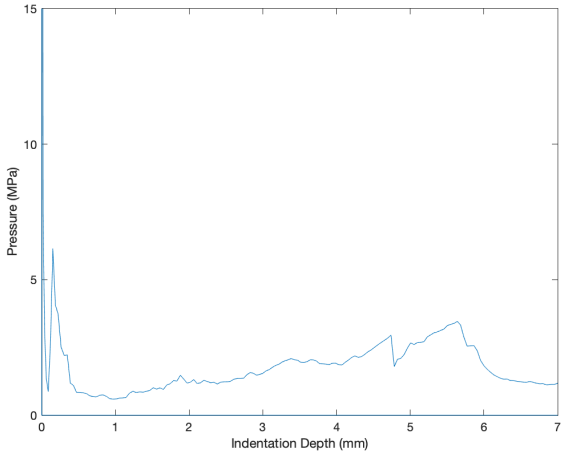

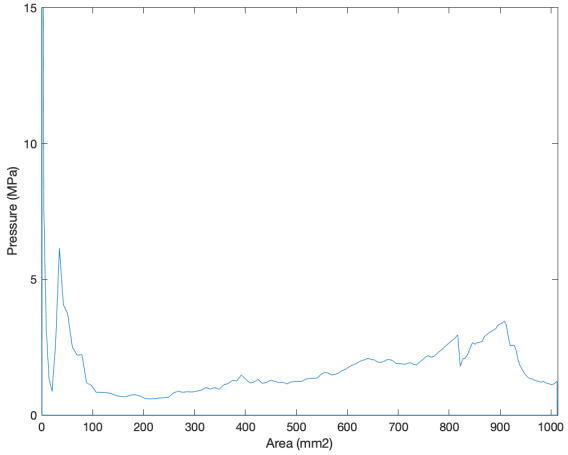

Upper image omitted due to poor quality.

2021_07_07_(9)-65-10

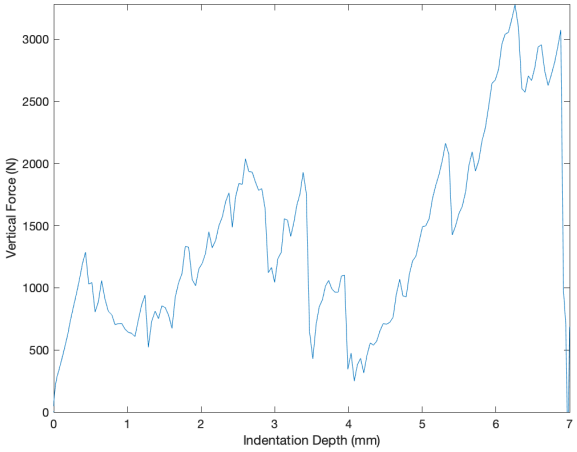

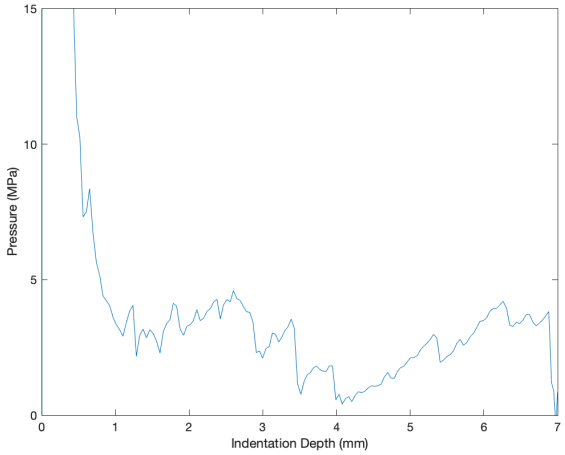

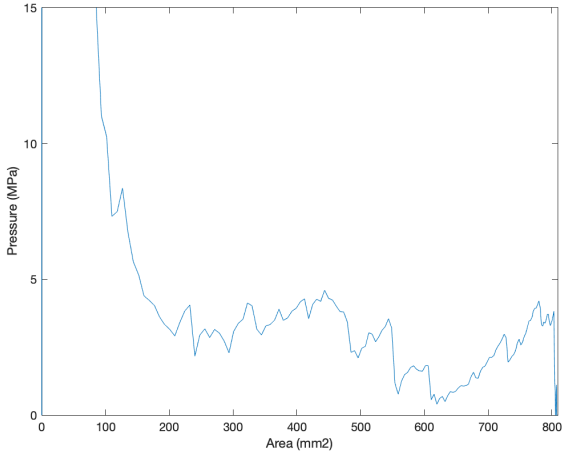

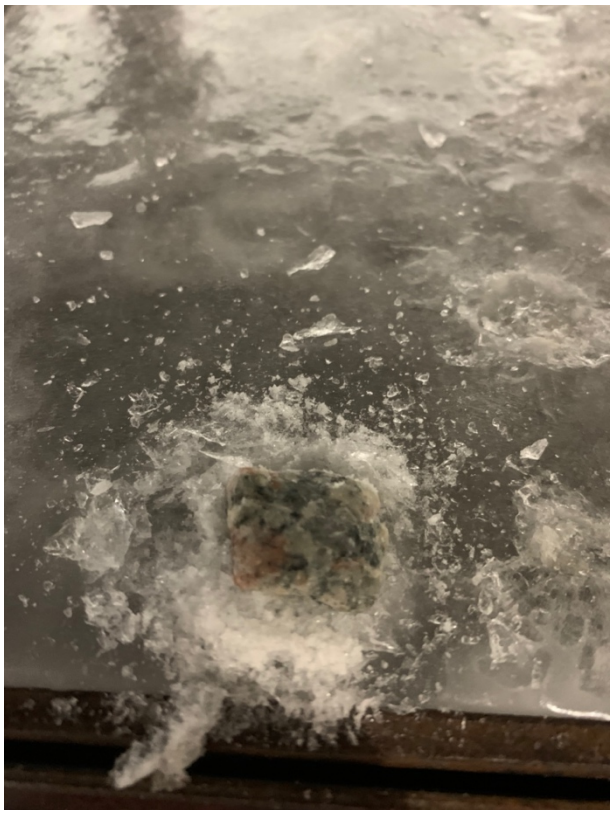

2021_07_07_(10)-65-10

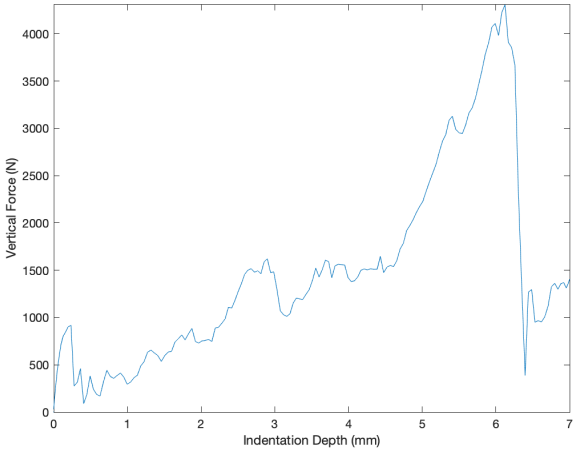

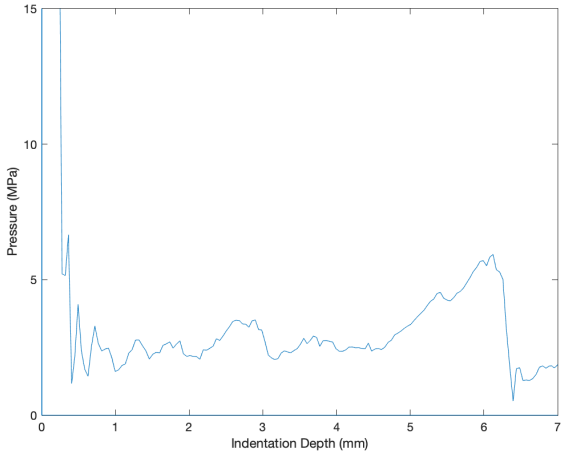

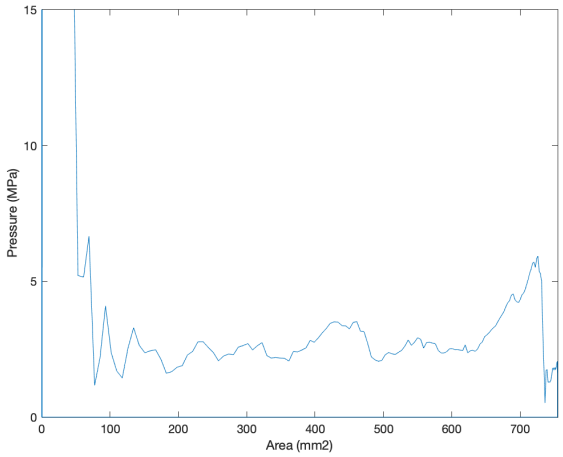

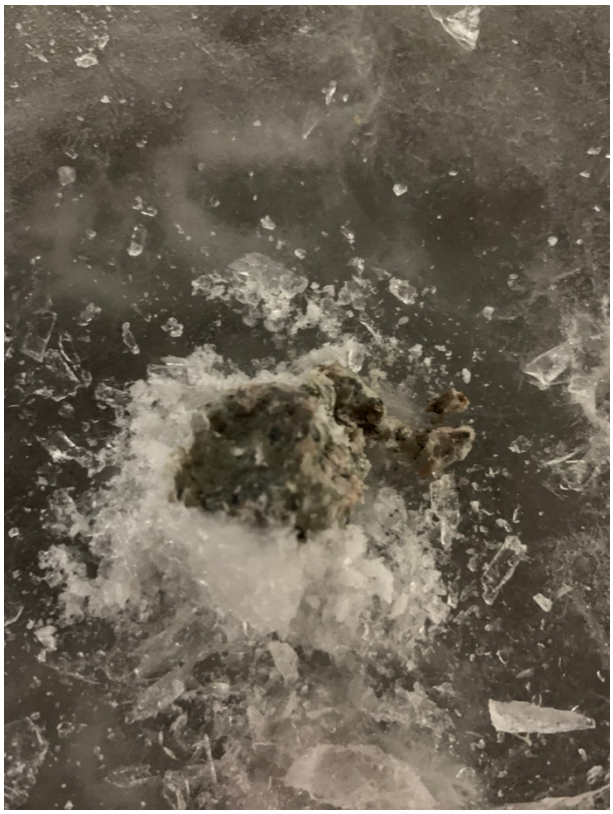

2021_08_07_(1)-26-10

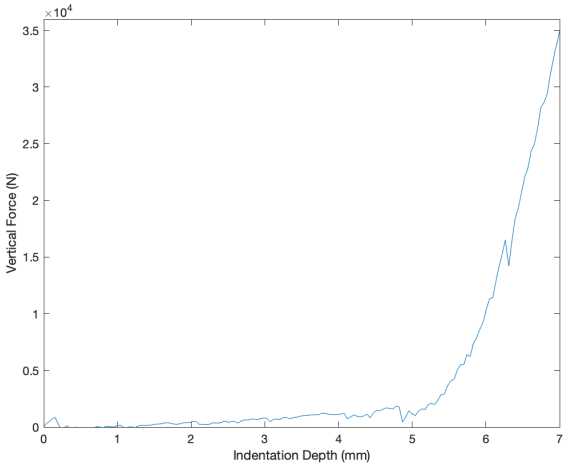

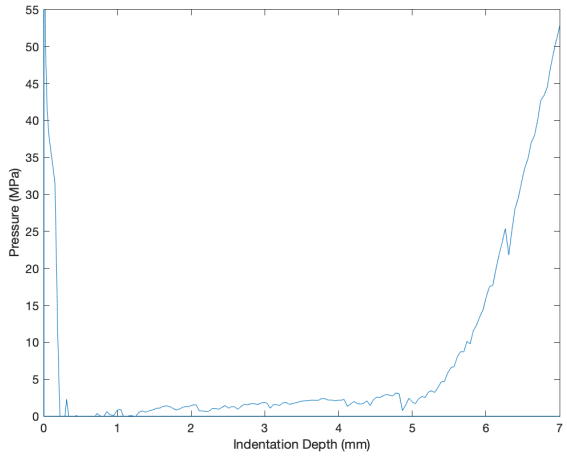

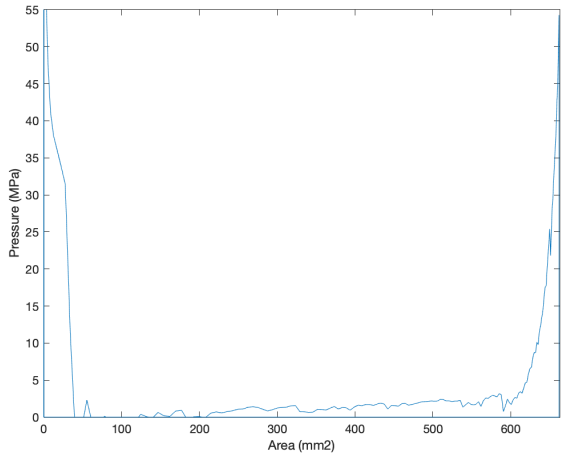

Upper image omitted due to poor quality.

2021_08_07_(2)-26-10

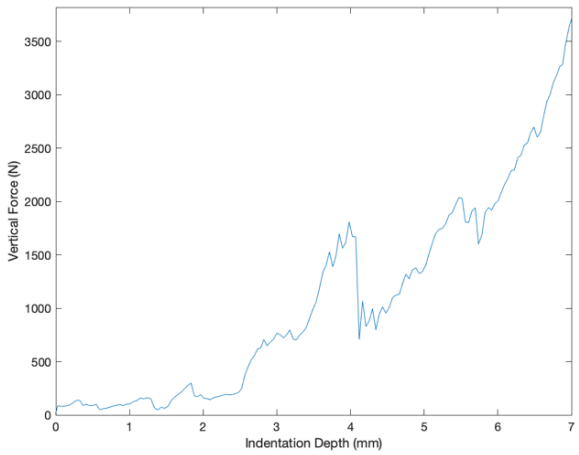

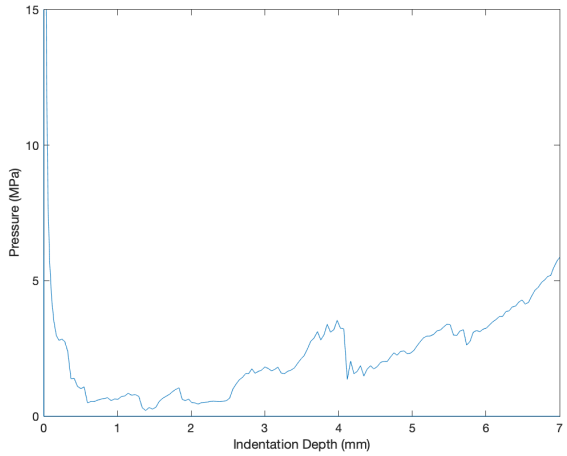

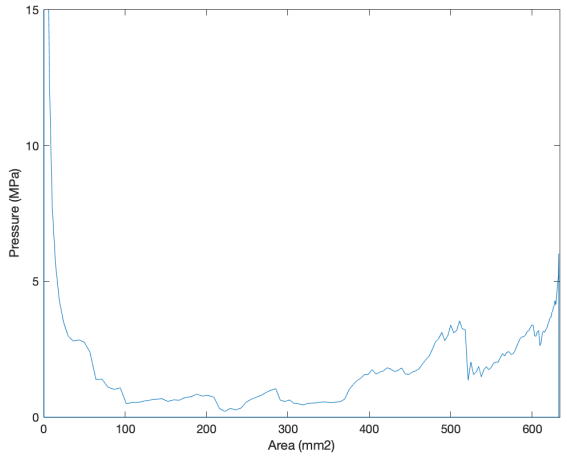

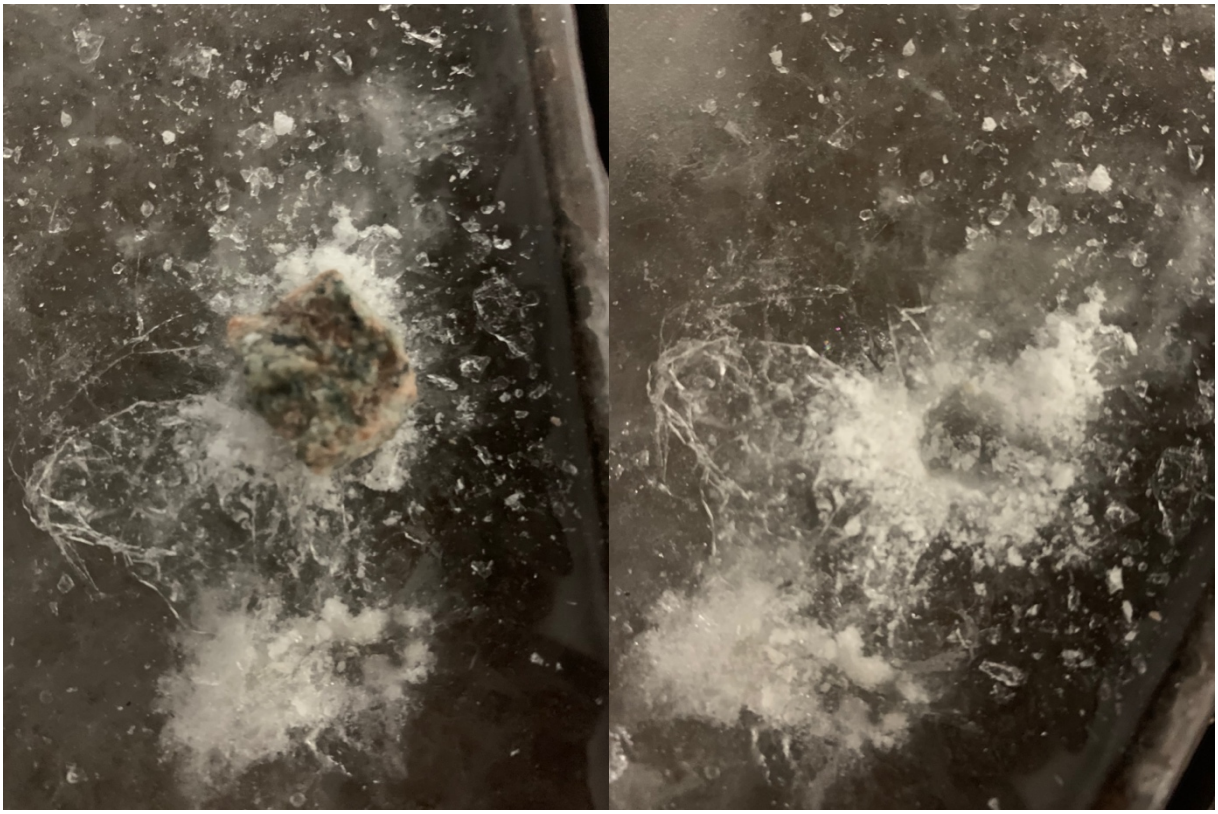

Upper image omitted due to poor quality.

2021_08_07_(3)-26-10

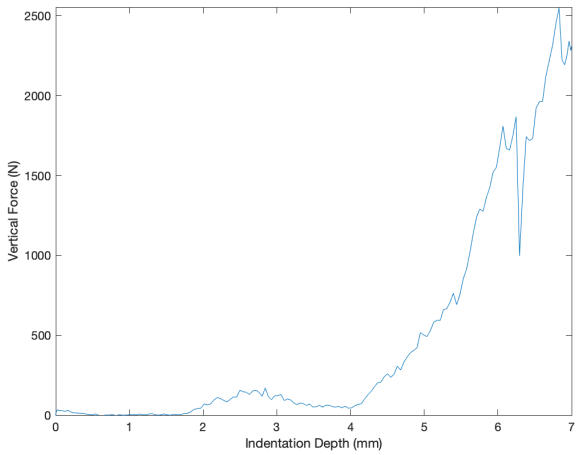

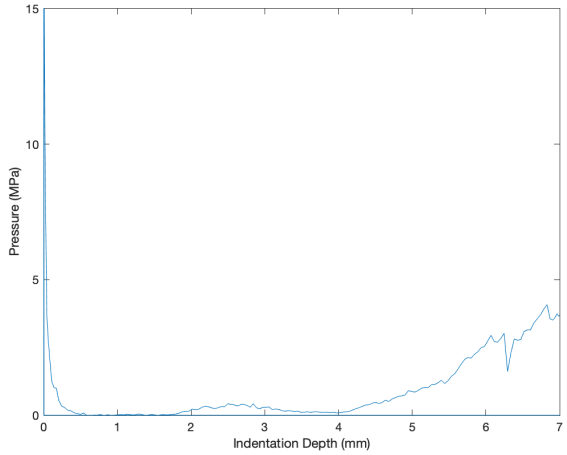

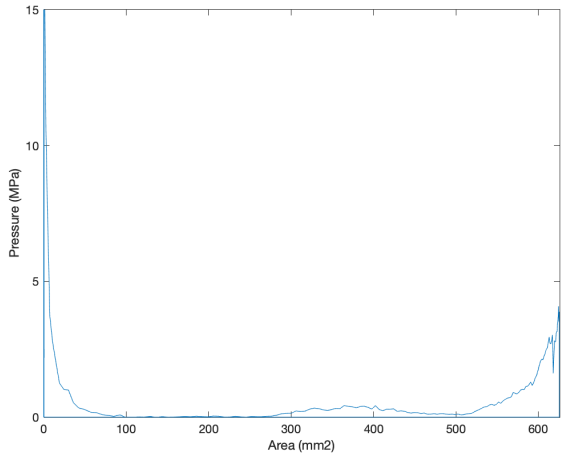

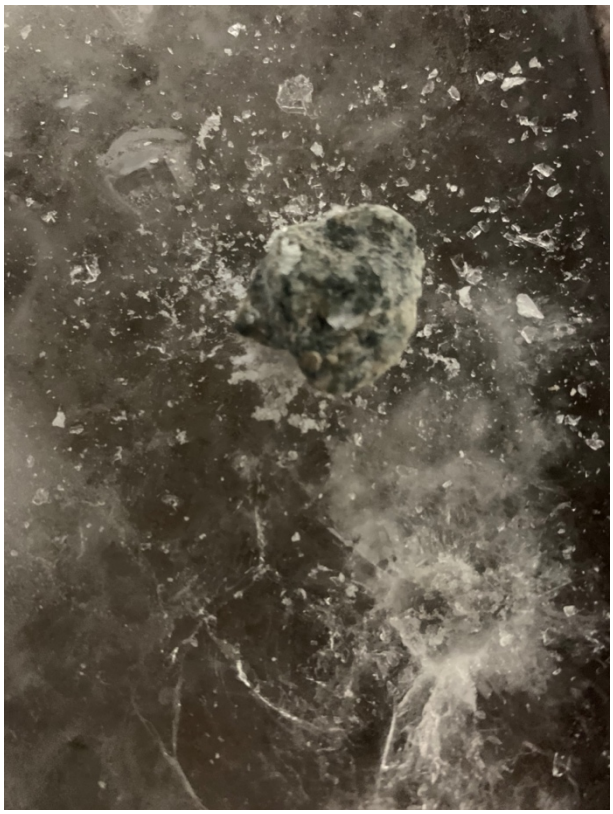

2021_08_07_(4)-26-10

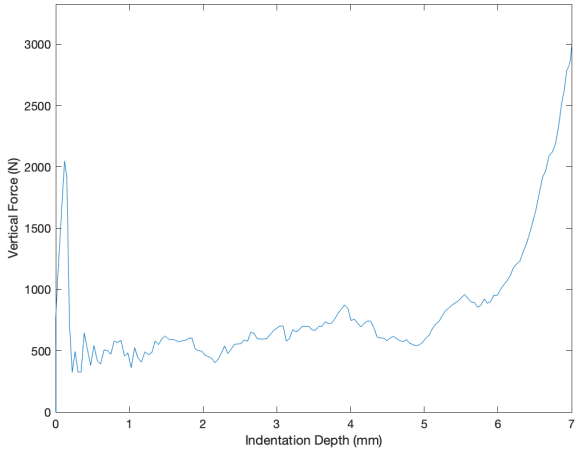

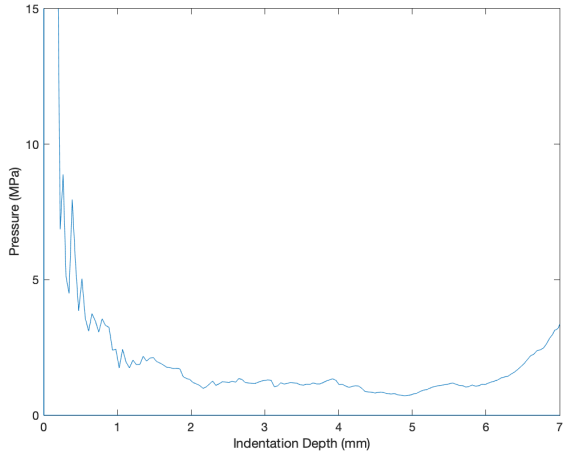

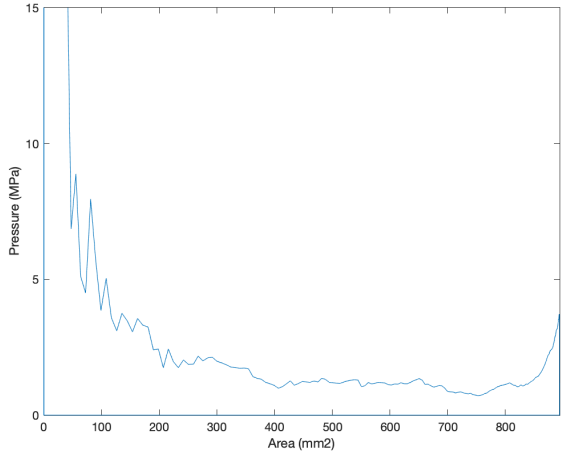

2021_08_07_(5)-26-10

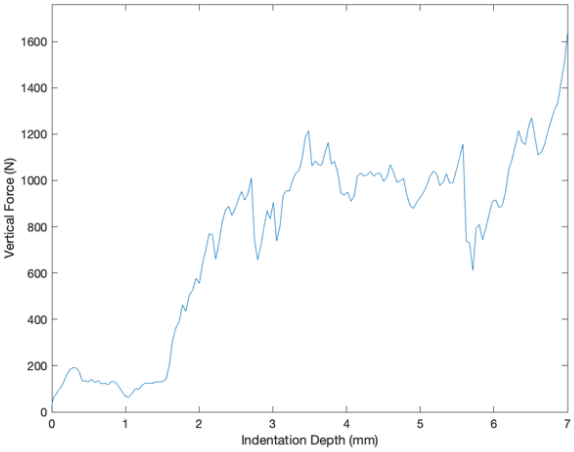

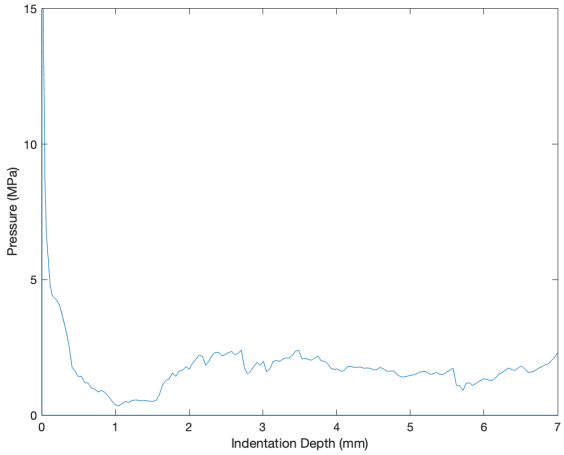

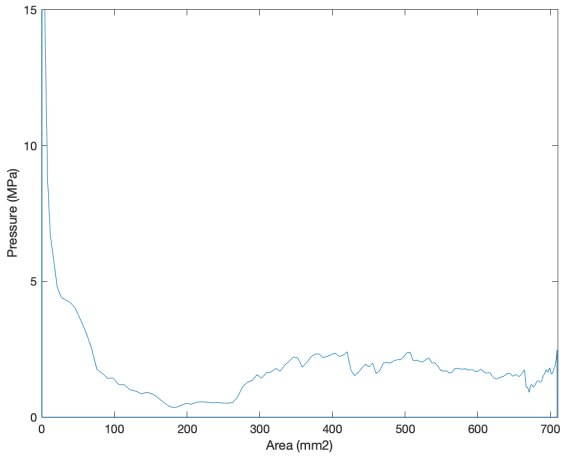

2021_08_07_(6)-26-10

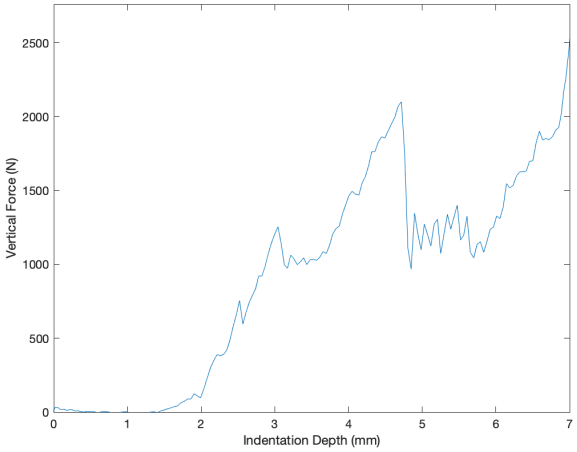

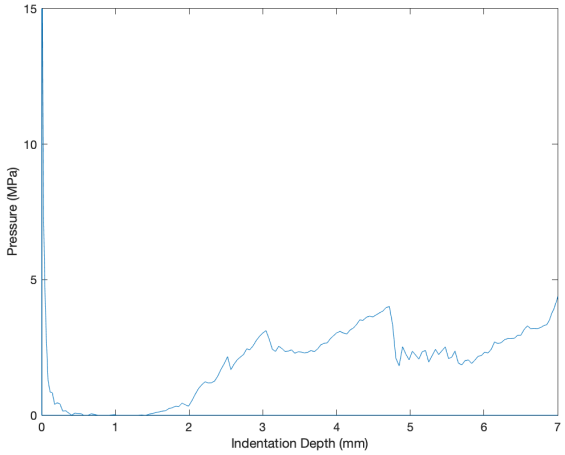

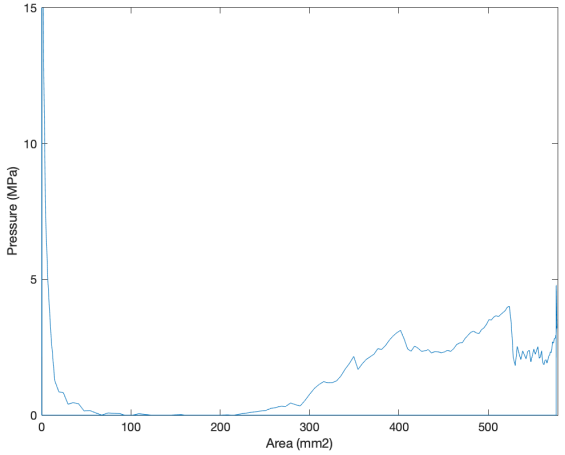

2021_08_07_(7)-26-10

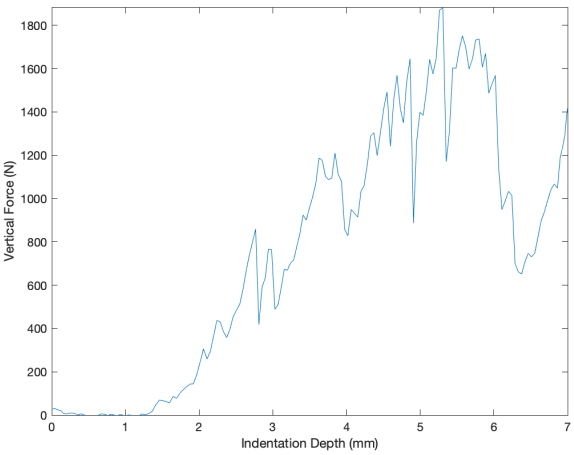

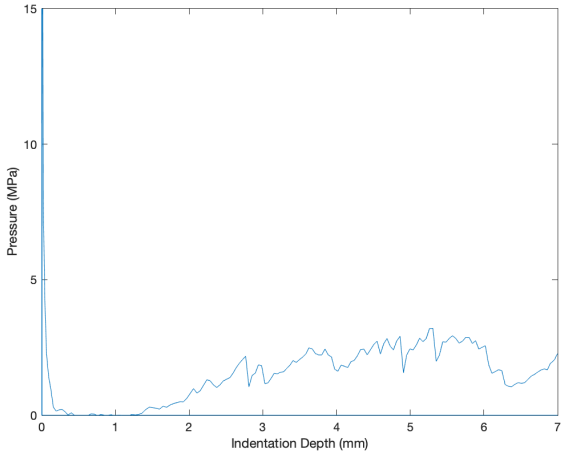

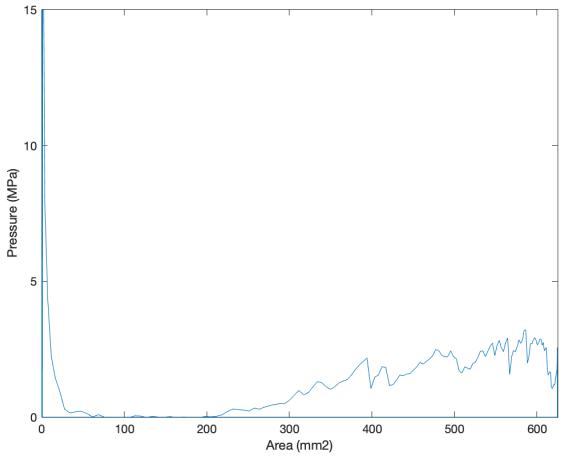

2021_08_07_(8)-26-10

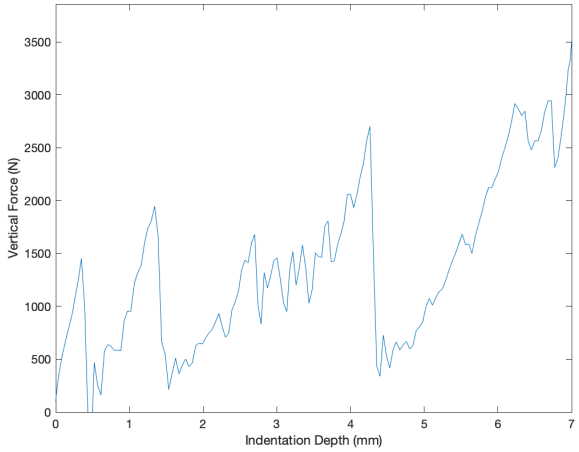

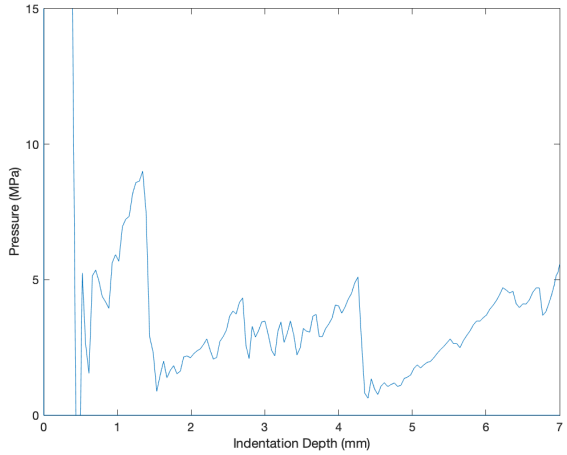

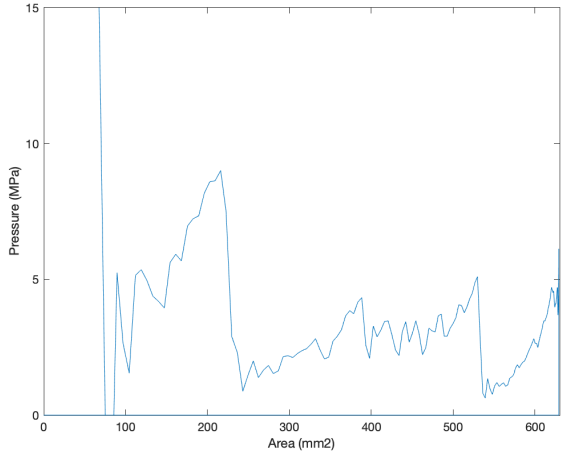

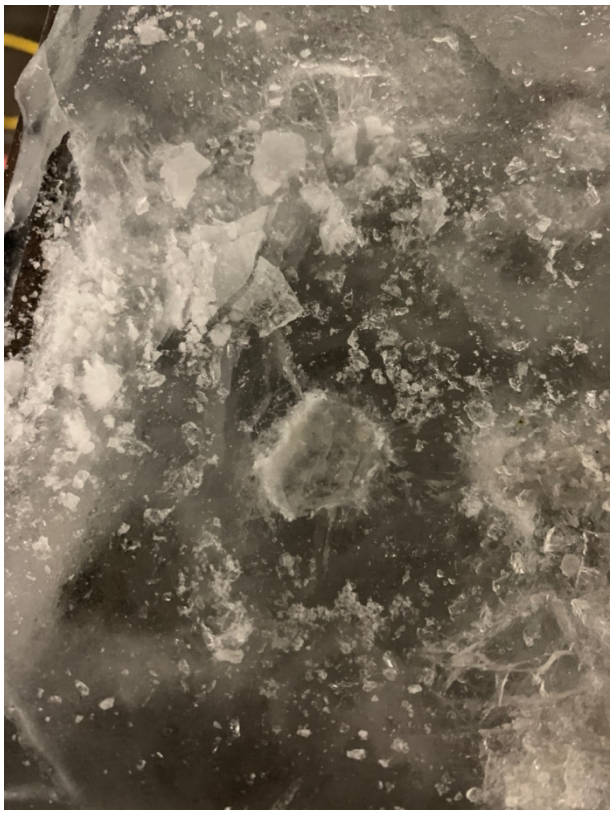

2021_08_07_(9)-26-10

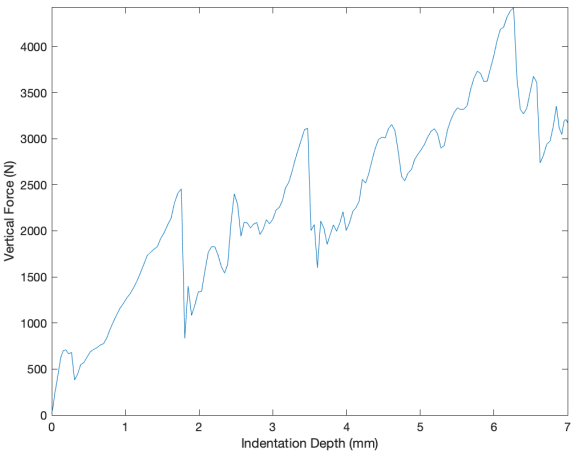

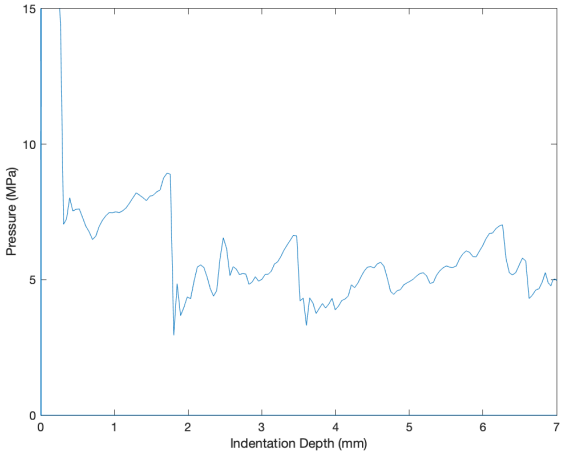

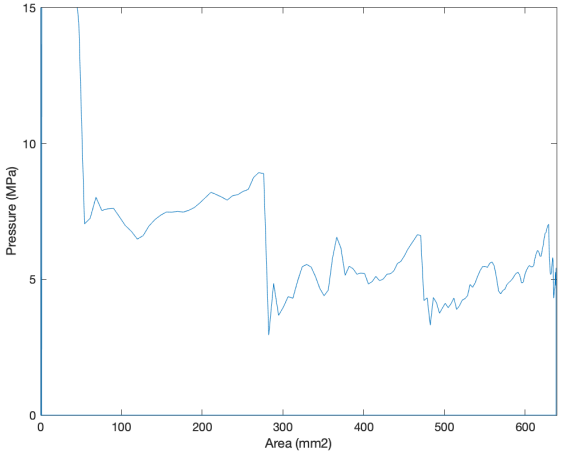

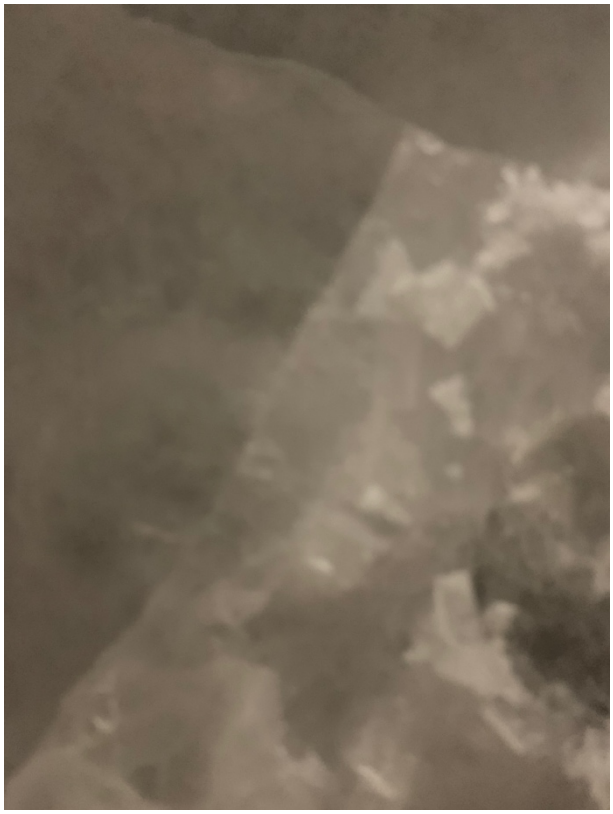

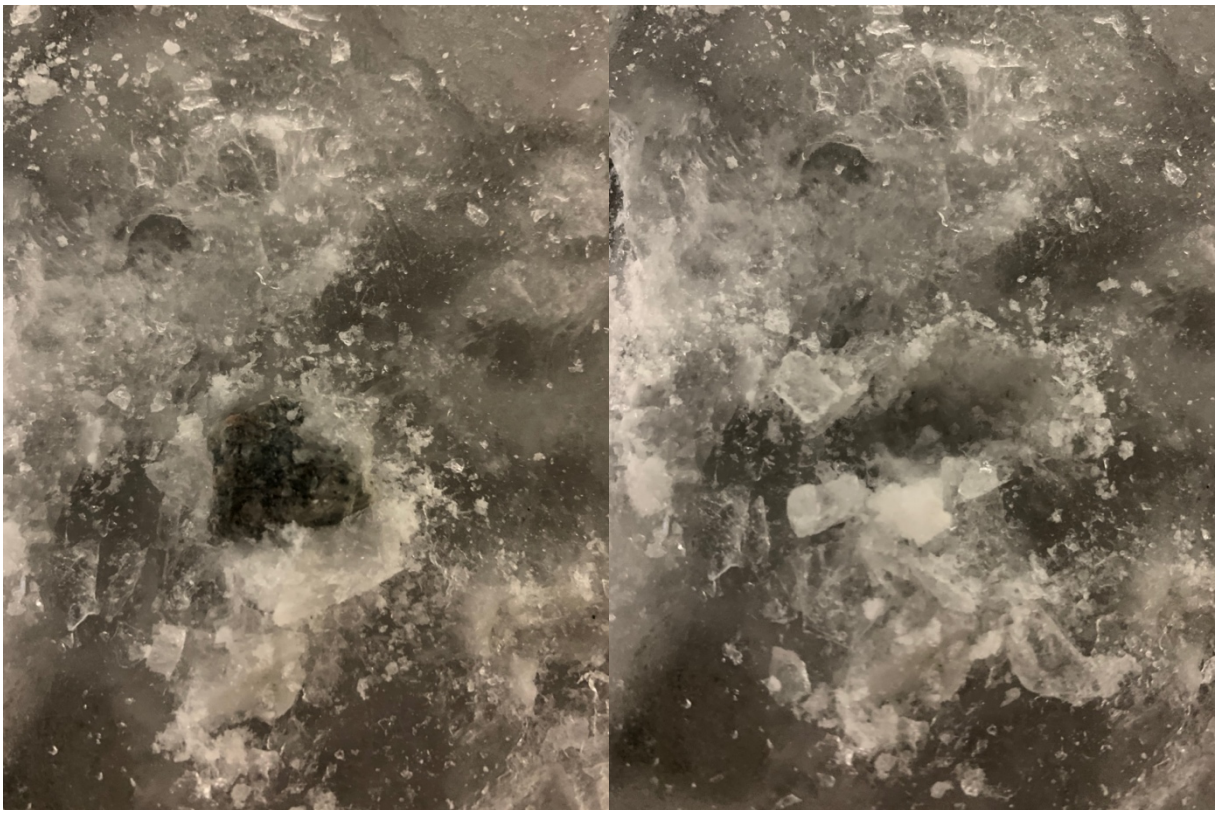

2021_08_07_(10)-26-10

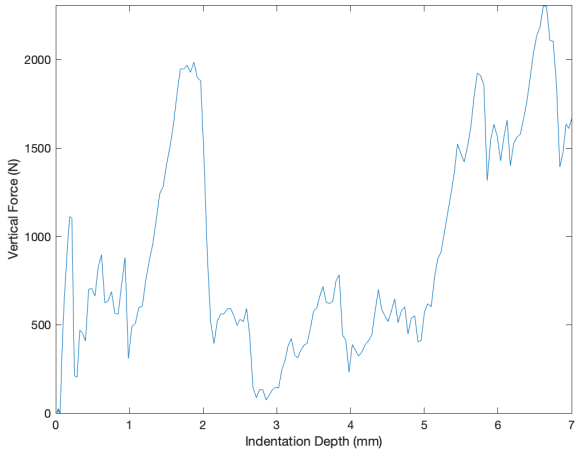

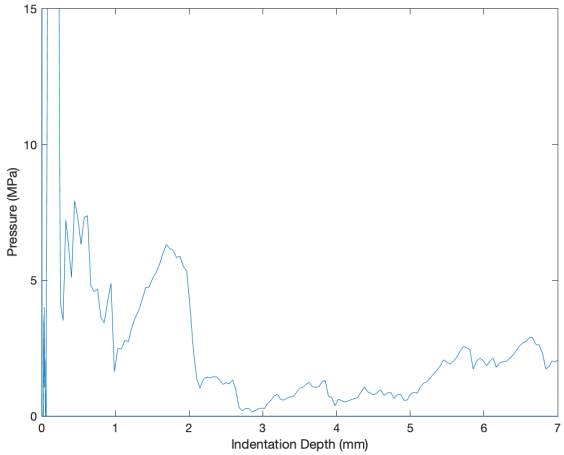

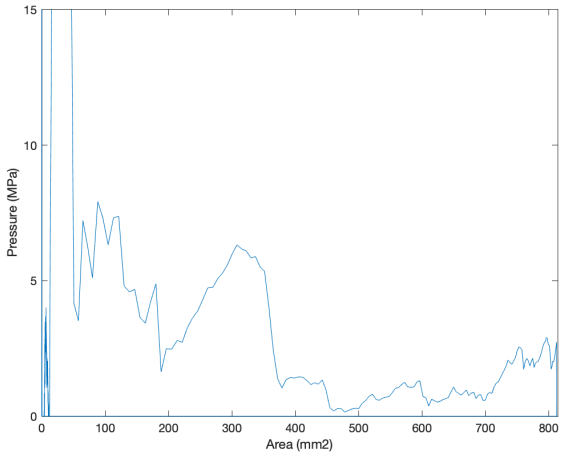

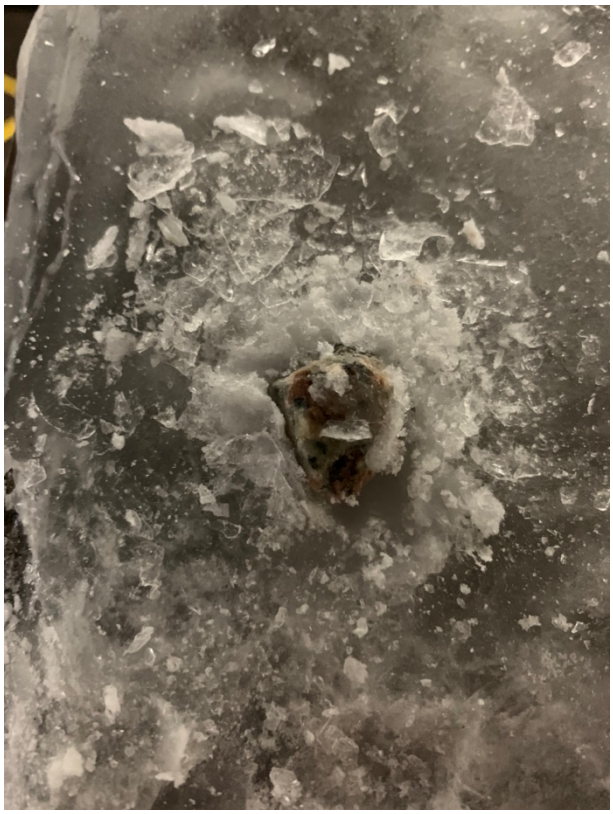

APPENDIX B – Additional Multiple Particle Test Results: Total Load, Images Taken After Indentation.

2020_09_11_(1)-15-0-1

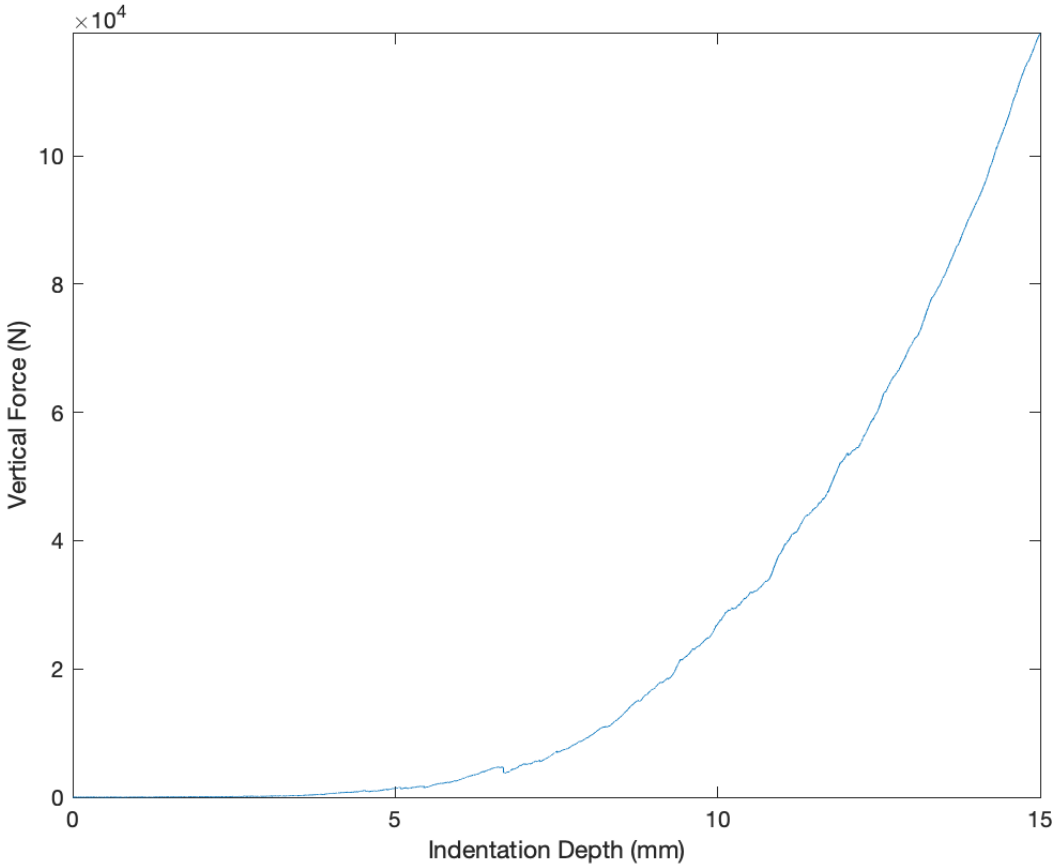

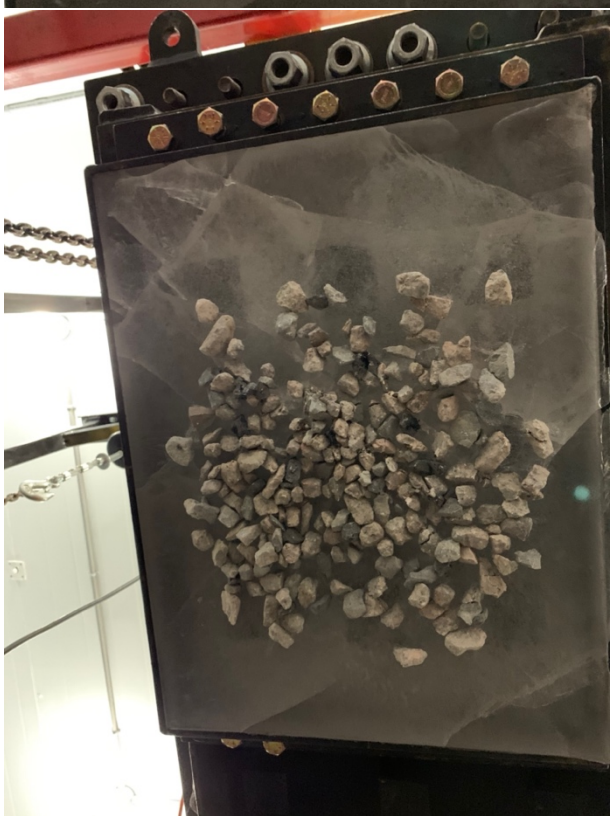

2020_10_11_(1)-15-0-1

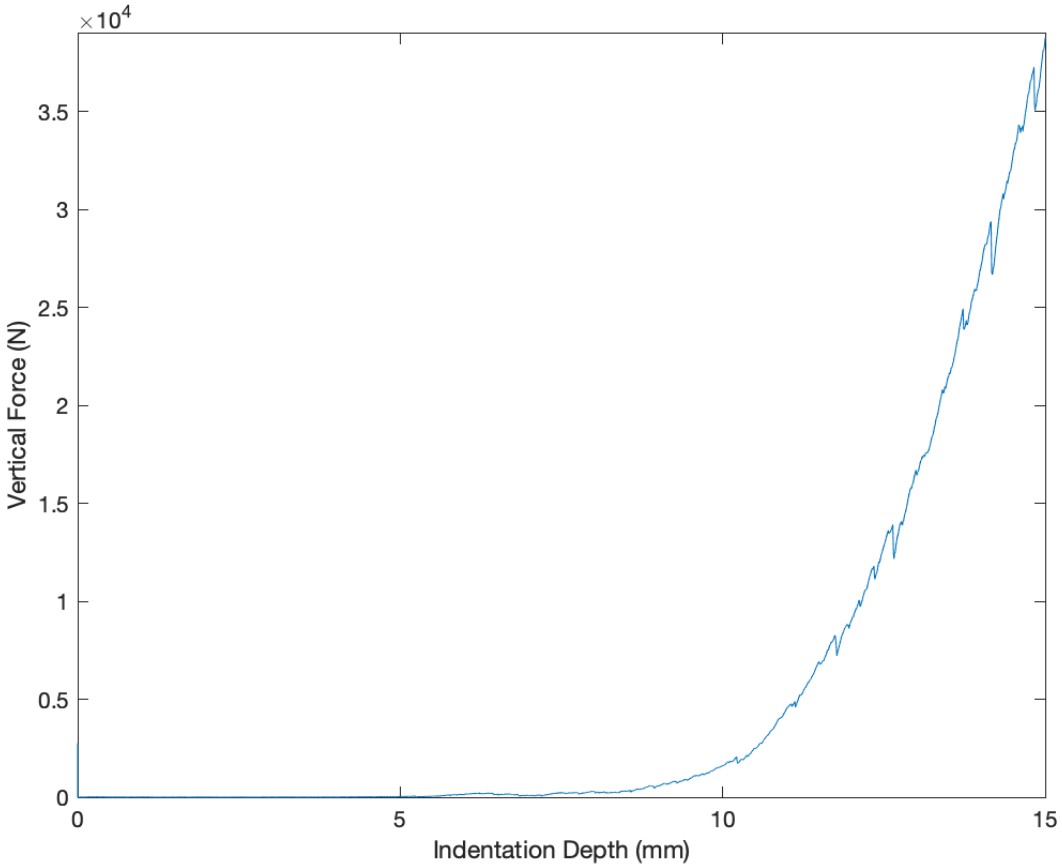

2020_10_11_(2)-15-0-30

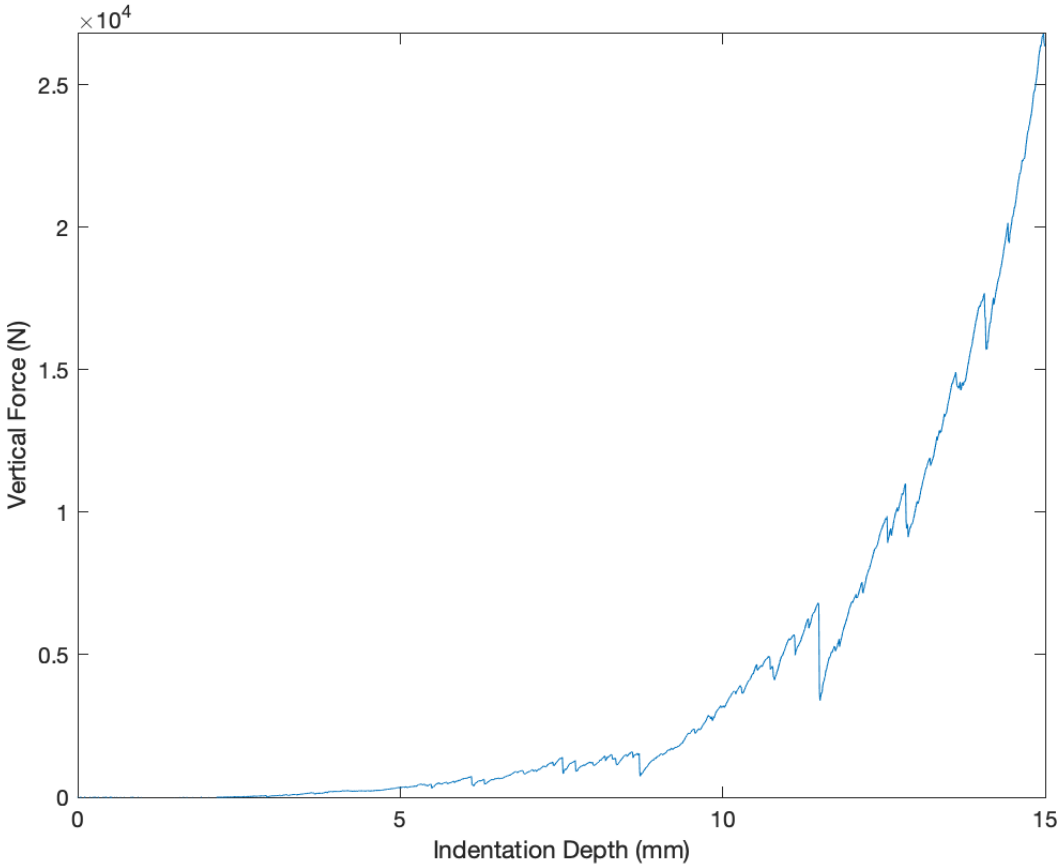

2020_12_11_(Failed)

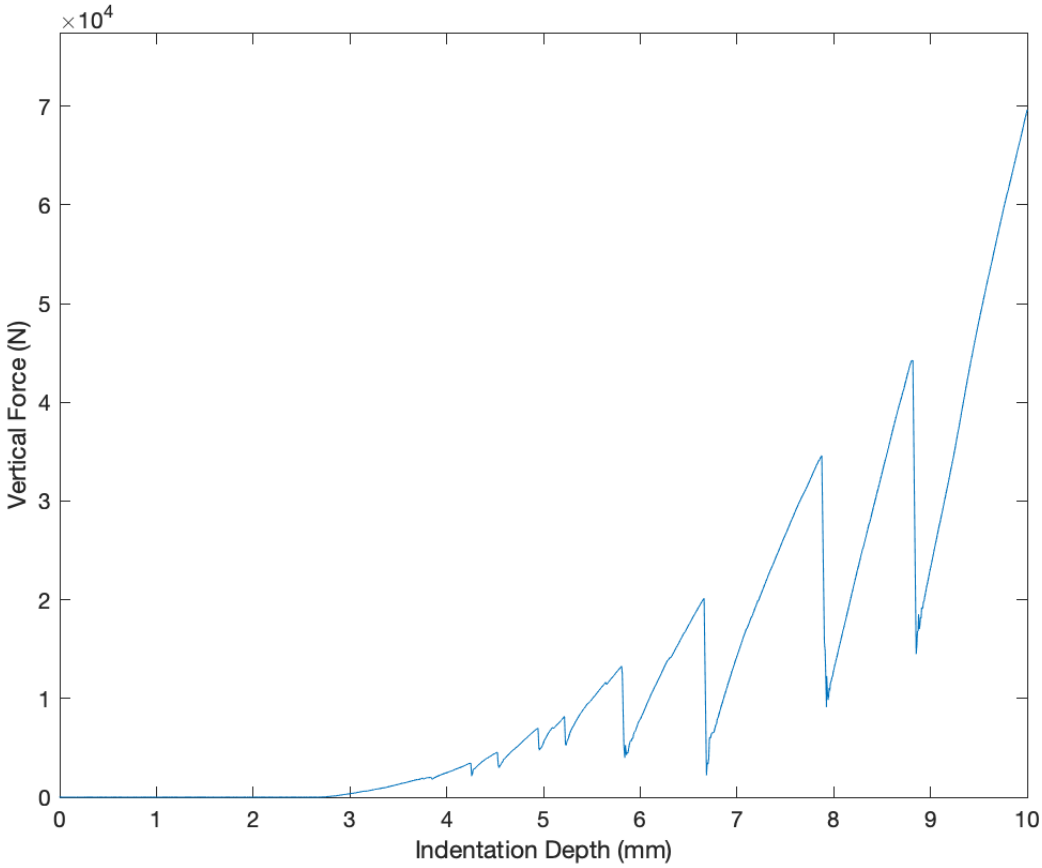

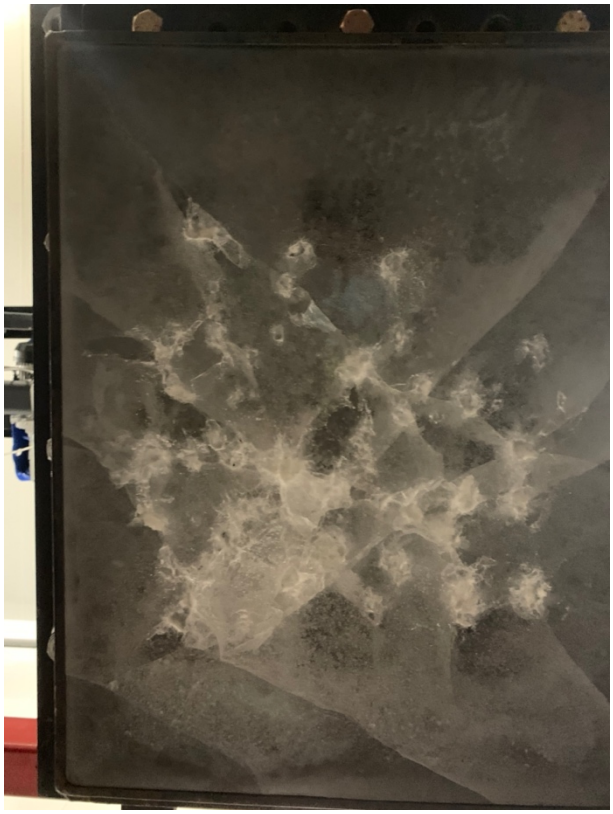

2020_13_11_(1)-5-0-1

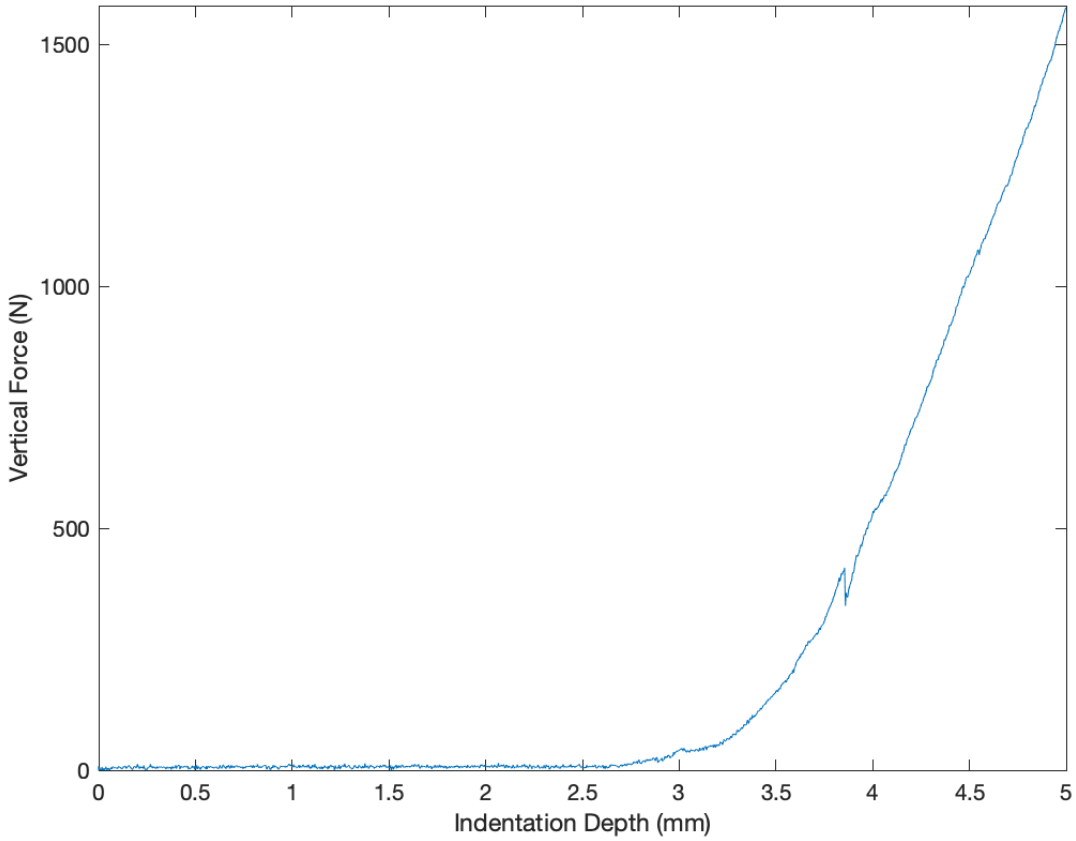

Images omitted due to poor quality.

2020_13_11_(2)-5-0-1

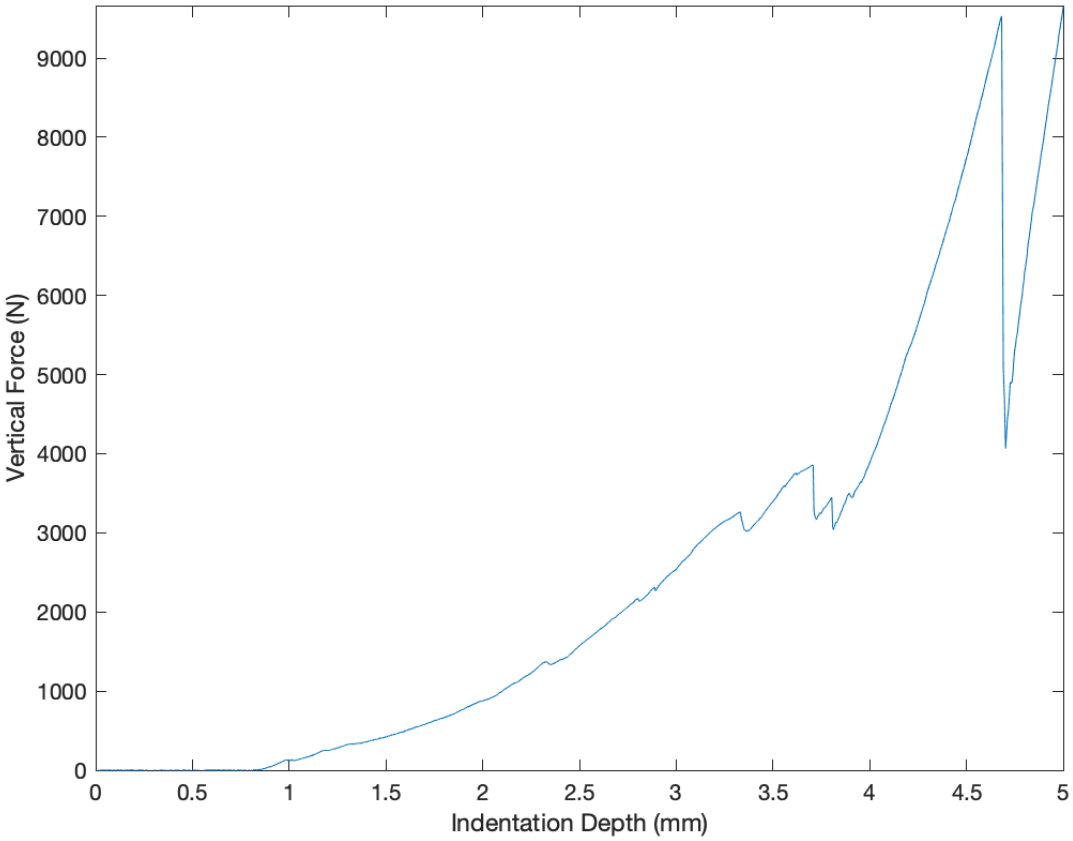

Images omitted due to poor quality.

2020_13_11_(3)-5-0-1

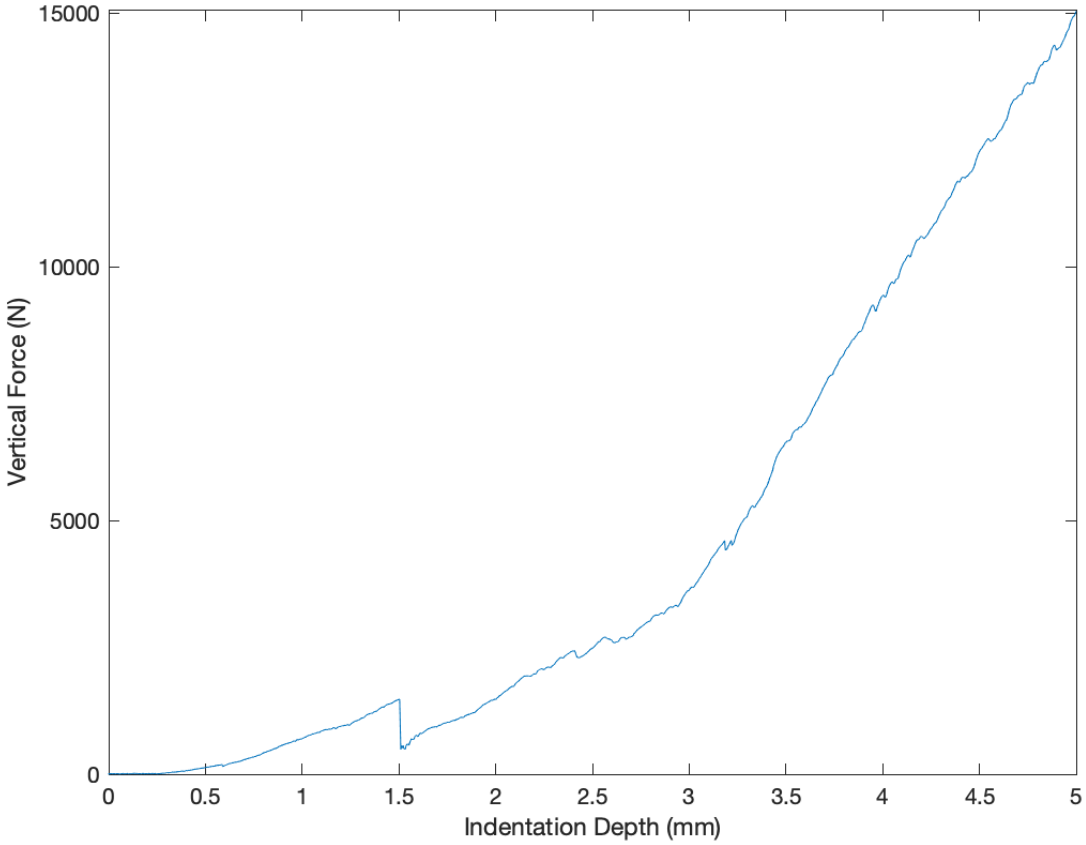

Images omitted due to poor quality.

2020_13_11_(4)-5-0-1

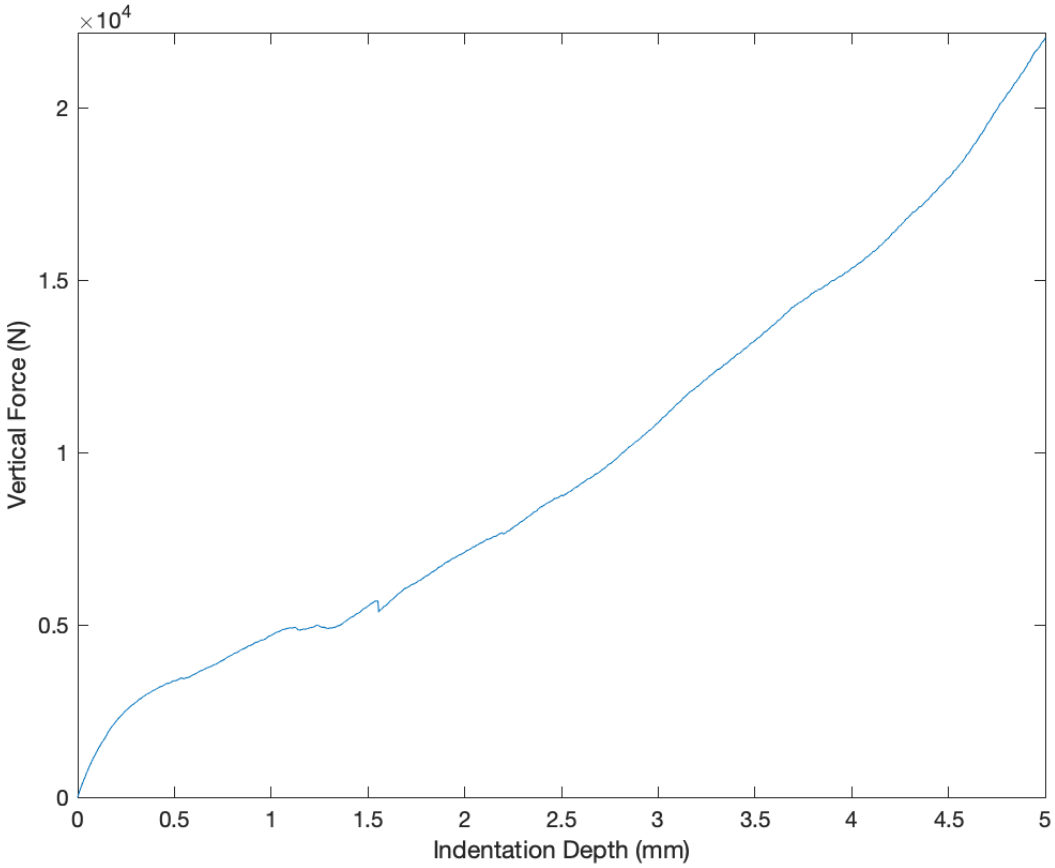

Images omitted due to poor quality.

2020_16_11_(1)-5-0-1

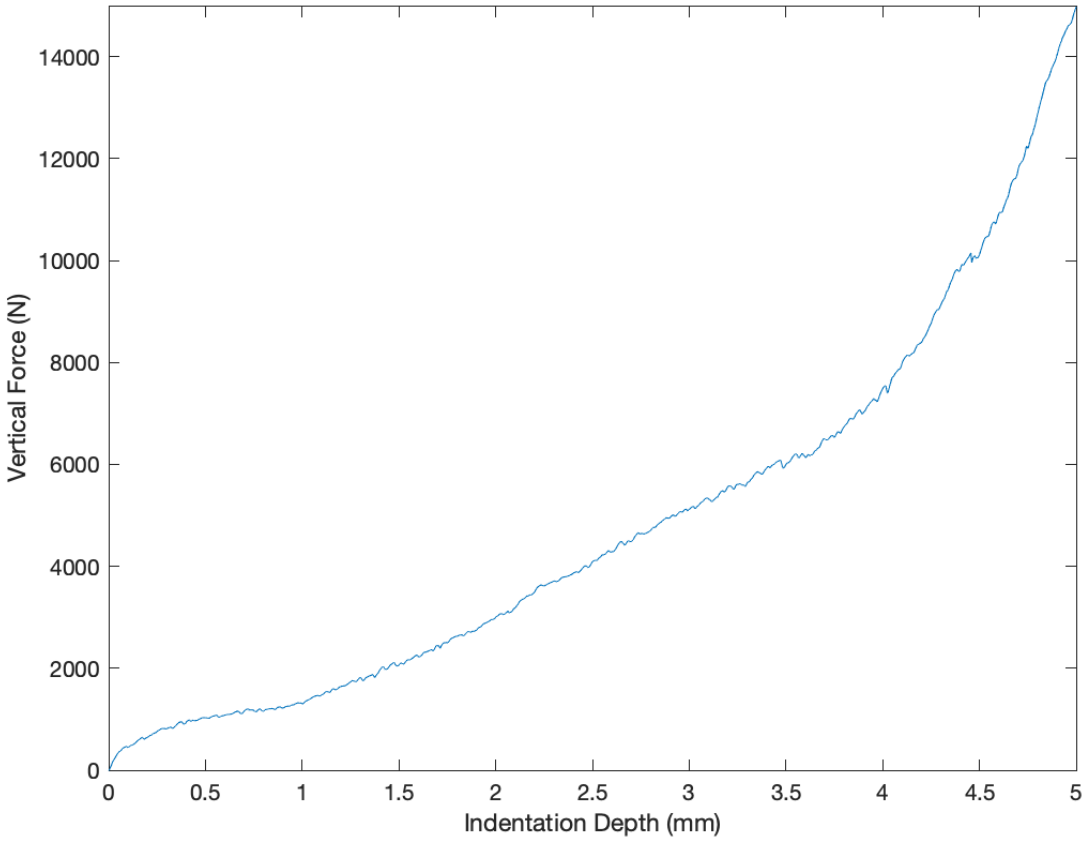

Images omitted due to poor quality.

2020_16_11_(2)-5-0-1

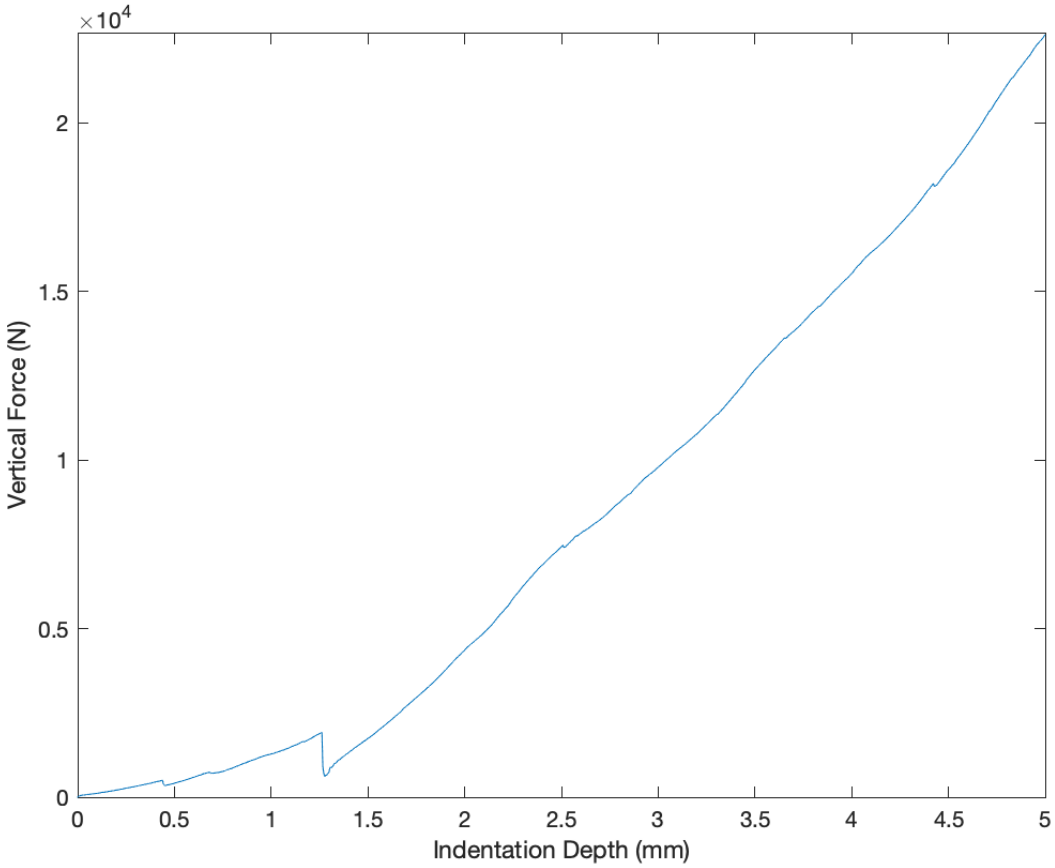

2020_16_11_(3)-5-0-1

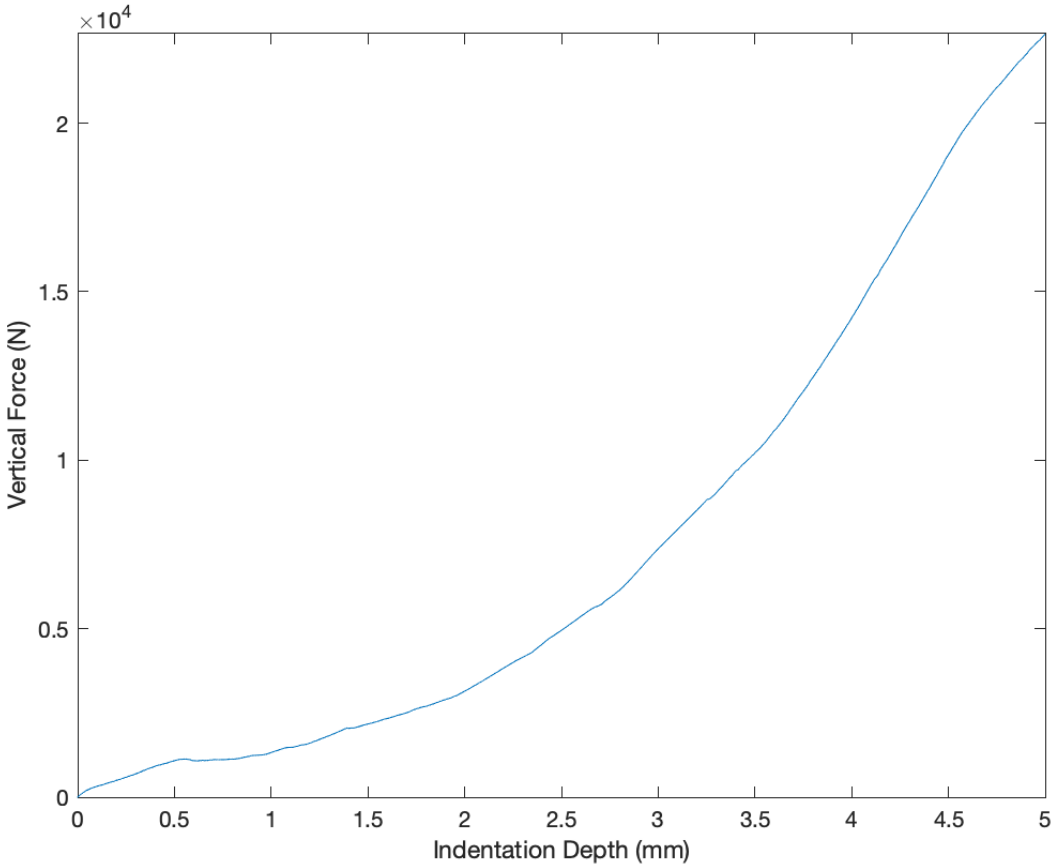

2020_16_11_(4)-5-0-30

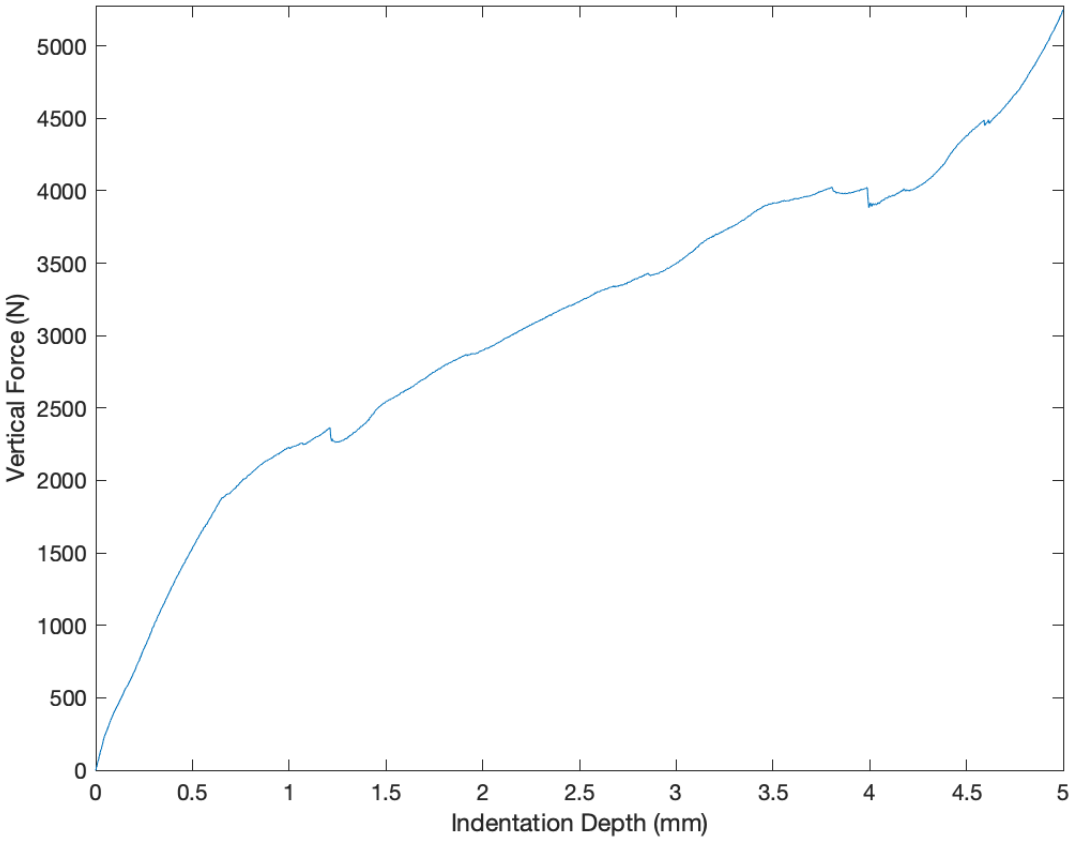

Images omitted due to poor quality.

2020_16_11_(5)-5-0-30

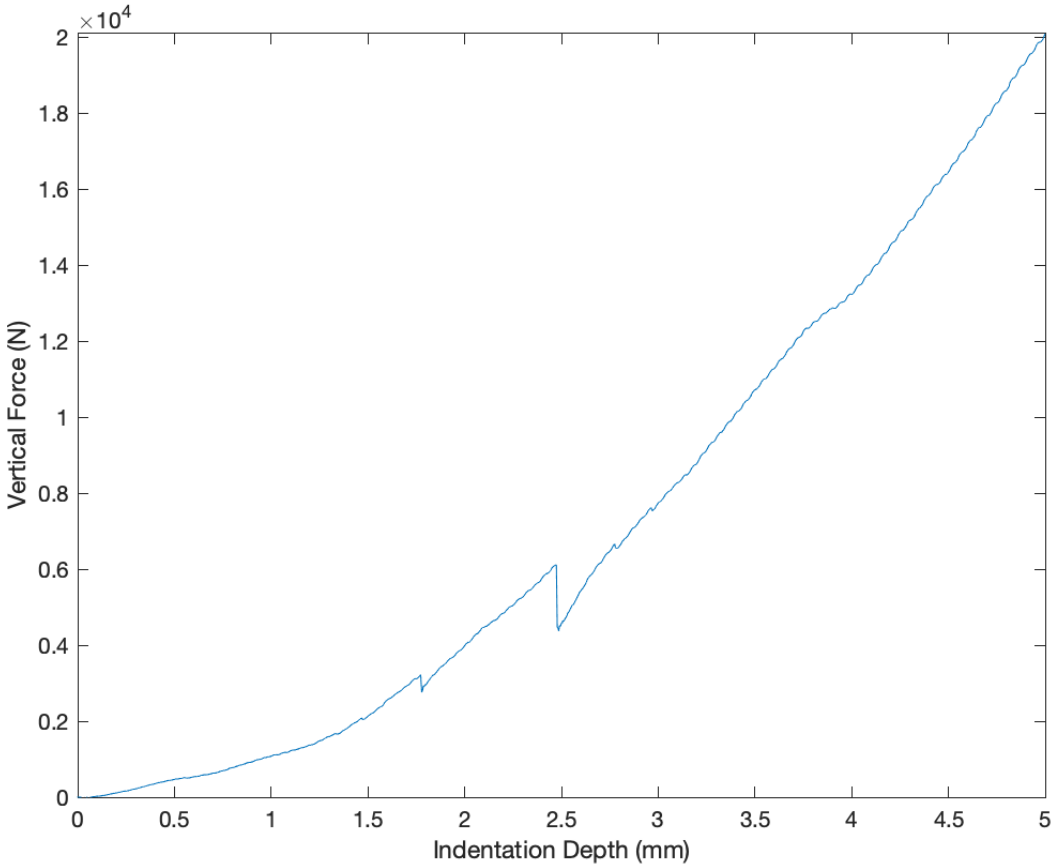

2020_16_11_(6)-5-0-30

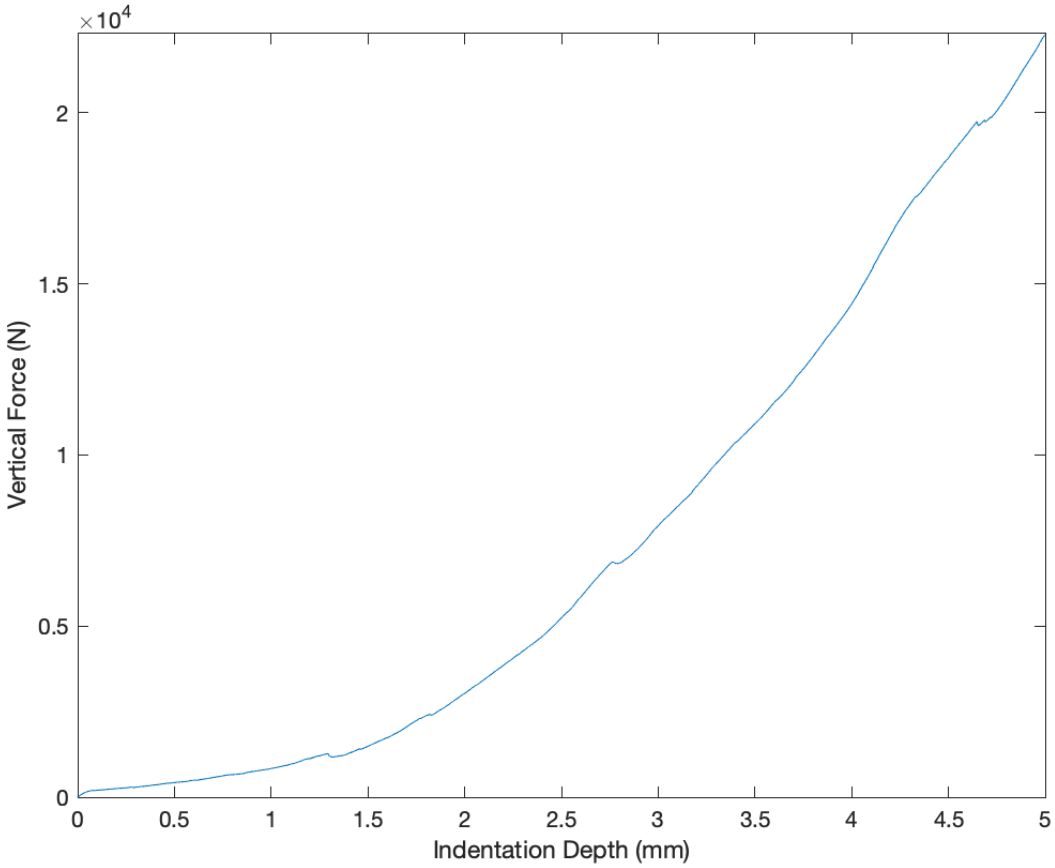

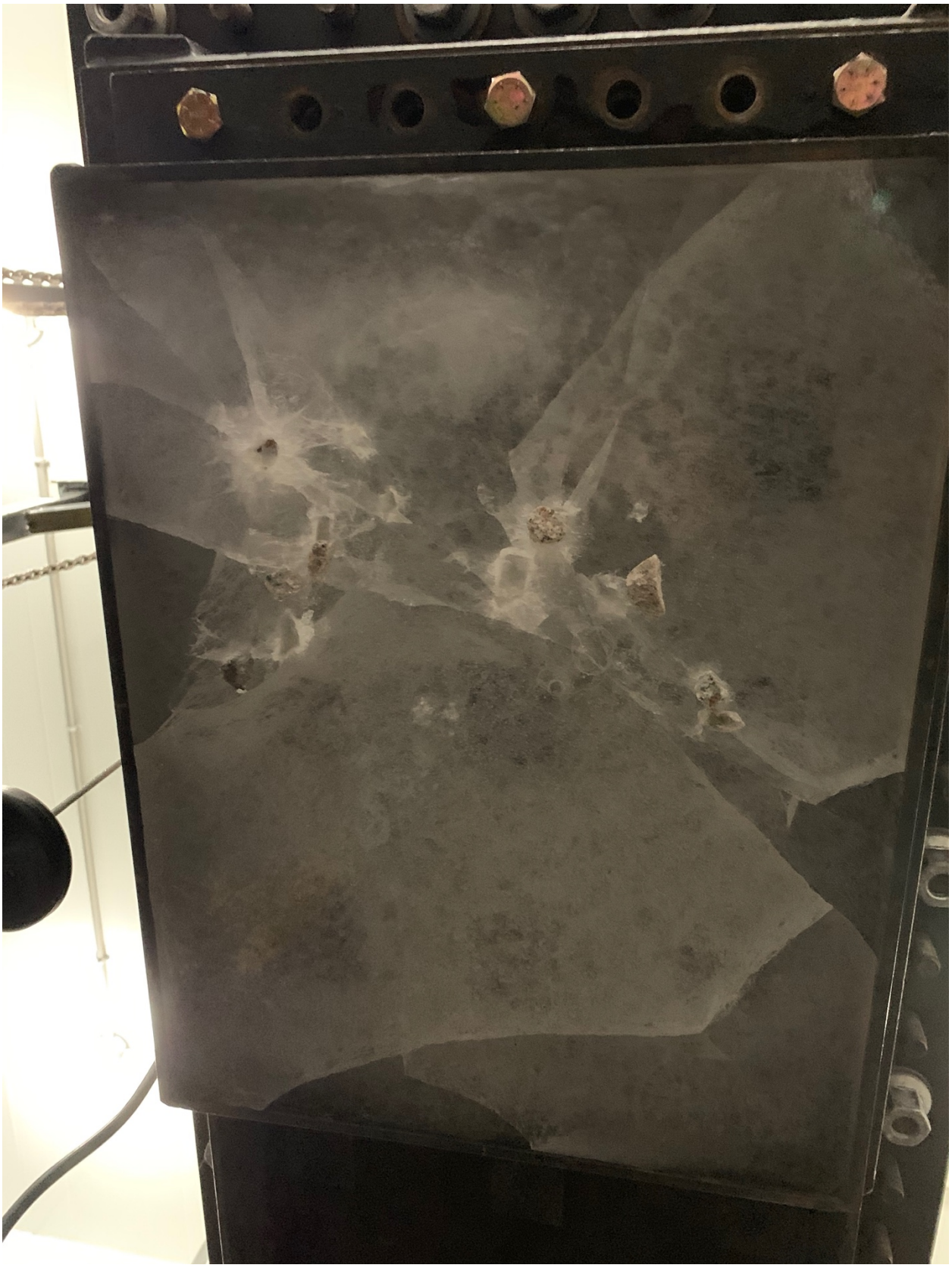

2020_18_11_(1)-7-0-1

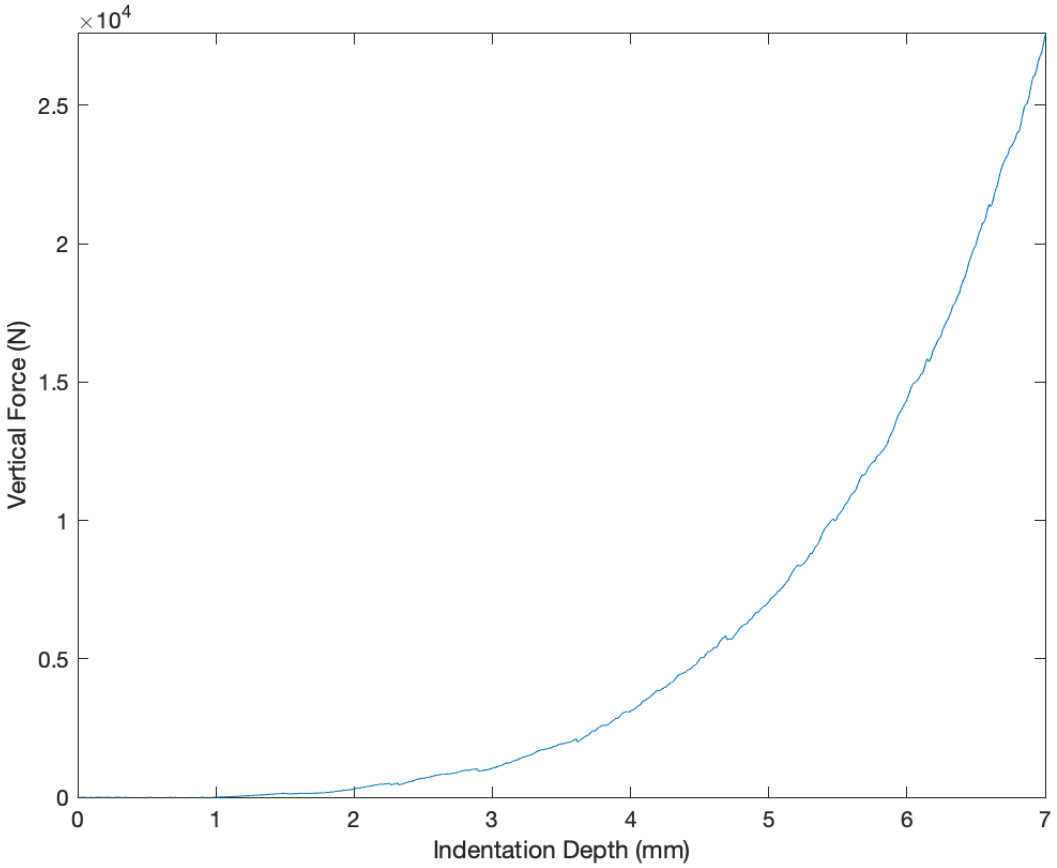

2020_18_11_(2)-7-0-1

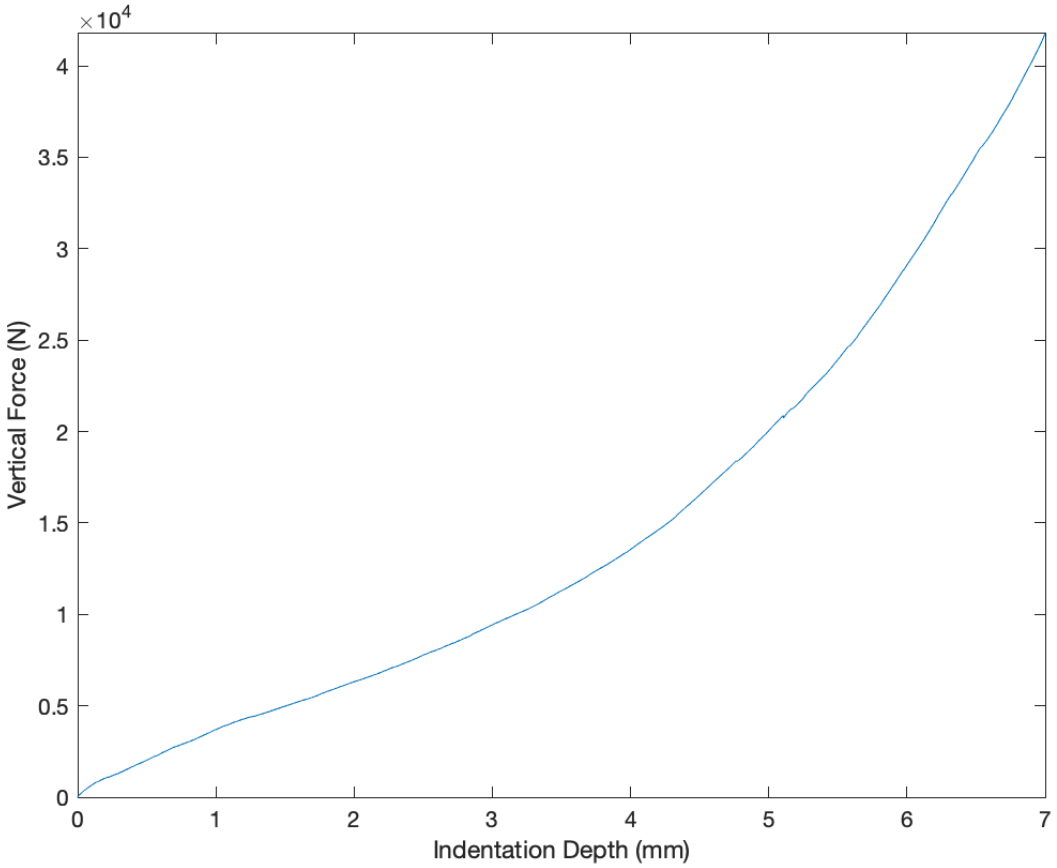

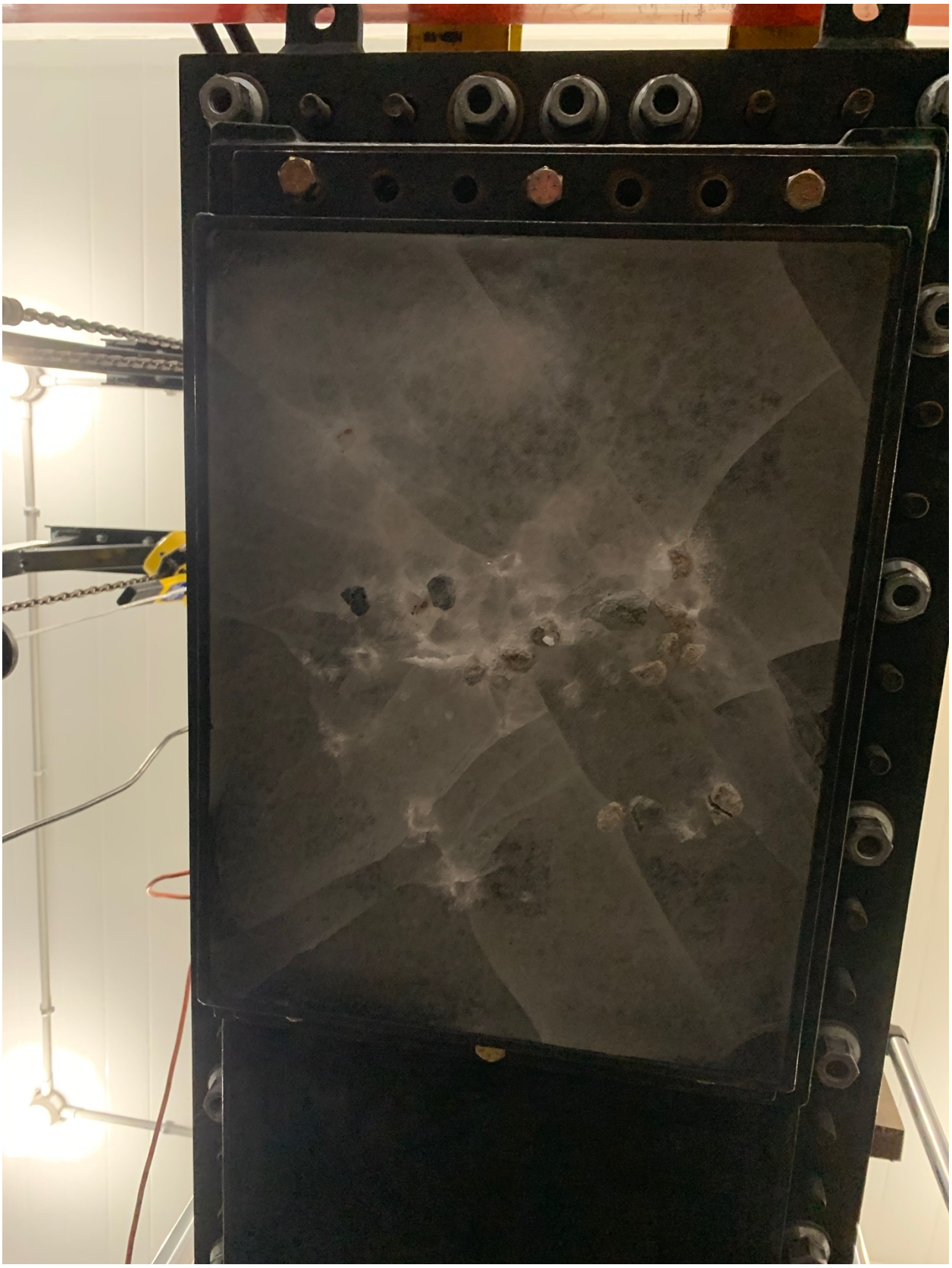

2020_18_11_(3)-7-0-1

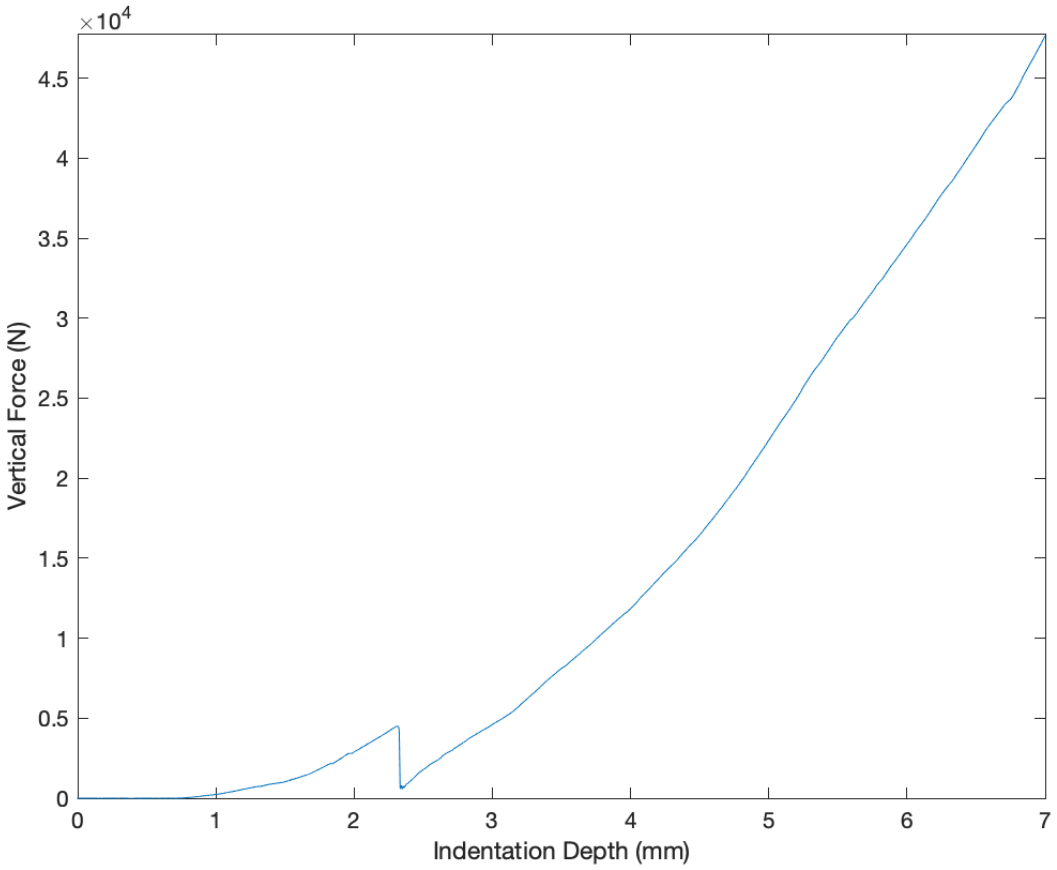

2020_18_11_(4)-7-0-30

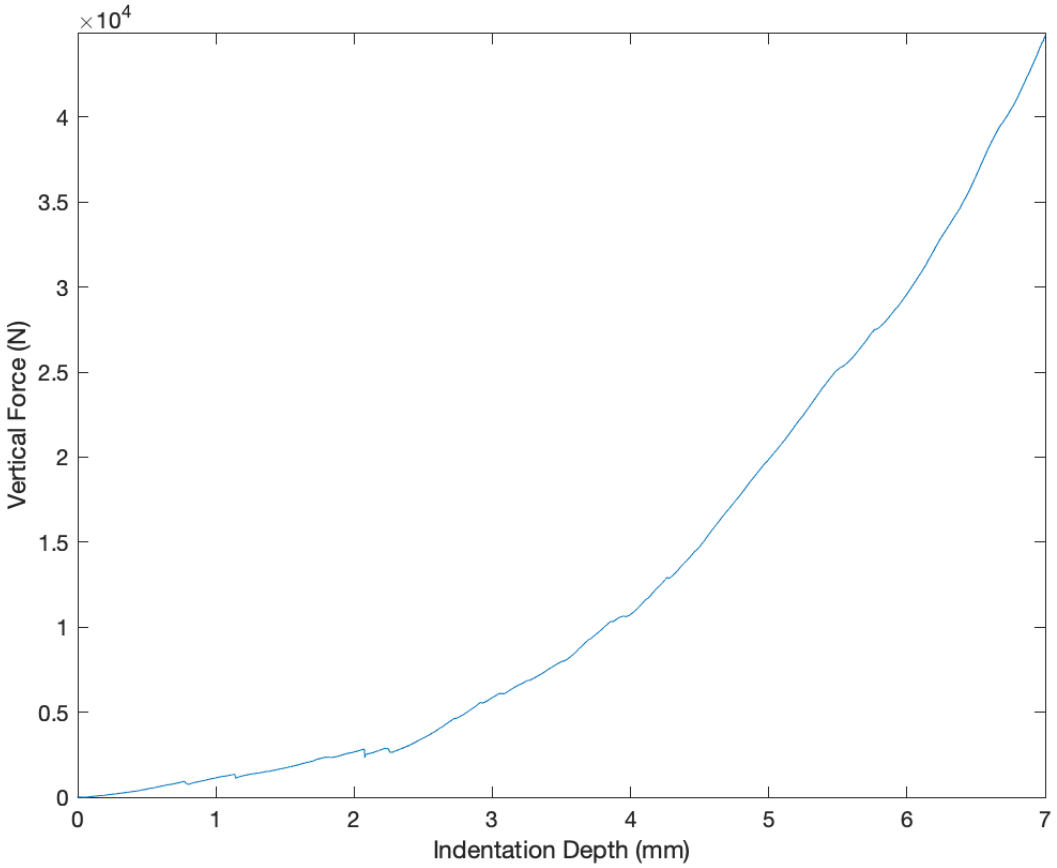

2020_18_11_(5)-7-0-30

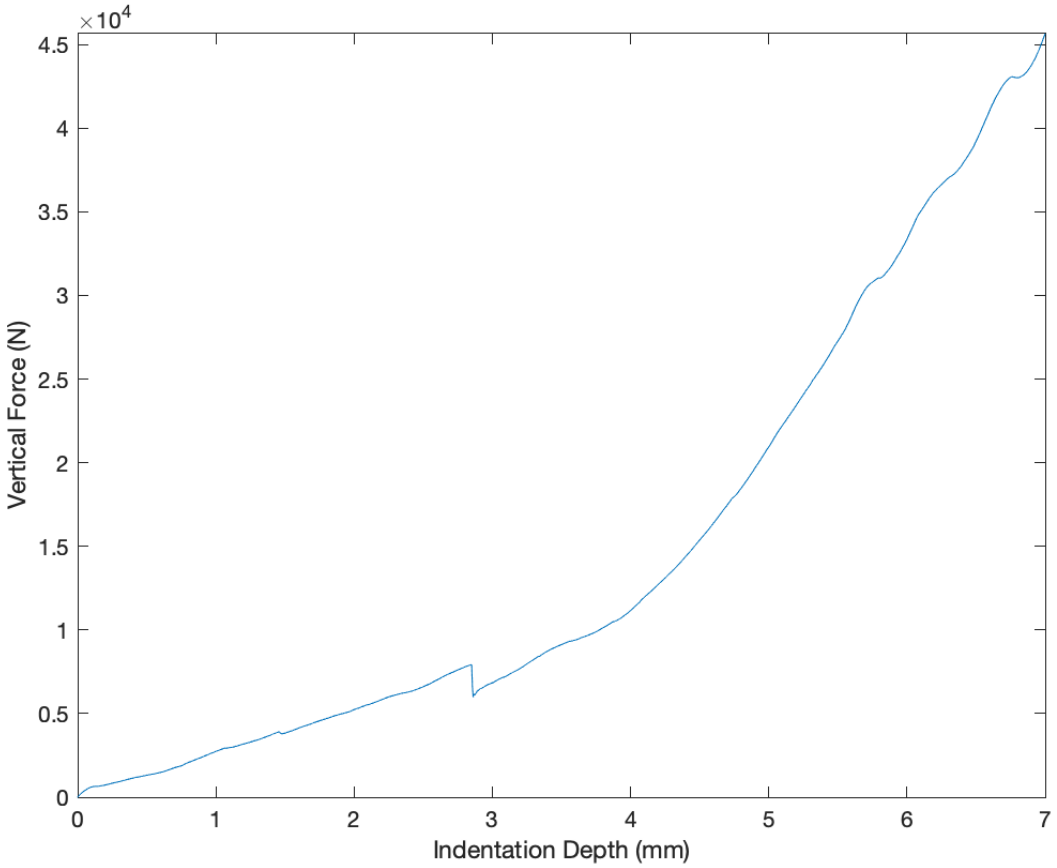

2020_19_11_(1)-7-0-1

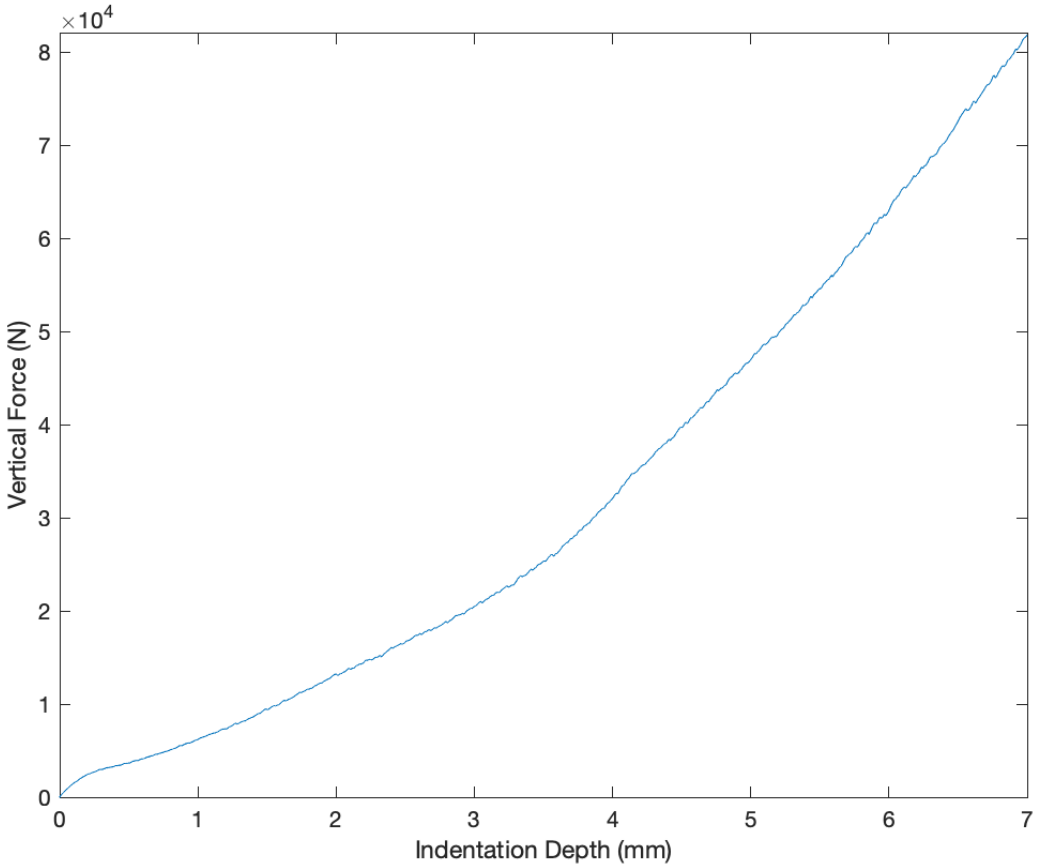

2020_19_11_(2)-7-0-1

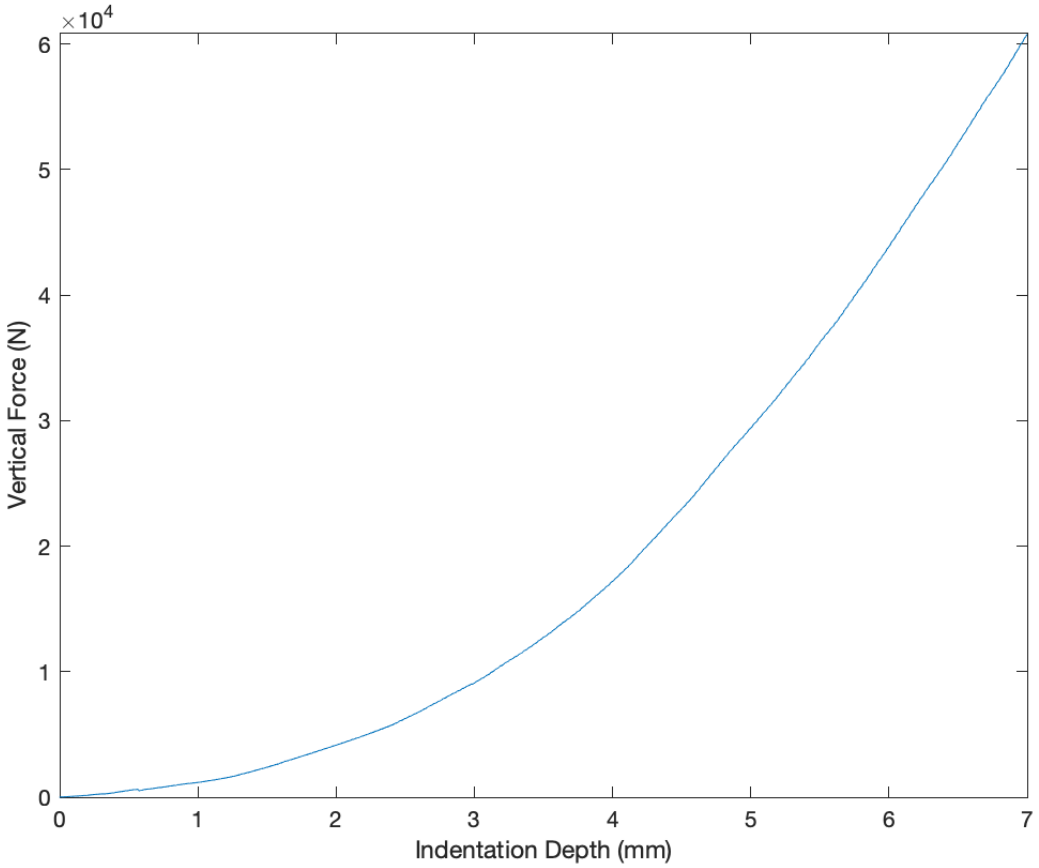

2020_19_11_(3)-7-0-1

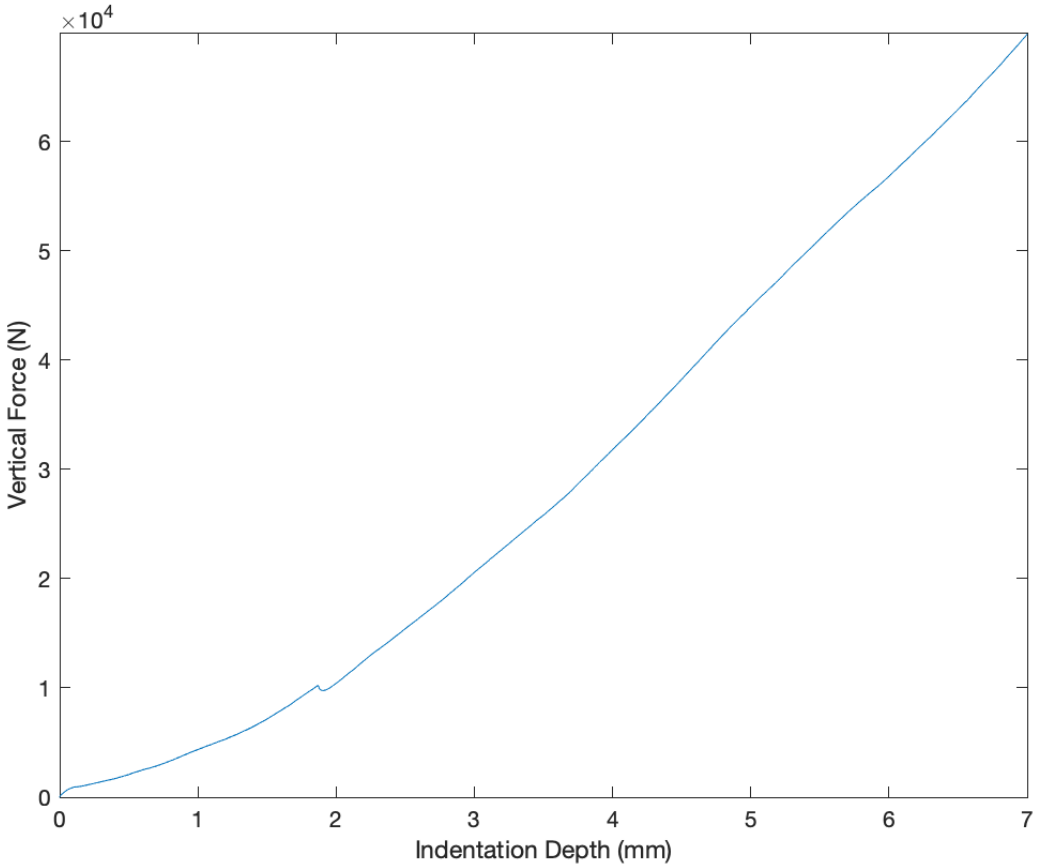

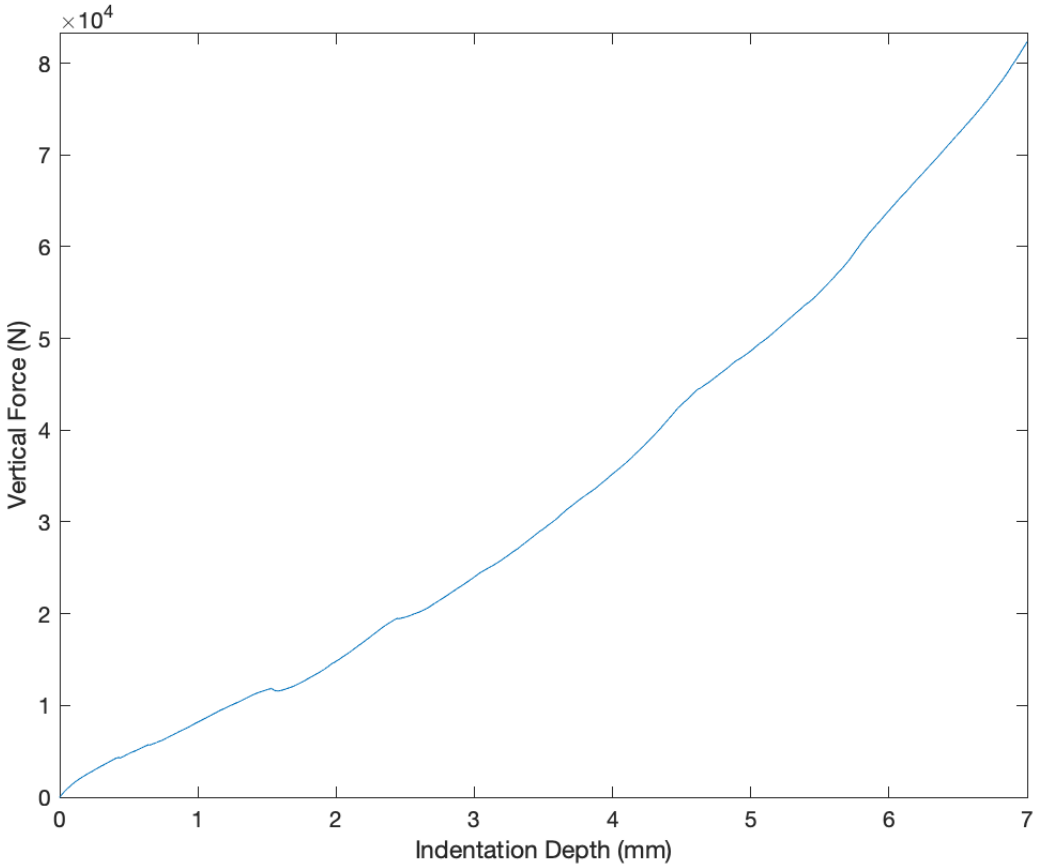
×10^4
8
7
6
5
4
3
2
1
0
Vertical Force (N)
0
1
2
3
4
5
6
7
Indentation Depth (mm)

2020_19_11_(5)-7-0-1

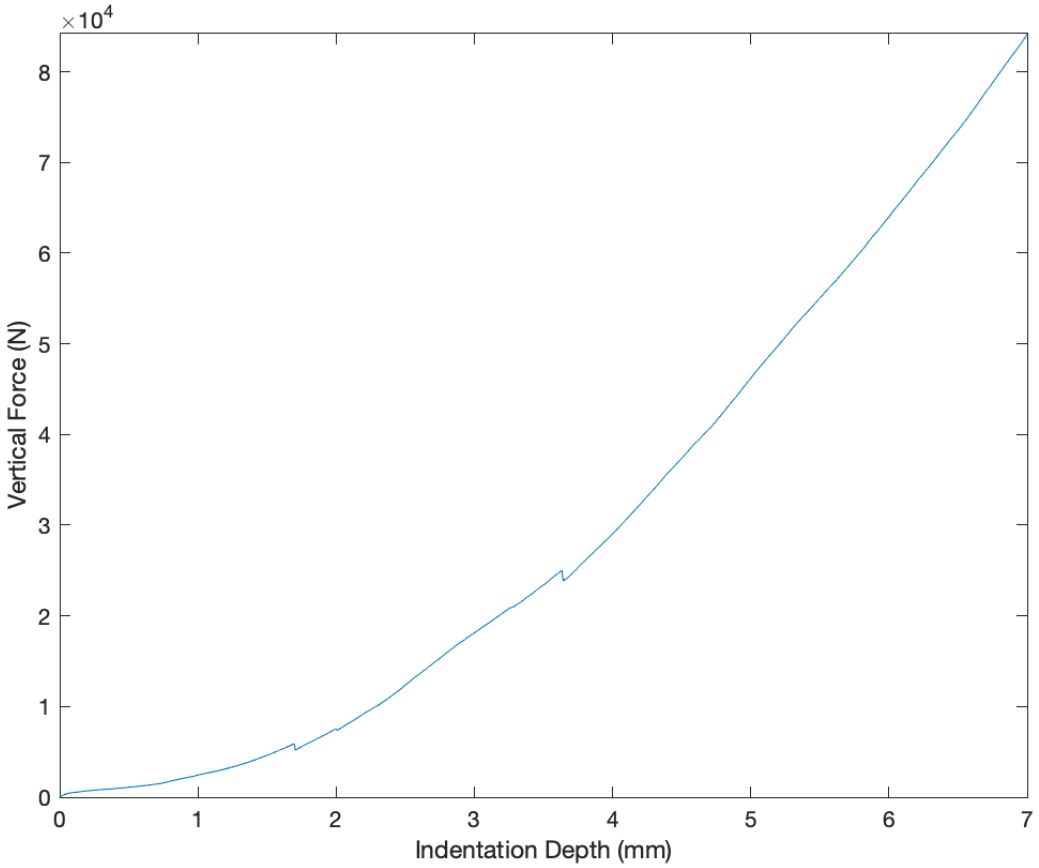

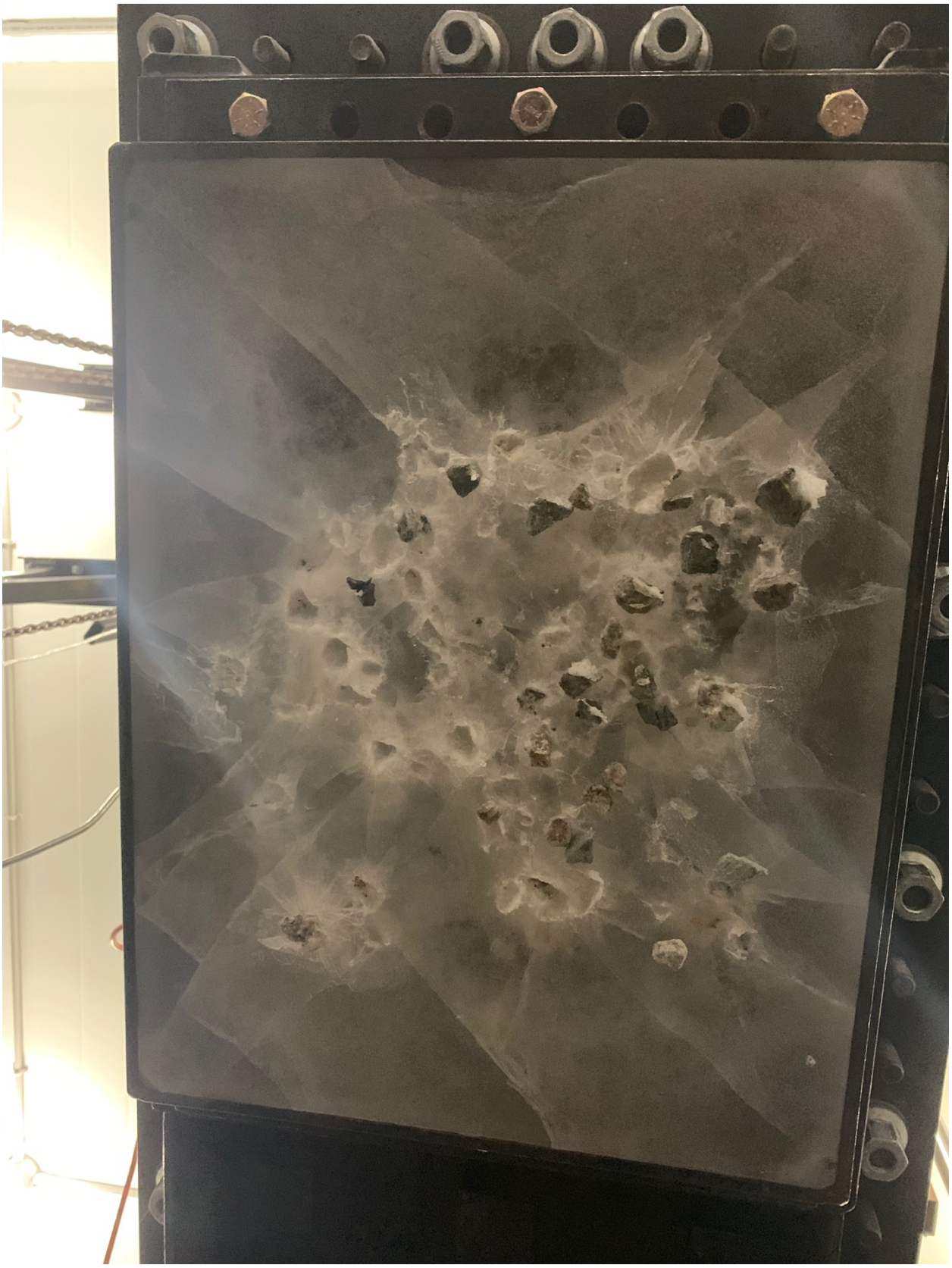

2020_19_11_(6)-7-0-1

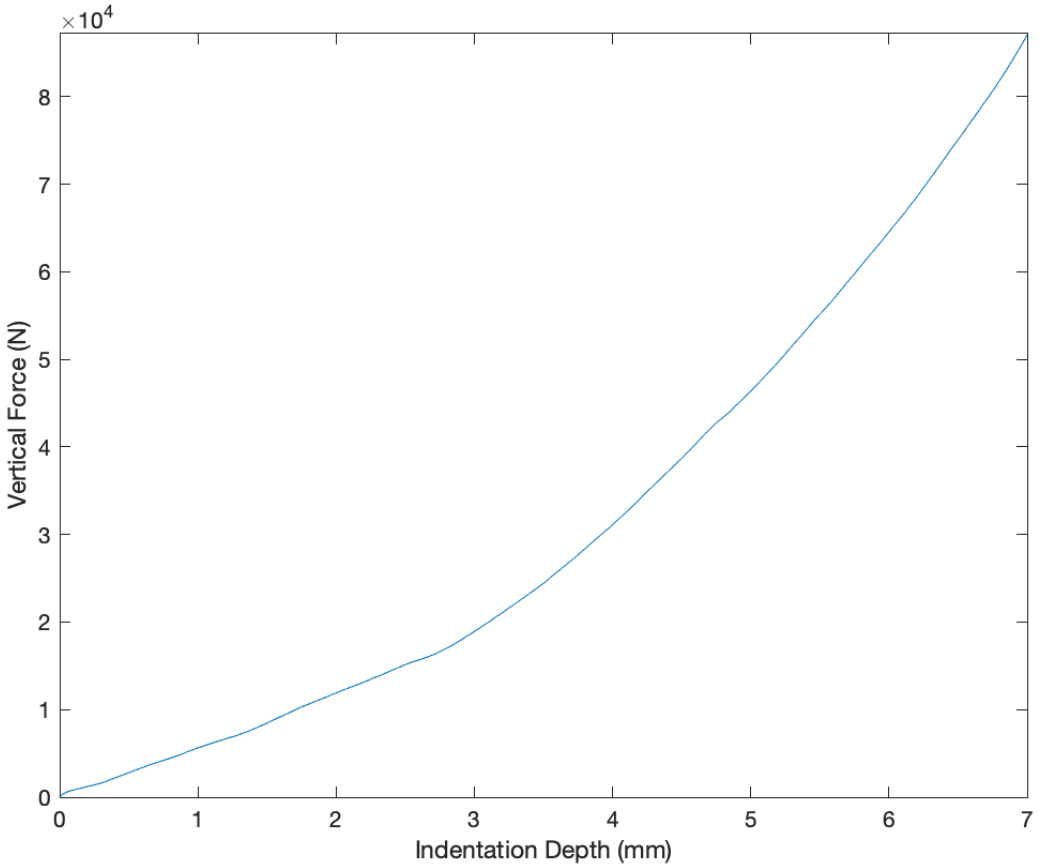

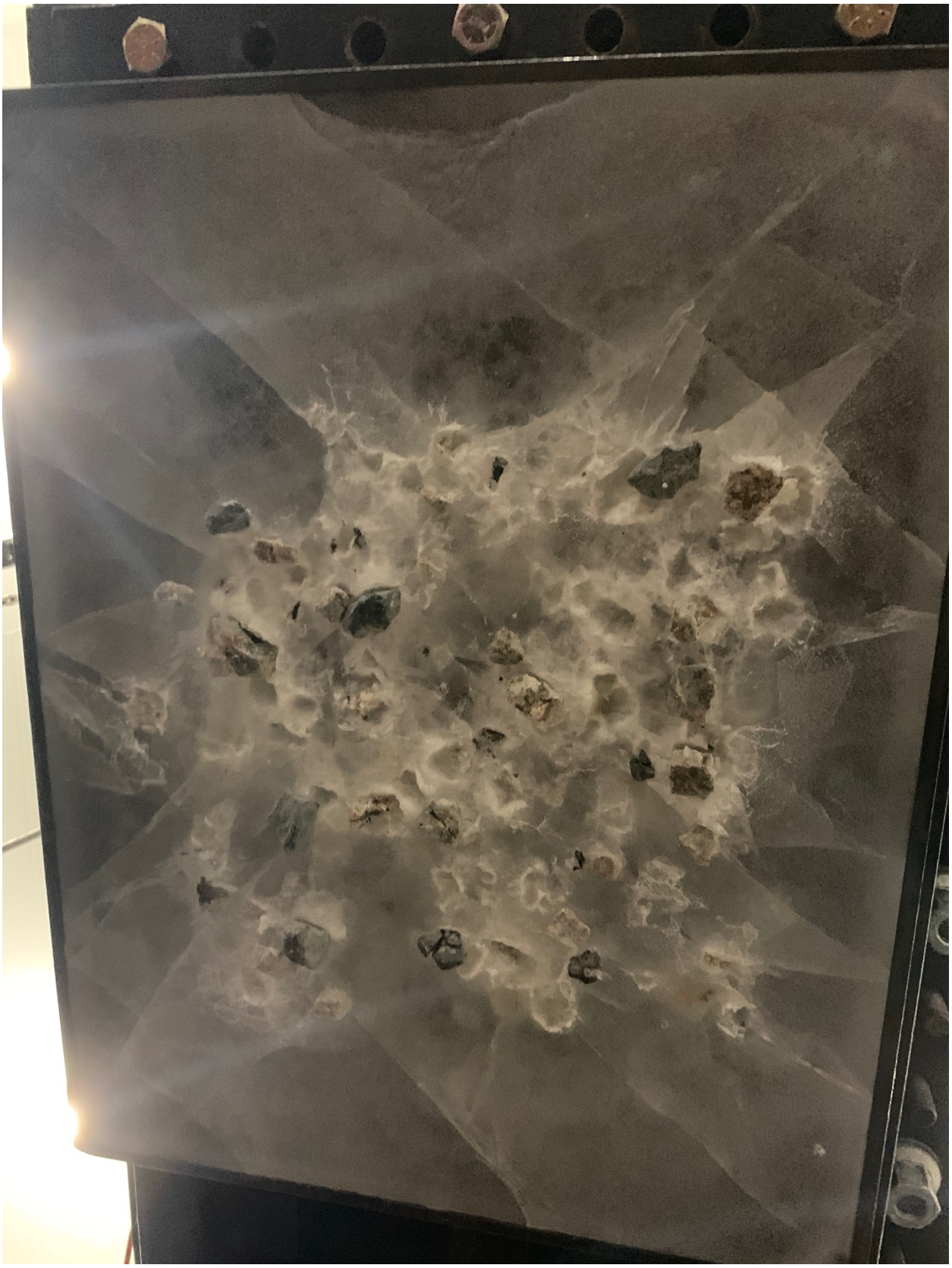

2020_20_11_(1)-7-0-30

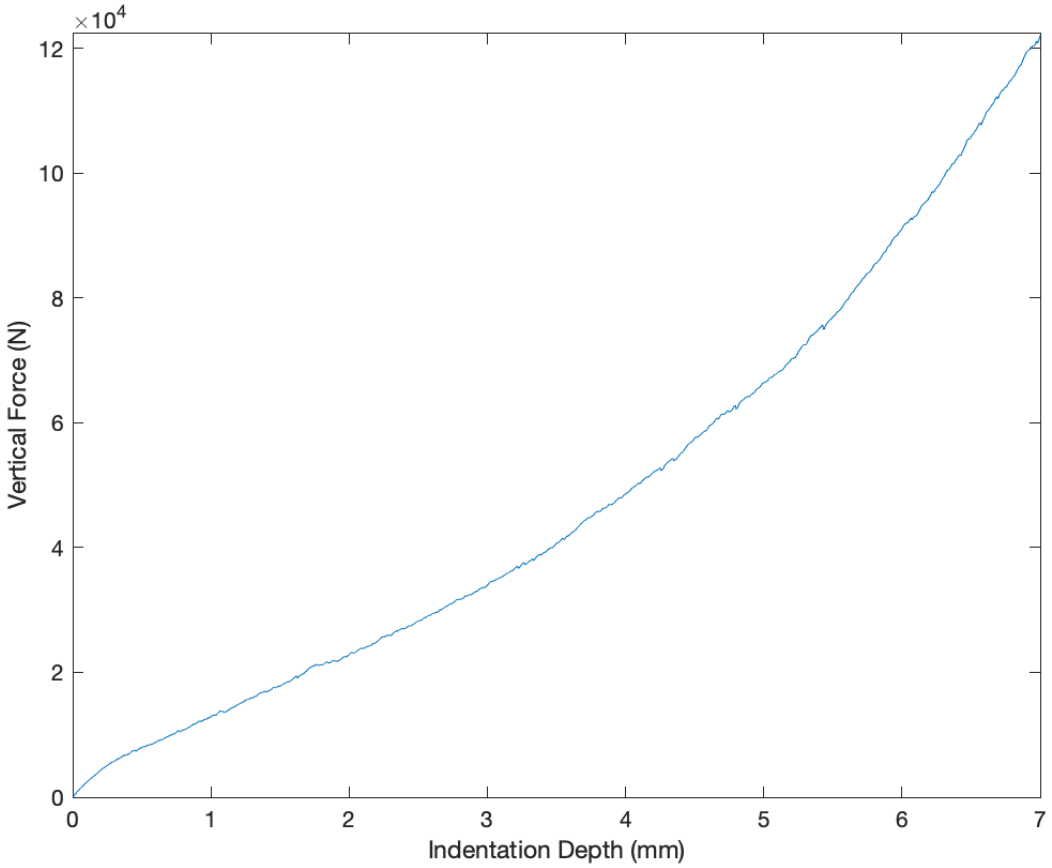

2020_20_11_(2)-7-0-30

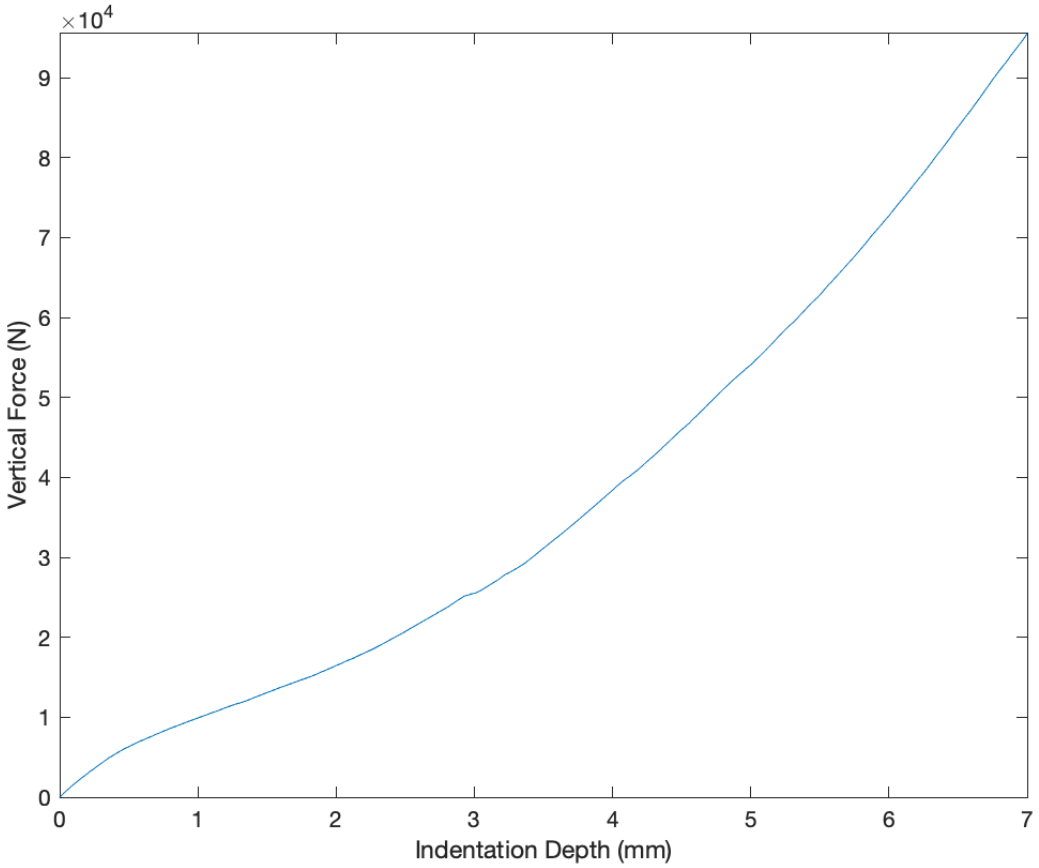

2020_23_11_(1)-7-0-1

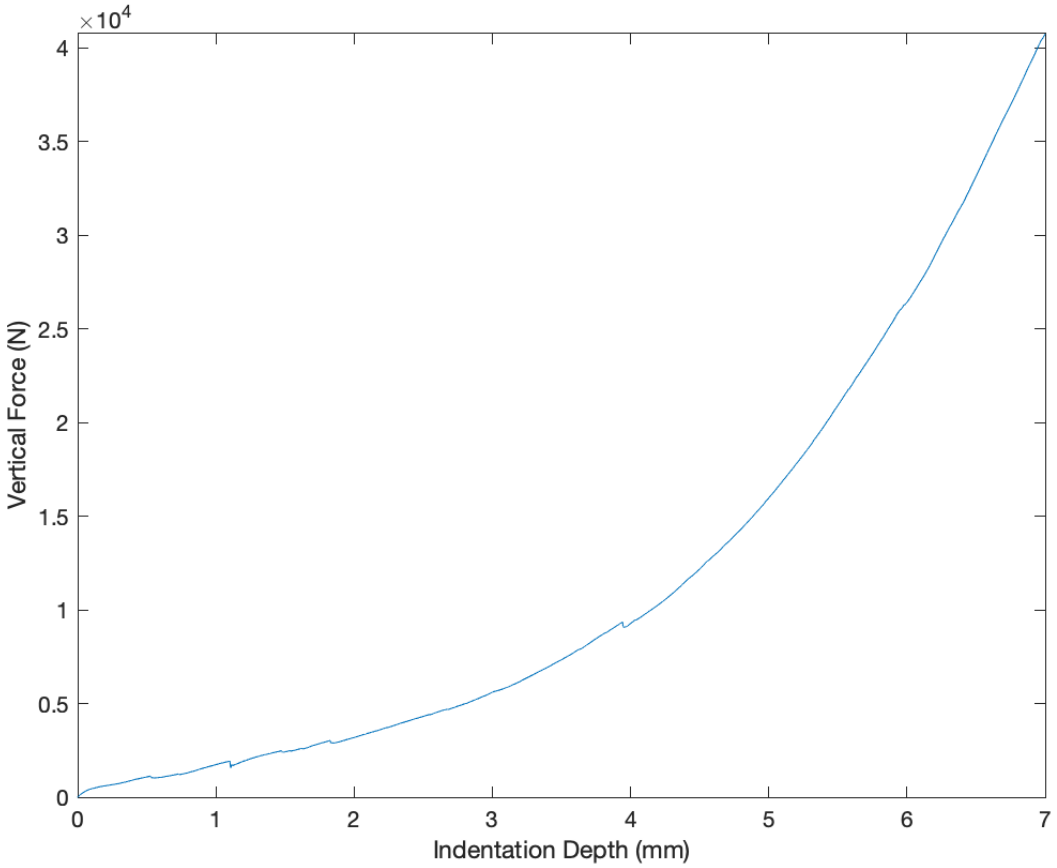

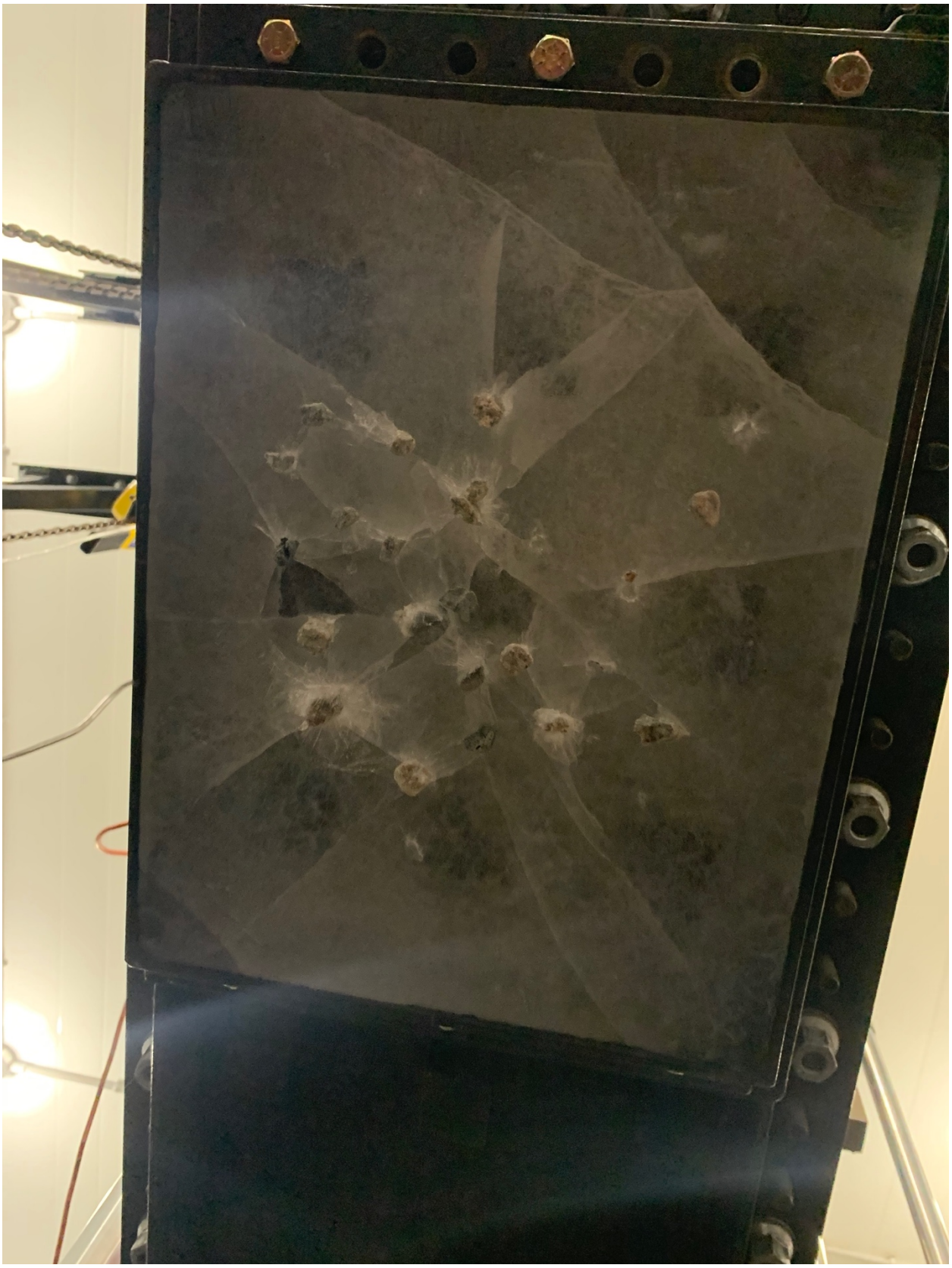

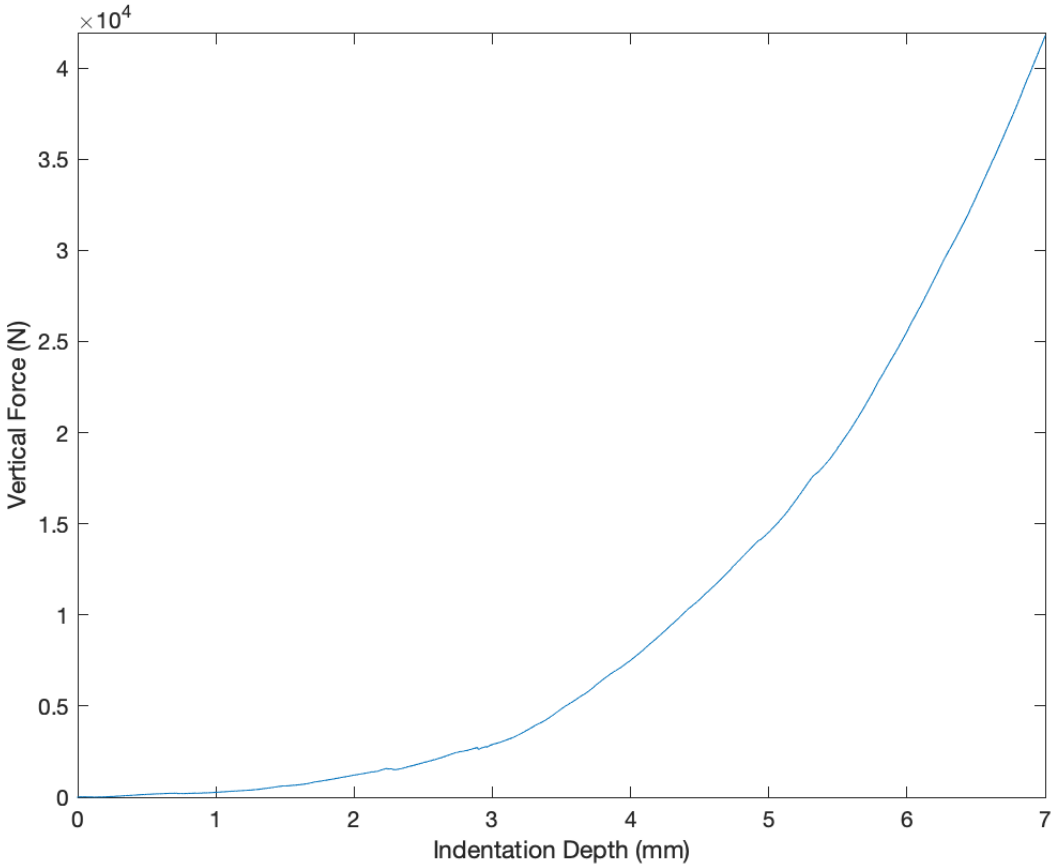
×10^4
4
3.5
3
2.5
2
1.5
1
0.5
0
Vertical Force (N)
0
1
2
3
4
5
6
7
Indentation Depth (mm)

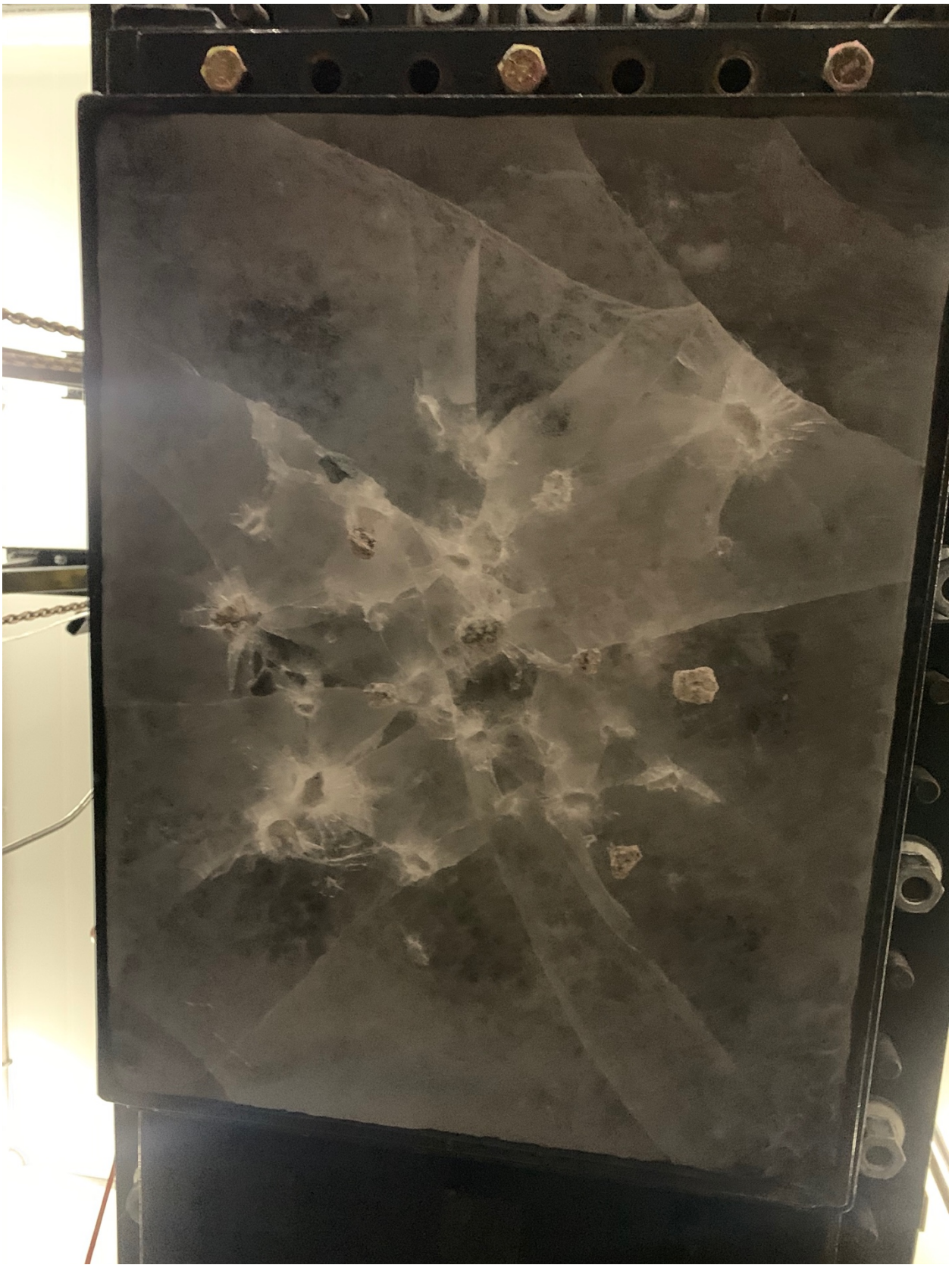

2020_23_11_(3)-7-0-1

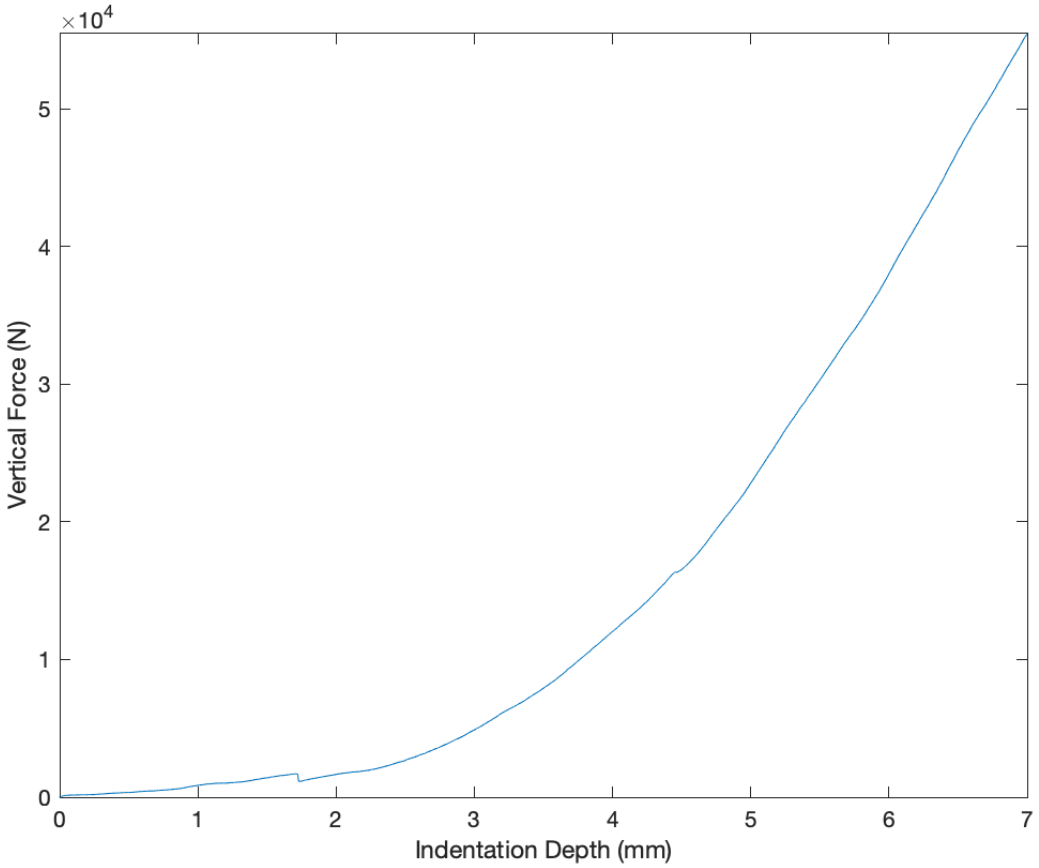

2020_24_11_(1)-5-5-1

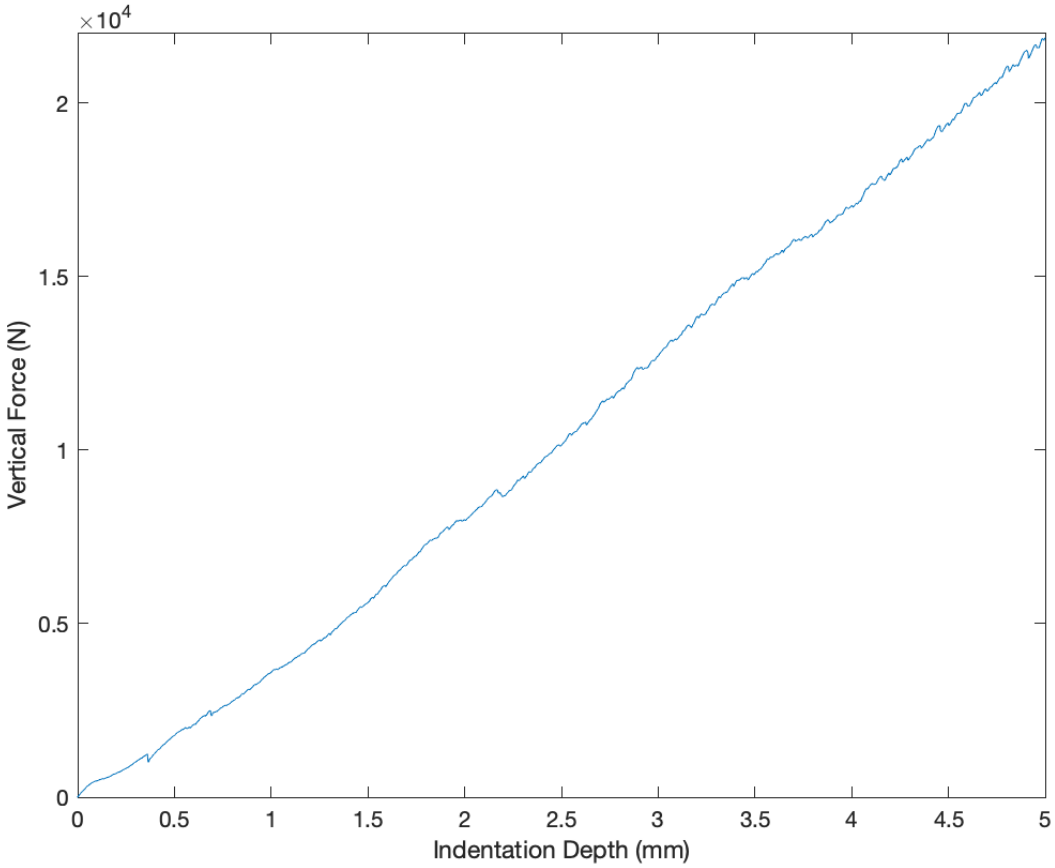

2020_24_11_(2)-5-5-1

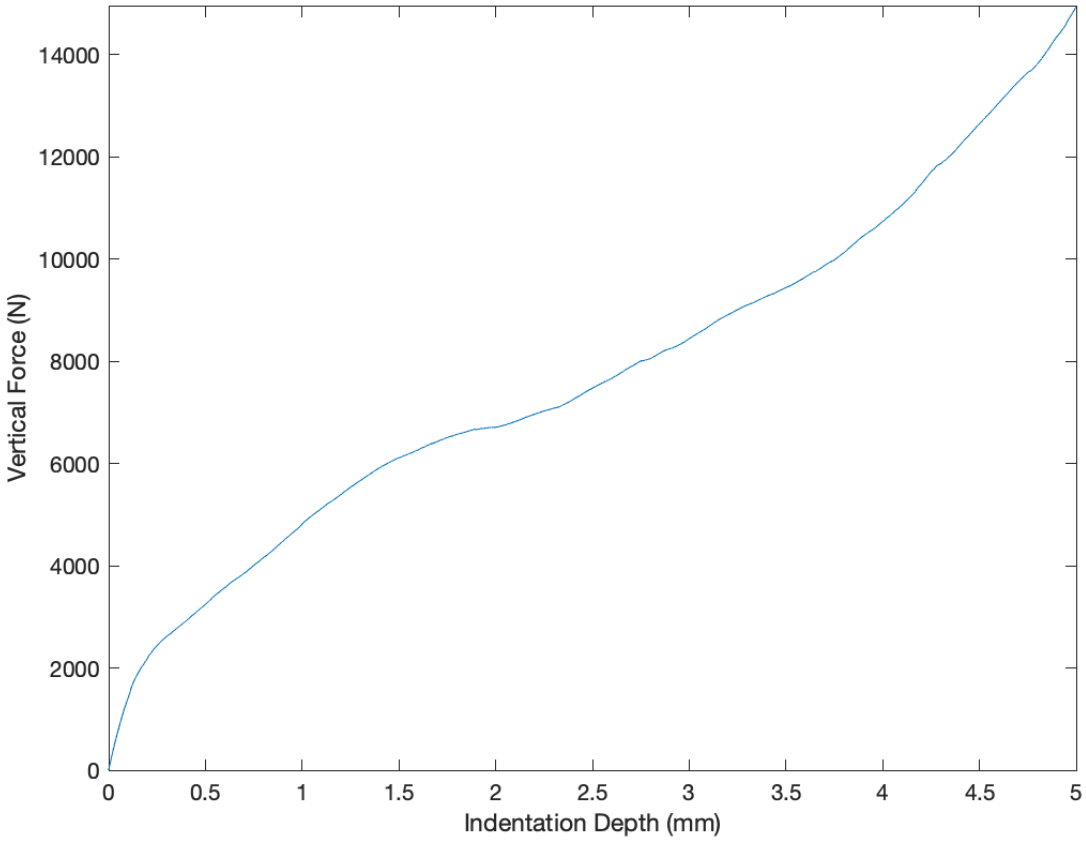

2020_24_11_(3)-5-5-1

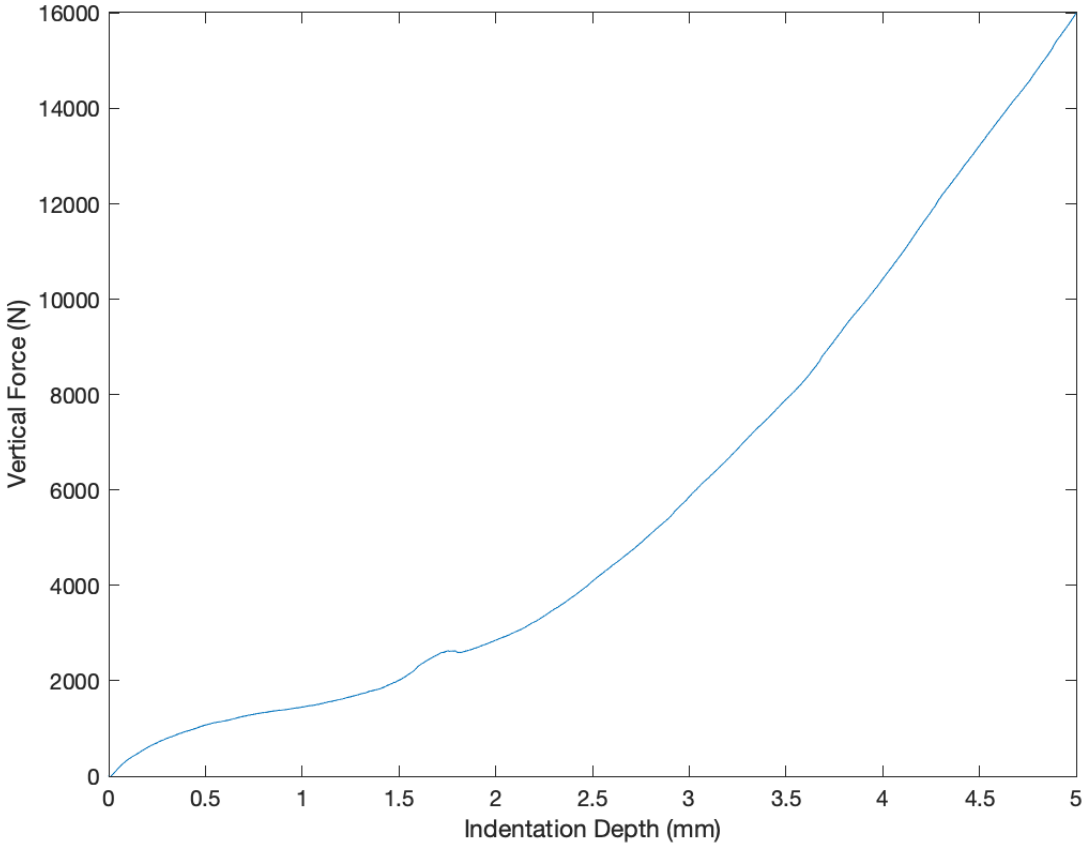

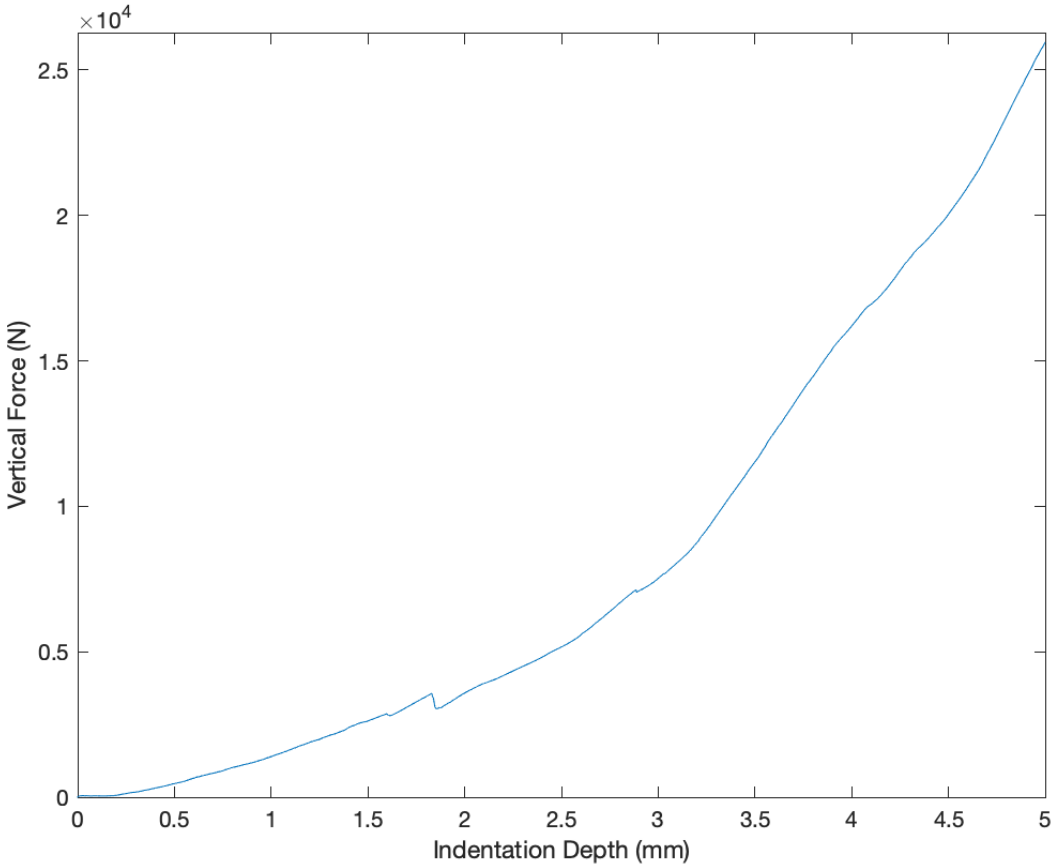
×10^4
2.5
2
1.5
1
0.5
0
Vertical Force (N)
0
0.5
1
1.5
2
2.5
3
3.5
4
4.5
5
Indentation Depth (mm)

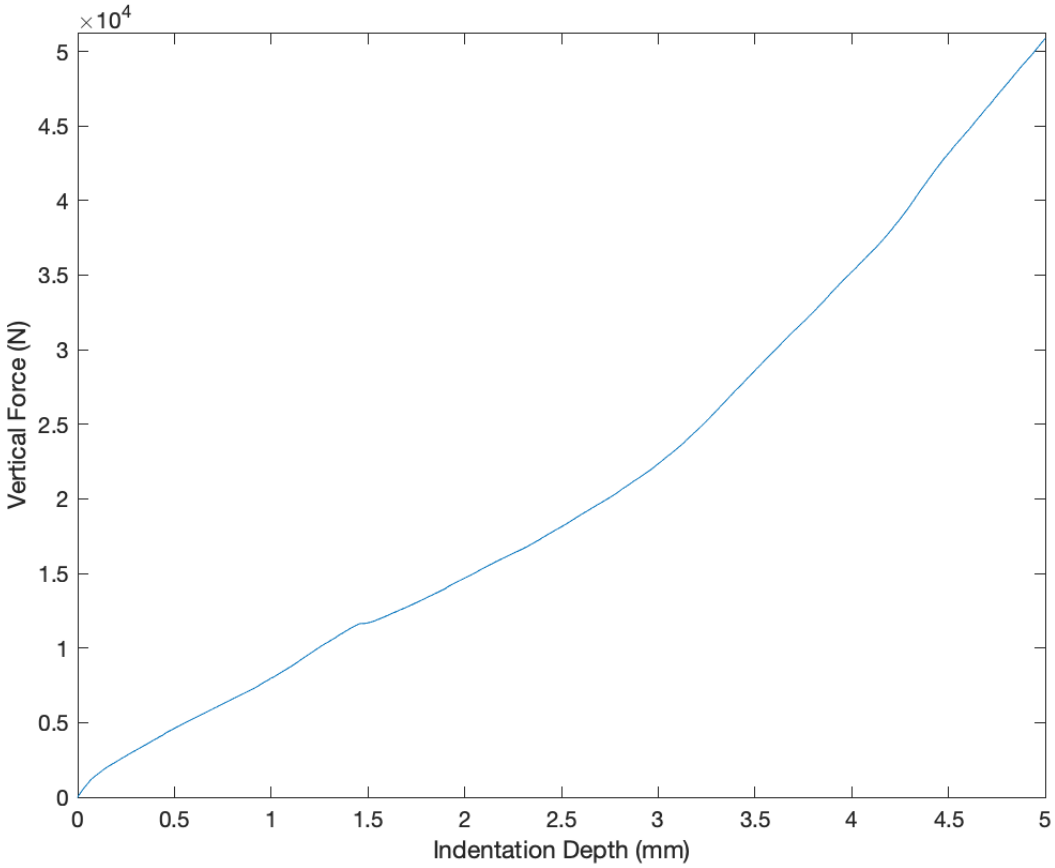
×10^4
5
4.5
4
3.5
3
2.5
2
1.5
1
0.5
0
Vertical Force (N)
0
0.5
1
1.5
2
2.5
3
3.5
4
4.5
5
Indentation Depth (mm)

2020_24_11_(6)-5-7-1

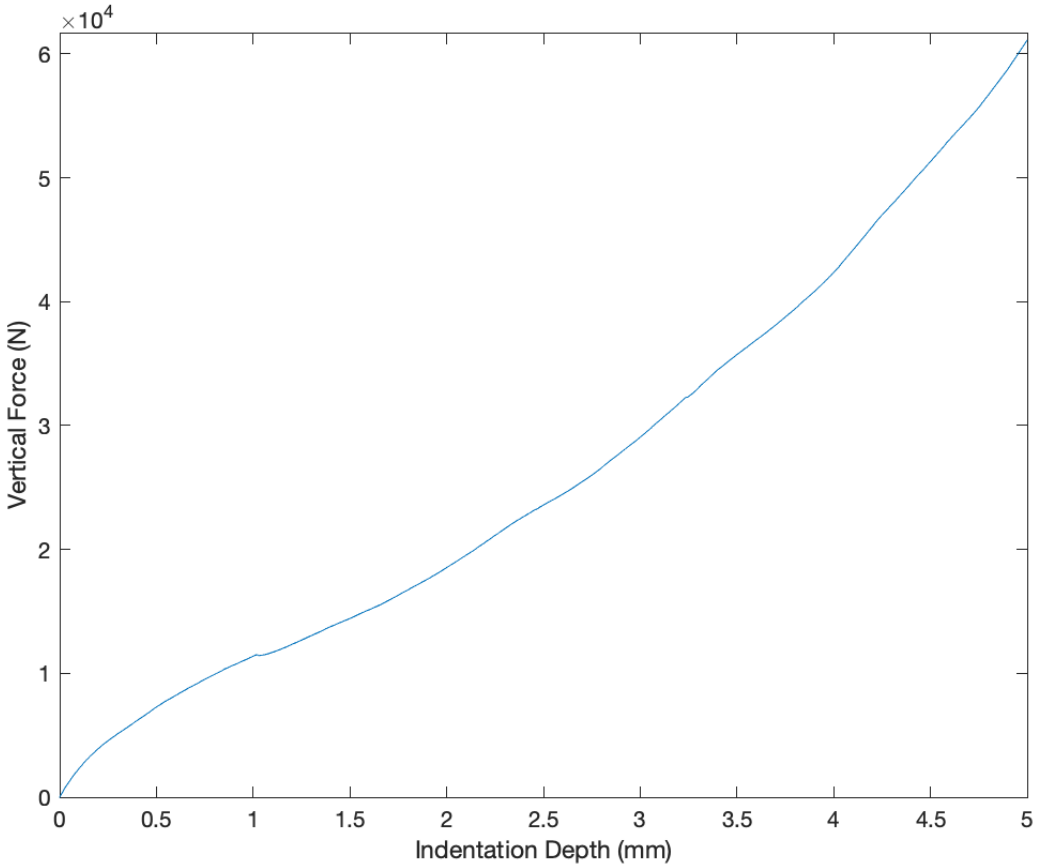

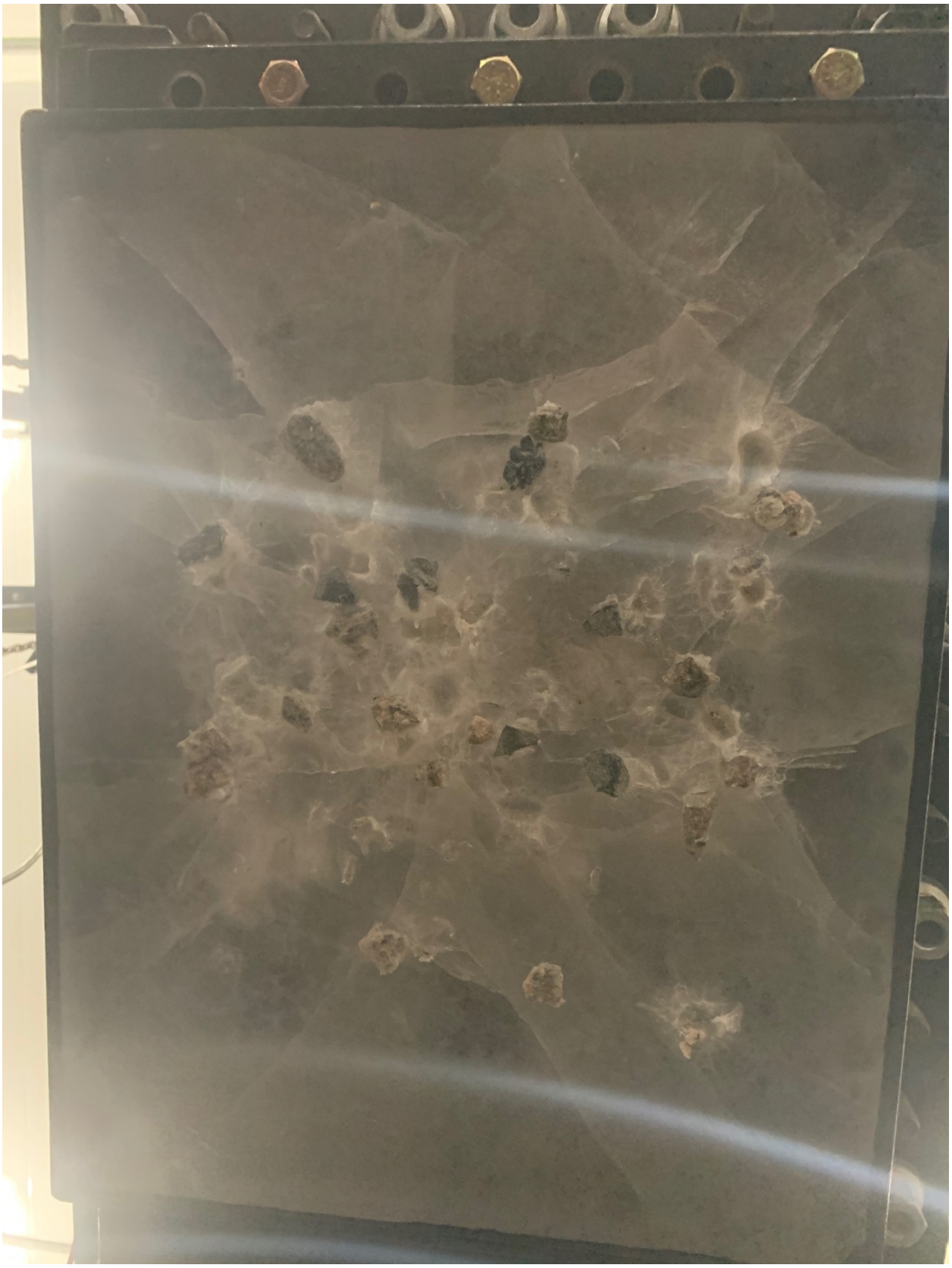

2020_25_11_(1)-7-5-1

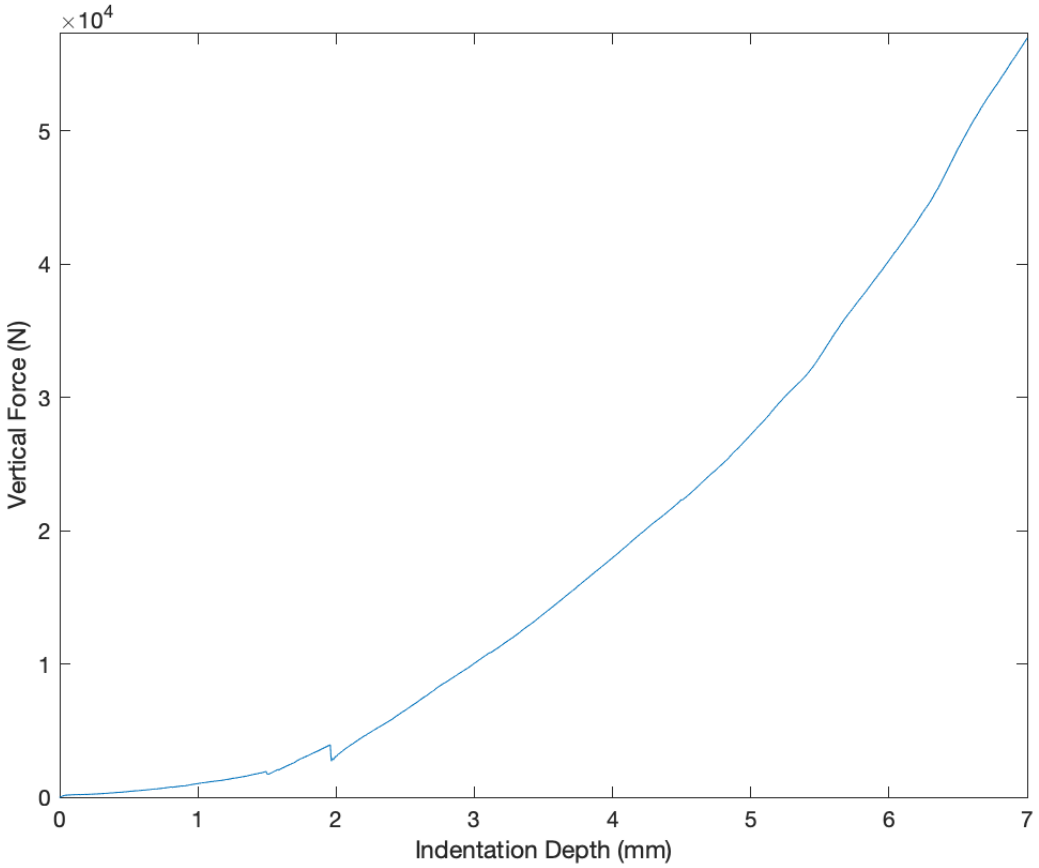

2020_25_11_(2)-7-5-1

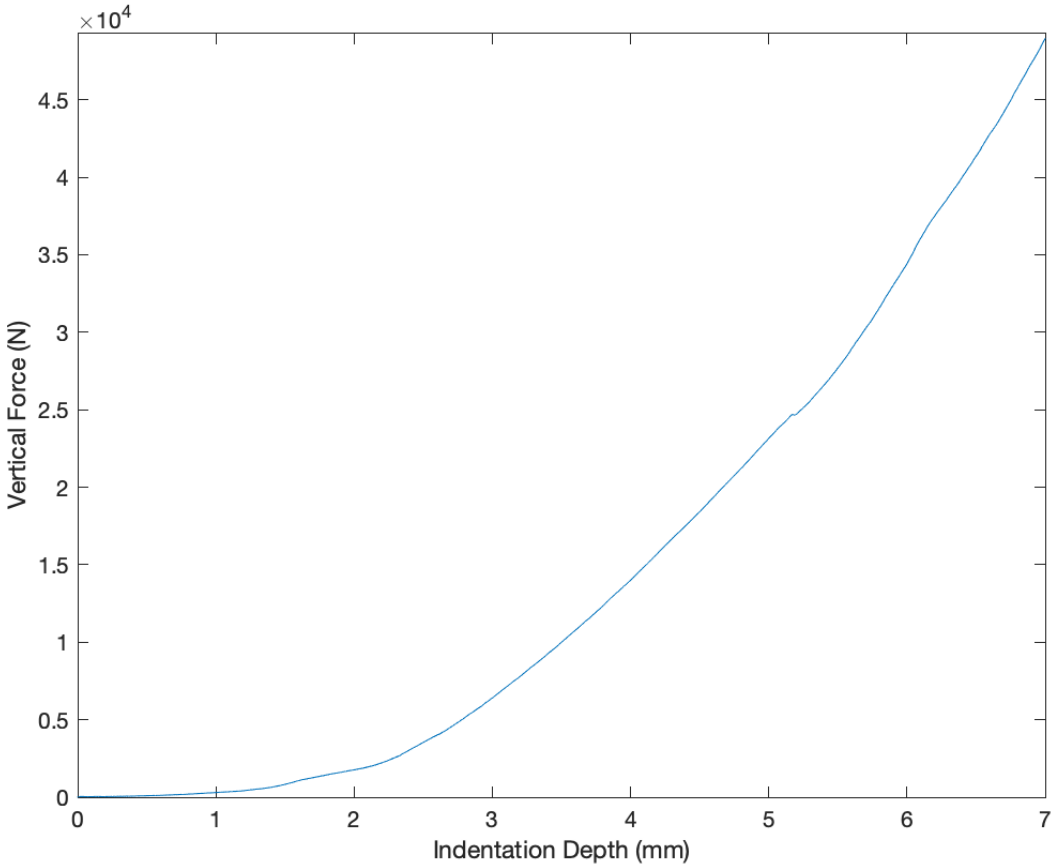

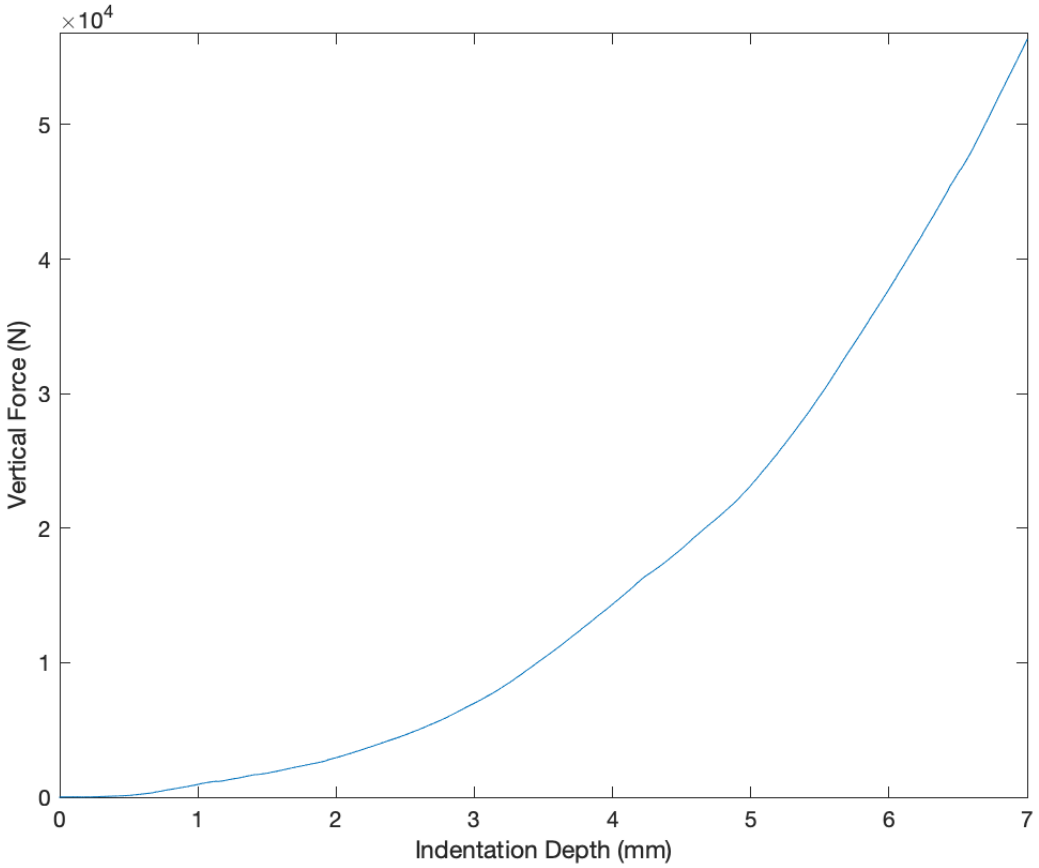
×10^4
5
4
3
2
1
0
Vertical Force (N)
0
1
2
3
4
5
6
7
Indentation Depth (mm)

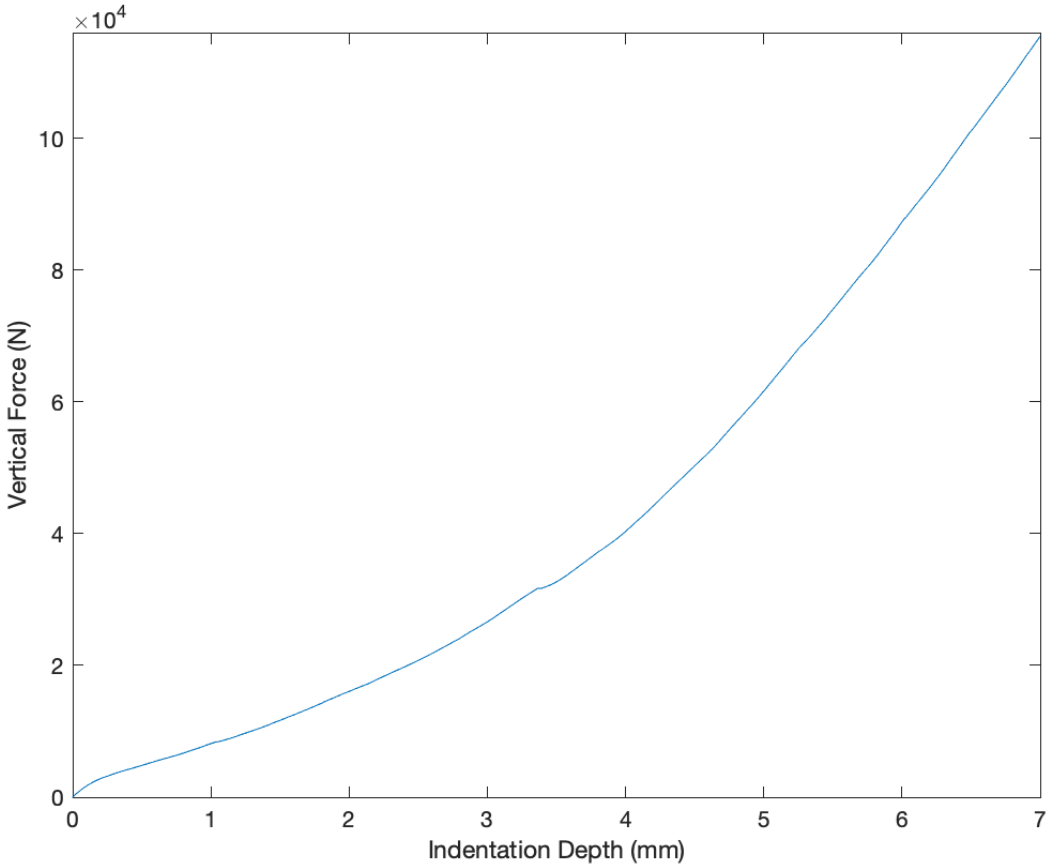
×10^4
10
8
6
4
2
0
Vertical Force (N)
0
1
2
3
4
5
6
7
Indentation Depth (mm)

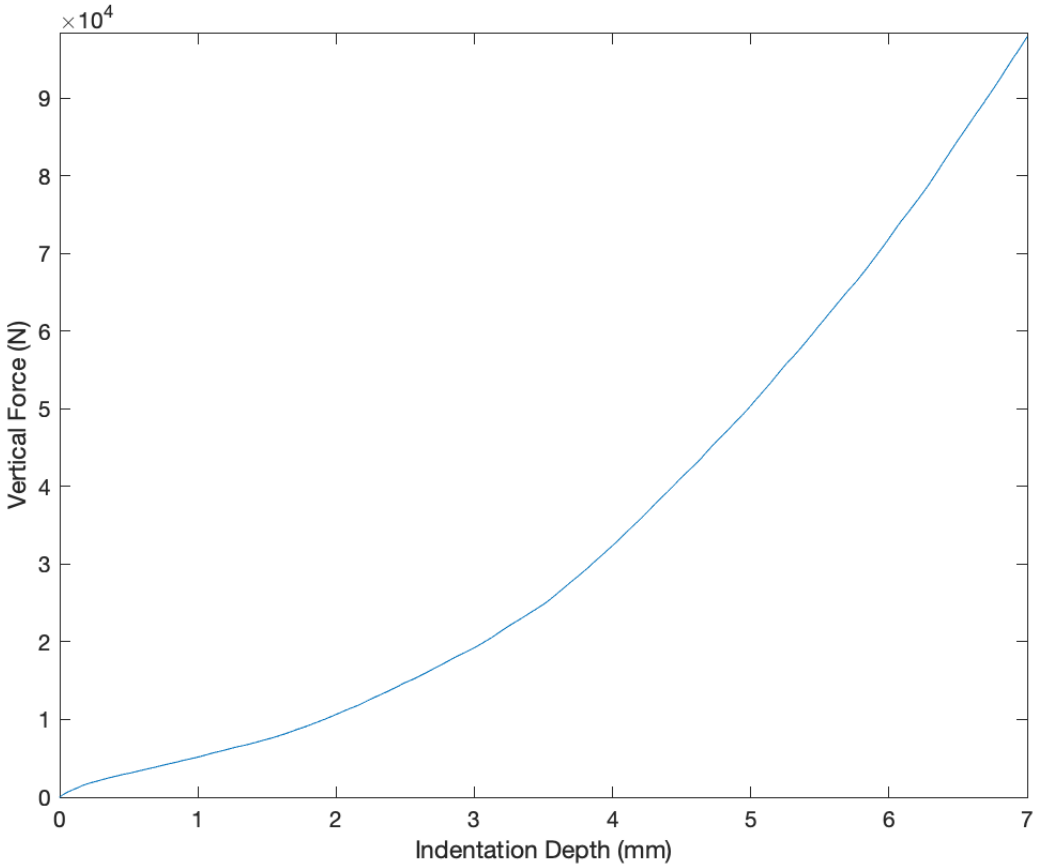
×10^4
9
8
7
6
5
4
3
2
1
0
Vertical Force (N)
0
1
2
3
4
5
6
7
Indentation Depth (mm)

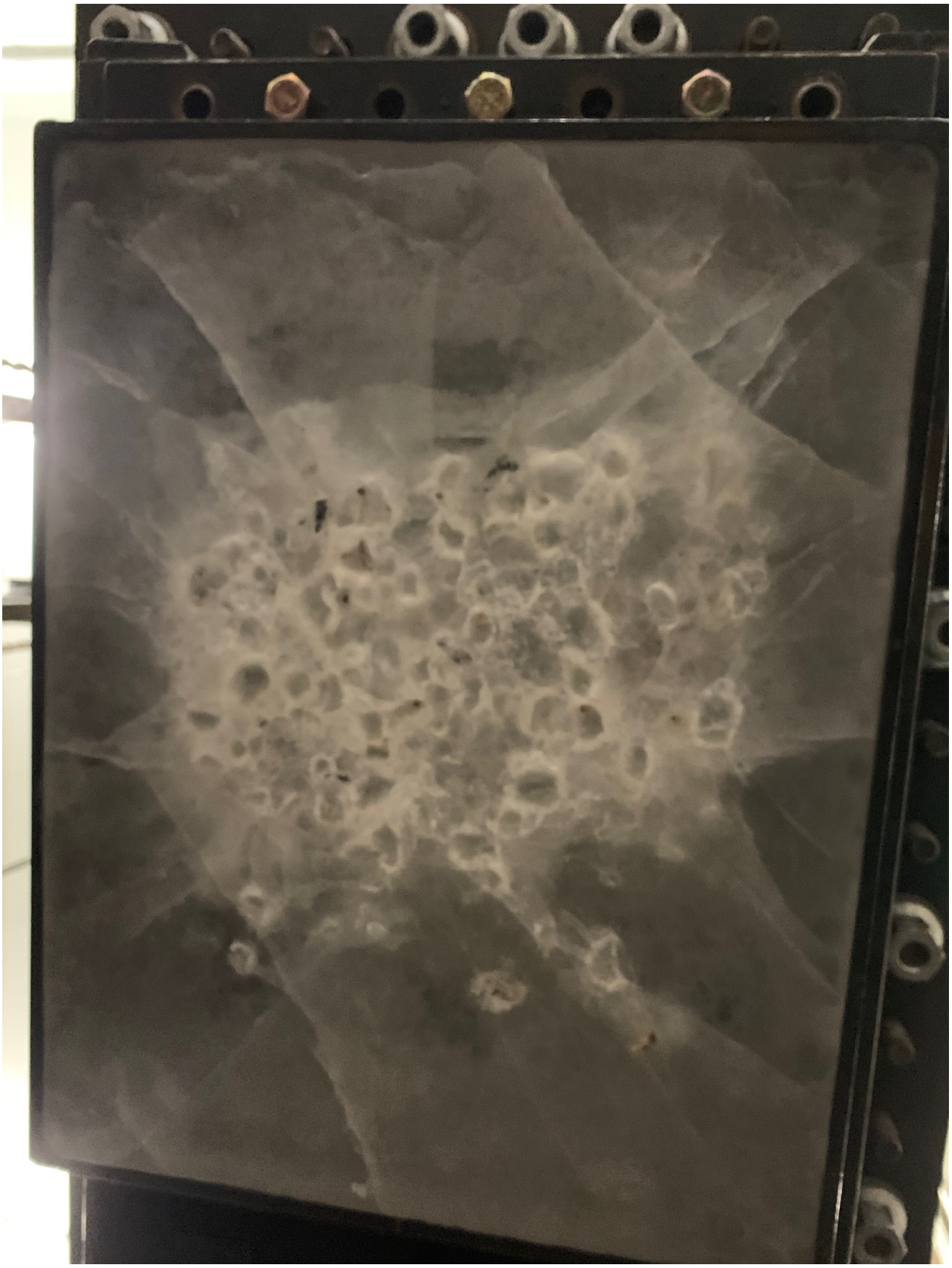

2020_25_11_(6)-7-7-1

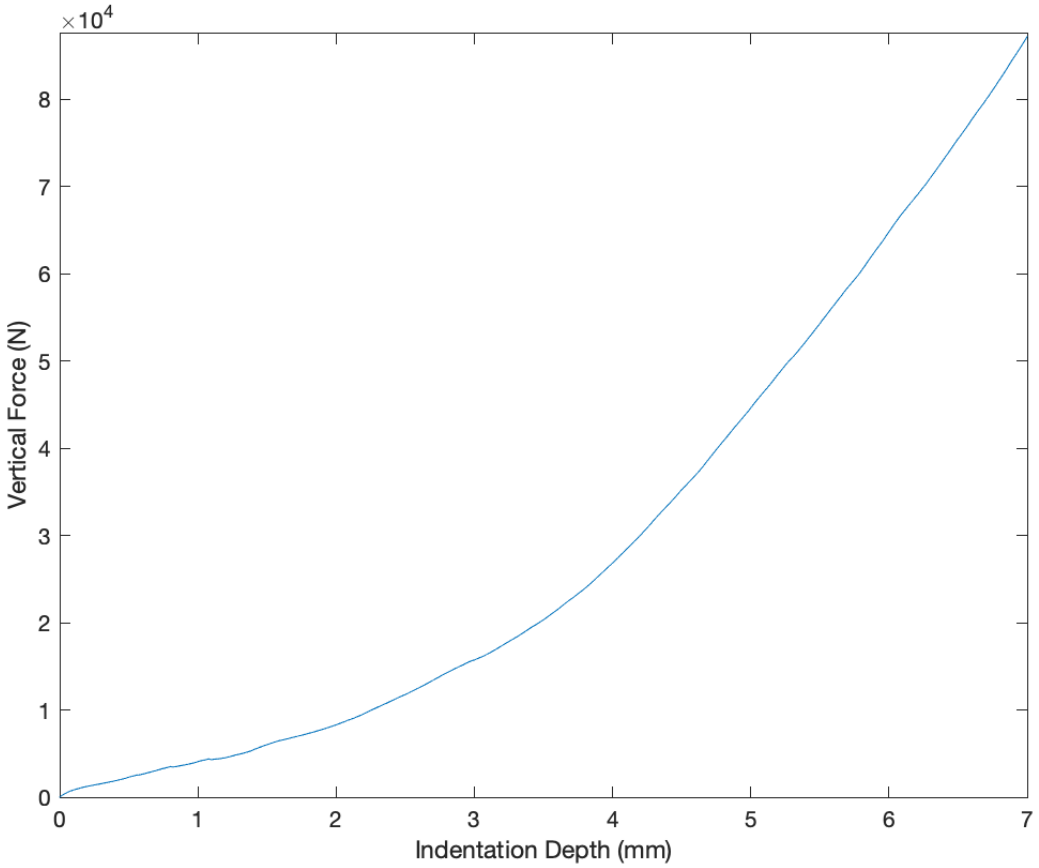

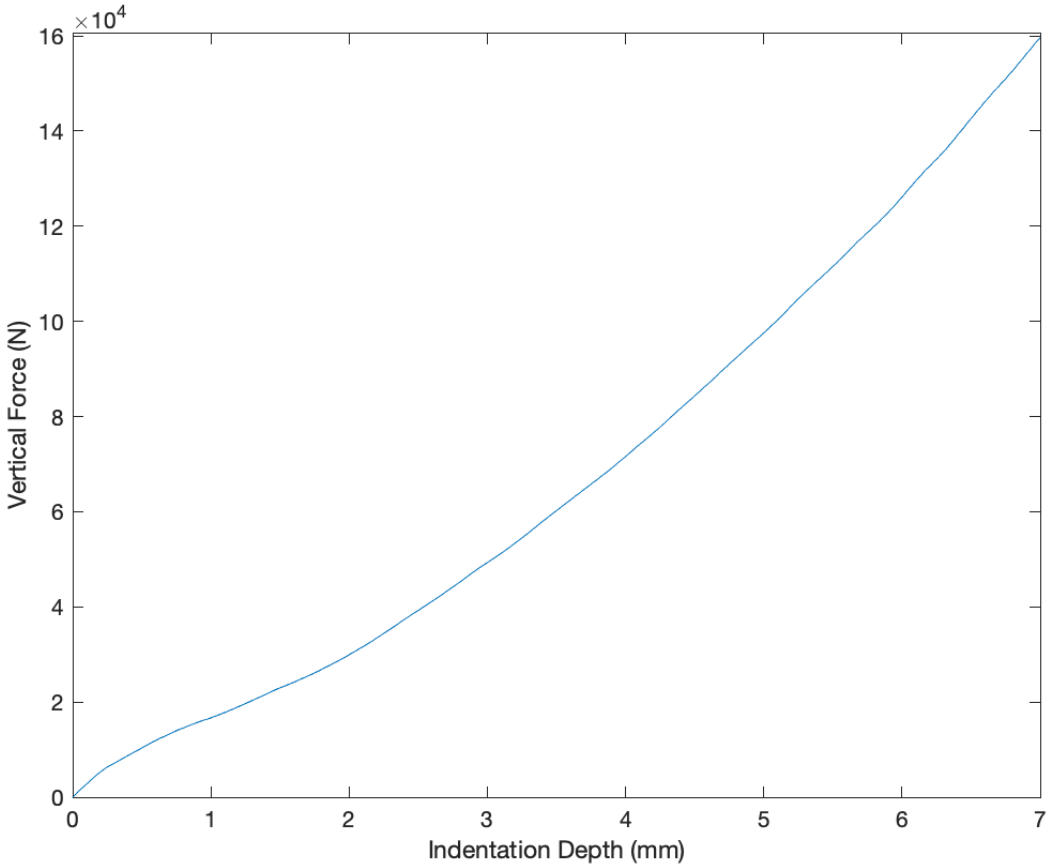
×10^4
16
14
12
10
8
6
4
2
0
Vertical Force (N)
0
1
2
3
4
5
6
7
Indentation Depth (mm)

2020_26_11 (2)-7-7-1

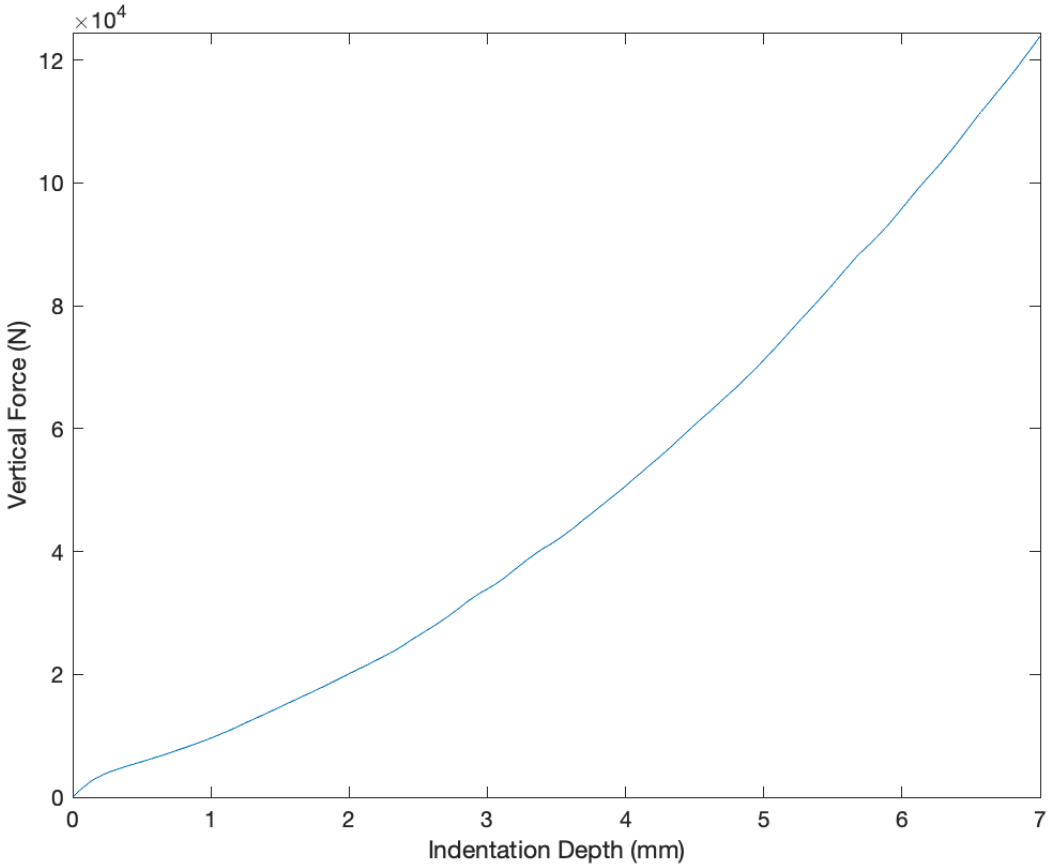

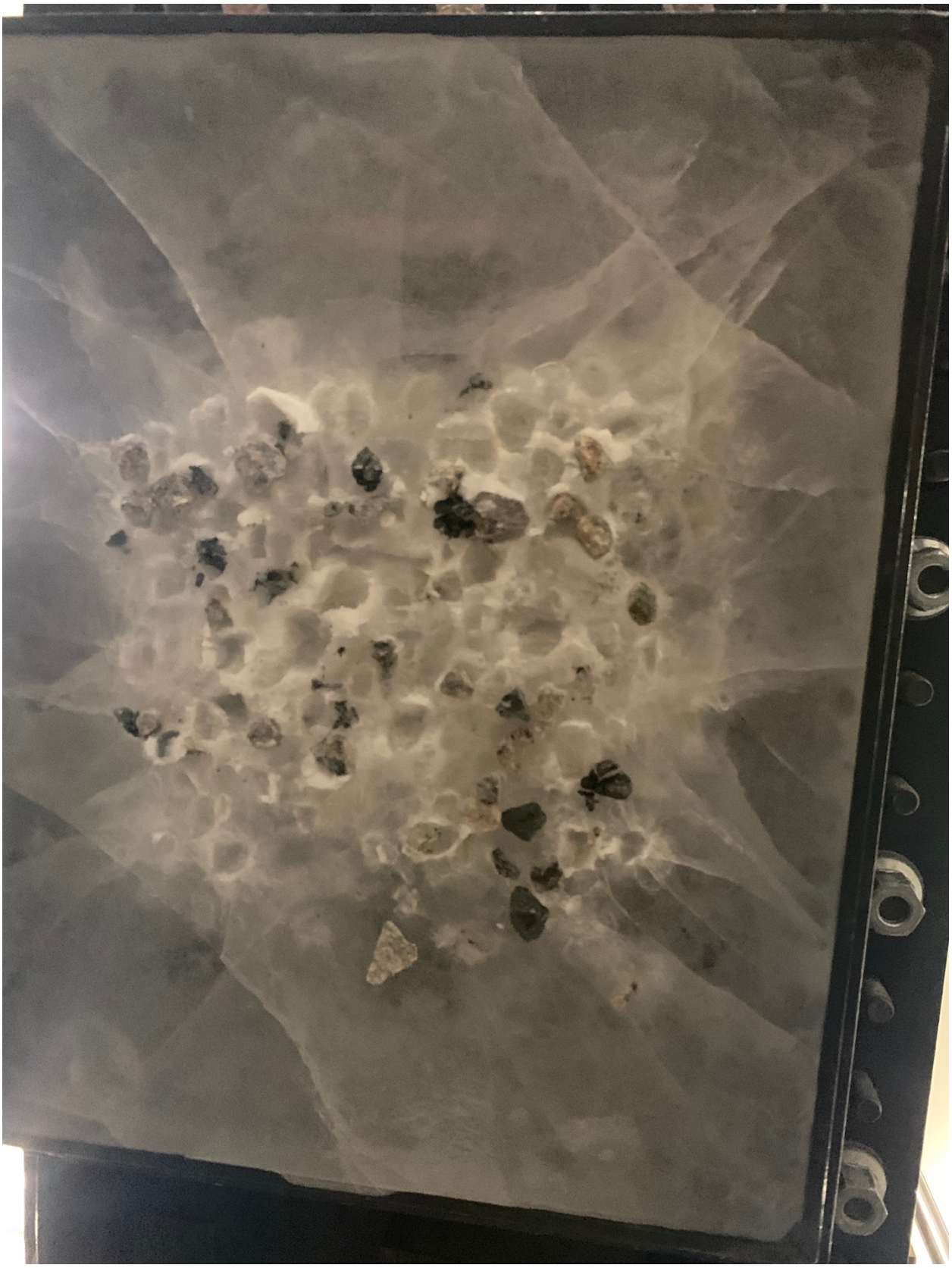

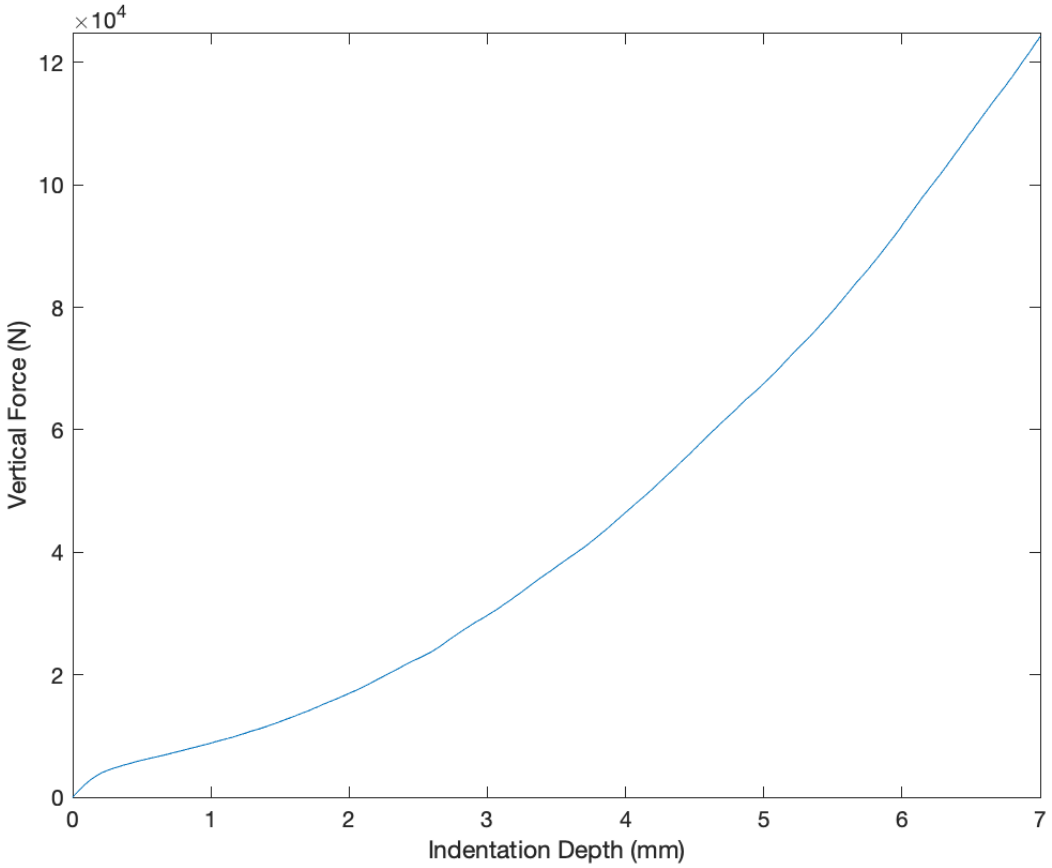
×10^4
12
10
8
6
4
2
0
Vertical Force (N)
0
1
2
3
4
5
6
7
Indentation Depth (mm)

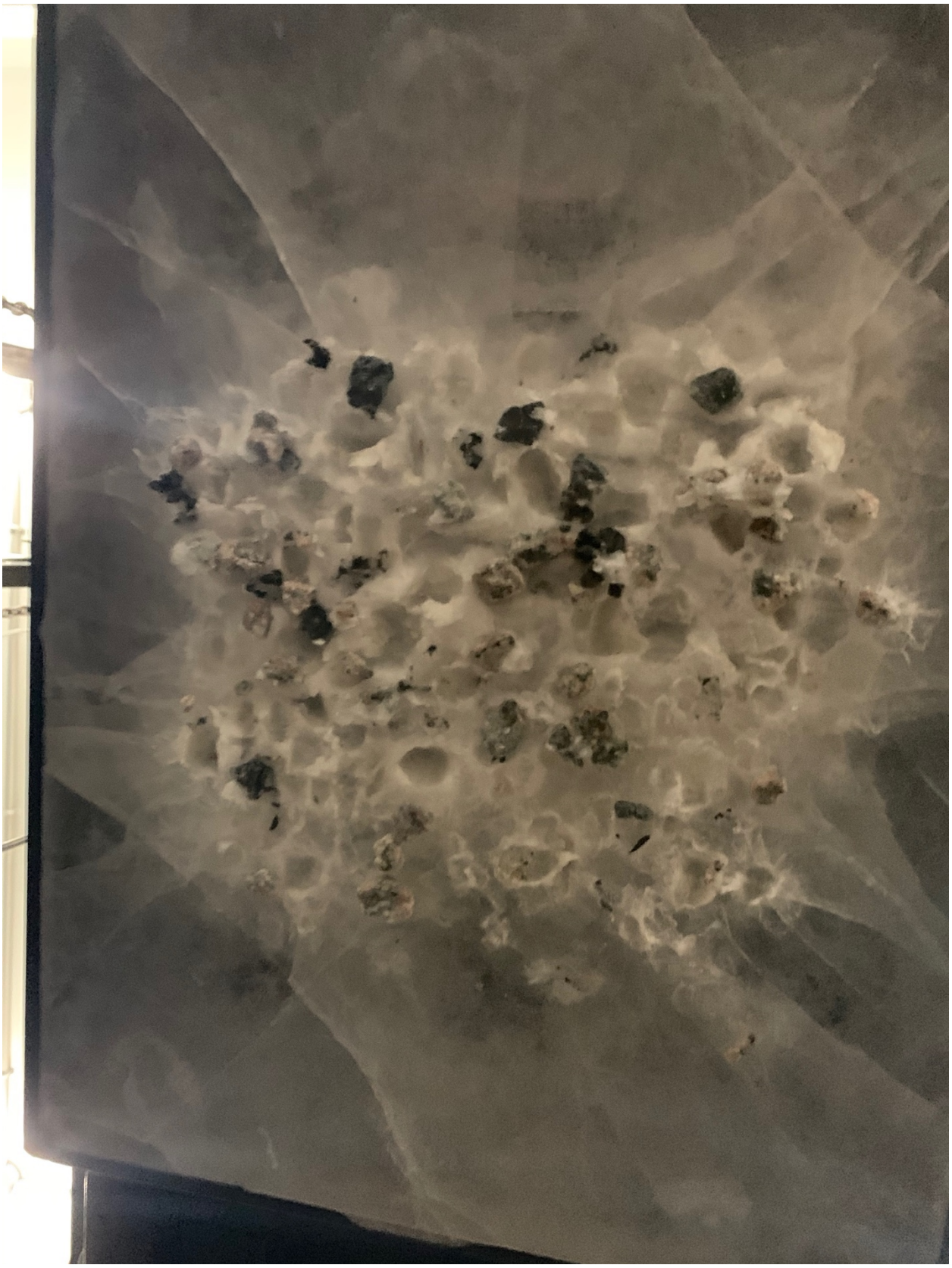

2020_27_11_(1)-7-7-1

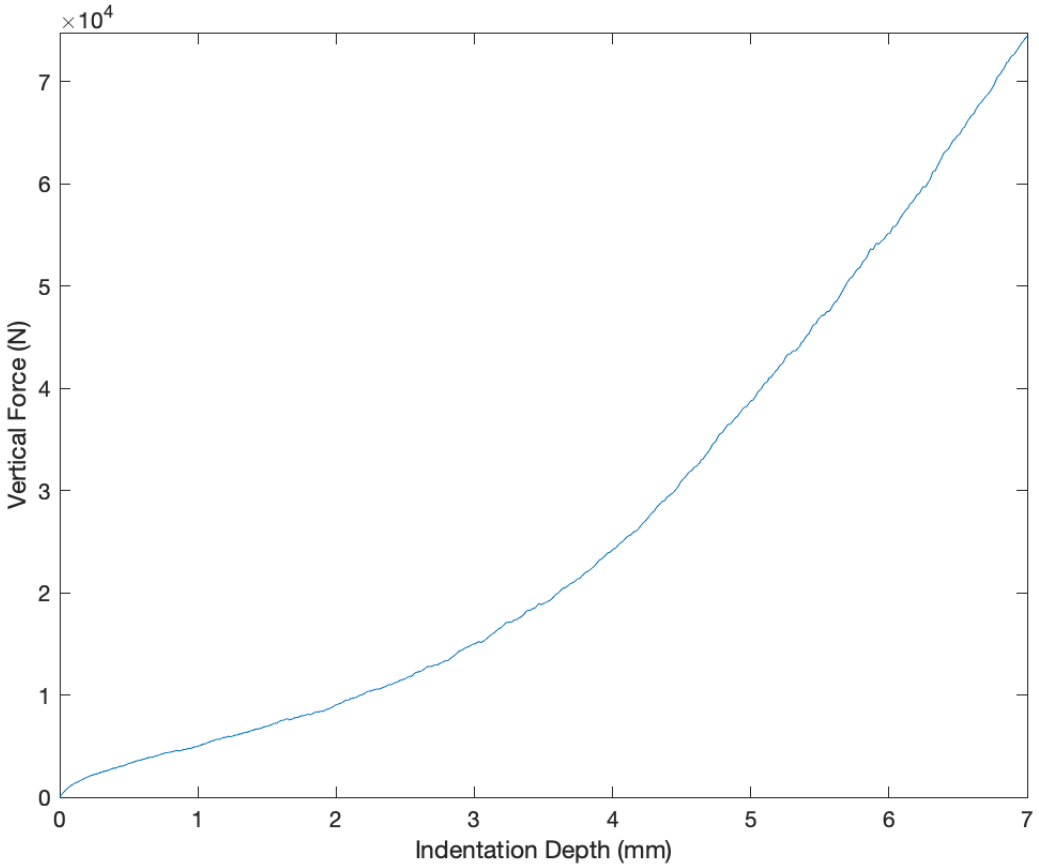

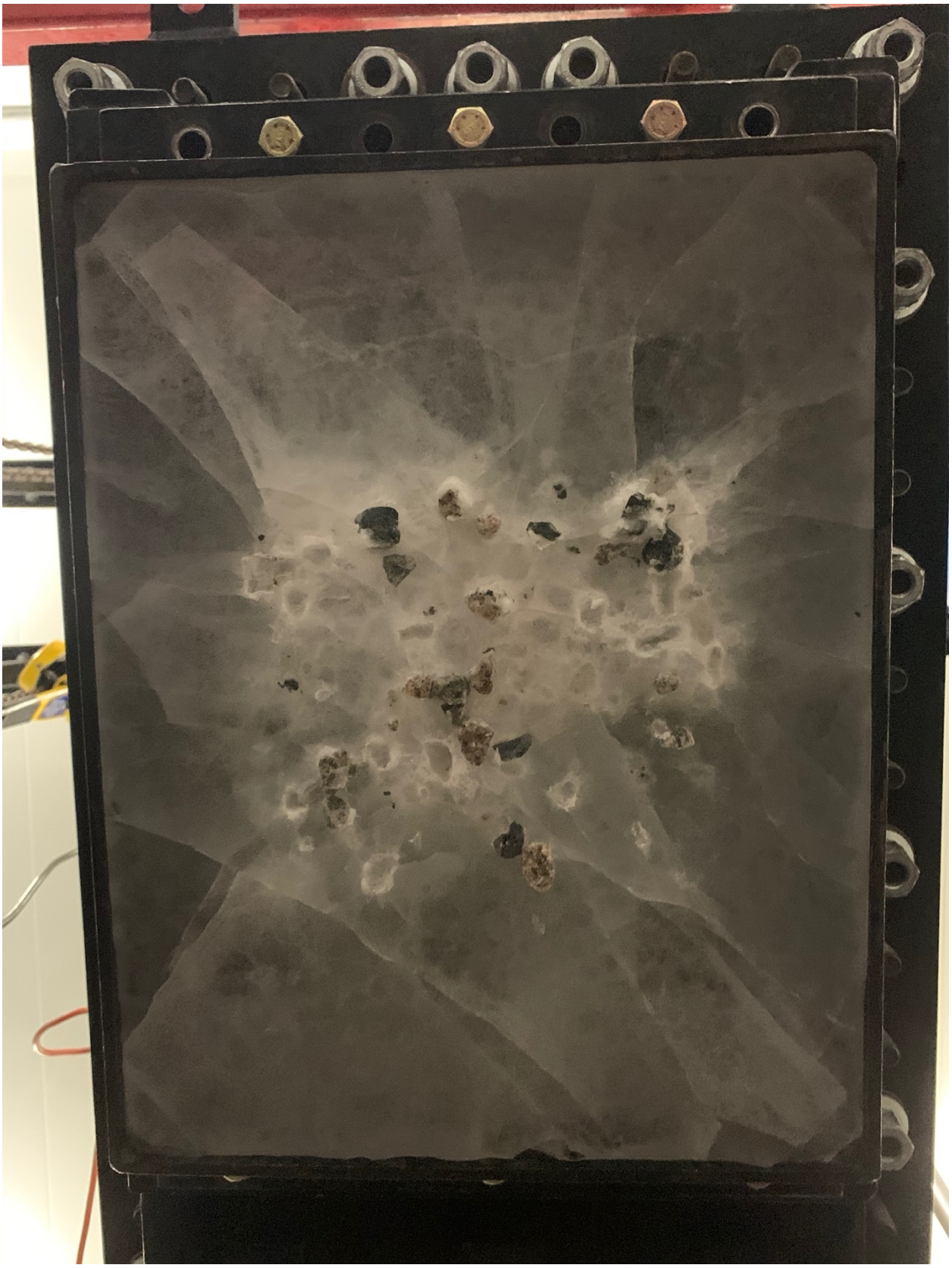

2020_27_11_(2)-7-7-1

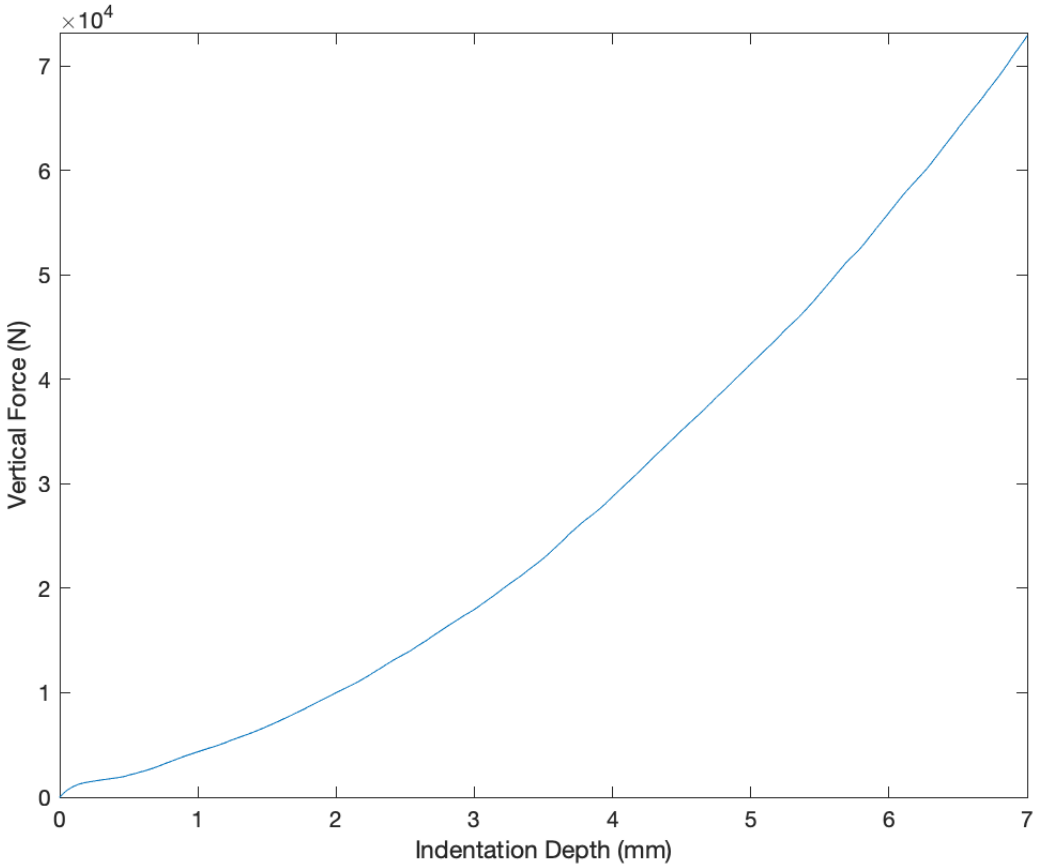

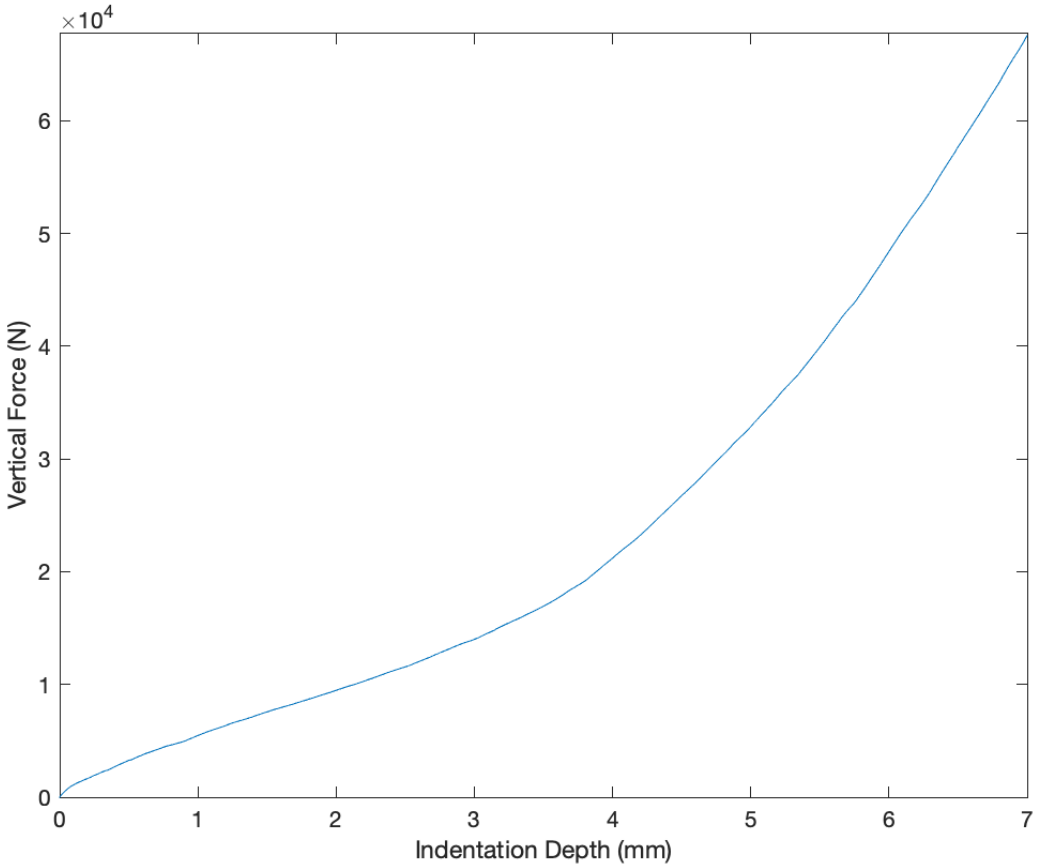
×10^4
6
5
4
3
2
1
0
Vertical Force (N)
0
1
2
3
4
5
6
7
Indentation Depth (mm)

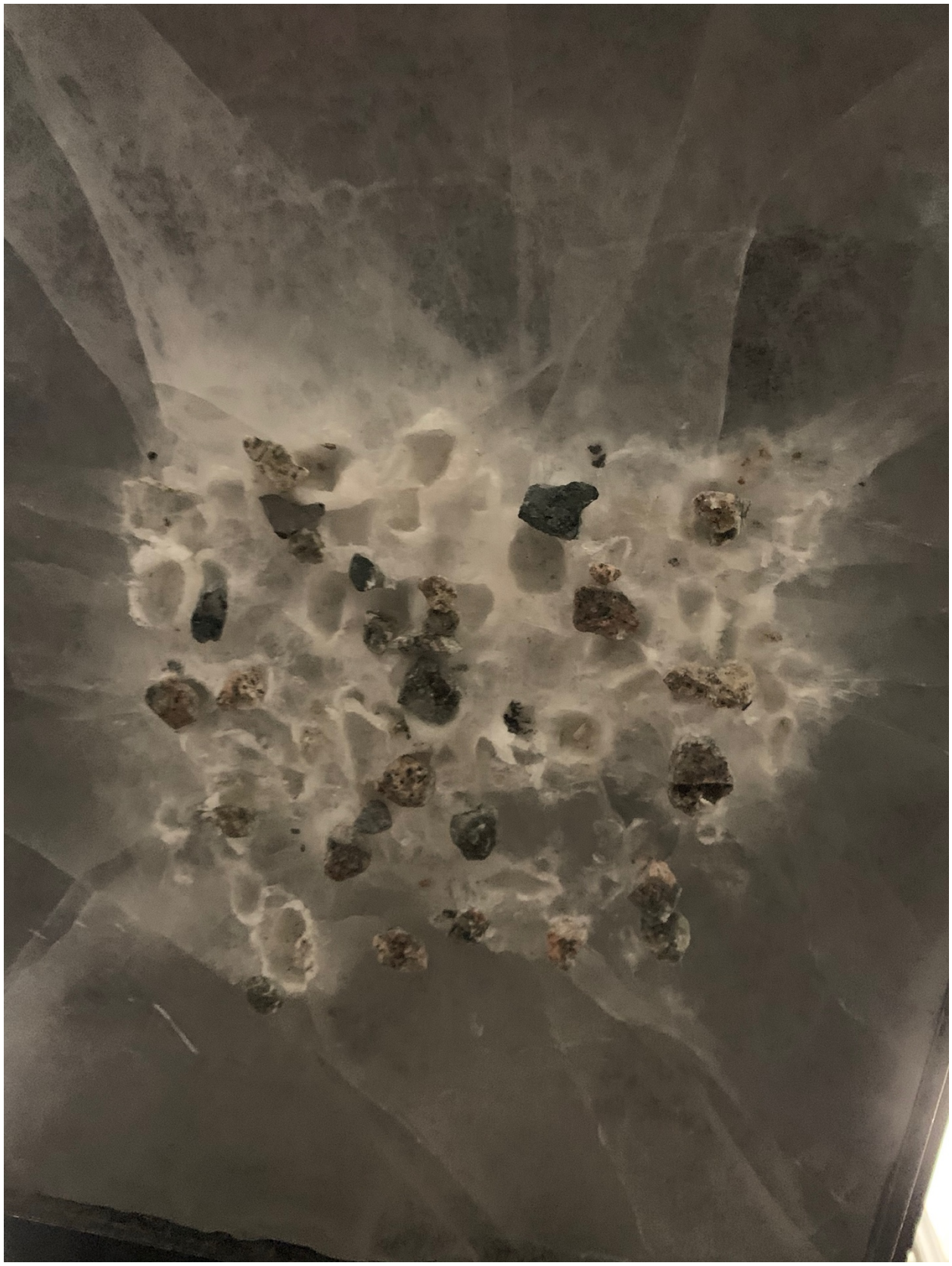

2020_17_12_(1)-7-5-1

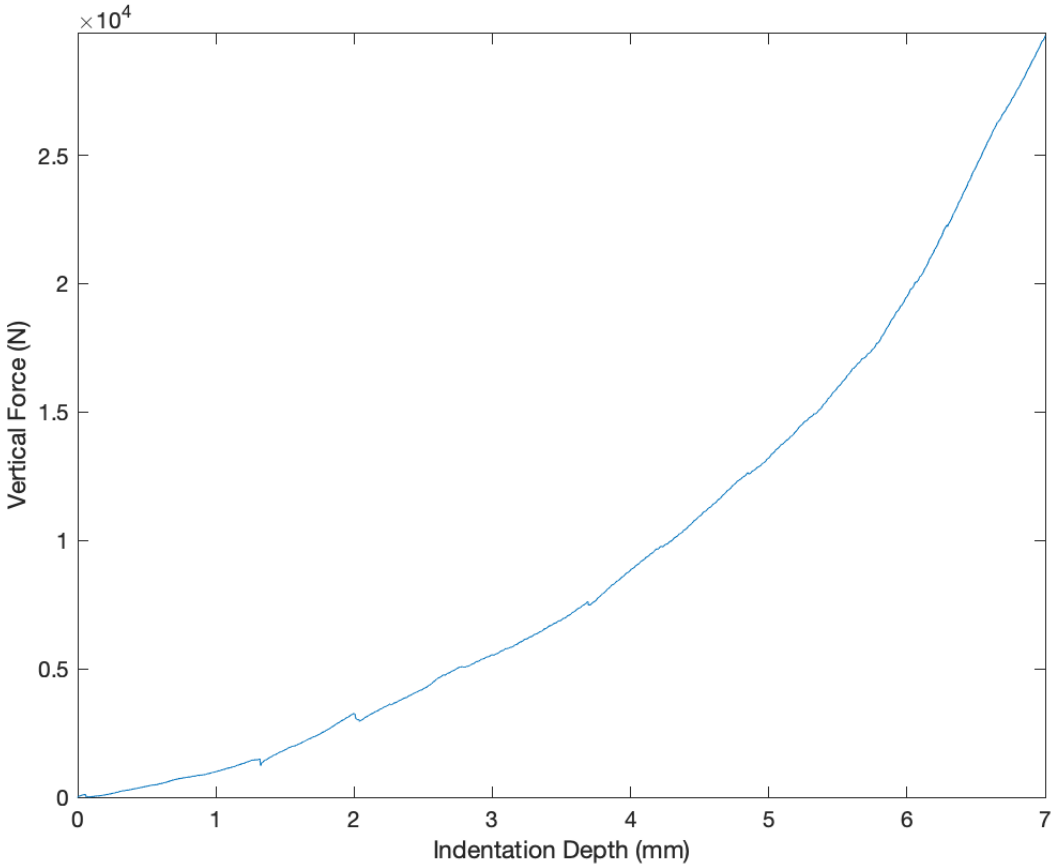

Image omitted due to poor quality.

2020_17_12_(2)-5-7-1

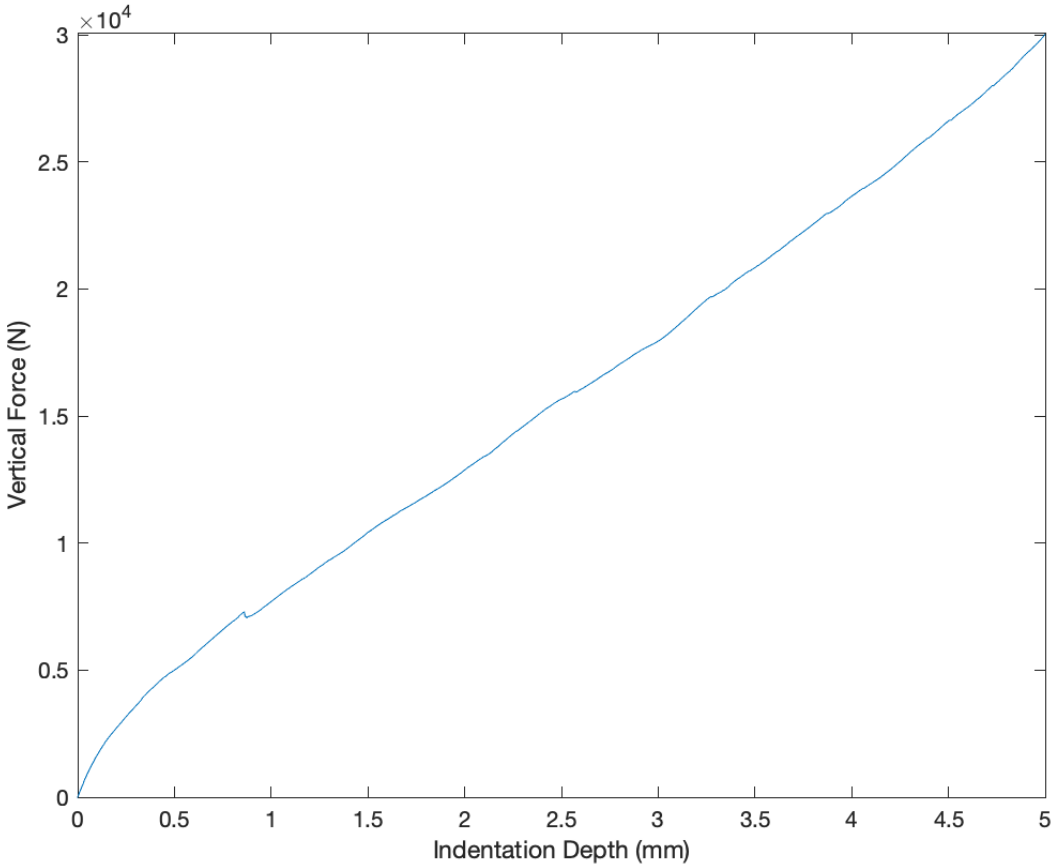

Image omitted due to poor quality.

2020_17_12_(3)-5-5-1

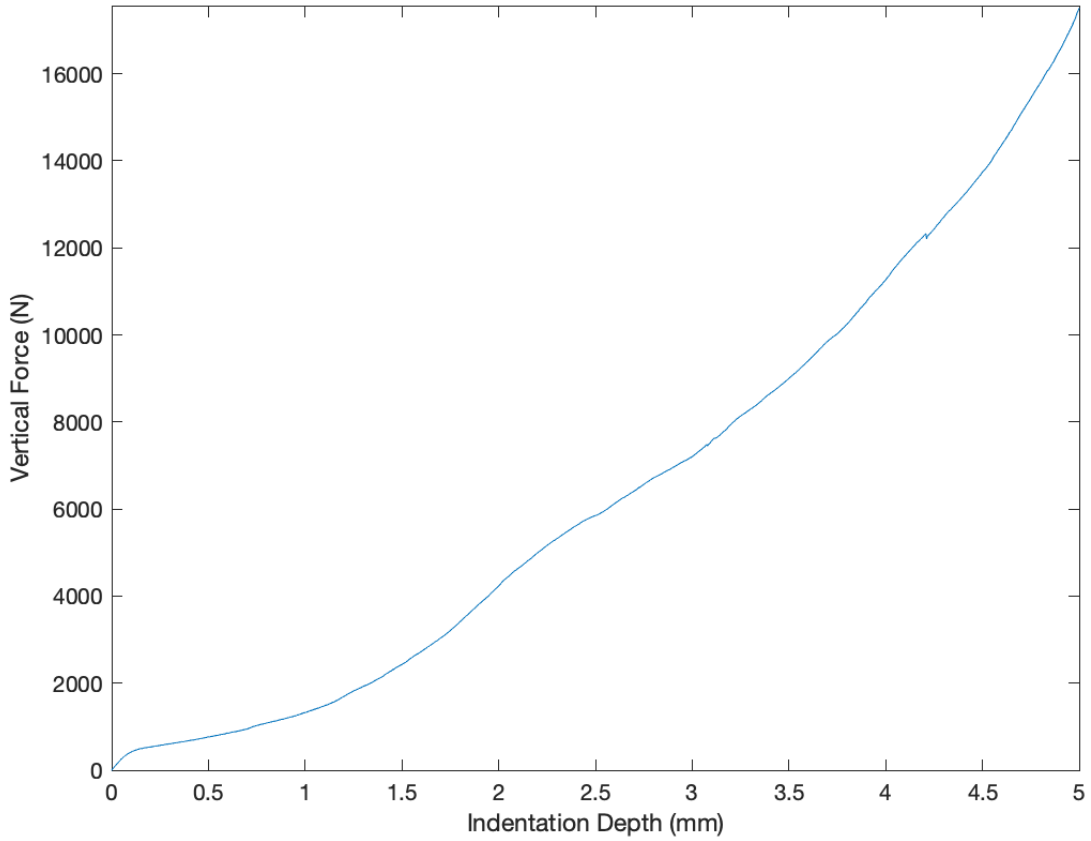

Image omitted due to poor quality.

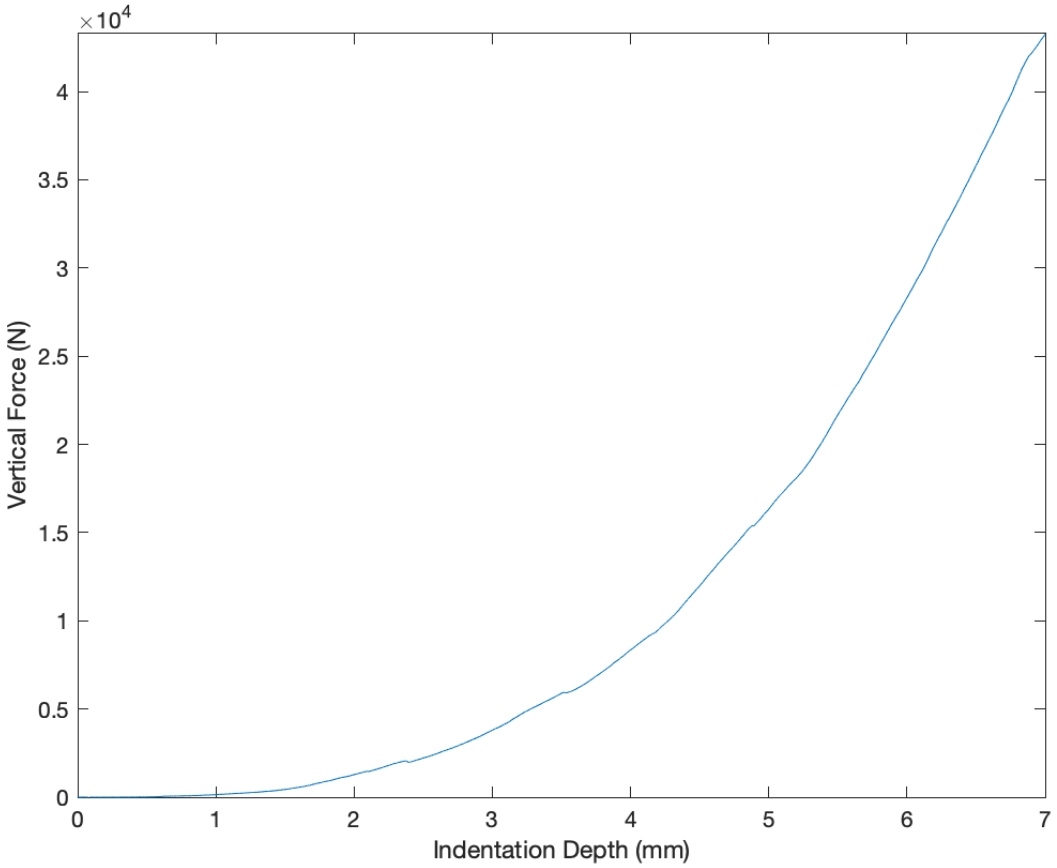

Image omitted due to poor quality.

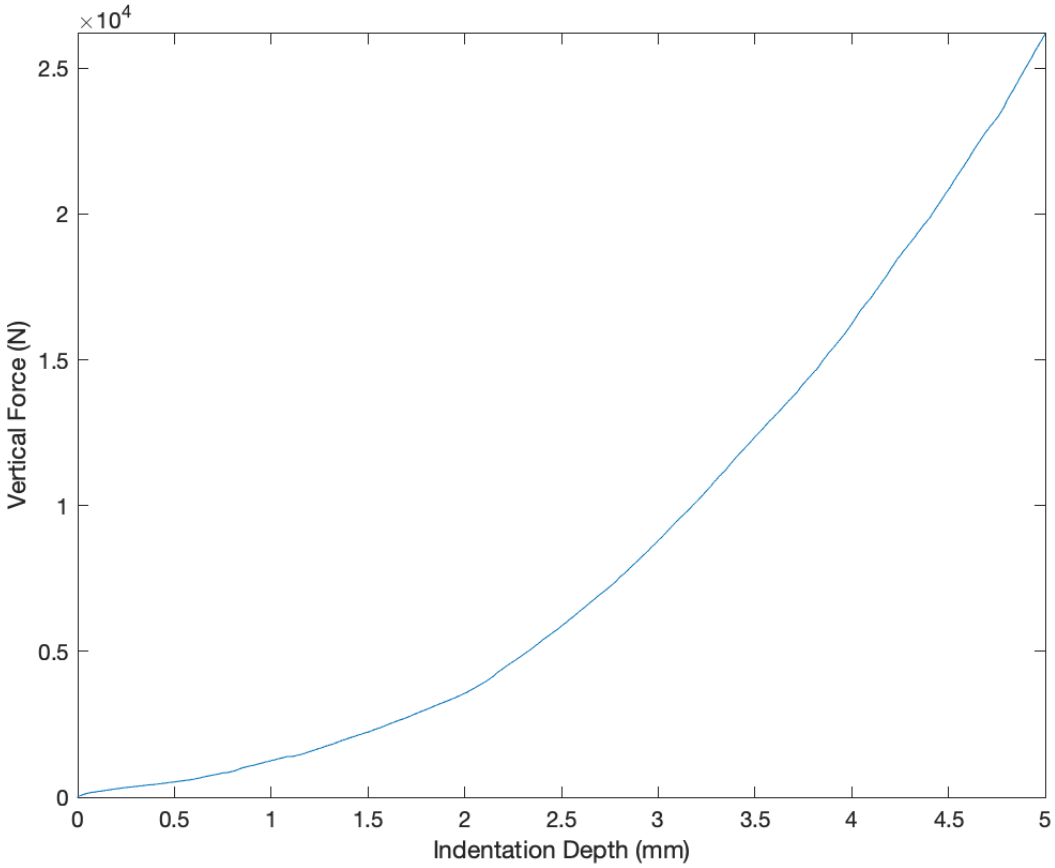

Image omitted due to poor quality.

2020_17_12_(6)-5-5-1

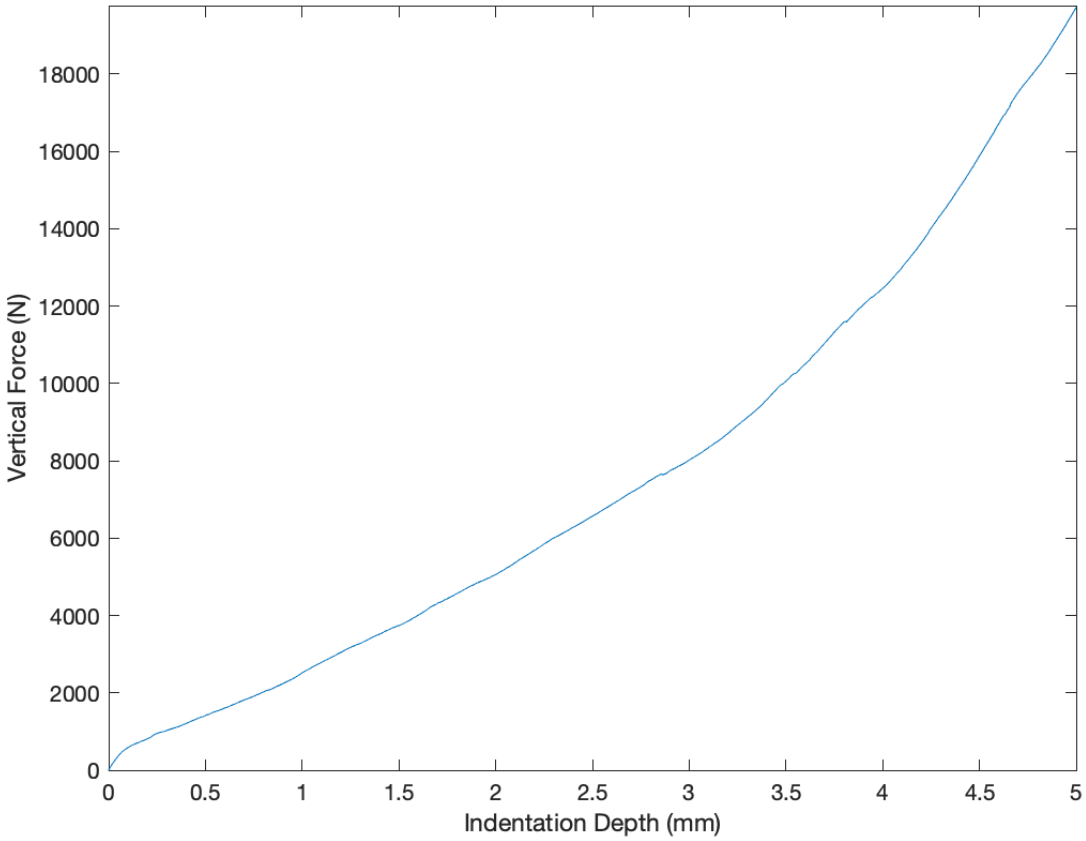

Image omitted due to poor quality.

2020_17_12_(7)-7-7-1 Water froze on gravel sample

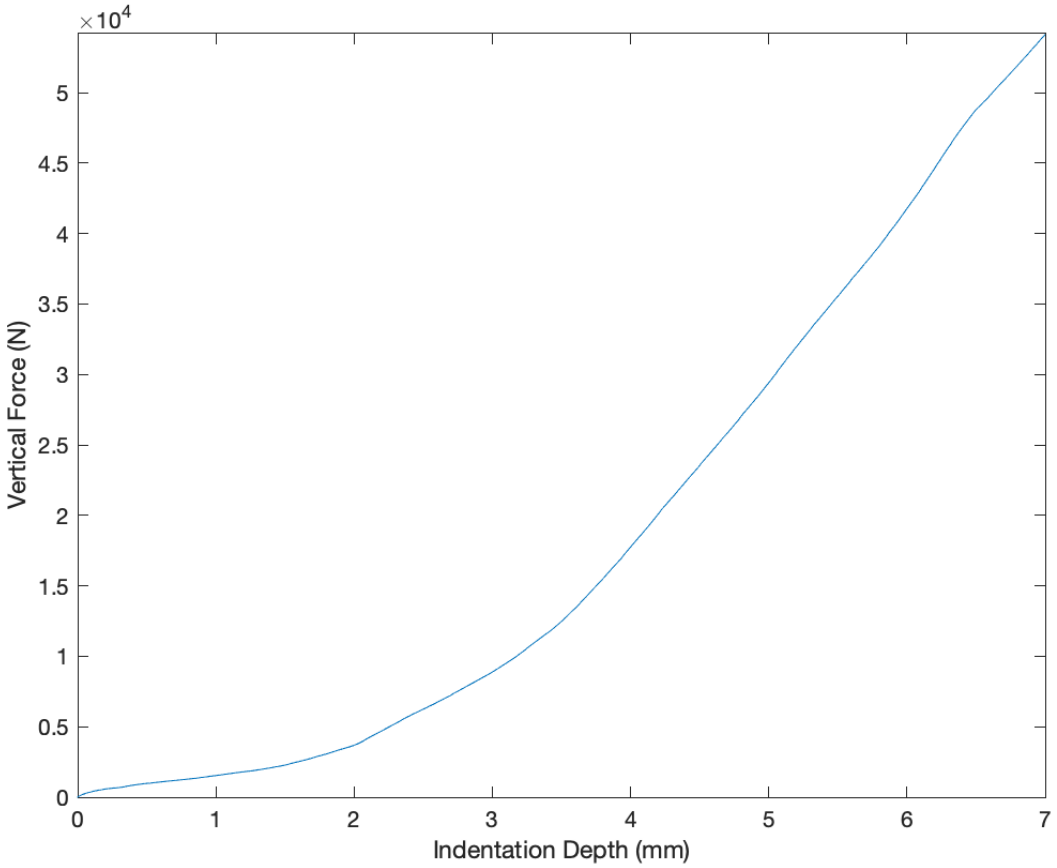

Image omitted due to poor quality.

2020_17_12_(8)-5-7-1

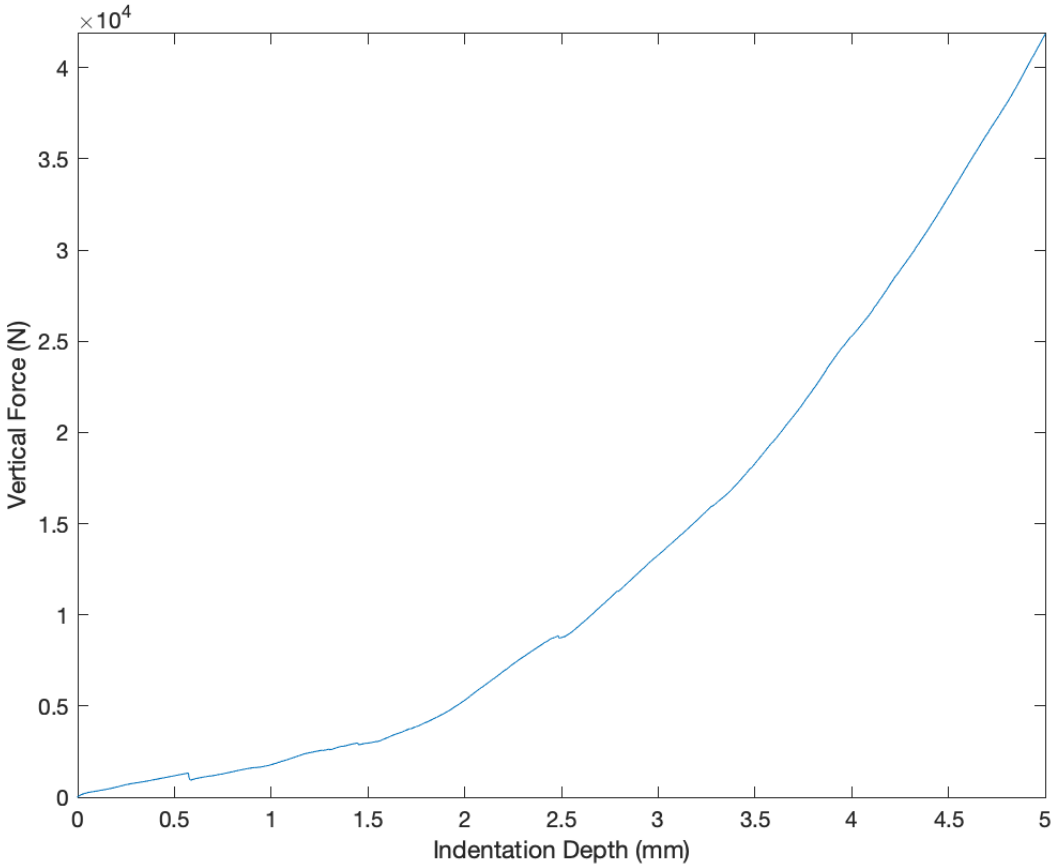

Image omitted due to poor quality.

2020_17_12_(9)-7-5-1

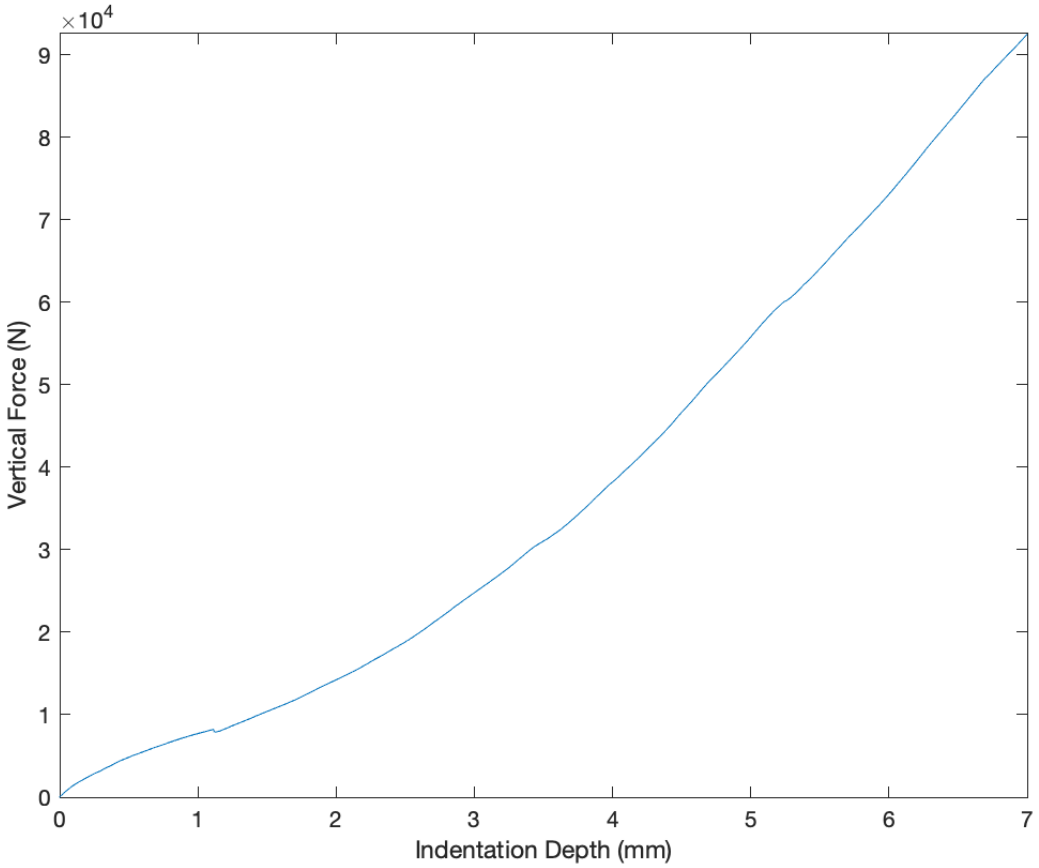

Image omitted due to poor quality.

2020_17_12_(10)-5-5-1

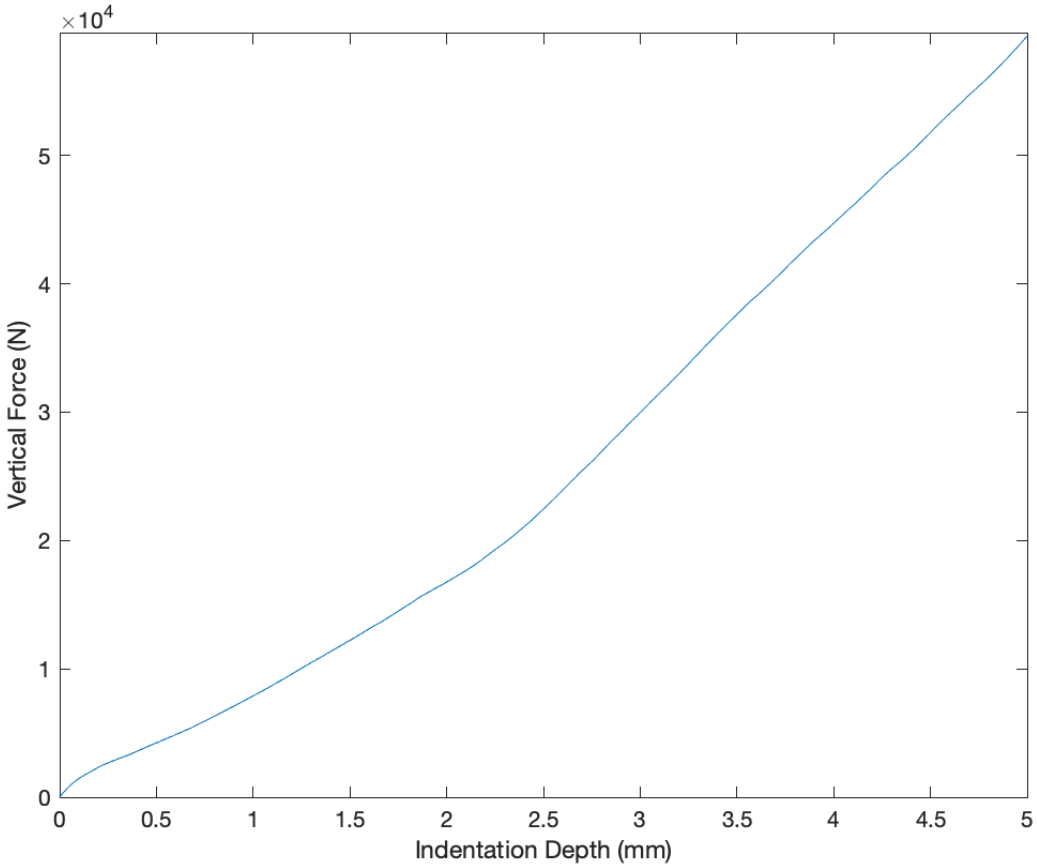

Image omitted due to poor quality.